Imperial College London

DEVELOPMENT OF AN ONLINE PROGRESSIVE MATHEMATICAL MODEL OF NEEDLE DEFLECTION FOR APPLICATION TO ROBOTIC-ASSISTED PERCUTANEOUS INTERVENTIONS

Elnaz Salehzadeh Nobari

Mechanical Engineering

Imperial College London

December 2015

This thesis is submitted to Imperial College London in partial fulfilment of the requirements for the degree of Doctor of Philosophy.

DECLARATION OF ORIGINALITY

I declare that the research presented in this thesis is my own work and contains no material previously published, or substantially overlapping with material submitted for the award of any other degree at any institution, to the best of my knowledge. Information extracted from other's published or unpublished work has been acknowledged in the text, and references are provided in the bibliography.

Elnaz Salehzadeh Nobari

August 30, 2015

ABSTRACT

A highly flexible multipart needle is under development in the Mechatronics in Medicine Laboratory at Imperial College, with the aim to achieve multi-curvature trajectories inside biological soft tissue, such as to avoid obstacles during surgery. Currently, there is no dedicated software or analytical methodology for the analysis of the needle's behaviour during the insertion process, which is instead described empirically on the basis of experimental trials on synthetic tissue phantoms. This analysis is crucial for needle and insertion trajectory design purposes. It is proposed that a real-time, progressive, mathematical model of the needle deflection during insertion be developed. This model can serve three purposes, namely, offline needle and trajectory design in a forward solution of the model, when the loads acting on needle from the substrate are known; online, real-time identification of the loads that act on the needle in a reverse solution, when the deflections at discrete points along the needle length are known; and the development of a sensitivity matrix, which enables the calculation of the corrective loads that are required to drive the needle back on track, if any deviations occur away from a predefined trajectory.

Previously developed mathematical models of needle deflection inside soft tissue are limited to small deflection and linear strain. In some cases, identical tip path and body shape after full insertion of the needle are assumed. Also, the axial load acting on the needle is either ignored or is calculated from empirical formulae, while its inclusion would render the model nonlinear even for small deflection cases. These nonlinearities are a result of the effects of the axial and transverse forces at the tip being co-dependent, restricting the calculation of the independent effects of each on the needle's deflection. As such, a model with small deflection assumptions incorporating tip axial forces can be called "quasi-nonlinear" and a methodology is proposed here to tackle the identification of such axial force in the linear range.

During large deflection of the needle, discrepancies between the shape of the needle after the insertion and its tip path, computed during the insertion, also significantly increase, causing errors in a model based on the assumption that they are the same. Some of the models developed to date have also been dependent on existing or experimentally derived material models of soft tissue developed offline, which is inefficient for surgical applications, where the biological soft tissue can change radically and experimentation on the patient is limited. Conversely, a model is proposed in this thesis which, when solved inversely, provides an estimate for the contact stiffness of the substrate in a real-time manner. The study and the proposed model and techniques involved are limited to two dimensional projections of the needle movements, but can be easily extended to the 3-dimensional case. Results which demonstrate the accuracy and validity of the models developed are provided on the basis of simulations and via experimental trials of a multi-part 2D steering needle in gelatine.

DEDICATION

To my loving mother and caring brother, who are my backbone in life…

And to my father, to whom I owe everything I am, and will ever be.

ACKNOWLEDGMENTS

I owe my family, friends and many colleagues for the completion of this work, as long as it took. It has been as long a journey to many of them as it has been to me, and they have shared the ups and downs of this work. I would not have been able to finish this work had it not been for their continuous kindness, support and patience.

I would like to first thank my supervisor, **Doctor Ferdinando Rodriguez Y Baena**, who guided and helped me with incredible patience during this work, and has been fundamental in shaping and molding the work in thesis from an idea, to something presentable. He provided me with guidance and support while allowing me to work at my own eccentric and unpredictable methodology. Above all else, Dr Rodriguez has my immense gratitude for believing in my work and encouraging me, even at stages when it became incredibly frustrating and tiresome.

I would also like to thank **Dr Danielle Dinni,** who supported me throughout the work and especially during my transfer, providing me with solid grounding and practical scientific knowledge, which became essential in building the framework of the work. In addition, I thank **Professor Brian Davies**, who assisted in giving a professional and academic voice to my written thesis, while pointing out practical limitations and issues surrounding the work.

Mathew Oldfield, Seong Young Ko and **Luca Frasson** were all undeniably instrumental in surviving the first years of my Ph.D. Mathew has taught me how to look at results and data in a reasonable and methodological way, and assisted me throughout learning of FEM. Seong Young helped me with my MATLAB coding at times where I was beating my head against the monitor, and Luca provided me with a practical idea of the experimental setup and background of the needle studied in this work. I also thank **Stuart Bowyer,** who assisted me in coding, and maintaining my sanity throughout the last stages of the work.

Professor John Dear, **Kate J Lewis** and **Professor Andrew Amis** all provided me with support and understanding during personal problems I had to deal with while writing this thesis, and gave me the chance to finish it despite external circumstances delaying my progress. I would not have been able to finish it had it not been for their continuous understanding and help.

Special thanks is given to all past and present members of the MIM Lab specially **Tassanai, Sandra, Gorkem, Yaroslav, Hadi, Chris, Jassim** and **Ryo,** all encouraging and great colleagues and friends, who have each helped me in completing my work in various shapes and forms.

I thank my friends **Farnaz Ostovari**, **Nasrin Shahedkhah** and **Sara Moslemizadeh**, present and future Ph.D.s in their own right, who have sat through psychotic episodes of my hysterics, and calmed me with infinite tea and laughter. Farnaz with her level head, inspiring calmness and immense kindness, Nasrin through her loving sarcasm, incredible strength, and undying friendship, and Sara with her steadfast motivation, support and dependable presence, have made this work happen.

My brother, **Amin** and Mother, **Sharareh,** have both been put through more than any sibling and mother should endure through the course of the work. My brother has brought me numerous box of krispy krem and tolerated my screaming when I have hit walls in my work, walking me home at odd hours of the night. My mother has pushed and motivated me with undying love and kindness throughout the work. She has done ten times a Ph.D. I have, while having an infant daughter (me), and I am constantly in awe of her strength and love.

Lastly, and most important, I thank my Father, **Professor Ali Salehzadeh Nobari**. He has guided, supported, instructed and tolerated me throughout this work and been there every step of the way. He pushed me to move forward at every bump in the road, and removed immense obstacles no-one else was able to. His brilliance, encouragement and love is the *single most important reason* I ever attempted to do this work and was able to finish it despite everything. He has dealt with far more in my thesis and in my life that anyone can possibly imagine, and I doubt any other daughter in the world is as blessed as I am in her father. I cannot thank him enough if I tried, anything I am and everything I have, is because of him.

CONTENTS

TABLE OF FIGURES

TABLE OF TABLES

NOMENCLATURE

Parameter	Definition	Unit
a_i	Participation Factor of trial function N_i	-
k	Stiffness of distributed springs along the length of needle	[N/m^2]
l	Offset length of needle	[m]
q_1	Net Distributed contact force, acting on the top and bottom surface of the probe on L_{off} prior to offset geometry.	[N/m]
q_2	Net Distributed contact force, acting on the top and bottom surface of the probe on l at the offset geometry.	[N/m]
A	Cross sectional area of beam model of needle	[m^2]
C_i	Constants of trial function	-
E	Young's Modulus	MPa
E_f	Flexural Modulus	MPa
I	Second area of moment	[m^4]
L_i	The deflected length from the base of the needle to the tip	[m]
$L1_i$	The deflected length from base of the needle to the offset	[m]
N_i	Trial functions of the galerkin method	-
P	Acting force in three point bending test	[N]
R	Tip Cutting Force	[N]
R_v	The vertical component of the cutting force at the tip	[N]
R_h	The axial component of the cutting force at the tip	[N]
R_Ω	Residual of the Galerkin	-
W_i	Weight function of the WRM	-
Y_t	The deflection of the tip of the beam	[m]
Y_z	The deflection of the beam at section Z	[m]
Z_t	The z coordinate of the tip of the beam	[m]
α	Angle of curvature of any point on beam	[Radian]
γ	Cutting angle of the needle tip.	[Radian]
ϵ	Strain	-
ϵ_f	Flexural strain	-
λ	Regularization Parameter	-
π	Potential Function	-
ρ	Density	kg/m3
σ	Stress	Pa

τ_1	Top surface Distributed friction force acting on L_{off} prior to offset geometry.	[N/m]
τ_2	Top surface Distributed friction force acting on l at offset geometry.	[N/m]
τ_3	Bottom surface Distributed friction force acting on L_{off} prior to offset geometry	[N/m]
τ_4	Bottom surface Distributed friction force acting on l at offset interlock geometry.	[N/m]
φ_n	Mode shape of beam model of needle	-
ω	Natural frequency of beam model of needle	(Hz)
GSVD	Generalized Singular Value Decomposition	-
SVD	Singular Value Decomposition	-
TSVD	Truncated Singular Value Decomposition	-
WRM	Weighted Residual Method	-

1. INTRODUCTION

1.1. ROBOTIC ASSISTED NEEDLE STEERING

Recently, due to the development of robotics and the growing interest in minimally invasive surgery (MIS) procedures, robotic surgery has attracted much interest and research. Robotic assistance during surgery enables better control over the surgical instruments, as well as better visualisation of the surgical site. Robotics was initially used in neurosurgical procedures to aid the surgeon in manual surgery (Davies 2006), wherein fixtures were located at predefined locations near the head of the patient. Since then, mechatronics has progressed, and the use of robots in medical and surgical application has become commercially and medically viable across many surgical specialties.

One use of robotics in surgery is the subcutaneous inclusion of needles and other thin surgical instruments into soft tissue. It is employed to reach targets to perform surgery, as well as deliver drugs and other substances to predefined targets, while avoiding specified obstacles, such as nerves and vital blood vessels. During the procedure, the operating surgeon has limited visual and haptic feedback compared to conventional methods of surgery. Needle insertion is a necessary step in most medical procedures, including biopsy to obtain a specific tissue sample for testing, drug injections, stereotactic neurosurgery and brachytherapeutical cancer treatment. For example, the visual example of one of the recent procedures employing needle insertion is percutaneous vertebroplasty (PVP), presented in figure 1-1 (Kobayashi, Arai et al. 2009). PVP is a recent treatment for painful malignant vertebral compression fractures (PMVCF). During this procedure, bone cement is inserted into the targeted area with use of a metallic needle (figure 1-1A). The Needle is inserted under fluoroscopic guidance. The needle is retracted from the tissue after injection of cement (figure 1-1C) (Kobayashi, Arai et al. 2009).

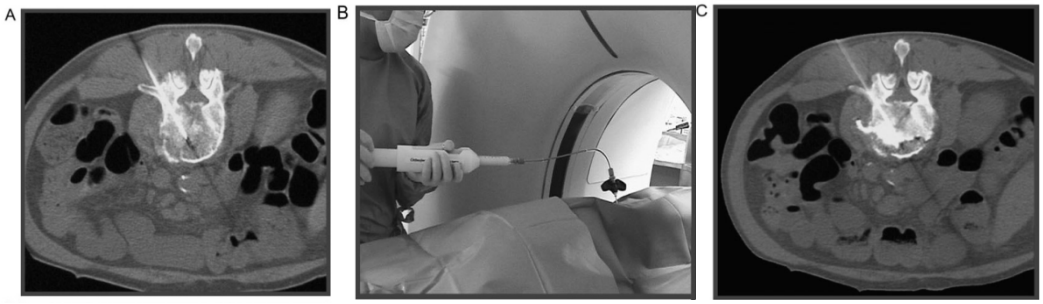

Figure 1-1 PVP.(A)Insertion of needle with fluoroscopic guidance.(C) Retraction of needle after injection(Kobayashi, Arai et al. 2009)

Employment of needles in MIS has many advantages. Due to the smaller incision needed when compared to conventional methods, the risk of infection, blood loss and haemorrhaging is significantly reduced. The decrease in scarring is an aesthetical advantage that becomes crucial in some procedures. The smaller tissue tearing, as well as the reduced strain on the internal surrounding organs, results in less postoperative pain inflicted on the patient. The reduced amount of recovery time is also economically efficient.

One of the difficulties of medical robotics is in soft tissue surgery, wherein the tissue deforms during the procedure (Davies 2006). This makes prediction of the outcome of the procedure difficult, due to the complexities of biological soft tissue. During procedures, the physician must be able to access predefined targets inside organs, without damaging surrounding tissue. During needle insertion, this condition introduces two difficulties; the needle must be able to reach the target sometimes surrounded by delicate tissue; at the same time, the path defined for the movement of the needle can be complex. Naturally, the needle must not miss its target, as this can result in the needle intersecting with areas of the surrounding tissue, with the potential to damage critical structures (e.g. a vessel). The lack of haptic (sense of touch) and visual feedback for the operating physician increases the reliance on experience and the physician's kinaesthetic knowledge of the procedure and his/her 3D anatomical knowledge of the lesion and organ being operated upon (i.e. three dimensional visualization).

1.1.1. ADVANTAGES OF STEERABLE NEEDLES

Various studies have been conducted on the use of robotically steered flexible needles inside soft tissue (Alterovitz, Goldberg et al. 2005, Crouch, Schneider et al. 2005, Goksel, Dehghan et al. 2009). A series of flexible bevel tip needles which bend in soft tissue (Webster, Kim et al. 2006, Swaney, Burgner et al. 2013) have been developed, wherein bending of the needle is achieved due to the asymmetry at the bevel edge. The asymmetries of the tip of these needles produce bending forces along the tip of the needle, which, along with the flexibility of the needle shaft, provide bending. Previous experiments have shown that this allows the needle to follow predefined curved paths, avoiding obstacles in the tissue (Misra, Reed et al. 2010). In order to avoid obstacles during insertion into soft tissue, multiple curvatures are desirable. To this end, a biologically inspired highly flexible multipart needle is currently under development at the Mechatronics in Medicine Laboratory (Imperial College, London, UK), as is explained bellow.

1.1.2. OVERVIEW OF THE STING PROJECT

The aim of this highly flexible needle is to enable effective soft tissue traversal with reduced stress delivery, achieved by means of a reciprocating mechanism, which is inspired by Nature (Frasson, Ko et al. 2010). Indeed, the needle's mechanical design is based on that of the ovipositor of the wood wasp Sirex-Noctilio (Figure 1-2), which plants eggs in wood with the use of a unique drilling mechanism (Vincent 1995).

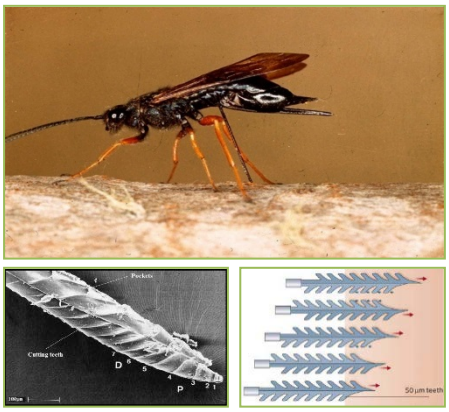

Figure 1-2. Wood wasp, Sirexnoctilio, drilling into wood (a), scanning electron microscope view of the ovipositor tip (b), schematic view of the drilling mechanism, image courtesy of New Scientist (c) (Vincent 1995).

This unique type of boring motion is being used to allow forward penetration along arbitrary curvilinear trajectories, with reduced tissue tear during MIS, as evidenced by recent work based on Particle Image Velocimetry, where the insertion of a needle prototype into a gelatine phantom is measured viao an optical based tecnique (Oldfield, Burrows et al. 2014). The design of the needle is explained in the following section.

1.1.3. MULTI-PART NEEDLE DESIGN

In the work first presented in Frasson et al. (Frasson, Ko et al. 2010), the biologically inspired multipart needle is composed of two interlocked parts, which move in a predefined order creating an offset (figure 1-3). Frasson conducted experiments (Frasson, Ko et al. 2010), which demonstrated that the needle can steer in a compliant medium along multiple curvilinear trajectories with different radii. This was empirically concluded to be due to the offset between the two parts and the bevel angle of the two tips. The experiments showed that one single radius of curvature is achievable per offset configuration and an approximately linear relationship between offset and curvature of the path generated by the tip was demonstrated. The multipart needle achieves bending as a result of the force asymmetry at the bevel tip, as well as the offset geometry, and its flexible material (figure 1-3).

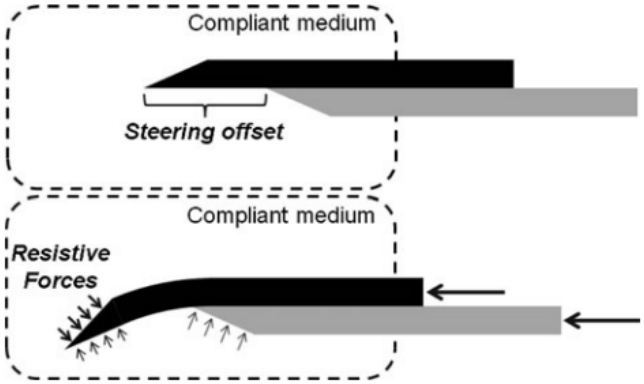

Figure 1-3 Programmable bevel tip concept: the offset between two interlocked segments of a flexible needle determines the steering direction of the tip (Frasson, Ko et al. 2010).

Due to the thin structure of surgical needles and the lack of visual feedback, they are generally difficult to manoeuvre and the complexity of the path of insertion due to locations of obstacles can sometimes add to the complexity of the situation. Inexact needle insertion, needle bending and tissue deformation can all cause complications during surgery, and cause the needle to deviate from its predefined path.

To minimise damage during needle insertion, offline analysis of the process must be conducted for the definition of path and insertion methodology, and a control system must be developed to bring the needle back onto its predefined path, with minimum disruption to the surrounding tissue. A method allowing both would involve the development of a model of needle-tissue interaction for the prediction of needle and tissue behaviour, allowing optimisation of the needle insertion process. The model could then be incorporated into the control system of the needle steering module, for online rectification of needle deviations from a predefined path. Modelling of needle-tissue interaction also allows surgical simulation for training physicians, using virtual reality for simulation of the conditions of the surgery, thereby enhancing the efficiency of their surgical ability and minimising the cost and time of surgery (Bro-Nielsen 1998). Further, extracting forces acting between the needle and the tissue by inverse solving this same model can aid in developing haptic feedback for the surgeon. In addition, prediction of the needle deflection, and its relation to soft tissue deformation, can aid path planning and needle insertion optimisation, by avoiding vital and delicate targets, such as blood vessels and nerves (Frasson, Ko et al. 2010). Subsequently, modelling the needle deflection allows minimisation of steering complications, by allowing

models of the needle structure and the substrate material to be optimised, while taking into account geometrical and mechanical parameters affecting needle deflection during insertion.

Previously, to optimise the insertion of the multipart biologically inspired needle, preliminary studies on the effect of the geometry (specifically on the cross-sectional geometry and "bevel" tip at the end of each segment) and insertion technique (reciprocal motion strategy) on the manoeuvrability (i.e. the ability to control the bending and buckling of the needle while steering inside soft material) have been conducted (Ko, Davies et al. 2010). Frasson (Frasson 2010) conducted three sets of experiments on the needle with the aim to show that the needle can:

- Steer in a compliant medium along curvilinear trajectories with different radii.
- Steer in a compliant medium along curvilinear trajectories with reduced buckling.
- Steer in a complaint medium along multiple curvilinear trajectories.

These results are summarised here for convenience. The first set of experiments tested the "programmable bevel" concept. Previous experiments (Alterovitz, Goldberg et al. 2005, Alterovitz, Lim et al. 2005) (Webster, Kim et al. 2006) (Webster, Memisevic et al. 2005) have demonstrated that a bevel tip needle will bend inside soft tissue due to the moment induced by these asymmetrical forces at the tip. For a specific situation in which the soft tissue parameters, bevel angle and needle stiffness are set, only one curvature can be achieved. One of the main advantages considered during designing the multipart structure of the needle was the concept that different curvatures can be obtained by changing the relative position between the needle segments. This concept was tested in experiments wherein different offsets between the leading and lagging segment of the needle were defined. In each experiment, the offset and the radius of curvature obtained were recorded and plotted in a graph. The results demonstrated that the relationship between the radius of curvature and the offset was approximately linear.

1.1.4. INVESTIGATION OF THE BUCKLING OF THE FLEXIBLE NEEDLE

To investigate the buckling of the multi part needle, the needle was first inserted reciprocally into the tissue (i.e. one segment at a time, repeatedly and by a set amount), and then inserted with a direct push into the tissue. The results demonstrated that the buckling in the direct push motion was slightly more pronounced (Frasson 2010).

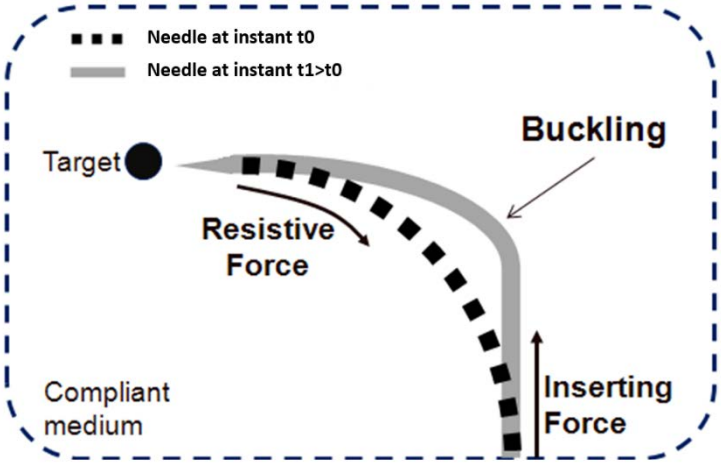

Figure 1-4 needle buckling inside a soft substrate. At time t0 the needle is bent inside the substrate; at consequent time t1, due to the forces acting from the substrate onto the needle, the insertion force causes the body of the needle to buckle, while the tip does not progress further. The "reciprocal motion" insertion method is anticipated to reduce the buckling (Frasson 2010).

One important point is that, due to the fact that the needle must bend to steer inside the tissue, and at the same time avoid buckling during insertion, the balance between the stiffness of the material (i.e. the tissue's ability to resist axial force along the needle) and of the needle (such that it is able to steer inside the substrate) is important - in this respect and for the needle, a needle with a larger Young's modulus than flexural modulus are desirable. During the experiments it was shown that the material chosen for the needle was suitable, as it did not cause evident buckling in a material with brain-like consistency. The experiments were then conducted outside of the tissue (figure 1-5), wherein an obvious reduction in buckling of the needle was witnessed during reciprocal motion, as opposed to direct motion. It must be noted that the reciprocal motion vs direct motion is not the focus of this thesis and has not been considered in the work, and is being mentioned here so as to give the reader a better understanding of the needle's advantages and the capabilities provided by the two-part needle geometry design.

The ability of the needle to steer along multi-curvature trajectories through the combination of the bevel tip and reciprocal motion was then tested, in which a double-curve trajectory (Frasson 2010) was achieved with the inversion of the steering offset halfway through the insertion process. The results qualitatively confirmed that a multi-curvature trajectory can be achieved with the multipart needle. It was deduced that the variety of curvilinear trajectories depend on the relationship between needle length and maximum achievable curvature, which in turn depend on the material flexibility and cross-sectional dimensions.

Frasson also performed 2D optimisation of the interlocking geometry of the needle. From the 2D model of the interlocking mechanism, the cross sectional interlocking stiffness was extracted. Inputted into the buckling equations of a beam, the interlocking stiffness allowed identification of the critical buckling load. With due simplifications, boundary conditions for the failure of the beam based on different actuation strategies were obtained. For two interlocked needle segments, one stationary and one pushed forward with an actuation force, the biggest possible actuation force avoiding buckling of the needle was found. The buckling load found was over 20% larger than the critical buckling load of the needle segment

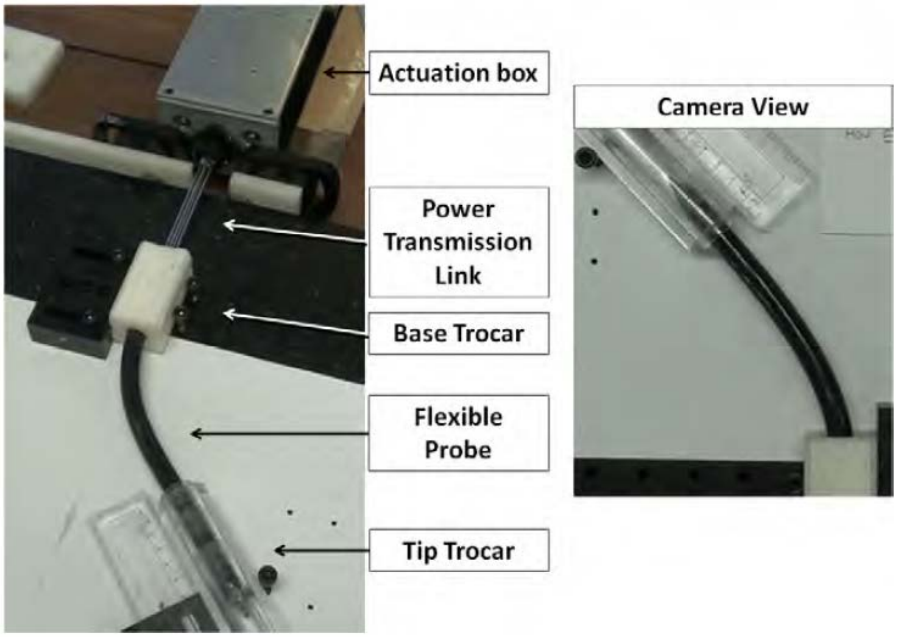

Figure 1-5 In this experiment, the needle is positioned to pass through two lubricated trocars at an angle of 30 degrees. The part of the needle showing between the two trocars is 125mm long. Thus, in the absence of the forcing acting from the surrounding substrate onto the needle body, the central part of the needle's body between the two trocars is free to buckle because.

featured with the interlock geometry of the current prototype. Frasson demonstrated that the interlocking geometry affects the buckling of the needle. In addition, three of the problems encountered during the experiments were segment deformation (the deformation of the segment during insertion), needle twisting (the twisting of the needle along its axis during reciprocal motion) and segment separation (separation of the segments of the needles during motion). It was suggested that one of the reason these occurred could be due to the frictional forces between the needle segments and between the needle surface and the substrate.

More recently, Leibinger (Leibinger, Oldfield et al. 2014) developed a design optimisation procedure for a four part version of the flexible needle, by identifying the parameters affecting the separation of the needle segments of the needle, and its buckling during deflection. Finite Element Modelling (FEM) is applied for modelling the forces and interactions between the segments of the needle during deflection using generalised plane strain elements, and a decision making process is used for comparing the results of the model for four chosen design parameters. The work showed that the smaller design of the components of the interlock geometry results in less friction between the segments, facilitating them sliding against each other. The reduced size of the interlock geometry components in turn, has a negative effect on the interlock strength, necessitating a negotiation between reducing friction during the sliding of the segments, and reducing the risk of the segments separating. As a result, a compromise between the parameters is maintained through an optimised design for the four part needle

1.1.5. Advantages of Needle-Tissue Interaction Modelling

The results of the work cited above, although supporting the theory behind the main assumptions associated to the biologically inspired needle steering system, are experimental and somewhat empirical. For the optimisation of the needle's design and dynamic variables, explicit relationships between the desired parameters and effecting variables are desirable. This is possible through the development of a needle-tissue interaction model explaining the relationship between the geometry of the needle and the tissue deformation. Before surgery, a path for the needle is defined, which, for example, avoids critical regions to intersect a target with minimum risk to the patient. During surgery, the needle actuation strategy is applied via a closed loop control system (Frasson, Ko et al. 2010). As previously mentioned, due to the complex nature of biological tissue, the needle may deviate from its original path at any point during the insertion. In this scenario, the controller will need to be able to steer the needle back on path, with minimum additional disruption to the tissue. As it is not possible to model all possible scenarios pre- surgery, the controller would benefit from real-time prediction of tissue deformation in response to the insertion commands (speed, path, angle…), needed to correct the needle's motion when it deviates from its intended path. This can be achieved via a model incorporating real-time prediction of soft tissue behaviour as a result of needle deflection. Assuming quasi static needle insertion, wherein the inertia parameters are not considered, the needle deflection itself is a function of geometrical and mechanical characteristics of the needle, and the reaction forces from the soft tissue, which in turn is a

function of the properties of the soft tissue itself, and the predefined needle insertion path. In order to develop an efficient needle-tissue interaction model, the relationship between the geometric parameters (offset, bevel angle, radius, cross section, etc.) of the needle, the mechanical characteristics (Young's modulus, Poison's ratio, etc.) of the needle, the forces acting on the needle during insertion, and its deflection must be defined. Furthermore, to optimise the needle geometry and material as variables affecting the deflection, an accurate mechanical model describing the relationship between the geometry and mechanics of the needle and the deflection is needed.

1.2. Summary and Present Research

The steering of a highly flexible multipart needle along a predetermined curve is challenging due to the unpredictable state of soft tissue and complexity of the needle path. This difficulty results in inevitable deviations of the needle from its path during insertion. The needle must then be brought back on path with minimum possible additional disruption to the surrounding material, while minimising the drift experienced by predefined targets in the tissue. One solution to this problem is to develop a real-time feedback control system to compensate for these deviations.

To aid such a control system, a mathematical model of the needle deflection is developed as a function of its geometric and mechanical properties. The mathematical model can also be used offline for optimisation of the needle, such as to increase its manoeuvrability inside the substrate.

It is proposed that a large deflection nonlinear beam model be employed for the modelling of the highly flexible multipart needle during insertion into soft tissue, and an inverse solution is sought for the model to identify the loads acting on the system. The stiffness of the soft tissue can also be identified by this inverse solution, by employing the coordinates of the tip of the needle as it is inserted progressively inside the tissue. By extracting model parameters from a model, the input variables of which are the actual coordinates of the tip through time, eliminates any errors associated with the assumption that the tip path and the needle shape after completion of an insertion, are the same. Also, the nonlinear nature of the soft tissue material can be identified in this manner, providing valuable information regarding the true deflection shape of the probe during insertion. By application of the extracted forces on a finite element model of the soft tissue condensed to the nodes for which deflection

minimisation is desired, the solution resulting in minimal deflection of a given target inside the soft tissue can be obtained.

1.2.1. AIM

Within the context of ongoing work on a flexible multi-part needle for soft tissue surgery, currently under development at Imperial College, the aim of this work is to develop and show the applicability of a 2D nonlinear progressive model which describes the relationship between a flexible two part needle and its interaction with soft tissue, during various steps of insertion, such as to predict the soft tissue response and aiming to minimise the disruption to the tissue due to control limitations, as the needle moves along a predefined curvilinear trajectory.

1.2.2. OBJECTIVES

The objectives are simplified under three main headings to aid understanding for the reader, as follows:

1. Development of a quasi nonlinear forward model that incorporates the effect of axial force during the insertion process, which includes the following steps:
   a. Development of physical free body model of the needle, including definition of the forces acting on the needle and its simplified geometrical representation.
   b. Development of a mathematical model of the needle, with equations describing the relationship between needle deflection and the forces, geometry and mechanical parameters of the needle.
   c. Development of a computational method incorporating a numerical solution to the mathematical model equations for the quasi-nonlinear model.
   d. Development of a reverse solution to the quasi-nonlinear mathematical model of the needle, allowing identification of the forces acting on the needle as a function of deflection, in the small deflection range.

2. Development of a progressive nonlinear beam model to allow simultaneous modelling of large deflections during the insertion process, which includes the following steps:
   a. Development of a mathematical model which describes large deflection in a beam.
   b. Development of an insertion modelling strategy, providing a quantified relationship between the deflections at each step of the insertion.

c. Incorporation of the insertion model into the nonlinear beam model, providing a link between current step deflection and previous step deflection, thus allowing computation of the deflection of the tip as a function of the insertion.
d. Development of an inverse solution strategy, allowing identification of the forces acting on the needle at any step of insertion.
e. Development of a computational method, incorporating a numerical solution to the mathematical model equations for the nonlinear model.
e. Development of a reverse solution strategy for the nonlinear mathematical model of the needle, facilitating identification of forces acting on the needle from deflections in the small deflection range.

3. Design and implementation of experiments for validation of these models:
   a. Validation of quasi-nonlinear and nonlinear models via experiments, by comparing the performance of the two models for reproduction of the experimental data.
   b. Derivation of axial and body forces during insertion from experiments and models.

1.2.3. METHODOLOGY

Initially a linear mathematical model of the needle's bending as an Euler Bernoulli linear beam is presented, which predicts the deflection of any point along the beam as a function of the forces acting on it, and its mechanical and geometrical parameters. The model is then solved for the tip of the beam, allowing prediction of the beam's tip deflection as a function of its geometrical and mechanical variables, and the forces acting on it. By inverse solving the beam's deflection solution, a method to obtain the forces acting on the beam (which caused said tip deflection) at any point in time is then developed. This inverse solution enables the forces acting on the needle during insertion to be identified without the need for the material properties of the substrate. A "quasi nonlinear" model is then developed to allow identification of axial force and cutting angle during insertion, by application of the Galerkin method to the resulting equations. The model is subsequently applied to a proposed model of the insertion process, which is expanded to include large deflection nonlinear beam modelling and force identification. In order to validate the developed models, experiments are designed and tip deflection results are compared with those predicted by the models.

1.2.4. SPECIFIC THESIS CONTRIBUTIONS

Development of a model with the following novel characteristics:

- The needle model allows the estimation of forces (with some simplifications) acting on a highly flexible multipart needle, without need for soft tissue material models, which are complex and volatile.
- The needle model is independent of any assumptions regarding the shape of the needle during its insertion into a soft tissue (e.g. constant curvature).
- The needle model is a function of the tip deflection during insertion, as opposed to the needle body shape, removing the assumption that these are the same.
- Axial forces and cutting angles are assumed to vary during insertion and their values are estimated throughout the insertion process.
- The model is applicable to large deflections, making it suitable for application to highly flexible needles.

1.3. STRUCTURE OF THE THESIS

In chapter 2, a survey into current literature on needle modelling is presented. Based on these findings, chapter 3 describes the theoretical backbone for the thesis. The preliminaries of needle modelling for a progressive solution and inverse identification of forces are included in chapter 3, where force identification and inverse problem solving are studied. The stages of the insertion process, deflection categories, and assumptions regarding the forces acting on the needle are explained in chapter 4. The beam model of the needle is presented in section 4.1, where the mathematical formulation, assumptions of the beam model and linear and nonlinear beam modelling are also studied. In section 4.2, the general stages of development of a model are expanded upon (Linear and Nonlinear) and the methodology for the development of the model is presented. The linear needle model development is included is 4.3, where the derived linear needle model and the equations solved are presented. Chapter 5 focuses on the quasi nonlinear model, and introduces the reader to the weak form of the Euler Bernoulli equation. Explanations on the addition of a varying axial force into the linear needle model previously developed is presented in section 5.1 and the mathematics behind the Galerkin solution to the weak form of the Euler Bernoulli equation are presented in section 5.2. and 5.3. The mathematical model of the insertion process and its application to progressive modelling through the iterative Taylor expansion and the Galerkin solution are discussed in chapter 6. In chapter 7, the nonlinear model of the beams large deflection is developed, while a computational method to derive solutions to the forward and reverse

nonlinear problems are presented in chapter 8. The results and discussion of the experimental and finite element validation of the models is presented in chapter 9, and conclusions are presented in chapter 10, ending with future work based on these findings.

2. NEEDLE MODELLING: CURRENT WORK

2.1. INTRODUCTION

In chapter 1, the basic concept of developing a mathematical model of needle deflection during insertion into a soft substrate was explained. Based on the explanation presented, it can be deduced that the needle deflection, subsequent tissue deformation, and the needle-tissue interaction models must be employed in conjunction, such as to define an insertion optimisation strategy within application constraints. Based on this, needle insertion modelling is categorised here into three areas:

- Soft tissue modelling and characterisation
- Needle modelling and characterisation
- Needle-tissue interaction modelling and characterisation

Each area of modelling is briefly explained in the following chapter. In order to develop a modelling strategy suitable for online application during insertion of the multipart needle, the affecting parameters, applications and restrictions of different soft tissue, needle deflection and needle-tissue interaction modelling methods, are examined, and a combination suitable for online applications is defined.

2.2. CONTINUUM MODELLING

Modelling of tissue deformation plays an important role in the overall modelling of the interactions between needle and tissue. For simplified physical problems, which relate to material property modelling, analytical solutions can be obtained. In case of complex material properties, loading, and boundary conditions, simplifications are made to produce a

mathematical model providing a feasible solution to the problem, while preserving the parameters of importance to the problem, such as for instance the fracture-related properties.

The mathematical model represents the actual physical model, including significant boundary conditions, loads, and assumptions imposed on the physical problem. In structural dynamics, the number of independent coordinates necessary to specify the configuration or position of a system at any point in time is referred to as the number of degrees of freedom (DOF)(Paz 2003). Thus, in order to model the system mathematically, the physical properties of the system must be represented mathematically, including all degrees of freedom. Though any object made of continuous material has infinite degrees of freedom, for the physical model of the problem, the degrees of freedom are generally reduced to discrete numbers to improve modelling efficiency. The most simple case is the one degree of freedom model, whereas the structure's position is defined by one coordinate only, such as a single truss supported by a wall. Physical properties of systems are included by use of spring, mass and damping elements, and excitations. The excitation represents all external forces and moments acting on the system, such as friction and actuation forces and moments, acting on the centre of mass of the object. The spring element is used to model the potential energy storage and elastic force properties of the material. The mass element introduces the inertial property of the mass of the object into the systems dynamics. A damping element represents the internal frictional components of the material, affecting energy dissipation and its time dependency. For example, in viscoelastic materials, the relaxation/viscose effect of the material is generally modelled by means of a damper. Now, the complexity of the physical model will determine the number of elements in the model, which may lead to systems as simple as 1 DOF up to very complex systems with hundreds or tens of thousands of DOFs. It must be noted that the properties each basic element present in the system is not presentable by any other element, as, for example, the mass cannot demonstrate energy dissipation effects and the damper does not include inertia effects (Paz 2003).

In order to create a mathematical model of any given material, a diagram of the actual setup must be drawn, establishing where each force acts and how the elements are linked, with springs and dampers in parallel, or in series, etc. These models are called the constitutive models of the material properties. In order to form a model to predict material behaviour, a specific combination of mathematical representations of the parameters affecting the setup, which, as a whole, exhibits the behaviour of the material, is needed. For validation of the model, experiments are generally required, for example relaxation and creep curves of

materials are extracted with use of appropriate loading experiments. If the resulting model agrees with the properties extracted from experimental data (e.g. hysteresis, relaxation, creep etc.), the model itself becomes an elaborate representative of the material, allowing prediction of material response in situations not available through experiments. The complication arises in that, for live tissues, the mechanical properties and sometimes even the constitutive models change with the state of the body, e.g. tissue properties changing with emotional/physical state. This volatility may introduce instantaneous change in the tissues characteristics due to conditions of the surgery, resulting in short time spans during which the properties are valid. Also, in some cases, it may not be possible to retract a sample of soft tissue suitable for material testing without harming the patient, or the properties may be patient-specific or change based on age, history and other effecting parameters.

Based on this, a soft tissue model is desirable, which must ideally be selected, such that the parameters affecting the model:

- Can be defined (are obtainable) at any point in time.
- Can be obtained by means other than experimental measurement.

An explanation of soft tissue models and their affecting parameters and applications are now presented, for consideration in the implementation of optimal insertion strategies for the multipart needle.

2.3. SOFT TISSUE MODELLING

Previous literature has commonly cited biological soft tissue as hyperelastic and visco-hyperelastic (Cover, Ezquerra et al. 1993, Fung 1993). Fung (Fung 1993) rules out simple realistic material models, as biological soft tissue exhibit highly non-linear stress-strain relationships, mechanical anisotropy, large deformations, heterogeneity and viscoelasticity. In addition, for live tissues, the mechanical properties and sometimes even the constitutive models change with the state of the body, e.g. tissue properties can change in response to changes to the surroundings (e.g. temperature). In order to derive valid mathematical models of tissue, experimental models have been adapted to model and parameterize the characteristics of biological soft tissue. Miller and Chinzei (Miller and Chinzei 1997) conducted experiments on swine brain to determine the mechanical properties of brain matter. Miller (Miller 1999) proposed a linear, large deformation viscoelastic model, of polynomial form with time dependent coefficients. This model is easy to implement into

existing software, such as ABAQUS (Miller and Chinzei 2002). Miller defined the parameters needed for the model based on the unconfined compression experiment (Miller and Chinzei 1997) results. The results of the theoretical model and the actual experimental data are appropriate for compression levels reaching 30% and for loading velocities varying over five orders of magnitude.. Mendis (Mendis, Stalnaker et al. 1995) modelled the brain under high strain-rate loading conditions, developing a time dependent polynomial model from the strain energy function. Due to the high strain rate conditions, this model can be employed for modelling injury, whereas Miller and Chenzei's model is suitable for low strain rates and thus appropriate for the modelling of surgical procedures. For finite element analysis, as it is a nonlinear viscoelastic model, parameter identification is difficult and it is computationally expensive. Kataoka et al. (Kataoka, Washio et al. 2002) determined the mechanical characteristic of prostate tissue by use of separately measured tip and frictional forces during needle insertion (Kataoka, Washio et al. 2002). In the procedure, the mechanical characteristics of prostate tissue are determined by characterising both friction forces and tip behaviour.

The methods employed to model soft tissues presented above are efficient for offline prediction of tissue deformation. The need for experimentation on the soft tissue and application of finite element analysis during surgery makes them less efficient for scenarios where tissue experimentation is restricted, properties are patient specific, or time constraints do not allow finite element modelling at each step. Consequently, an insertion optimisation strategy for online application would likely not be dependent on a pre-existing soft tissue model, but rather allow tissue deformation prediction through mathematically defined variables, which can be identified at any state of insertion. As the deformation of soft tissue during insertion is a result of needle deflection and resulting interaction loads, definition of these mathematical variables as a function of the needle deflection and acting loads at each point in time would provide a mean for time specific tissue deformation estimation, without need for a pre-existing soft tissue model. This means establishing a relationship between the needle's deflection at any point in time and soft tissue deformation at said time, allowing study of soft tissue behaviour as a function of needle deflection at any given instant.

As surgical needle materials are much less volatile and complex than biological soft tissue, modelling their behaviour is significantly easier. To this end, needle modelling methods and applications are briefly explained in the following section, and the selection of an appropriate model of the multipart needle is investigated.

2.4. NEEDLE MODELLING

Medical needles can be classified in three main groups: rigid needles, highly flexible needles and moderately flexible needles (Goksel, Dehghan et al. 2009). Rigid needles maintain their shape during insertion into soft tissue and have negligible bending. Highly flexible needles, on the other hand, experience significant bending when being inserted into soft tissue, and thus allow movement along curvilinear paths to avoid obstacles. Some needles, such as brachytherapy needles (figure 1-1) lie in-between these two groups, as they can experience significant deflection during insertion, but a large insertion force is needed to produce said deflection. The structure and material of the multipart needle makes its behaviour effectively similar to highly flexible needles. As can be expected, the steering of highly flexible needles along a curve is especially challenging due to the complexity of the needle paths and flexibility of the needle (Misra, Reed et al. 2010). As such, the model of the multipart needle should be applicable to highly flexible needles with large curvatures. To define the necessary characteristics of such a model, a summary of modelling methods and their applications are presented.

Previous models of needles have been developed wherein the mathematical relationship between model parameters and mechanical and geometrical properties of the tissue and needle are not known (DiMaio and Salcudean 2002, Alterovitz, Goldberg et al. 2005, Webster, Memisevic et al. 2005, Hing, Brooks et al. 2006, Webster, Kim et al. 2006, Kyle B.Reed 2008, Misra, Reed et al. 2008, Reed, Okamura et al. 2009, Yan, Podder et al. 2009). More recently, Asadian et al (Asadian, Kermani et al. 2012) developed a mathematical model wherein the forces acting on the base of a needle during insertion are measured via sensors, and the forces acting on the needle from the tissue are estimated as a function of measured base forces, with some simplifications. The variables of the model do not represent physical parameters that can be employed directly to optimise the needle design, and it is not possible to identify individual forces acting on the needle to aid our understanding of the mechanics of the problem. This results in complications in achieving an optimised design for the needle geometry and estimate mechanical properties pre-surgery, as it not possible to establish an explicit relationship between the needle's deflection and its mechanical and geometrical characteristics. To allow optimisation of parameters through modelling of needle deflection, physical parameters must be defined in the model, and studied in relation to a mathematical measure of needle deflection, as explained below.

Generally, in order to quantify the deflection of the needle during insertion, its curvature at every stage of insertion is needed. This brings about the necessity of assumptions regarding the mathematical equations which describe its shape. Webster et al. (Webster, Kim et al. 2006) developed a kinematic model based on steering due to bevel tip asymmetry, where, for a single insertion without any axial twist of the needle, the curvature was considered constant. The model does not incorporate the effect of any geometrical parameters of the needle, and the empirical parameters must be determined using previously acquired data from insertions of the needle through the same material. This makes it unsuitable for surgical procedures, where testing on the material is limited. Other models (Alterovitz, Goldberg et al. 2003, Webster, Memisevic et al. 2005, Goksel, Dehghan et al. 2009) also assume constant curvature during needle deflection. This introduces inaccuracies that are somewhat minimised by the fact that the needles used are fixed at the tip, and thus provide a constant curvature that can be compared with that of the needle's shape at the end of the insertion (Webster, Memisevic et al. 2005). For validation of most of the developed models, the physical variables defined in the model are estimated during insertion experiments, and the resulting needle curvatures compared. This brings about the importance of accurate measurement of the needle's curvature as it deflects during experiments.

Numerous needle insertion experiments have been conducted wherein the needle's tip path during insertion is recorded, and assumed to be the same as the deflected shape of the body of the needle, and thus a valid measure of its curvature (Alterovitz, Goldberg et al. 2003, Webster, Memisevic et al. 2005, Abolhassani and Patel 2006, Misra, Reed et al. 2010, Asadian, Kermani et al. 2012). In these experiments, the high stiffness of the needles used has minimised errors resulting from this assumption, as the body generally follows the tip closely during insertion. As can be imagined, in cases involving a highly flexible needle, this assumption may no longer hold. In order to address this, Robert et al (Robert, Chagnon et al. 2013) mapped a needle's shape via Computer Tomography (CT) scans during insertion, and by fitting B-splines to the shape, defined a black box mathematical model (i.e. with no physical parameters attached to the model) to describe the needle's deflection. This method, although removing assumptions about the tip path and needle curvature, neglects axial forces acting on the needle, and is validated for a very stiff needle in very small deflection (under 5%).

To date, the axial force at the tip and subsequently the cutting angle of flexible needles has been generally assumed to be constant (Misra, Reed et al. 2010, van Gerwen, Dankelman et al. 2012, Robert, Chagnon et al. 2013). This can cause inaccuracies in highly flexible needles,

as the bent shape of the body and buckling stability of the needle are highly influenced by the tip axial force. The constant tip forces are calculated by means of needle insertion experiments on the tissue beforehand (Misra, Reed et al. 2010) or from force sensors attached to the base of the needle (Wittek, Dutta-Roy et al. 2008), rendering the methodology unsuitable for surgical experiments where inhomogeneous materials are involved. In cases where the needle's deflection is modelled as a function of physical parameters beforehand, forces acting on the needle during insertion must be calculated. To achieve this, insertion experiments are conducted and theoretical models of forces acting on the needle tip presented based on experimental findings (Misra, Reed et al. 2010). Additionally, to date, the magnitude of these forces are calculated as a function of the soft tissue parameters, which make them unsuitable for applications where there is limited tissue available for experimentation, and volatile materials, where material behaviour may change through the insertion process.

Abolhassani et al (Abolhassani and Patel 2006) defined a model wherein the force readings at the needle base and the bevel angle are used to predict needle deflection. The needle is modelled as a linearly elastic cantilever beam undergoing small deflection. This model uses mechanical parameters, including the base moment and forces, as input variables, allowing for the effect of the geometrical parameters on the mechanical variables to be studied. Due to its small deflection assumption, its applicability is very limited in the context of soft and highly flexible needles. However, modelling the needle as a beam allows expansion of the model to highly flexible needles, employing large deflection nonlinear models (this concept is further explained in section 3.4). The model was later (Abolhassani, Patel et al. 2007) employed to control the deflection of brachytherapy needles during insertion into soft tissue, by assuming a predefined force pattern along the length of the needle. Lehmann et al. (Lehmann, Tavakoli et al. 2013) adopted the model to predict the deflection of the tip of brachytherapy needles during insertion into soft tissue, assuming a different force pattern, and inserted the needle into homogenous phantom tissue samples to validate the model. The force profile assumed along the length of the needle was more complex than that of Abolhassani et al., and the model shows promise for tip deflections modelling for rigid needles in small deflection range.

Rucker et al. (Rucker, Das et al. 2013) developed a model to be incorporated into an adaptive control algorithm that does not depend on tissue properties, and allows the needle to reach a target inside soft tissue. The disadvantage of the model is that it does not allow estimation of the forces acting from the material onto the body, which may not be an objective due to the

model being developed and tested for a Nitinol needle with a Young's modulus, E=75 GPa. Whereas, for highly flexible needles, the deformation of the body of the needle must also be considered when controlling the needles path during its insertion into soft tissue.

Based on the previously developed needle deflection model (Misra, Reed et al. 2010) and force patterns (Misra, Reed et al. 2008) observed by Misra et al., Abayazid et al. (Abayazid, Roesthuis et al. 2013) developed kinematic and mechanic based models of a Nitinol needle, which take into account the forces acting on the tip of the needle during single and multiple curvatures inside gelatine. The inputs into the mechanical model are the forces acting on the needle, and the curvature of the needle during deflection. The forces acting on the needle are assumed to be constant during insertion and are defined as a function of the material properties of the surrounding gelatine. The tip deflection is assumed the same as the body shape, and is fitted to a circle to allow extraction of curvature values. Both these assumptions can be argued to be accurate (in small deflection range) due to the high Young's modulus of the needle, but if the model was to be applied to a needle being inserted into soft tissue, the extraction of material properties for the surrounding tissue (such as to be able to define forces acting on the needle) would be an issue. Later Roesthuis et al. (Roesthuis, Kemp et al. 2014) extended the work to 3D modelling of needle deflection using the mechanic and kinematic based models previously developed. The mechanical model employed is the 3D extension of the model previously developed (Abayazid, Roesthuis et al. 2013). This method employs the energy method, which is then solved using the Rayleigh Ritz method. Applying the Rayleigh Ritz necessitates the definition of the essential boundary conditions for the actual mathematical formulation of the model (this concept is extensively explained in section 3.4). This means that, if the needle being modelled varies in geometry throughout its insertion (for instance with the possible offset variation of the needle being modelled in this work) the geometry changes, and redefining the trial functions of the Rayleigh Ritz becomes time consuming and complicated. In addition, in the case of energy dissipation due to possible friction, the definition of a functional can be extremely complex. The method also assumes linear beam bending and as such disregards the rotation of the tip forces, which can make a significant difference in the bent shape of the needle (beam), specifically in the case of a highly flexible embodiment.

More recently, Boroomand et al. (Boroomand, Tavakoli et al. 2014) developed an energy based dynamic deflection model of a moderately flexible needle inside soft tissue, such as to be incorporated into closed loop control. The model is dependent on mechanical properties of the surrounding material, and the developed model assumes a homogenous material

surrounding the needle during insertion. The model, although mathematically sound, is tested through simulations, and its actual experimental validation is subject to a dynamic identification algorithm allowing extraction of soft tissue properties during insertion of the needle.

To summarise, all needle deflection modelling methods mentioned have taken into account one or more of the following assumptions:

- The needle is assumed to have constant curvature during insertion
- The axial force and the cutting angle at the tip of the needle are assumed to be constant during insertion
- The needle tip path during insertion is assumed to be the same as the needle body shape after insertion
- The forces acting on the needle are calculated as a function of soft tissue properties

These assumptions, although valid for stiff needles undergoing small deflections, introduce inaccuracies for highly flexible needles undergoing large deflections. Consequently, for a model representing highly flexible needle behaviour during insertion into soft tissue, the following objectives are desired:

- Removing assumptions regarding the shape of the needle during insertion
- Removing assumptions of the body of the needle following its tip during insertion, i.e. that the body shape and the tip path are the same
- Assumption of varying cutting angle and axial force during insertion
- Obtaining magnitude of forces acting on the needle at any point in time during insertion

By examining the characteristics of highly flexible needles and soft tissue models, the conditions that have to be met for a model to be applicable to the insertion process of the multipart highly flexible needle, have been defined. It must be noted that needle deflection models dependent on the predefined material properties of the soft tissue surrounding the needle are assumed here to be inapplicable to online applications. In the same sense, any model of the deflection of the highly flexible needle inside soft tissue must have the potential to be able to be used in conjunction with a soft tissue model in real-time, so as to allow definition of the needle-tissue interaction characteristics. In order to develop an understanding of currently existing models incorporating the relationship between needle

deflection and tissue deformation, a summary of the major findings related to existing needle-tissue interaction models is included in the following section.

2.5. NEEDLE-TISSUE INTERACTION MODELLING

As previously mentioned, in order to mitigate needle deviations from a predefined path, with minimum distortion to the surrounding tissue and displacement of predefined targets, the state of the tissue at each stage of motion, and a model predicting the deformation of the tissue as a result of further movement of the needle, are needed. This can be achieved by using two models in conjunction, at each stage of motion; one representing needle deflection, and another, tissue deformation because of needle deflection. This is assuming the tissue to be soft relative to the needle and the needle motion being solely responsible for tissue deformation. The conditions which the soft tissue and needle model have to meet were defined in sections 1.3 and 1.4, respectively. In order to be able to form a relationship between these two models, a model representing the interaction between needle and tissue during insertion is needed.

Generally, tissue deformation during needle insertion is modelled using experimental procedures, finite element models, discrete models, or a combination. It is generally difficult due to its nonlinear, inhomogeneous, viscous, and elastic behaviour, though the two latter sources of complexity are only significant for fast insertions, where rate-dependent effects become important. The accuracy of the tissue properties employed as modelling parameters is thus of immense importance. A brief explanation of each method generally employed in needle-tissue interaction modelling is now presented.

2.5.1. EXPERIMENTAL PROCEDURES

A good example of the use of experiments in needle-tissue interaction modelling is provided by the work of DiMaio and Sacludean (DiMaio and Salcudean 2002). They used image-based marker tracking during calibration and boundary probing (figure 2-1) to estimate the amount of tissue deformation.

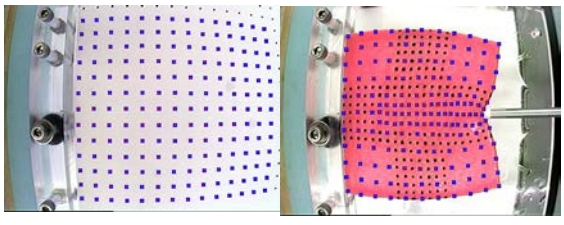

Figure 2-1. Image based Marker Tracking ((DiMaio and Salcudean 2002))

A CMOS camera was used to take pictures of the surface of a tissue phantom with known properties, to estimate the deformation of the top surface in 2-D. Using the relation between the pixel width and the distance between the markers on the surface, frames were tracked and processed with a marker tracking algorithm offline. The material markers were tracked over the entire sequence of image frames, using a matching algorithm. Using the profile of force distribution along the needle shaft derived from the experimental setup and a FEM based linear tissue model, a simulation of the needle insertion process was developed. The experimental results used for simulation demonstrated that the axial friction between the needle and the tissue phantom is relatively uniform along the needle shaft. The simulation system employs a linear elastic FEM model, which clearly makes for an inaccurate assumption, was the method to be extended to biological soft tissue. Due to the large matrix formulation in FEM models and topological and boundary condition changes during the needle insertion simulation model, it is not suitable for application to real-time applications, and hence will not be considered as a candidate for the optimisation (design) strategy of the multipart needle.

In order to obtain the force profile during tissue deformation, (Szegedi, Rassiah-Szegedi et al. 2012) used a method where fudicial markers are used in porcine liver phantom, while electromagnetic tracking (EMT trace recording) is employed to track the markers during voxel deformation. The disadvantage of the work is that the mm scale of the markers necessitates imposing the same scale spacing when used in a measurement grid, limiting the resolution of the results. Van Veen et al. (van Veen, Jahya et al. 2012) was able to produce high resolution results and microscopic observations, but the methodology does not allow quantitative measurements of the deformation of the tissue. The method adopted by Quinn and Winkelstein (Quinn and Winkelstein 2010) produces high resolution images of the strain in the tissue, allowing quantification of the deformation of tissue. The disadvantage is that, at its current stage, the method is only viable for thin-enough samples of tissue to be able to transmit a polarised light source.

Recent developments include the method developed by Oldfield et al. (Oldfield, Burrows et al. 2014) in work connected to the needle presented in this thesis. A Digital Image correlation (DIC) based technique was adopted to analyse needle–tissue interactions for a multi-part flexible needle during its insertion into a soft substrate (gelatine) using Particle Image Velocimetry (PIV) (Raffel, Willert et al. 20017). In the method adopted by Oldfield (Kerl, Parittotokkaporn et al. 2012), micrometre scale particles are embedded at spatially random

points in the gelatine sample, allowing extraction of time resolved displacements (TRDs) and strains in an Eulerian description of behaviour (Oldfield, Burrows et al. 2014). This results in captured stress/displacement data with relatively high resolution (at least an order of magnitude higher than previous work (Oldfield, Burrows et al. 2014)) , with the caveat that the substrate must be transparent for the technique to be viable.

2.5.2. DISCRETE MODELLING

Discrete models of natural systems are very widely used in engineering and scientific works. There are several techniques that can be used to discretise a continuous system, and these are different in their approaches and result in different discrete models with varying accuracy. Accuracy in this context is defined in terms of how well the model's behaviour resembles that of a real system. There are different methods for building discrete physical models. The four most widely used are finite elements methods, finite difference methods, boundary integral methods, and lumped parameter models. These techniques are different in the accuracy of the physical model they produce, though all of them result in the same "type" of mathematical models. These techniques are not going to be compared in detailed here, but in general, the Finite Element Method (FEM) is the most accurate and most efficient of these. On the other hand, the simplest technique is the Lumped Parameter Method. In this method the solid under consideration is simply discretised by using springs and point masses to model the elasticity and mass of each point of the solid, respectively. As is evident from figure 2-2, a continuous infinite degrees-of-freedom system has been replaced by a physical model which has 5 degrees of freedom. Each segment of the continuous system has been discretised by representing its elasticity by a spring "K" and its mass has been divided between two nodes on the boundaries of the segment. By increasing the number of discretisation stations from $n = 4$, the accuracy of the model increases and if $n = \infty$, then the discrete system will converge to a continuous system.

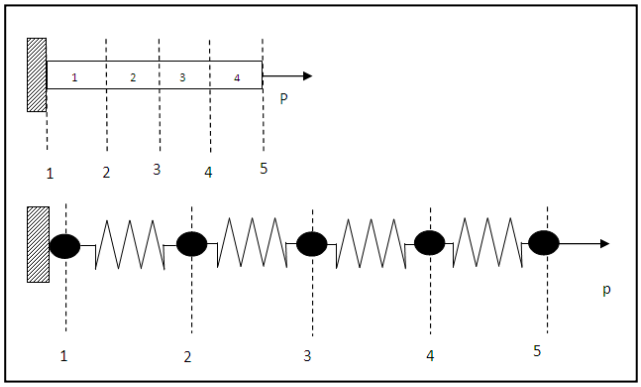

Figure 2-2. Lump Parameter Model

2.5.2.1. FINITE ELEMENT MODELLING

Finite element modelling consists of the object's geometry defined by a set of nodes interlinked with a mesh over which an interpolation function acts, approximating the real deformation field. Tissue deformation is a result of infinite points of contact between needle and tissue. FEM allows for computational methods to numerically calculate the stress distribution and other parameters needed in modelling. The accuracy of the results heavily depends on the fact that the tissue properties and materials used for the model must be an accurate representation of the actual material. There are three main categories of deformation models: Heuristic Models, Continuum mechanics models and hybrid models (Famaey and Vander Sloten 2008). Heuristic models encompass straightforward geometry-based models such as deformable splines, the mass-spring damper model, linked volumes and the mass-tensor model. Famaey discards the first category due to its limited physical realism and uses the continuum mechanics approach, because of its higher fidelity and because it forms the basis of computationally less expensive hybrid approaches. In spite of this fact, heuristic models are still used for some surgery simulations due to their computational efficiency and reasonable accuracy (Cotin, Delingette et al. 2000, Radetzky and Nürnberger 2002, Choi, Sun et al. 2004). The second category is based on the laws of continuum mechanics, which are solved by numerical techniques through two main approaches, the boundary elements method, and the finite elements method. During surgical procedures, generally one area or region of the tissue is less prone to large deformations over a small space and therefore less in need of high accuracy. Hence, a coarser mesh can be used, allowing for fewer computations. Lastly, hybrid models allow the selection of heuristic models and continuum mechanics models based on the conditions of the region being modelled, avoiding extra computation (Famaey and Vander Sloten 2008).

2.5.2.2. LUMPED PARAMETER NEEDLE-TISSUE INTERACTION MODELS

Discrete modelling has been widely used to represent soft tissue by means of spring and mass elements (Terzopoulos, Platt et al. 1987, Pieper 1989). In 1987, Terzopolous, Platt and Fleisher (Terzopoulos, Platt et al. 1987) developed a discrete simulation model used to animate facial tissue, in which they employed a simplified version of the elastic theory for homogeneous isotropic materials. Later, Terzopolous modelled synthetic facial tissue as a deformable lattice of point masses connected by springs, that is, a discrete deformable model (Terzopolous and Waters 1991).

One of the drawbacks of mass spring models is the complexity of the structure of the models, when expanded to 3D. Cover et al (Cover, Ezquerra et al. 1993) used mass spring models to model gallbladder tissue for surgery simulation. The deformation of the gallbladder was simulated using a surface based mass-spring model. The main problem with surface based models is that they cannot represent the effect of surrounding matter in the whole volume on the deformation of the specified region and for efficient modelling, volumetric models must be used. Kuhnapfel et al (Kühnapfel, Çakmak et al. 2000) used mass-spring models in the KISMET simulation system, which provides a 3D simulation environment with the ability to model in real-time the interaction between tissue and instruments. They reduced the volumetric characterisation problem by introducing parent nodes, connecting the surface nodes on the surfaces of the object. This method, although more exact an approximation, is complex, due to the fact that mass nodes are usually interlinked and spring cross over each other. In addition, the material is modelled as an elastic volume, which is a risky simplification when soft tissue is involved.

2.5.3. INCREASING THE COMPUTATIONAL EFFICIENCY OF FEM

Finite element modelling of soft tissue, although more accurate than spring-mass models, requires mesh regeneration for online application during needle insertion, making it less time efficient. Alterovitz et al (Alterovitz, Goldberg et al. 2005) proposed a finite element based model, wherein the tissue deformation as a result of cutting forces is calculated using a FEM simulation of the soft tissue, and the needle is modelled as a stiff needle of constant curvature. As mentioned, due to tissue deformation during insertion, the FEM used in this model requires mesh regeneration during insertion and is time consuming. Alterovitz modelled the soft tissue as linearly elastic, simplifying the FEM model. Although this can be expanded to nonlinear materials, the FEM of the insertion would be much more time consuming and much more complex.

In order to eliminate computational time during finite element modelling, Bro-Nielson (Bro-Nielsen 1998) proposed a method employing condensation, in which the stiffness matrix is pre-calculated, resulting in less computational time throughout the simulation. He developed a semi-implicit solution method, based on a finite element model wherein the system is defined by a mass and stiffness matrix. Using time discretisation, the resulting differential equations were solved. Regarding the mass lumped at nodes as in lumped mass models, and regarding the edges of the FEM model as springs, the corresponding spring-mass models were solved. The method, although a good approximation, does not emphasise the effect of the dynamical parameters, such as viscosity of the material, and is more useful to models where the dynamic effects of the model on the internal mechanics of the material is not of interest, i.e. low speed needle insertion, as is the case with the flexible needle being studied in this work.

The condensation method is an efficient method which, based on the preservation of the strain energy of the global system, reduces the size of the global system by a considerable amount. The main advantage of this method is the preservation of the strain energy and hence the volume. Unfortunately, the method does not preserve the kinetic energy and for this reason it is not exact for dynamic problems. The error for the dynamic problem is considerably reduced when the dynamic process is very slow (i.e. inertia effects are small) and when proper selection of master degrees of freedom (essential degrees of freedom characterising the dynamic behaviour of a structure in FEM) has been conducted. Once the system is condensed down to its master nodes and degrees of freedom, the elements of the condensed mass matrix represent the masses of the spring damper system and the elements of the stiffness matrix represent the springs. Developing a method to conserve the accuracy of a finite element model while preserving time efficiency through the condensation method would be applicable to an online system for tissue deformation modelling, for application to low speed needle insertion, though a method for extracting soft tissue parameters that is not dependent on linear elasticity and homogenous material is needed.

To this end, some work (Deussen, Kobbelt et al. 1995, Goksel, Dehghan et al. 2009) has been done on relating discrete lumped parameter models and finite element models together, by establishing relationships between material properties (such as the Young's modulus) and material stiffness. Deussen et al (Deussen, Kobbelt et al. 1995) proposed a stochastic method, simulated annealing, for optimisation of the configuration of the mass-spring network in 2D. The advantage of the nodal system to others is the diagonallity of the mass matrix, allowing

easy mathematical handling for solving FE problems. In order for the FEM model to be comparable to a logic model, the K matrix of the FEM must be updated at every step. This, as previously stated, is very computationally expensive due to the large size of the K matrix in FEM cases. Elasticity is optimised by use of simulated annealing, in which, for elasticity optimisation, a lumped system with springs connecting all the nodes is created. Duessen heuristically defines a spring coefficient based on the Young's modulus of the material for all the springs, and optimises them by use of a "reference displacement" defined by an analytical solution to the displacement of simple bodies due to external forces (Deussen, Kobbelt et al. 1995). He considers the same configuration modelled by FEM and then applies 6 cases of forcing (tension-compression and shear) to both systems and plays with the K values (spring coefficients) of the reference system, such that the difference between the reference displacement and the FEM reference displacement for all nodes under all forcing states becomes minimum. The drawback is that this optimisation is valid for homogenous materials only, due to the fact that the constants for horizontal, vertical and diagonal springs representing the material are assumed to be equal.

More recently, models of tissue deformation have been developed (Miller, Joldes et al. 2007, Comas, Taylor et al. 2008, Horton, Wittek et al. 2010) (Jin, Joldes et al. 2014), where, similarly to the concept of FEM, a global mesh for all nodes in the system is formed and inverted at each step. Then, a stiffness matrix for each element is computed and the deformation is solved. This method was initially develop by Miller et al. (Miller, Joldes et al. 2007) using The total Lagrangian Explicit Dynamics (TLED), which allows the pre-computation of special derivatives, reducing time consumption. Horton et al (Horton, Wittek et al. 2010) improved time efficiency of the finite element model via a meshless model, though it must be noted that removal of the mesh from the geometry also results in less accuracy in the FEM solution, which is mainly based on the continuity of the model because of the mesh. Meshless techniques are difficult to apply to soft tissue, as they are sensitive to the points taken as nodes and are difficult to apply to complex boundary conditions and geometries (such as soft tissue). The model was applied to the modelling of brain shift during neurosurgery (Joldes, Wittek et al. 2009), incorporating registration to allow for patient specific geometry of the brain. In order to be able to define the mechanical properties of the model, a biomechanical model of the brain tissue was developed (Miller and Chinzei 1997, Miller 1999, Miller, Wittek et al. 2011) (Wittek, Joldes et al. 2010). The author notes that, due to the type of loading being a predefined displacement of the boundaries (Miller, Wittek

et al. 2010, Mostayed, Garlapati et al. 2013), the unknown deformation inside the boundaries is not highly effected by the mechanical properties of the soft tissue. In order to allow comparison of the work with real organ deformation, the model was used in conjunction with medical imaging (Li, Miller et al. 2015) to allow comparison of patient specific tissue deformation, by imposing displacements on the model surface (Wittek, Joldes et al. 2010). The author states that, in order for the work to be applicable to neurosurgical modelling, the known motion of the surgical tool must be known. This can be problematic in applications such as the insertion of highly flexible needles during neurosurgery, as the controllability of the needle can be taxing. The model was tested as a basis for non-rigid registration, by comparison of intra-operative and pre-operative brain shift data from images (Garlapati, Roy et al. 2014). This allowed assessment of the model's capability in aiding in neuro navigation during near-complete tumour resection. The model was demonstrated to have high accuracy when the patient experienced a craniotomy-induced brain shift higher than 3.3 mm (Garlapati, Roy et al. 2014).

Miller et al. (Miller, Wittek et al. 2010, Wittek, Joldes et al. 2010) who was involved in all the aforementioned works as an author, stated in his paper that: "When the intended application is for operation planning, the computational model must be patient specific: how to rapidly generate patient-specific computational methods still awaits a satisfactory answer." This also agrees with the survey done by (Abolhassani, Patel et al. 2007), where, having studied the current work at the time of the survey, it stated: "Several research groups have tried to model needle deflection during insertion; however none of the available models integrate mechanical properties of soft tissue. The shape of the needle tip is also a parameter to be considered in modelling needle deflection and current studies are now focused on this aspect."

Thus, having studied the characteristics of soft tissue, needle, and needle tissue interaction models suitable for application to the offline optimisation and online application of the highly flexible multipart needle during insertion into soft tissue, a summary of the findings and a proposed solution are now presented.

2.6. CONCLUSION

It can be seen from the this brief summary of modelling methods that a main drawback to finite element modelling is the low time efficiency when applied to real-time surgery, while lump parameter spring-mass models lack accuracy when applied to non-homogenous

nonlinear materials, such as soft tissue. Thus, any needle-tissue-interaction model suitable for application to aiding in online control of the highly flexible multipart needle must satisfy the following conditions:

- Include the effect of the non-homogenous and nonlinear elastic nature of soft tissue during insertion, on the needle deflection.
- Be time efficient, for application to online modelling during insertion.

Establishment of a relationship between needle deflection (which can be measured at any time) and the forces acting on the needle because of the stiffness of the surrounding material, at any given point in time, is thus needed. This will eliminate the inaccuracies caused by defining the parameters of the lumped spring models due to nonlinearity and non-homogenous materials, as the values extracted would be specific to the geometry (in relation to the needle) and time (at which the needle deflection was measured). Consequently, a model of needle deflection is required, which is not dependent on the existence of surrounding material properties, but includes the quantified effect of the tissue deformation through the forces acting on the needle from the tissue at any point in time.

To date the deflection of the needle has been modelled in small deflection domain, which limits the curvatures achievable by the needle during insertion. Many previous models also assume the path of the tip of the needle to be the same as the shape of the needle on completion of the insertion process, and assume constant curvature, and constant axial forces and cutting angle at the tip of the needle. However, the axial forces acting on the tip of a needle during insertion have a prominent impact on the deflection of the needle, but its consideration introduces nonlinearity into defining models, even when the deflection is small, in the sense that the deflection due to axial and transverse forces does not simply add, rendering a model considering this effect “quasi nonlinear”. The discrepancy between needle shape and its tip path also increases significantly during large deflection, yielding any model depending on the assumption that they are the same to be invalid. Finally, previous models also rely on existing material models of soft tissue for calculation of forces acting on the needle during insertion, rendering them inefficient for applications involving fast changing biological soft tissue and restricted experimentation on patients.

Based on the above, the author has endeavoured to develop a model of the highly flexible multipart needle during insertion into soft tissue. The model adopts a nonlinear beam model of the needle, predicting its deflection during large deflection into soft tissue. The forces

acting on the needle can be identified by obtaining the inverse solution to the model. The model can also provide a means to identify the stiffness of the soft tissue during the insertion process. In order to remove inaccuracies arising from the assumption that the tip path and the needle shape after completion of an insertion are the same, it is decided to develop a model in which the input parameters to identification are the coordinates of the tip through time.

3. INVERSE IDENTIFICATION: THEORETICAL BACKGROUND

3.1. INTRODUCTION

In the previous chapter, it has been proposed that a mathematical model be developed, allowing online identification of the forces acting on a flexible needle during insertion into a soft substrate, as a function of the geometrical and mechanical variables of the needle and the stiffness of the substrate, at every point in time. Previous literature suggests that the needle undergoing deflection during insertion can be modelled as a flexible beam, which allows derivation of a model in the form of an Euler Bernoulli Beam. In this chapter, the theoretical background of inverse force identification and the related mathematical issues are studied, and the mathematical methodology for inverse load identification from the beam deflection is developed.

3.2. INVERSE PROBLEMS

Two fundamental types of problems are recognised in mathematical modelling, namely the forward problem and the inverse problem (Uhl and Mendrok 2005). The forward problem can be characterised as solving the equations that govern the behaviour of a system, by inputting variables and imposing boundary conditions to the system, to define the responses and reactions. The schematic of these problems is illustrated in figure 3-1.

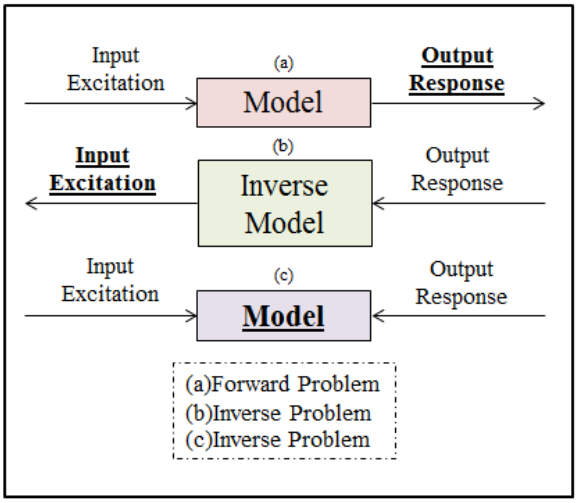

Figure 3-1 Schematic of forward and inverse problems. The solution in each problem is underlined.

The inverse problems can be grouped into two categories (Uhl 2007):

1. Classic Identification: identifying the model of the system based on known inputs to the system, the boundary conditions of the problem and the responses of the system.
2. Inverse Identification: identifying system inputs based on the boundary conditions of the problem, the defined model of the system, and known responses of the system.

One application of inverse and classic identification is modelling of the mechanical behaviours of a system. For modelling the system's response under loading, the force acting on the system is defined as the input to the problem, and the system's behaviour as the system response. A main application of inverse problems is in defining the contact forces between two structures, as a function of the system responses. In such cases, the magnitude of forces is not known, but the locations of the forces acting on either structure can be defined. This provides a means to define the operational loads acting on each structure. In order to obtain these loads, a model of the structure must be defined. A well posed problem can be defined as a problem where (Uhl 2007):

- For all reasonable data, there exists a globally defined solution to the problem

- The globally defined solution is unique
- The solution depends continuously on the input data.

Any problem which is not well posed, is deemed as ill posed. For example, if the initial conditions or state variables are not known for a forward problem, then it is considered as ill-posed. Inverse problems are mainly ill posed.

One of the main causes of ill-posed inverse problems is the practical limitations one faces regarding measuring enough data from a system's response. These limitations can be due to the either of the following factors:

1- Sensors will alter the system characteristics and hence a limited number of sensors can be attached to the system
2- Even if we use proximity sensors, still we are faced with the limitation on space and interaction between sensors
3- Not all desired parameters can be measured. For example, there is no sensor which can measure rotational responses.
4- Accessibility limitations. Usually most of the system is inaccessible or used for some operational purposes and hence a sensor cannot be attached to those parts.

For example, in physical systems where contact force determination is desired, sensors measuring system responses cannot always be placed at points at which the forces are acting. This can result in the sensors being insensitive to one or more of the forces acting on the system. Thus, there exists a lack of information about the system, and the problem will not meet the predefined conditions of a well-posed problem, rendering it ill-posed. In 1923, Hadamarad (Hadamard 1923) proved that inverse identification problems are ill-posed as they do not have one unique solution. In order to solve an ill-posed problem, the general idea is to obtain further information about the solution to the problem, thereby transforming the problem to a well-posed problem by a method called regularisation. An ill-posed problem can also be due to numerical ill conditioning of the model matrix (Anger 1988), which is measurable through checking the condition number of the matrix. The model matrix is a matrix incorporating the known constants of the system equations, and is mathematically formulated by obtaining an approximate solution to the system equations, by means of error minimisation methods. The mathematical significance of this matrix is that, for inverse load identification, it is generally inverted and multiplied with a matrix of measured system responses. Having acquired the model matrix, the numerical conditioning can be improved by

regularisation methods based on manipulation of the Singular Value Decomposition (SVD) of the matrix.

In this chapter, initially the general methodology of inverse load identification problems is presented and the approaches to formulation of the model matrixes from system equations are studied. The numerical conditioning of the model matrix is then explained, and the theoretical background and structure of the proposed method defined.

3.3. INVERSE FORCE IDENTIFICATION

The inverse identification of the acting loads on a system based on its responses can be achieved using several approaches, which are categorised into three main groups (Busby and Trujillo 1987, Anger 1988, Giergiel and Uhl 1989, Anger 1990, Dobson and Rider 1990, Uhl 2002):

1- Deterministic Methods
2- Stochastic Methods
3- Methods based on artificial intelligence

Deterministic methods involve defining the model parameters as a function of model simulation. This provides useful information regarding the system, but has heavy reliance on the mathematical conditioning of the model matrix, which in turn affects the inverse solution to the problem. In order to define the parameters of the defined model, experimental gathering of input and output data variables to the model must be obtained through functional observations of the system. This brings about the difficulty in modelling a nonlinear system, where identification of the parameters of the nonlinear inverse model is needed, as the relationship between inputs and outputs can be very difficult to ascertain.

Stochastic modelling is based on conducting experimental or theoretical observations of the system model and statistical study and analysis of the variable data obtained, thereby defining mathematical relationships through statistical occurrence. This method requires direct measurement of the model variables such as force, which as previously stated can be impossible due to the difficulties with placing sensors at the point of force application. One of the main stochastic methods employed for force identification is the regression model (Uhl 2007), the applications and limitations of which are studied in (Trujillo), and the methodology and application of which is presented in (Uhl 1998).

Load identification using artificial intelligence can be further divided into these main categories (Uhl 2007): Artifical Neural Networks (Uhl 2002), Fuzzy Algorithms (Góral, Bydoń et al. 2002) and Evolutionary Algorithms (Uhl 2003). In general, artificial intelligence based approaches involve the development of a relationship between the inputs and outputs of a system through learning, which necessitates direct measuring of the applied loads and system responses. This brings about complications during measurement of actual system responses, and one way around this is to facilitate numerical simulations of the system responses for the learning process.

As has been mentioned, of all the mentioned methods, the deterministic method has the advantage of allowing model parameter identification, avoiding possible complications related to measuring input and outputs of the model. The deterministic identification of loads acting on a system is typically either defined in the frequency domain or the time domain. Frequency domain methods are usually used in vibration problems, where the frequency response functions of the system and the range of measured responses is known. In some cases these methods involve employing the Heaviside mutual-energy theorem for identification of the range of acting loads from a measured system response (Hansel 1991).

Time domain identification methods are generated through developing a relationship between the input excitation and corresponding system responses, which can be iteratively approximated through time. Both approximation methods can be applied to linear and nonlinear problems, and in linear cases a solution can be obtained by calculating the least square error between the measured system responses and the calculated system responses, as a function of the identified loads. For nonlinear systems, the generation of the forces can require more complex solution approximation methods, as they typically involve higher order Partial Differential Equations (PDEs). In these cases, methods such as weighted residuals in the form of energy methods or boundary value problems, or iterative numerical solution approximation methods, such as the Rung Kutta, can be employed for solution approximation and force identification. The Rung Kutta approximation is an implicit or explicit numerical method employing time marching as a means of approximation and does not provide a close form solution. It allows discretisation of the equations, solved from step to step, providing a chain of data approaching the final solution to the problem. In a closed form solution, an equation must be provided, allowing estimation of a desired parameter as a function of its variables at any point. Thus, the limitation of explicit methods such as the Rung Kutta is that it fails in cases where the system state variables at every step are a function of other

dependent system variables at the same step. For example, in the following chapters it will be shown that, for a beam undergoing large deflection, the deflection of any point on its length at time t is a function of the curvature of the same point in time t. This makes methods like the Rung Kutta difficult to employ for higher order PDEs, such as those occurring in nonlinear system behaviours. Regarding the formulation of the inverse problem, the close form solutions of the weighted residual method have the advantage that they can provide information regarding the state of the current step of the solution. This is further explained in the next section.

3.4. WEIGHTED RESIDUAL METHODS

As previously defined, for obtaining an approximate closed form solution to the PDEs governing the equilibrium of a system, leading to required formulation for inverse identification, weighted residual methods (WRM) can be employed. The Rayleigh–Ritz method, which is based on the variational approach and minimum potential function principle, can also be used for this purpose. While WRM attacks the boundary value problem and hence its governing differential equations, the Rayleigh–Ritz method is applied to an energy functional called the potential function. The most powerful technique amongst WRMs is the Galerkin method. Other popular methods from this family include the least square and the collocation. Although Galerkin and Rayleigh–Ritz methods are different in their formulation, it can be shown that these methods are basically the same. However, since formulation of the boundary value problem is more feasible than identifying the functional for a particular problem and the Galerkin method is more flexible in handling of the boundary conditions, this method is usually preferred over Rayleigh–Ritz method. An explanation of the methods is presented below.

3.4.1. VARIATIONAL AND WEIGHTED RESIDUAL METHODS

Let's define x as an independent variable and y as a dependant variable belonging to the class of admissible functions that satisfy the essential boundary conditions of a boundary value problem. Using the principle of virtual work it can be shown that amongst all the admissible y's, the one which renders the integral in equation (3-1) a minimum represents the stable equilibrium state of the system governed by the above mentioned boundary value problem. Where in equation (3-1), π represents the potential functional, it can be said:

$$\pi = \int g(y, x, y', \dots) dx \tag{3-1}$$

Using the Rayleigh–Ritz method, an approximate solution as shown in equation (3-2) is defined and substituted in equation (3-1). Then one can find participation factors a_i in equation (3-2) such that the functional $\hat{\pi}$ becomes minimum:

$$\hat{y}(x) = \sum_{i=1}^{n} N_i \, . \, a_i \tag{3-2}$$

N_i in equation (3-2) is called a trial function and must possess certain properties which will be discussed in next section. Since the variational method is an energy method, and is derived from principle of virtual work, π is defined for a specific setup of the structure being studied, regarding the constraints and essential boundary conditions. This, in turn, means that the trial functions N_i in (3-2) must be chosen such that they satisfy the essential boundary conditions (such as geometry and position constraints) of the system. Natural or force boundary conditions can be introduced (for forward solutions) or extracted (for inverse identification) during the solution or identification process.

The WRM offers a higher level of flexibility for handling of the boundary conditions compared to the Rayleigh–Ritz method. This is due to the fact that, as explained above, a functional is defined for specific geometrical/essential boundaries, i.e. the essential boundary conditions of the problem are incorporated into the weak form of the equation (3-1). The boundary value method defines the equilibrium equation for an infinitesimal element of the system regardless of its boundary conditions, allowing inclusion of the boundary conditions after the general solution has been formulated. Thus, it allows higher flexibility in systems with complex boundary conditions. The writing of the equilibrium equations of the system lead to PDEs, which are then solved by approximate methods such as the weighted residual method. As has been mentioned, the Galerkin method is the most powerful method to achieve a close form solution to a nonlinear system of differential equations, where this nonlinearity can either be due to mathematical or boundary condition complexity. Compared to the Rayleigh-Ritz energy method, the method has the added advantage of being applicable directly to boundary value problems, and as such, does not require the functional π which is not always easy to develop. Since the method is intrinsically in weak form, it is very powerful in handling both natural boundary conditions and unsatisfied essential boundary conditions. It must be noted that the unsatisfied essential boundary conditions can reduce its accuracy compared to that of energy methods such as the Rayleigh Ritz, but the flexibility of the boundary conditions make it particularly efficient for inverse force identification problems,

where the boundary conditions of the problem may vary and cannot be predetermined with the same ease as a forward solution. The theoretical concept of the Galerkin method and its mathematical derivation is presented in the following section.

3.4.2. THE GALERKIN METHOD

It has been explained that the boundary value problem formulation involves the derivation of the equilibrium equation of a system. This is generally formulated as a differential equation which must satisfy the boundary conditions. Boundary conditions are either essential, in that the solution value is prescribed (geometry, displacement or kinematic BCs) or natural, where the derivative is provided (Force, stress BCs). In these cases, the exact solution to the problem is defined as a high order integral of the equilibrium differential equation, which can be complex or impossible to solve due to domain or boundary complexity. As such, the weighted residual method provides an approximate solution that satisfies the essential boundary conditions, but not the natural ones. Thus, the approximation will not satisfy the differential equation, and a residual between the approximated solution and the exact solution exists. The idea of the method is to minimise this residual by multiplying or "weighing" the residual with weighing functions forming the basis of the function space in which the approximation is presented, and integrating over the domain. This is mathematically defined as equation (3-3):

$$\int_0^L W_i[R_\Omega] \cong 0 \tag{3-3}$$

Where W_i is the weight function, i is the index of ith weighing function, and R_Ω is the residual between the approximate solution $\hat{y}$ and the exact solution y along the domain between 0 and L. The selection of the trial functions is what defines the difference between the different weighted residual methods, such as the least square method, Petrov-Galerkin , Babnov-Galerkin or the collocation method. In the Galerkin method, the approximate solution $\hat{y}$ is defined as a linear combination of trial functions in equation (3-4), such that:

$$\hat{y}(x) = \sum_{i=1}^{n} N_i\,(x).\,a_i + \varphi(x) \tag{3-4}$$

Where a_i is the participation factor, and N_i are the trial functions where, if $n \to \infty, \hat{y} \to y$. In the Babnov-Galerkin method, the trial functions are also used as weight functions for the residual minimisation in equation (3-3). The approximate solution $\hat{y}$ must satisfy the

essential boundary condition, and the accuracy of equation (3-4) is dependent on the correct selection of the trial functions, the conditions of which is discussed further on in the chapter. If all Ni are chosen such that they are zero on essential boundaries, then $\varphi(x)$ is chosen such that it satisfies essential boundary conditions. However, if N_i values themselves satisfy essential boundary conditions, then $(x) = 0$.

The Galerkin method is mainly used in two applications, namely the finite element Galerkin method, and the classic or traditional Galerkin method. It must be noted that conventionally finite element problems are formulated using either the variational (energy methods) or the boundary value methods. This is due to the fact that, for some problems, the definition of the functional is very complex, which is the case for non-conservative systems, where there exists dissipation of energy.

The finite element Galerkin method breaks the domain of the solution down to smaller increments, and employs the Galerkin approximation for each small increment. The classic Galerkin method applies the solution approximation to the entire domain of the solution, in the form of an explicit equation. Both Methods are subsequently explained.

3.4.2.1. THE FINITE ELEMENT GALERKIN METHOD

In the finite element Galerkin method, the solution to a differential equation is obtained by minimising the residual between the approximate solution to the problem and the actual solution. This is achieved through weighing the residual via a shape function (same principle as the trial functions) and defining its integral as zero, as previously shown in equation (3-3). The integral in equation (3-4) can be broken down into n elements and written as the total of its summation, as shown in equation (3-5), which results in a finite element Galerkin solution approximation.

$$\int_0^L N_i[R_\Omega] = \int_0^{L_1} N_i[R_\Omega] + \int_{L_1}^{L_2} N_i[R_\Omega] + \cdots + \int_{L_{n-1}}^{L_n} N_i[R_\Omega] \tag{3-5}$$

A schematic illustration of the elements along the length of a beam, as well as the shape functions associated with each node, is presented in figure (3-2) as an example, where a Galerkin approximation of the deflection of the beam is desired, using linear shape functions.

Figure 3-2. Schematic of beam element $\boldsymbol{e_i}$ between nodes $\boldsymbol{i}$ and $\boldsymbol{j}$. The shape functions $\boldsymbol{N_i}$ and $\boldsymbol{N_j}$ are each maximum (equal to 1) at the respective node for which they have been defined, and 0 at other nodes along the length of the beam.

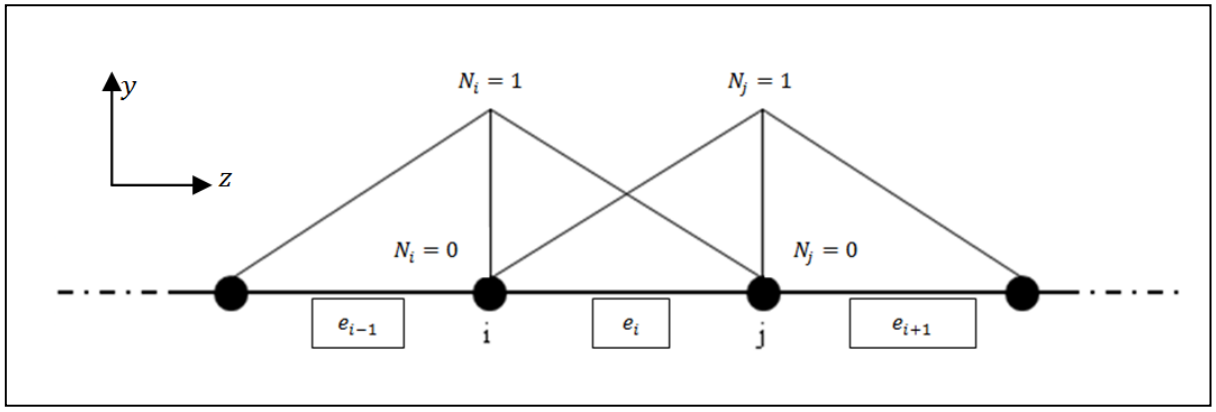

Each shape function N_i is defined individually over each element and is linked to its corresponding nodes, as will be shortly explained. From figure (3-2) it can be said that if the length of the element e_i is defined as h, the linear solution approximation for the element can be written as equation (3-6).

$$\hat{y} = \frac{z_j - z}{h} y_i + \frac{z - z_i}{h} y_j \tag{3-6}$$

Where it can be shown that for $z = z_i$, $y = y_i$. By this definition, the shape function of y_i, defined as N_i, can be written as $\frac{z_j - z}{h}$, and the same can be applied to y_j. This means that, for an element e_i, it can be said that:

$$\bar{\hat{y}_e} = N_i y_i + N_j y_j \tag{3-7}$$

Equation (3-7) provides the approximate deflection of the element e_i . For equation (3-7) to hold true along the length of the beam, the additional condition is defined that, if $z \geq z_j$, then $N_i = 0$ and, if $z \leq i$, then $N_j = 0$. This means that these shape functions are element specific, but are defined for common nodes such as node i between elements e_i and e_{i-1}. It can be seen that, as each shape function is element specific and zero across the rest of the solution domain, the total solution approximation can be written as the summation of the solution approximations for each element.

3.4.2.2. The Classic Galerkin Method

In classic Galerkin approximation to the beam deflection as in the example above, the trial functions are defined over the whole domain. A popular trial function of choice is the vibrational normal mode shape of a beam, with the same configuration and essential boundary conditions, as shown in figure (3-3) for a clamped-free beam. These trial functions are defined over the entire domain of the solution, as opposed to the piecewise definition of the shape functions for each increment, as defined in the finite element Galerkin method.

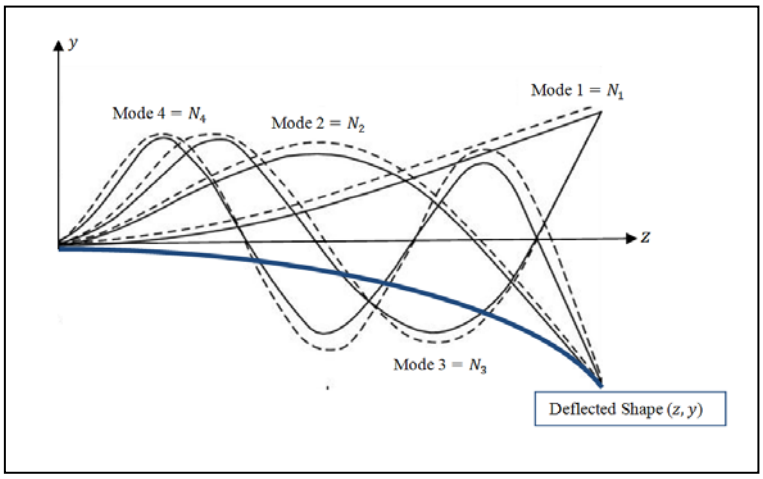

Figure 3-3 Mode shapes of a beam undergoing vibration employed as trial functions (base functions) to approximate the deflected shape via the Classic Galerkin Approximation.

It must be noted that, although for a smooth function y, such as the curved shape of a deflected beam, the classic Galerkin provides a simpler method for an approximate solution, the same cannot be said for irregular shapes with high variations in geometry and loading along the solution domain. In these cases, the solution approximation written as the summation of trial functions throughout the whole domain will not yield accurate results. In these cases the piecewise finite element Galerkin method has a distinct advantage, as definition of valid trial functions as bases for the function space of the solution can be impossible.

It was previously mentioned in section 3.4.2.1 that the trial functions selected have a high impact on the accuracy of the approximation. From the example above, it can be seen that the selection of appropriate trial functions for the solution approximation is crucial to residual minimisation, and as such the trial functions must satisfy the following conditions:

1. The trial functions must be linearly independent.
2. The trial functions must belong to a complete space.

Linear independence means that, if $\sum_{i=0}^{N} a_i N_i = 0$, then for $i = 1 \ldots n$, all of the participation factors a_i must be equal to zero. This means that one trial function cannot be defined as a function of others. This is necessary to the employment of the trial function as the bases of the function space of $\hat{y}$. The second condition dictates that, if $N \to \infty$ (i.e. an infinite number of trial functions exist in the solution approximation), then the residual

$\|y - \hat{y}\| \to 0$. This means that the limit of the summation series of trial functions must exist in the function space defined for the solution approximation. For example, if the odd functions $sin(nx)$, where $n = 1 \ldots \infty$, are defined as trial functions for the approximation of an even function, although they are linearly independent, no matter how many trial functions are added to the approximation, the residual cannot be minimised. The same applies to discontinuous functions; an infinite number of continuous trial functions will not approximate a discontinuous solution, and discontinuous trial functions must be added to the base functions to allow a complete function space. In other words, a function space is complete if any function can be defined in it. For the $sin(nx)$ example, the addition of $cos(nx)$ will render the function space complete. This has significant bearing on the problem in hand, as the probe is made of two sections with discontinuity in the geometry, and hence the proper trial functions must be used to fulfil the requirement for completeness.

As was defined in section 3.4.1, the weight of each of the trial functions in the solution is defined as the participation factor, a_i. The participation factor is defined as a measure of the participation of each of the trial functions in the solution. This must not be confused with the weights of the residuals, which are the trial functions. By visualizing the solution approximation as a vector in function space, the trial functions are the bases of the space the vector is defined in, as illustrated in figure (3-4), for a solution y defined in three dimensional function space (three trial functions).

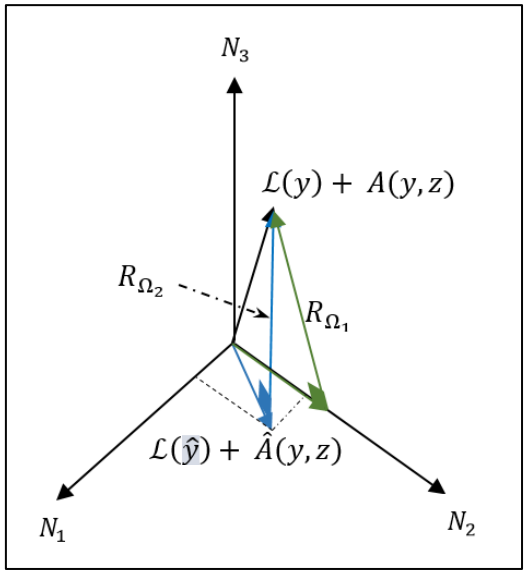

Figure 3-4 Schematic of solution $\boldsymbol{y}$ defined in three dimensional function space. The residual decreases in length with the increase from the one dimension to the two dimensional approximation, $\boldsymbol{R_{\Omega_1} > R_{\Omega_2}}$

The solution y is approximated in a three dimensional functional space as $\hat{y} = \sum N_i a_{\mathrm{i}}$. The residual of the approximation is minimised by defining the $\int_0^L N_i R_\Omega \, dz$ as zero for $i = 1,2,\ldots..N$, which is represented schematically as the residual vector R_Ω being normal to the base function vectors N_i. Let us assume that the true solution y belongs to the space of (N_1, N_2, N_3), and is approximated once with one trial function (or defined with one base function) resulting in $\hat{y}_1$, and once with two trial functions, resulting in $\hat{y}_2$. The residuals to each approximation is defined as R_{Ω_1} and R_{Ω_2} respectively. For $\hat{y}_2$, where there exists more than one trial function/base functions, the participation factors a_1 and a_2 dictate how close the approximation $\hat{y}_2$ is to each of the base functions (includes the weight of each trial function). This can be visualised as if $a_2 > a_1$, then the vector $\hat{y}_2$ will be closer to the base function N_2 , than to N_1. It is also shown in figure (3-4) that the magnitude (length) of R_{Ω_2} is less than R_{Ω_1}. This indicates that, as the number of the bases of the function space increase, the residual decreases. As previously mentioned, if the number of the trial functions in the approximation approaches infinity, the residual will tend towards 0 and an exact solution is obtained, provided that N_i constitutes a complete space.

Having defined the correct criterion for the trial functions, the classical method can be applied to a system's differential equation governing its equilibrium state. The residual minimisation integral (as defined in equation (3-3)) is written for the differential equation $l(\hat{y}) = R_\Omega$.The order of the differential is then reduced by integration by parts, and the natural boundary condition applied to the solution. This results in the same order of differentiation for both the approximated solution $\hat{y}$ and the trial functions N_i. The approximate solution $\sum_{i=0}^{N} a_i N_i$ (equation (3-4)) is then substituted into equation (3-3). This will yield the final equation in the form of equation (3-8):

$$\sum_{j=0}^{N} K_{ij} a_j = f_i \,, \qquad i,j = 1, \dots, N$$

$$[K]_{n\times n}\{c\}_{n\times 1} = \{F\}_{n\times 1} \tag{3-8}$$

and

$$K_{ij} = \int_0^1 \frac{dN_i}{dx}\frac{dN_j}{dx}\,dx$$

Where the known variables are in the right hand side of the equation, shown as f_i . The coefficient matrix (model matrix) K is symmetric if the underlying differential equation is symmetric, and the final matrix equation has N equations with N unknown participation factors.

It has been mentioned in section 3.2 that the model matrix must be numerically conditioned to obtain an accurate solution to the system equations. It can be seen here from equation (3-8), that the model matrix must be inversed to obtain the participation factors of the trial functions. If the matrix is ill-conditioned, this may results in inaccurate results and amplification of the natural inaccuracies in the matrix $\{F\}$, which although within reasonable bound, may be multiplied to form a significant error. The ill-condition is particularly a problem in an inverse problem and inverse problems are naturally more prone to ill-condition, as will be explained in next section. The regularisation of the model matrix incorporated into the matrix calculations to investigate and rectify numerical ill-conditioning is explained in the following section.

3.5. Regularisation Methods

As previously explained, a mathematical problem can be ill posed due to lack of sufficient information regarding the system, and/or the numerical ill conditioning of the model matrixes. This can be measured by calculating the condition number, defined as the ratio of the maximum and minimum singular values of the matrix, which if high, can result in inaccurate or unstable solutions. The Singular Value Decomposition (SVD) of the model matrix can be used to improve the numerical condition of the problem, and thus can be classified as a regularisation method.

Regularisation can be achieved through these methods:

1. Generalized cross-validation
2. Singular Value Decomposition (SVD) methods
3. Tikhonov regularisation

The methods mentioned above are direct regularisation methods, i.e. the solution is defined by direct computation, as opposed to iterative regularisation methods such as Conjugate Gradients, Bi-diagonalisation and Extension to General-Form problems (Hansen 2008), which are outside the scope of this work. An explanation of some of the main regularisation methods is presented below, the main emphasis being on the SVD and Tikhonov methods.

3.5.1. GENERALISED CROSS VALIDATION

Cross validation involves eliminating a point from a set of measured system response data points used to formulate the inverse solution, and obtaining the inverse solution to the problem by using the rest of the data set. For a complete and well posed problem, the identified parameters are supposed to be consistent with all of the data points (including the eliminated ones). The eliminated data points then provide a free observation, and the accuracy of the identified model can be determined by comparison of the eliminated data points and those estimated by the identified model. By calculating a sum of the squares of the errors of all the data points by the same method, a numerical measure evaluating the performance of the model is defined. For modelling problems where data with noise exists, the cross validation method has the advantage of permitting parameter estimation without prior knowledge of the noise statistics, as it utilises the data points themselves.

3.5.2. SINGULAR VALUE DECOMPOSITION REGULARISATION

The SVD regularisation method is based on the decomposition of the system matrix and study of its singular values. In order to solve the numerically ill conditioned identification problem, the smallest singular values are identified and the corresponding sections of the matrix are either eliminated from calculations, or the matrix condition is improved to obtain an accurate solution despite the numerical deficiency.

Three of the main tools needed for SVD regularisation are the singular value decomposition (SVD), generalised singular value decomposition (GSVD), and the truncated singular value decomposition (TSVD). The first is a measure of the complexities associated with numerical ill conditioning of the matrix, the second provides the means of regularisation via introducing additional data, and the third provides the means of regularisation by eliminating the

numerical source of ill conditioning. These concepts are further explained in the following section.

3.5.2.1. SINGULAR VALUE DECOMPOSITION (SVD)

One important example of the effect of numerical ill conditioning is in solving system equilibrium equations in the time or spatial domain by discretization. This usually results in a system of equations, such as equation (3-8), in the format $[A][x] = [B]$, where in its most general case (like Petrov Galerkin method) will lead to a least square solution, as shown in equation (3-9).

$$min\|[A][x] - [B]\| \to 0, A \in \mathbb{R}^{m \times n}, \qquad m > n \tag{3-9}$$

In order for the problem in equation (3-9) to be well posed, the model matrix A must be numerically well-conditioned. To this end, the singular value decomposition (SVD) of A is calculated. Assuming A is a rectangular matrix where $A \in \mathbb{R}^{m \times n}$ and $m \geq n$, the SVD of A is defined as equation (3-10).

$$A = U\Sigma V^T = \sum_{i=1}^{n} u_i \sigma_i v_i^T \tag{3-10}$$

Where $U^T U = V^T V = I_n$, $U = (u_1, \dots, u_m)$, and $V = (v_1, \dots, v_n)$ have orthonormal columns, which represent the eigenvectors of $A\,A^T$ and $A^T A$, respectively. Also, the matrixes u_i and v_i are the left and right singular vectors of A, respectively. The Σ is diagonal mxn matrix with elements $\sigma_1 \dots \sigma_n$, where σ_i are the non-negative singular values of A and $\sigma_1 \geq \cdots \geq \sigma_n \geq 0$. The matrix U represents the range of the matrix A, while the columns of matrix V which correspond to zero singular values represent its null space.

The SVD of each matrix must be unique; this can be shown by calculation of $A^T A$ and $A\,A^T$ in equation (3-11) :

$$A^T A = V\Sigma^2 V^T, A\,A^T = U\Sigma^2 U^T \tag{3-11}$$

It can be seen that the SVD of A is heavily related to the spectral decompositions of the two product matrixes $A^T A$ and $A\,A^T$, which are positive and symmetric. As a result, the SVD of a matrix will be distinctive, except in singular vectors associated with multiple singular values (Hansen 2008).

The condition number of A is defined as ${\sigma_1}/{\sigma_n}$, and is a measure of the numerical conditioning of the matrix. i.e., if the condition number is too high, (${\sigma_1}/{\sigma_n} \gg 1$), it indicates that A is ill conditioned. This means that, if matrix A is inversed to solve for unknown variables such as $[x]$ and a known matrix $[B]$, small changes ϵ in matrix $[B]$ will result in significant changes in the variable matrix $[x]$,the upper bound of which is the condition number. This is known as high sensitivity to perturbations in A or B and is mathematically shown in equation (3-12).

$$[A][x] = [B],\ [A][x'] = [B + \epsilon], \text{ where } \|\epsilon\| \ll \|b\| \\ \rightarrow \|x - x'\| \ll condition\ number \tag{3-12}$$

In addition to A being ill conditioned (high sensitivity), it is often found that, if the singular values σ_i of matrix A gradually decrease to zero, the problem $[A][x] = [B]$ will be ill posed (Hansen 2008). The general decrease of σ_i leads to an increase in the number of small singular values with increase of the dimension of A. This indicates that, in addition to high sensitivity, there is no "adjacent" problem where the coefficient matrix A is well conditioned and numerically well-determined.

Another usual indication of ill-posed problems is that the elements of the right and left singular matrixes U and V have frequent sign changes, as σ_i decreases and i increases. This can be shown by studying the two relations in equation (3-13), where for $i = 1, \dots, n$:

$$\begin{cases} Av_i = \sigma_i . u_i \\ \|Av_i\|_2 = \sigma_i \end{cases} \tag{3-13}$$

It can be seen that, compared to $\|A\|_2 = \sigma_1$, the magnitude of the small singular value σ_i indicates the presence of a specific combination of the columns of A, defined by the elements of v_i, where $\|Av_i\|_2$ is small. This means that A is almost rank deficient, and null vectors of matrix A are the v_i vectors corresponding to the small singular values σ_i. Thus, it can be deduced that the coefficient matrix A of an ill-posed problem can be significantly ill-conditioned with a null space of vectors with high sign variation.

The SVD also gives a measure of the smoothing (Hansen 2008) during vector mapping. Assuming the mapping of the vector x via matrix A to Ax, the SVD of x and Ax is calculated in equation (3-14).

$$x = \sum_{i=1}^{n} (v_i^T x) v_i$$
$$Ax = \sum_{i=1}^{n} \sigma_i (v_i^T x) u_i \tag{3-14}$$

It must be noted that the increase in oscillation of the singular vectors v_i and u_i can be seen with the decrease in σ_i. From equation (3-14) it can be said that, as a result of the multiplication of σ_i, a lower frequency component of x will be less damped after being mapped to Ax, compared to a higher frequency component. The reverse will occur in solving inverse problems through systems of equations or least squares problems in the forms of equation (3-9); where the high frequency oscillations in B will we amplified, causing inaccuracies in the solution. In order to solve this, for inverse solving of problems in the form of $Ax = B$, where the matrix B has high frequency oscillations (noise), a pseudo-inverse or Moore-Penrose inverse of A is calculated, as shown in equation (3-15).

$$A_{m\times n}{}^{+} = V^T \Sigma^{-1} U$$
$$\begin{cases} if\ m > n\ and\ A\ full\ rank, A^+ = (A^T A)^{-1} A^T \\ if\ m < n\ and\ A\ full\ rank, A^+ = A^T (A A^T)^{-1} \end{cases} \tag{3-15}$$

For the problem defined above, $x_{pinv} = A^+ B$ is the least squares solution. This removes the amplification of any noise in the data in matrix B, due to the numerical ill conditioning of the matrix A, during inverse solutions.

From the explanations above, it can be seen how the SVD can be employed to measure the mathematical conditioning of matrix A. In order to obtain an accurate mathematical solution to the inverse problem, the SVD can be manipulated to rectify the ill conditioning, through methods such as the generation of the GSVD, TSVD and the Tikhonov Regularisation. These methods are explained in the following sections.

3.5.2.2. The Generalised Singular Value Decomposition (GSVD)

For solving of the matrix system $[A][x] = [B]$ as previously mentioned, in some cases noise in the data in matrix B, or an underdetermined matrix A, can create an ill-posed problem. One method to solve this is the introduction of a matrix L to be paired with A, which includes an estimated condition of the solution x, such that $Lx = B^*$. This can be shown in equation (3-

16) for an arbitrary matrix L and a two dimensional matrix of unknowns x_1 and x_2 , where the estimate of x_1 is b_1^L and the estimate of x_2 is b_2^L , which form matrix B^*.

$$A = \begin{bmatrix} a_{11} & a_{12} \\ \vdots & \vdots \\ a_{m1} & a_{m2} \end{bmatrix}, B = \begin{bmatrix} b_1 \\ \vdots \\ b_m \end{bmatrix} , \begin{bmatrix} a_{11} & a_{12} \\ \vdots & \vdots \\ a_{m1} & a_{m2} \\ \begin{bmatrix} 1 & 0 \\ 0 & 1 \end{bmatrix} \end{bmatrix} \begin{bmatrix} x_1 \\ x_2 \end{bmatrix} = \begin{bmatrix} b_1 \\ \vdots \\ b_m \\ \begin{bmatrix} b_1^L \\ b_2^L \end{bmatrix} \end{bmatrix} \tag{3-16}$$

It can be said that, for the two matrixes $A \in \mathbb{R}^{m \times n}$ and $L \in \mathbb{R}^{p \times n}$ where $m \geq n \geq p$, as the square roots of the generalised eigenvalues of the matrix pair $(A^T A, L^T L)$ is the generalised singular values of (A, L) , The GSVD of the matrix pair (A, L) is a generalisation of the SVD of A. This can be shown in general terms in equation (3-9), where, for $\Sigma = diag(\sigma_1 \dots \sigma_p)$ and $M = diag(\mu_1, \dots, \mu_p)$, it can be stated that:

$$A = U \begin{pmatrix} \Sigma & 0 \\ 0 & I_{n-p} \end{pmatrix} X^{-1}, L = V(M, 0)X^{-1} \tag{3-17}$$

Where $X \in \mathbb{R}^{n \times n}$ is nonsingular and $V \in \mathbb{R}^{p \times p}$ and $U \in \mathbb{R}^{m \times n}$ are orthonormal. The diagonal elements of the matrices M and Σ are positive and are structured, as shown in equation (3-18).

$$0 < \mu_p \leq \cdots \leq \mu_1 \leq 1 , \quad 0 \leq \sigma_1 \leq \cdots \leq \sigma_p \leq 1 \tag{3-18}$$

Based on the above, the generalized singular values γ_i of (A, L) are then defined as:

$$\begin{gathered} for\ i = 1, \dots, p \\ \gamma_i = {}^{\sigma_i}/_{\mu_i}, \quad {\mu_i}^2 + {\sigma_i}^2 = 1 \end{gathered} \tag{3-19}$$

Where γ_i are in increasing order. The generalised singular values, although having no direct relation to the original singular values, bear some of their characteristics. For example, for small σ_i values approaching zero, the generalised singular values also approach zero. Some analysis of the x_i is also possible by examination of the GSVD values, for example, a smaller $\gamma_i$denotes higher sign changes in the x_i.

This method allows rectification of the numerical ill conditioning through the introduction of additional information to the system, which improves the numerical conditioning of the system matrix. Other approaches such as the generation of the TSVD of the model matrix,

rectifies the issue by removing the elements of the matrix that cause the numerical ill conditioning, as explained in the following section.

3.5.2.3. TRUNCATED SINGULAR VALUE DECOMPOSITION REGULARIZATION (TSVD)

Previously, it has been shown in section 3.5.2.2 that the development of the GSVD of an ill conditioned coefficient matrix A by substitution of $\begin{pmatrix} A \\ \lambda L \end{pmatrix}$ can provide a viable solution to a numerically ill-posed problem. Another method is to extract a well-conditioned matrix from A by eliminating the elements that are the cause of its ill-conditioning. This is achieved by generating the SVD of A as defined in equation (3-9) by a full rank decomposition, and defining a number k of highest singular values which are kept, replacing the rest with zero and keeping only the first k columns of U and V (equation (3-9)). This results in a rank deficient (or truncated) SVD, providing the closest approximation A_k of A (based on second norm) which is of rank k. In other words, the closest rank deficient approximation of A, namely A_k can be determined by truncating the SVD, as shown in equation (3-20):

$$A_k = \sum_{i=1}^{k} u_i \sigma_i v_i^T \, , k \leq n \tag{3-20}$$

The truncated SVD can be used to solve the numerically ill-posed $Ax = b$ by solving the problem $min\|x\|_2$ subject to $min\|A_k x - b\|_2$. It can also be used in connection with the GSVD, as defined in section 3.5.2.2, to find a solution to $min\|Lx\|_2$ subject to $min\|A_k x - b\|_2$. The solution to both problems is defined in equation (3-21).

$$x_k = \sum_{i=1}^{k} \frac{u_i^T b}{\sigma_i} v_i \quad , \qquad x_{L,k} = x_k - V_k (LV_k)^{\dagger} L x_k \tag{3-21}$$

Where $V_k \equiv (v_{k+1}, \dots, v_k)$ and $(LV_k)^{\dagger}$ is the pseudoinverse of LV_k. This means that the adjustment to the x_k defined in equation (3-21) is the least square solution to $min\|(LV_k)z - Lx_k\|_2$.

It must be mentioned that all other regularisation methods have at least one element in the numerical null-space of A, such as to allow the desired properties of the solution (as governed by L). The solution x_k obtained by the TSVD method is unique, in that it possesses no element in the numerical null-space of A, spanned by the columns V_k (Hansen 2008). This introduces a limitation of variables that can be identified via this method, i.e. the exclusion of

the selected singular values represents the exclusion of the effect of the corresponding components in the model matrix A. This can result in difficulties in defining variables with lower effects in the solution, when compared to other more significant variables. One method that allows a compromise between the mathematical condition of the matrix and the inclusion of the variables for identification is the Tikhonov Regularization, which is explained below.

3.5.2.4. TIKHONOV REGULARISATION

It has been shown that one of the main methods of regularisation is to obtain further information about the desired solution, such as imposing a known governing condition of the solution. One approach is to incorporate the condition of the solution having a small 2-norm and define a preliminary estimate of the solution x^{est}. It can be said that, for a regularised solution, there exists the added constraint that the difference $\Omega(x)$ between an estimated solution x^{est} and the actual solution x must be minimised, as shown in equation (3-22).

$$\Omega(x) = \|L(x - x^{est})\|_2 \to 0 \tag{3-22}$$

Where L is an identity matrix I_n , or a banded matrix of full low rank which is a $p \times n$ discrete approximation of the $(n-p)$ −th derivative operator (Hansen 2008). This is based on the idea that, as in the case of least squares problems, a solution close to the real unknown solution to the unperturbed problem will have a small residual norm and a small (semi)-norm. The introduction of the error minimisation in equation (3-22) compromises the condition that $Ax = b$, as defined in equation (3-12), instead producing a solution with a balance of a minimum $\Omega(x)$, while minimising the residual norm $\|Ax - b\|_2$ at the same time. The Tikhonov Regularization (A. N. Tikhonov , Phillips 1962, A. N. Tikhonov & V. Y. Arsenin 1977) defines the solution x_λ such as to minimise a desired combination of the added constraint and the residual norm, by the definition of a Regularization Parameter λ, as shown in equation (3-23).

$$x_\lambda = argmin\{\|Ax - b\|_2^2 + \lambda^2\|L(x - x^{est})\|_2^2\} \tag{3-23}$$

The balance between the minimisation of the residual normal versus the added constraint is decided by the magnitude of the parameter λ, i.e a higher λ produces higher regularisation through sacrifice of the minimisation of the residual norm for a small semi-norm solution. It can be shown that λ also dictates the sensitivity of x_λ to perturbation in A and b, the bound of which is proportional to λ^{-1} (Hansen 2008). If the perturbation of A and b is E and

e respectively, and, if the exact solution to the problem is $\bar{x}_\lambda$, it can be shown that $b_\lambda = Ax_\lambda$ and $r\lambda = b - b_\lambda$:

$$\frac{\|x_\lambda - \bar{x}_\lambda\|}{\|\bar{x}_\lambda\|_2} \leq \frac{\|A\|_2\|X\|_2\lambda^{-1}}{1 - \|E\|_2\|X\|_2\lambda^{-1}} \times \left(\left(1 + cond(X)\right)\frac{\|E\|_2}{\|A\|_2} + \frac{\|e\|_2}{\|b\lambda\|_2} + \frac{\|E\|_2\|X\|_2}{\lambda}\frac{\|r\lambda\|_2}{\|b\lambda\|_2}\right) \tag{3-24}$$

It can be seen from the equation above that, for the regularised solution x_λ, the perturbation bound is proportional to the norm of X and the magnitude of λ^{-1}. The norm of the matrix X is calculated in (Hansen 1989) and it is shown that $\|X\|_2$ is approximately bounded by the inverse of the smallest singular value of L (Hansen 2008). From this it can be said that the sensitivity of the regularised solution is controlled by L and λ.

It must be noted that these equations hold true only under the assumption that, in the right hand side of the equation, the errors are unbiased, with a covariance matrix proportional to the identity matrix. Where these assumptions do not hold true, additional calculations are needed (Zha and Hansen 1990). Generally, It can be said that the Tikhonov regularisation method provides a good balance between the numerical conditioning of the matrix, and the production of a result including the desired variables characteristics. This makes it efficient for reverse load identification, where the effect of the system variable on the desired parameter (applied loading in this case) must be observed, while numerical conditioning must be considered for accurate solution approximation.

3.6. CONCLUSION

In this chapter the theoretical background and mathematical methodology of inverse load identification methods have been studied. Based on this, the author proposes that a boundary value problem in the form of the equilibrium equation of a beam element be formulated for estimation of the needle deflection. The inverse solution to the beam model would allow load identification as a function of the deflection, through the solution of equilibrium PDEs using the classic Galerkin method. As the inverse identification will involve measured system data i.e. measurements from the flexible needle and the substrate, some inaccuracies in the results can be expected. As a result, it is proposed that the solution accuracy be controlled via the numerical conditioning of the defined model matrixes by applying the Tikhonov regularisation method.

4. MODEL DEVELOPMENT

4.1. INTRODUCTION

In previous chapters, various approaches to developing a model of the deformation of needles inside soft tissue has been discussed. It has been concluded in chapter 2 that, during the deformation of the needle, a mathematical model of the needle deflection can be developed, and an inverse solution to the model can be obtained, allowing identification of the forces acting on the needle throughout insertion. In chapter 3, possible identification techniques involving inverse problem solving have been explained, and the mathematical methodology of solving an inverse problem studied. Subsequently, based on the advantages and disadvantages of each methodology, it has been concluded that a boundary value problem be defined for the needle's deflection through a system equilibrium equation, and the Galerkin approximation method be applied to solving the problem leading to force identification. In this chapter, the methodology for definition of a simplified physical model of the needle as a beam is studied, for which an equilibrium equation can be written and the boundary value problem subsequently developed.

4.1.1. Model Parameters

As mentioned in chapter 3, to develop a boundary value problem of the needle deflection, a simplified physical model of the needle must be defined, the equilibrium equation of which is needed. This equilibrium equation is usually in differential form, which must then be solved over the independent variables domain of the problem (time, displacement etc.) to obtain the deflection of the needle at each point of insertion. Solving this equilibrium equation over its domain can be attempted through different solution approximation methods. Variational based computational methods such as the finite element (FE) method or the classical Galerkin or Rayleigh-Ritz method can be efficiently used for nonlinear problems with complex boundary conditions. The selection of the correct method is dependent on the nature of the problem. For example, in chapter 3, it was explained that, for a beam structure of relatively smooth shape, the classical Galerkin provides accurate solutions to its equilibrium equation and subsequent deflection, without the time cost associated with the piecewise calculations of FE. In addition, the emphasis on the parameters of the model performance, such as accuracy and time efficiency, can vary with model application, and as such are a factor in selection of the solution approximation method. Although non variational computational methods, such as the Rung Kutta and finite difference, can be employed for solution approximation, they are not as efficient as variational based methods in handling of a complex problem, such as the inverse solution to the nonlinear progressive insertion of a needle.

As discussed in Chapter 2, based on application, various approaches have been taken to modelling needle deflection during insertion into soft tissue. Two of the main approaches are finite element modelling (FEM)(Webster, Memisevic et al. 2005), and mathematical modelling (Asadian, Kermani et al. 2012) employing either non-variational or variational computational methods for solution approximation. It has been seen that both approaches introduce advantages and limitations; FEM, although accurate, can involve significant calculations and mesh regeneration of the soft tissue during insertion, and may not be ideal for time-sensitive applications, such as real time surgical simulation. On the other hand, classical methods can decrease calculation time, but may compromise the accuracy of the model by removing meshing and/or employing explicit empirical equations of the needles deflection as a function of predefined parameters. As such, the best modelling method for any problem must be selected based on the desired performance parameters, which is a function of its individual application.

It has been explained in chapter 1 that, as well as being a valuable tool in designing and optimising the needle path, the model under development in this work is aimed at application to real time needle insertion for neurosurgery, such as to aid the control of the needle through force identification and needle deflection prediction. Although FEM is valuable for crack propagation modelling, its application to modelling of the deflection of a needle during insertion can necessitate re-meshing of the material surrounding the needle, i.e. the brain, and patient specific brain material property definition, both of which are time consuming and complex. In addition, as explained in chapter 3, the selection of an efficient computational method is dependent on the behaviour of the physical system being modelled. Beam deflection equations can be solved efficiently with a classical Galerkin method, whereas a system with high fluctuations of dependent variables would be efficiently solved with FEM, due to its piecewise nature allowing for the fluctuations. As the needle deflection is not expected to fluctuate significantly along its length, during insertion, the application of a classical variational computation method, such as the classical Galerkin, can provide accuracy, while eliminating the time and calculation costs associated with FEM.

In addition to the importance of the selection of a computational solution approximation method for the solving of the equilibrium equations of the needle, the definition of the physical model of the needle deflection during insertion can have a high impact on the accuracy of the solution provided by that model. This is because the numerical results of the defined equilibrium equations of the needle may carry the inaccuracies associated with the

assumptions and simplifications of the physical model chosen for the needle deflection. This brings about the importance of the definition of the simplified physical model and the assumptions regarding the insertion process, for which the boundary value problem is defined. Thus, in addition to selection of an appropriate computational solution approximation method, an appropriate physical model of the needle and valid assumptions regarding its insertion process must be defined.

In Previous work (DiMaio and Salcudean 2002, Alterovitz, Goldberg et al. 2003, Webster, Memisevic et al. 2005, Hing, Brooks et al. 2006, Webster, Kim et al. 2006, Misra, Reed et al. 2008, Reed, Okamura et al. 2009, Yan, Podder et al. 2009, Misra, Reed et al. 2010) , 2D cantilever beams undergoing bending under external loading and moments have been used as physical models of surgical needles undergoing deflection during insertion. This is due to the geometrical shape of needles (high length to thickness ratio) and the fact that it is very unlikely that the needle will suffer any local deformations through its thickness. As such, the curved shape of needle deflection during insertion into the tissue, which is of importance to avoiding obstacles and reaching targets, schematically resembles that of a cantilever beam undergoing bending. The assumptions regarding the geometry, boundary conditions, forces and moments of the chosen beam model are defined based on the parameters of the insertion process, and the mechanical and geometrical characteristics of the needle under study. As such, in order to define an accurate physical model of the needle during insertion, the geometrical and mechanical parameters of the needle, and its insertion process (during which deflection is being modelled), must be studied. In the following section, a description of the needle's structure and mechanical parameters relevant to the definition of its physical model is presented. The complete explanation of the needle insertion mechanism and technical characteristics is presented in chapter 9.

4.1.2. Needle Structure and Insertion Process

The schematic of the bio-inspired two-part needle prototype (at the stage of development when studied in this work) is presented in figure (4-1). The needle is designed with the aim to achieve 2D curvatures in a plane of insertion through a substrate, and consists of two interlocked segments, each of which has a bevel shaped tip. Recent research on the needle design has shown 3D bending of the needle during insertion into a substrate, by developing a body consisting of four segments (Burrows, Secoli et al. 2013), which is out of the scope of this project and the subject of future work. The interlock geometry is shown in figure (4-1.c), which is designed such that the two segments move relative to each other, without separating.

The segments of the probe are made of a flexible material, Tango Black DM_9895 (hardness of 95 Shore Scale A, tensile strength of 20MPa, elongation at break of 30 %) and are manufactured using rapid prototyping. The rapid prototyping manufacturing process can cause roughness on the surface of the needle, which can lead to friction between the segments. As such, they are lubricated with a water-based agent prior to assembly of the needle, to aid sliding with respect to each other and avoid buckling

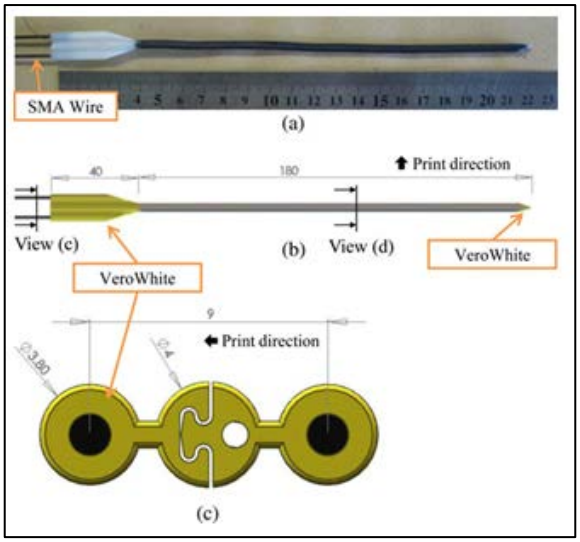

Figure 4-1. Schematic diagram of the two-part needle (a).The needle is constructed of two materials, rigid Vero White (at the tip and base) and flexible Tango Black (along the body) (b). The two segments are held together via an interlock geometry, as shown in figure (c) (Ko and Rodriguez y Baena 2013).

The tip of the needle is constructed of a rigid material named Vero White (hardness of 83 Shore Scale D, tensile strength of 50Mpa, elongation at break 20%) so as to allow efficient cutting performance. The base of the needle is also made of Vero White and is “wing” shaped, such that, despite the reduced cross sectional area, each segment can be pushed from the back (Ko and Rodriguez y Baena 2013). The base features metal rods connected to DC motors with 6 Watt rating (A-max22, Maxon Inc., USA) (Burrows, Secoli et al. 2013), which provide a forward pushing force for insertion into the substrate.

A hole is designed inside the segments, allowing the passing of wires from the base of the needle through to the tip, in order to allow application of a sensor to measure its tip coordinates during progression. It must be noted that at this stage of the project, due to design and hardware limitations, the information regarding the deflection of the needle during its insertion is collected via sensors placed at its tip. As such, the data captured during insertion is the track of the tip of the needle through time during insertion. This brings about the necessity of a modelling process that can utilise the tip deflection for experimental validation, as opposed to a model needing the deflection of various points along the length of the needle.

As previously explained, the needle is designed to progress inside a soft substrate along multi-curvature trajectories in a plane. This is achieved by manipulating the needle geometry and moving its two segments in a predefined sequence, based on the curvature desired. A basic predefined sequence of segment movements aimed to achieve a single curvature in a plane is illustrated in figure (4-2).

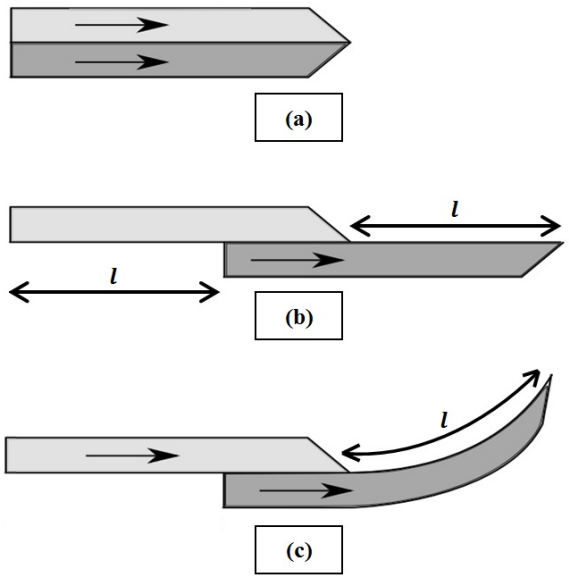

Figure 4-2 Simple Insertion Sequence. (a) Both segments are aligned. (b) One segment (the leading one) progresses forward an offset ***l***, with respect to the other segment. (c) Both segments are pushed forward, maintaining the offset l between them.

As can be seen in figure (4-2), the needle insertion process is completed in three steps. These steps are defined from the point in time after which the needle has punctured and penetrated the substrate boundary, and resides within it. Twisting and buckling along the length of the needle are minimised by guiding it through a specifically designed catheter prior to insertion into the soft tissue, the structure of which is explained in chapter 9. This catheter helps reduce buckling and ensures that the needle stays straight when pushed from the base into the substrate. Initially, in step (a), both segments of the needle are inserted an equal distance into the substrate, as seen in (4-2.a), where the arrows denote the progression direction. In this step, as the tips of the segments are aligned prior to insertion into the substrate manually, the needle is symmetric, and the needle does not deflect during the progression. In the next stage (b), depending on the direction of curvature desired, one segment is stationary while the other is pushed forward a distance l, which is defined as the offset, as shown in (4-2.b). For small

offset lengths l, the leading segment is expected to not deflect during its progression at this stage. Finally, both segments are pushed forward together in stage (c), while maintaining the offset l between them, as shown in (4-2.c). In this stage, the offset geometry and bevel angle of the leading segment will cause the whole body of the needle to curve while progressing. As the needle will bend in the direction of the leading segment bevel angle in stage (4-2.c), the segment chosen to lead in stage (4-2.b) is selected based on the desired direction of curvature. As the curvature of the beam occurs in stage c of the insertion process mainly as a function of the offset and geometry and the forward insertion, the physical model of the needle must be designed such as to encompass the offset geometry occurring at this stage. During all three steps, the needle is designed such as to deflect in the plane of insertion, avoiding off plane deflection. This is assuming that the needle will not twist around its axis during insertion, and will keep the initial alignment manually assigned. The insertion process is very slow (approximately 1mm/s) such as to avoid dynamic effects and high frequency variations in the needle deflection. Based on these defined geometrical and insertion process parameters and simplifications, the preliminary assumptions and geometry of the beam model of the needle can now be defined.

4.1.3. Model Geometry and Insertion Assumptions

Based on the explanations above, a 2D beam of varying cross section, incorporating the offset geometry and insertion process is illustrated in figure (4-3). The geometry of the model is based on the following assumptions:

1. The two segments of the needle slide with respect to each other without buckling during stage (b), and do not separate from each other during stages (a) and (b) due to friction with the surrounding substrate and/or each other. This is expected, as the needle segments are lubricated prior to assembly and insertion.
2. The offset between the two segments of the needle is maintained as constant during stage (c) of insertion, and the two segments of the needle are aligned throughout stage (a), maintaining zero offset length.
3. The needle does not twist during any stages of insertion, and thus maintains a 2D curvature along the plane of insertion.
4. The needle base does not have any transverse displacement at the boundary of the substrate (i.e. it is constrained) during all stages of motion, and can only move along the axial direction. This is a valid assumption, as the needle is physically constrained

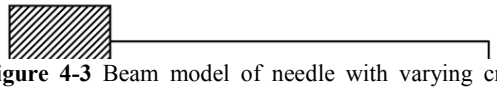

Figure 4-3 Beam model of needle with varying cross section. At any step in time, the needle deflection is assumed to follow that of a cantilever beam.

at the base by the motors and passes through the catheter between its base and the substrate boundary, thus restricting all transverse displacement.

As can be seen from figure (4-3), the bevel angle at the tip of the needle is simplified to a straight ended beam. It must be noted that the theoretical physical effect of the bevel tip, i.e. the horizontal and vertical forces and so called cutting angle is accounted for in the forces defined to be acting on the model, as will be explained later in the chapter. This geometrical simplification allows ease of calculations further on in the model, and as the needle tip geometry is relatively small, is expected to cause negligible inaccuracies. It is obvious from figure (4-3) that the general geometry of the needle model is one single beam of varying cross section, thus representing any point of time in stage (c) of insertion, when the two segments maintain the offset. This does not mean that it is not applicable to stage (b) of insertion, where the offset varies, or to an insertion process with varying offset, nor that the method cannot be extended to the cases where shear forces between soft tissue and needle might be significant. In such cases, the length of the offset must be adjusted at every step, as will be explained further on.

The constraint at the boundary of the beam model of the needle, shown in figure (4-3), fully restricts its movement, and does not incorporate insertion. This is due to the fact that the equilibrium equation is written at every point in time (note that the term time here is only used to capture the insertion process and since the insertion process is very slow in comparison to the time constant of the beam, no dynamic effects are considered in this study), and as such the beam is illustrated at any given point in time as being stationary, and held at its base. The insertion process is incorporated further on, using a two stage motion model inspired by the model developed by Barbe (Barbé, Bayle et al. 2007),wherein the motion of the needle is broken down into infinitesimal steps. Each step is then defined by two stages: one during which the needle moves forward along its tip configuration without deflection and loading is applied upon the entire length, including the small length inserted at the initial stage of insertion, and one during which the needle bends when moving forward due to loading. The mathematics of this motion model is fully explained further on. However, in order to be able to efficiently define the equilibrium equation for the model, the forces and moments acting on the needle during insertion must be initially understood and studied.

The forces acting on the needle from the substrate at any point in time can be assumed to be due to three main factors, namely contact, cutting and friction. The contact force is applied as

pressure along the length of the needle, the pattern of which is dependent on the assumed interaction between the needle and the surrounding substrate during insertion. Previous work (Misra, Reed et al. 2010, van Gerwen, Dankelman et al. 2012, Robert, Chagnon et al. 2013) has demonstrated that, for a single segment bevel tip needle, after the initial penetration of the bevel tip into the substrate, the interaction of the slope of the bevel tip with the substrate causes propagation of a crack in the substrate, and the needle tip practically moves inside the crack opening, which further propagates as the needle inserts. As such, excluding the bevel geometry, it can be assumed that the needle is in contact with the surrounding substrate at every point along its length, and that the contact force is normal to the needle at any point. This contact force may or may not vary during the insertion of the needle due to needle–substrate interaction during crack propagation, substrate deformation and offset geometry. For any one point on the needle, the contact force can change as the surrounding substrate deforms and the needle progresses inside the substrate, and is thus not constant during insertion. This makes sense, as with further insertion, the larger deflection of the needle can result in a larger deformation in the substrate and consequently a larger reaction contact force due the substrate elasticity. The same can be assumed for the length of the needle, i.e. the points along the needle undergoing larger deflection should undergo larger reaction contact forces from the substrate. Thus, it can be concluded that, for any point along the length of the needle, there should exist a relationship between the deflection at the needle and the magnitude of the contact force acting on the needle. This type of force can be physically represented in a quasi-static scenario as springs acting between the needle and the substrate boundary at each point, wherein the amount of force acting on the needle from the spring is a function of the deflection of the needle at each point, and the stiffness of the springs. The stiffness of these springs will mathematically encompass the effects of the elasticity of the surrounding substrate, as the energy stored in them is dependent on the strain energy of the substrate throughout its deformation. As the contact forces acting on the needle are normal to it at each point, the springs representing the contact forces can be imagined to be rotated such as to be normal at each point of the needle. This does not mean they are 2D springs, as they only produce force along their length, but for large enough deflections, due to their rotation, the produced force will have vertical and horizontal components. In general, for both the contact force variations during insertion and along the length of the needle, the amount of deflection of the needle plays a significant part in the assumptions and simplifications regarding the forces acting on the needle itself. As the needle is modelled as a beam, this effect is quantified by categorising the beam's deflection as either large (roughly defined as a

maximum deflection over 10% of the length of the beam) or small, the detailed math and explanation of which is presented later in the chapter. At this stage, it must be noted that, if the needle's deflection is small enough, the variations of the contact force along its length and during insertion can be considered as negligible, and the concepts explained above are mainly of importance during large deflections of the needle.

In addition to contact forces acting along the length of the needle, contact forces exist along the bevel tip surface, and the interlock geometry of the leading needle segment at the offset. Due to the small contact surface of the leading segment at the offset, although the interlock geometry can cause the contact force behaviour to differ from that of the contact force acting on the outer surface of the needle, the difference is expected to be negligible. As such, the same rules for the contact force along the length apply to the offset interlock geometry. For the bevel angle, the weight of the effect of the contact force acting on the bevel surface is influenced by the size of the bevel, i.e. the bevel angle and the radius of the needle. Experiments (Misra, Reed et al. 2010) on a single bevel tip needle have shown that the contact forces acting on the bevel tip were not constant along the length of the bevel, the pattern of which being a function of the bevel geometrical parameters. As the beam model applied for the inverse solution and load identification of the needle has been assumed to have a flat tip, the assumptions regarding the contact force pattern on the bevel tip are substituted with a cutting force acting on the tip. The cutting force at the tip of the needle is a result of the substrate resisting its forward progression. It is assumed to always be in the direction of the cutting angle, which has been shown to have a direct correlation with the geometry of the tip of the needle (Misra, Reed et al. 2010). The cutting angle and magnitude of the cutting force may vary during the needle insertion, as the substrate deforms and the crack propagates, and as such should not be assumed constant, except for cases of small needle deflection, the categorisation of which will be defined further in the chapter.

The most important and difficult part of load modelling is related to the modelling of the axial component of the cutting force, which can render the equilibrium equations nonlinear, as will be demonstrated in chapter 5. As can be imagined, when modelling the needle as a cantilever beam in its original undeflected shape, the application of an axial force to the tip of the beam will only cause it to compress. As such, the contribution of the axial component of the cutting force to the deflection of the beam at any point in its insertion will be a function of its deflected shape at the same point in time. This effect can also result in its buckling instability, which must be avoided. The shape of the deflected beam is thus highly influenced

by the axial component of the cutting force. Also, the effect of the bevel geometry, although eliminated from the beam, arises in the inclusion of the cutting angle, reducing inaccuracies associated with the assumption of a flat tip beam as a model of the bevel tipped needle, especially, when considering that the bevel dimensions are small compared to those of an offset. If the geometry varies, it will be relatively simple to include the bevel geometry in the model for which the bevel geometry is considered to make a sizable difference.

The next group of forces to be studied are the frictional forces. The frictional forces acting on the needle can be categorised into three main types: the frictional forces between the substrate and the circumferential surface of the needle along its length, the frictional forces between the substrate and the leading segment interlock geometry along the length of the offset, and the frictional forces acting between the two segments of the needle (figure 4-2). The frictional forces acting on the surface of the bevel can be disregarded when compared to the other forces, due to the small area of contact. As mentioned in previous sections, the rapid prototyping of the needle can cause friction along its length during insertion, which is somewhat reduced by lubricating it prior to insertion. The frictional forces between the leading segment's interlock geometry and the substrate can vary with the friction along the length of the needle due to the design of the interlock, although the effect of this difference is reduced by the relative ratio between the length of the offset and the total length of the beam. The frictional forces between the two segments are also assumed to be minimised due to lubrication of the segments prior to the assembly of the needle, allowing the two segments to slide with respect to each other and avoid buckling during stage (b) of the insertion (figure 4-2), when a force is applied to the back of the leading segment. As the needle is modelled as one beam of varying cross section, the internal effects of the two individual segments of the needle on each other, such as friction, are neglected. For very large values of deflection and/or large values of needle thickness, this effect might become significant and must be included in the modelling.

Based on the explanations above, the assumptions regarding the forces acting on the needle during insertion are made for the beam model:

1. The substrate applies a normal contact force along each point of the length of the needle during insertion. This force is always normal to the needle at every point and may vary along the length of the needle, and as such is not considered constant, except for small deflections of the needle. Thus:

   a. The contact forces are considered to act like springs between the needle's beam model and the substrate boundary along its length. For small deflections, spring stiffness is constant while for large deflections the stiffness is considered to vary by insertion.
   b. For large deflections, the contact forces are assumed to rotate with the bending of the needle, thus remaining normal to the needle at ever point. For small deflections, the small angle of rotation is assumed to allow horizontal projection of the contact forces along the needle.
2. The contact stiffness varies during different insertion steps, and contact stiffness is assumed constant only for a small enough window of time, which is defined based on the deflection range, as will be further explained. This means that, for smaller deflections, the contact stiffness of the substrate can be considered constant for a larger window of time, whereas for larger deflections, the forces have to be updated regularly based on the configuration.
3. The cutting force at the tip of the needle rotates with the deflection of the needle, i.e. the cutting angle may not be constant in magnitude or direction during insertion, whether small or large. The cutting angle is assumed to carry the significant effect of the bevel geometry of the tip of the needle, reducing the errors associated with the flat ended beam model representation of the bevel tip. The cutting force is assumed to have two main components, horizontal and axial, the latter having a significant effect on the needle's tendency to buckle.
4. The frictional forces between the circumferential length of the needle and the substrate, and the frictional forces between the interlock geometry of the leading offset segment and the substrate are not considered to be equal per unit length. Both are expected to be negligible due to the lubrication of the needle prior to insertion, as will be examined in later stages. The frictional force between the segments during insertion is neglected throughout the model, as the needle is assumed to be one single beam of varying cross section. It must be noted that the interlock force between the two segments is an internal force and also not considered in this model, due to the same reason.

It can be seen from these explanations that the beam model assumptions regarding the forces acting on the needle will vary considerably for small and large needle deflection during insertion. As can be imagined, a general model for large deflection would hold true for small

deflections also, but would involve unnecessary calculations. As such, the logical course of action is to employ two separate models for large and small deflection, and apply each within its respective domain. As the large deflection is a high complexity extension of the small deflection model, it makes sense to initially develop a small deflection model of the needle, and then examine its accuracy against existing deflection data during insertion. Based on the above assumptions, a free body diagram of the 2D small deflection beam model of the needle at any point in time is shown in figure (4-4), where the definition of the forces are explained in table (4-1) .

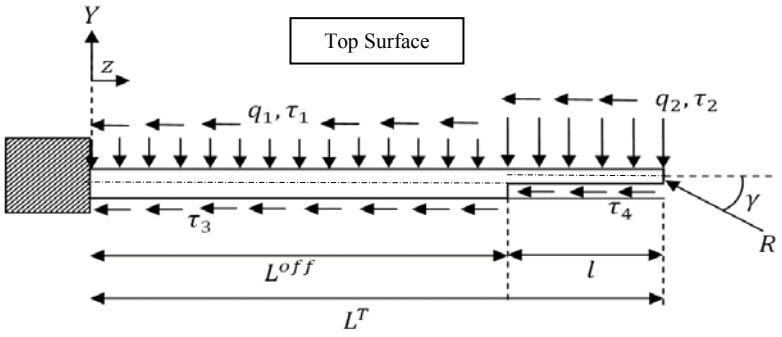

Figure 4-4 Free body diagram of beam model representing needle undergoing small deflection.

Parameter		Unit
q_1		[N/m]
q_2		[N/m]
τ_1	Top surface Distributed f… L_{off} prior to offset geometry.	[N/m]
τ_2	To… …ometry.	[N/m]
τ_3	Bottom surface Distributed friction force acting on L_{off} prior to offset geometry	[N/m]
τ_4	Bottom surface Distributed friction force acting on l at offset interlock geometry.	[N/m]
R	Tip Cutting Force	[N]
γ	Cutting angle	[Radian]
L^T	Total insertion length of the needle	[m]
L^{off}	Total length of needle prior to offset geometry	[m]
l	Offset length of needle	[m]
Z	Direction of insertion (forward movement) of needle.	

Table 4-1 List and definition of Notations in Figure (1)

It must be noted that, as well as the assumptions regarding the geometry of the needle and the forces acting on it, some assumptions are made regarding the application of these forces to the geometry of the beam model, influencing the effect of these forces in the modelled needle deflection. These are as follows:

1. The neutral axis of the beam model has two parts, as shown with the dotted line in figure (4-4). The first part ends at L^{off}, through the beam's geometry between the base and the offset geometry, and is located on the middle axis of the beam. The second part is at the offset section, running between the offset geometry and the tip of the needle. The neutral axis is also assumed to be at the middle axis of the offset geometry of the beam. This simplification results in the discontinuity of the neutral axis at the point where the geometry changes at the offset.
2. It is assumed that the net result of the two compression forces acting on the beam on both surfaces can be applied to the top surface for calculations, in the form of q_1 and q_2. Practically, for a straight undeformed needle, the compressive loads from top and bottom surfaces must cancel each other. This equilibrium is disturbed due to deflection of the needle, as a result of which, the compressive loads on the bottom surface increase and those on the upper surface decrease. This variation in compressive loads (which are a function of deflection in the "y" direction) is zero at the root and is maximum at the tip. Now, for linear range and deflections that are small in comparison to the diameter of the needle, the effect of uniform compression takes hold of the contact load distribution. This is especially true for short needles with a short offset, as their deformations are usually very small in comparison to the needle length. As the deflection increases, the effect of the non-uniform contact loads represented by contact stiffness takes over.
3. The cutting force, which in reality is applied to the tip point of the bevel, is assumed to act on the point on the beam tip where the flat beam surface intersects the neutral axis of the offset. This makes sense for the designated beam model, but due to the high importance of the axial cutting force on the stability of the bending deformation of the needle, may have a noticeable impact on the shape of the needle body.
4. Based on the material properties of the selected material, it is concluded that the axial Young's modulus of the beam is much larger than it's bending Young's modulus and hence axial deformation of the needle is assumed to be negligible.

Based on the assumptions made above, the free body diagram of the beam model of the needle at any point during small deflection is developed. For linear range, each insertion configuration is assumed to start deforming from its straight unloaded configuration, i.e. the deflection history is insignificant in the small deflection range. This is a valid assumption since, for the small deflections, history has no bearing on the outcome. In the large deflection range, the history becomes important and, as such, a progressive model is required to account for the insertion progress, in which deformation at each stage of the insertion depends not only on the loads applied on the needle, but also on the deformed shape of the previous insertion, as will be explained in depth in following chapters. Based on the above explanation, in order to develop the beam model of the needle's deflection, the fundamental equations governing the bending behaviour of a beam is addressed next.

4.2 BEAM THEORY

As previously explained, a beam can be defined as a structure having a high length to thickness ratio. Beam theory is used to explain the response of beams to external loading and moments, such as bending and torsion. Bending is generally defined as the response of a beam, when transverse or combined transverse-axial forces are applied to it. Buckling can be characterised as an unstable bending, i.e. a bending that is associated with compressive axial and transverse loads. In order to quantify these responses and study the effects of external loading on beams, different beam theories are developed.

Beams are generally assumed to be one of two categories, an Euler Bernoulli beam, or a Timoshenko beam. The two beams differ in the assumptions affecting their deflections. An Euler Bernoulli beam maintains a cross section normal to its centroidal line during bending, disregarding shear deformation, whereas the Timoshenko beam allows rotation between the two because of shear deformation. Thus, in the Euler Bernoulli theory, rotation is disregarded relative to translation and the angular distortion is disregarded relative to the bending deflection. The Euler Bernoulli theory is better applied to thin beams and is also known as the thin beam theory, whereas the Timoshenko theory is better applied to shorter, thicker beams. The difference between the application of the two is a function of the relative length to thickness ratio of the beam, i.e. the larger the ratio the less the difference. Regarding vibrational effects, Timoshenko's beam theory considers the rotational inertia of the cross section during bending, and as such is applicable to beam with higher frequencies, whereas the Euler Bernoulli beam disregards these effects. For some beams, the Rayleigh Beam

theory can be applied, where the shear deformation is disregarded while the rotational inertia considered for dynamic problems, is somewhere between the Timoshenko and the Euler Bernoulli beam theories.

The beam model developed in this work is the model of a needle, the structure of which resembles that of a thin beam. As such, the Euler Bernoulli theory is chosen for bending calculations. Care must be taken not to allow the needle to buckle inside the substrate during insertion and proper constraints must be applied to the identification process to prevent this. Vibrational effects are not considered, as the process is relatively slow, as previously explained. Should the frictional forces become significant during the insertion or twisting and rotation of the needle become considerable as a function of size and speed of insertion, the proposed solution can be extended to account for such effects. In the next sections, the Euler Bernoulli beam theory is explained and applied to the defined free body diagram of the needle's beam model.

4.2.1. EULER BERNOULLI: BEAM BENDING PRELIMINARIES

The Euler Bernoulli Beam theorem is a simplification of linear beam theory, defining the deflection of a beam as a function of loading during small deflections, as follows:

$$\frac{d^2}{dz^2}\left(EI.\frac{d^2y}{dz^2}\right) = q(z) \tag{4-1}$$

Where y is the deflection of the beam at any point z along its length, and q is the distributed load. It can be shown from (4-1) that the moment acting on the beam is defined as:

$$\frac{d^2y}{dz^2} = \frac{M(z)}{EI} \tag{4-2}$$

Where E is the Young's modulus, I is the second area moment of the cross section and M is the moment at cross section z when the beam deflects in the y direction. The left hand side of the equation $\frac{d^2y}{dz^2}$ defines the curvature due to bending at cross section z.

In order to apply this theorem to the needle, the variation of the relationship between bending moment and curvature due to application conditions is discussed.

The Euler Bernoulli theorem, as defined here, holds true in small deflection linearly elastic problems. Linear elasticity is defined as a state in which stress and strain have a linear relationship. This limit is determined for each material individually, by tension and flexural

tests recording the amount of stress as a function of strain. The following sections describe the variation of the bending theorem in cases of linear and nonlinear elasticity and small versus large deflection of beams.

4.2.2. LINEAR AND NONLINEAR ELASTICITY

The strain range on the stress strain curve wherein the stress and strain have a constant ratio (defined as the Young's Modulus) is considered as a small strain region. The material in a state of small strain is taken to be linearly elastic. The bending of a beam element based on the stress strain relationship is defined below, explaining the difference between linearity and nonlinearity in bending. Figure (4-5) shows a beam element undergoing bending.

In its unbent state, all axial threads of the beam in figure (4-5) are of uniform length equal to that of the neutral axis, OO' .The neutral axis is defined as the thread which does not extend or compress during deformation and is of constant length. During bending, the upper threads are compressed and the lower threads are extended, resulting in the stress profile in figure (4-5).

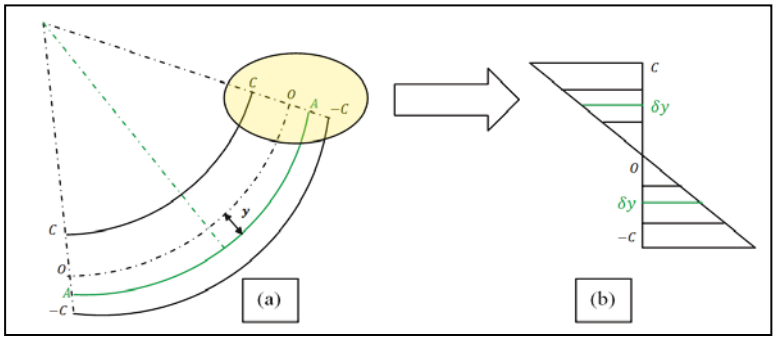

Figure 4-5 Beam Element Bending. (a) The beams neutral axis is depicted by $\boldsymbol{OO'}$ and the thickness of the beam is equal to $\boldsymbol{2C}$. $\boldsymbol{AA'}$ is an arbitrary thread, the distance from the center of the radius of curvature of the element being *y*. The pattern of the stress of the beam cross section from upper thread **C** to lower thread **−C** is shown in figure (b).

Defining the radius of curvature of the neutral axis OO' as R, it can be stated that, for the axis $AA'$with a distance y from the neutral axis, the strain ϵ is calculated as follows:

$$\epsilon = \frac{(R+y).\alpha - R.\alpha}{R.\alpha} = \frac{y}{R} \tag{4-3}$$

Where α is the angle of the arc OO'. Calculating the moments of the stress resultants σ of an element with the cross section dA, the moment acting on the beam is calculated as:

$$M = \int \sigma . dA . y . dy = \int \frac{Ey^2}{R} . dA . y . dy \rightarrow \frac{E}{R} \int y^2 . dA . dy \rightarrow \frac{EI}{R} \tag{4-4}$$

This defines the relationship between the bending moment and the radius of curvature of a beam, when the strain lies within the linear region. When the stress strain relationship is nonlinear, it can be defined as a nonlinear function in the form of:

$$\sigma = E . \epsilon^n \rightarrow \frac{E' . y^n}{R} \tag{4-5}$$

Where E′ is the instantaneous Young's modulus obtained at each strain, as acquired from the stress strain curve, and n is the degree of the stress strain relationship polynomial, i.e. for linear stress-strain, $n = 1$. For the case of the material of the needle used in this study, n=3, as explained in the following chapters. Nevertheless, the stress-strain relationship remains linear for a good portion of the needle bending, as will be further explained later in the thesis. Substituting into equation (4-4) for the thickness of the beam between $-C$ and C ,the equation yields:

$$M = \int_{-c}^{c} \sigma . dA . y . dy = \int_{-c}^{c} \frac{E' . y^n}{R} . dA . y . dy = \frac{aE}{R^n} . \frac{1}{n+2} . (C^{n+2} - (-C)^{n+2}) \tag{4-6}$$

In equation (4-6) , n must always be an odd number, due to the fact that if n is even, based on equation (4-5), the tension and compression strains will both yield positive stress, which is impossible. Equation (4-6) is then simplified to:

$$M = \frac{aE}{R^n} . \frac{1}{n+2} . (2 . c^{n+2}) \tag{4-7}$$

Inserting $n = 1$ into this equation yields:

$$M = \frac{aE}{R} . \frac{1}{3} . (2 . c^3) \tag{4-8}$$

This in turn is equal to the insertion of the second moment of area of a rectangular cross section, $I = \frac{bh^3}{12}$ into equation (4-5), defining linear elasticity, wherein $n = 1$. In order to define n for nonlinear materials, a curve must be fitted to the stress-strain data and the best order n found by trial and error. Generally speaking, a material enters the nonlinear elasticity region after a certain amount of deformation, which can be a function of its deflection. This

does not mean that the needle material will enter material nonlinearity when it enters large deflection; the two effects may or may not be coincidental. In order further understand this, small and large deflections are explained in the next section.

4.2.3. SMALL AND LARGE DEFLECTION

As mentioned in previous sections, the assumptions governing the forces and geometries in the developed free body diagram of the beam model representing the needle hold true during small deflections of the needle. It has been noted in the section 4.2.2 that equation (4-1) is valid for small deflections. It can be stated that equation (4-1) is a simplification of the general large deflection (small strain) beam equation between bending and moments acting on the beam, as depicted in equation (4-9):

$$\frac{M(z)}{EI} = \frac{y^{"}}{(1 + y'^{2})^{\frac{3}{2}}} \tag{4-9}$$

It can also be stated that, in order to classify the deflection as small or large in equation (4-9), if $(1 + y'^{2})^{\frac{3}{2}} \cong 1$, i.e. a maximum slope of 15~20 degrees, then the deflection can be considered as a small deflection. Physically, this represents cases wherein the ratio between the beam length and the tip deflection is not high. This allows for simplifications in calculations, but creates inaccuracies, if incorrectly assumed. A general rule of thumb is when the ratio between the deflection and the needle length is not larger than 10%. It must be noted that, as previously explained, small deflection does not necessitate linear elasticity and vice versa. A physical example is when the deflection is small, due to needle length and geometry, but, due to cross section dimension, strains are large causing nonlinear stress-strain at small deflections. The fishing rod is an example in reverse

By this point, the geometry and forces acting on the beam model of the needle undergoing small deflection have been developed. In the next section, by applying the Euler Bernoulli beam theory to the defined beam model as defined in this section, the equilibrium equations governing the relationship between the bending of the beam (and as such the needle) and the forces acting on it during small deflection, are presented.

4.3 EXACT MATHEMATICAL EQUATIONS OF BEAM MODEL

The general Euler Bernoulli bending equation (4-1) is in differential form, relating the curvature to the net moment acting on any cross section z along the beam. The net moment

itself is a sum of the individual moments of each force at cross section z along the beam. In order to derive the equilibrium equations governing the beam's small deflection as a function of the forces acting on it, the contribution of each force's moment to the deflection must be independently considered, and the total deflection then calculated. Assuming small beam deflections (i.e. small y′), defining the moment of each force at a point z and integrating equation (4-1) for each force, yields the following equations:

$$y_{q_1} = -\frac{1}{EI_1}\cdot q_1\left(\frac{{L^{off}}^2 z^2}{4} - \frac{L^{off} z^3}{6} + \frac{z^4}{24}\right)_0^{L^{off}} - \frac{1}{EI_1}\cdot\frac{q_1 {L^{off}}^3}{6}(z - L^{off}) \tag{4-10}$$

$$y_{q_2} = -\frac{1}{EI_1}\cdot q_2\left(\frac{\left(z^2 - {L^{off}}^2\right){L^{off}}^2}{4} + \frac{{L^{off}}^3}{6}(z - L^{off})\right) - \frac{1}{EI_2} q_2\left(\frac{\left(z^4 - {L^T}^4\right)}{4} + \frac{z^2(z - L^{off})}{4} - \frac{\left(z^3 - {L^{off}}^3\right)z}{6}\right) \tag{4-11}$$

$$y_R = \frac{1}{EI_1} R\sin\gamma\left(\frac{{L^{off}}^2 z^2}{2} - \frac{{L^{off}}^3}{6}\right) + \frac{1}{EI_2} R\sin\gamma\left(\frac{\left(z^2 - {L^{off}}^2\right)z}{2} - \frac{\left(z^3 - {L^{off}}^3\right)}{6}\right) \tag{4-12}$$

$$y_{\Delta\tau_1} = \frac{1}{EI_1}\Delta\tau_1 d_1\left(\frac{{L^{off}}^3}{3}\right) + \frac{1}{EI_1}\Delta\tau_1 d_1\left(\frac{{L^{off}}^2}{2}\right)(z - L^{off}) \tag{4-13}$$

$$y_{\Delta\tau_2} = \frac{1}{EI_1}\frac{\tau_3 d_1 (L^T - L^{off}){L^{off}}^2}{2} + \frac{1}{EI_2}(\tau_3 - \tau_4) d_2\left(\frac{z\left(z^2 - {L^{off}}^2\right)}{2} - \frac{\left(z^3 - {L^{off}}^3\right)}{6}\right) \tag{4-14}$$

Where y_{q_1} is the deflection due to the uniformly distributed load q_1, $y_{q_2}$is the deflection due to the uniformly distributed load q_2, y_R is the deflection due to the vertical component of the cutting force $Rsin(\gamma)$, $y_{\Delta\tau_1}$ is the net deflection due to distributed shear Loads $\tau_1$and τ_2 , $y_{\Delta\tau_2}$ is the deflection due to distributed shear loads τ_3 and τ_4, and d is the thickness (diameter) of the needle. The remaining parameters are as defined in table (4-1). It can be

seen that, for the four frictional forces, the net forces $\Delta\tau_1$ and $\Delta\tau_2$ are replaced, respectively. This is because, as illustrated in the free body diagram in figure (4-4), the frictional forces acting on the cross section are of equal distance to the neutral axis, and the resulting moments will thus be in opposite directions. As such, the net force can be calculated as acting on half the diameter of the needle for moment calculations.

Equations (4-10) to (4-14) are only valid if the horizontal component of R as well as the horizontal components of the spring loads, representing the substrate contact, is zero. When horizontal component of tip force is present, the problem becomes a nonlinear one, even for small deflections, due to the interaction of vertical and horizontal forces and the beam can become unstable due to buckling onset. Obviously, none of these effects are evident from (4-10) to (4-14). So, in order to be able to solve the model so as to account for the complexities introduced from the nonlinear interactions of the forces, further adjustments must be made to the model, as will be explained in the following chapter.

4.4 CONCLUSION

In this chapter, the Euler Bernoulli beam theory and the basic assumptions regarding the small deflection of the needle's beam model have been explained. Based on the defined free body diagram of the model, the linear equations governing the deflection of the needle as a function of each of the forces acting on it have been developed in equations (4-10) to (4-14). These equations can be used for two purposes, as follows:

1- To setup the sensitivity matrices connecting forces applied to the needle to its tip deflection. Using these equations and by taking advantage of measured tip deflection data, one can reverse calculate the loads causing these deflections. Of course, this is a very simplified view of the identification problem, as no axial loading at the tip and no contact stiffness are considered in the small deflection assumptions, as previously explained. These issues will be further considered in future chapters.
2- A second application of these equations, which is far more important, is to use them as the trial functions to express the approximate deflection of the beam using the Galerkin method, as is explained in detail in the following chapters.

Based on the above explanations, the necessary adjustments to the defined model, such as to allow for axial loading and large deflection assumptions, must be defined, so as to allow for

variation of contact forces during insertion, and inclusion of the effect of the axial force on the deflection of the needle. In the following chapters, the Galerkin solution to the boundary value problem of the needle's deflection will be defined, and the subsequent method of load identification explained.

5. QUASI NONLINEAR NEEDLE MODEL

5.1. INTRODUCTION

Previously, in chapter 2, it has been proposed that a mathematical model of the two part flexible needle deflection be developed, providing a means to identify the loads acting on the flexible needle during insertion into a substrate, such as to aid in its design, optimisation and control. In chapter 3 the methods of force identification suitable for different applications have been studied, and it has been suggested that a mathematical model based on the boundary value problem formulation be developed. As such, in chapter 4, the basic beam model of the needle has been developed, and, based on the insertion process of the needle, the assumption regarding the forces and their application have been established. It has been explained that the governing assumptions of the model are influenced by whether the needle's deflection is small or large, and that the large deflection assumptions introduce complexities in the beam equilibrium equations, that can be neglected in the small deflection scenario. Hence, the equations governing small deflection of the beam have been developed, and the individual contribution of different forces to the needle's deflection defined through these equations, providing a means to observe the role of each of these acting forces on the deflection.

In order to utilise these equilibrium equations to allow force identification, a reverse solution to the equations is needed, such as to obtain forces from tip deflections. In addition, it must be noted that the final goal of this model as, defined in chapter 1, is to aid in the design and control of the needle. This means that, should the needle deviate from its predefined path during insertion, the forces which the needle is subjected to must be identified. Subsequently, for the next movement to rectify the situation, the further deflections of the needle under the known set of forces should be predicted, allowing selection of the best way to get it back on its path. Thus, one aim of the identification of these forces is to predict further subsequent deflections of the needle, while subject to these forces. In addition, real time identification of the loads acting on the needle will provide a database for the loads likely to act on the needle and their dependence on the needle and substrate characteristics. In order to utilise the equilibrium equations such as to predict the deflections of the needle during insertion, a mathematical model of the insertion process is needed, to be applied to the equilibrium equations of the model, which hold true for each point in time. The insertion model will thus act as a link between the deflections of the needle at each time step, effectively modelling

deflections during insertion. The effect of this model is of immense importance during large deflection, due to the fact that the deflection at each step is a result of the forces acting on the needle at the same step, and its deflection resulting from its previous step. This effect is less pronounced in the small deflection region, as will be explained.

In addition to the introduction of the reverse solution and the insertion model to the equilibrium equations, in order to apply the model to the large deflection region of needle deflection, the equations must be expanded such as to include large deflection assumptions. As previously explained, the contact forces acting on the needle during large deflection may vary along the length of the needle at each point, as well as varying at each point at each step of the insertion. This means that the contact force acting on each point can be assumed to be constant for a very small length, in a very small window of time. The determination of the amount of time and length during which the force acting can be kept constant is dependent on the amount of the deflection variation during the said time window. In chapter 4, distributed springs acting between the needle length and the boundary of the substrate were proposed to be included in the small deflection model in order to represent the contact stiffness between the substrate boundary and the needle, effectively introducing the contact forces acting on the needle from the substrate as a function of the needle deflection. In addition, in the small deflection model, the normal forces acting on the needle tip are assumed to be in the horizontal and vertical directions due to the small range of deflection, whereas in large deflection the forces will rotate with the slope of the needle during insertion, and in addition to their magnitude, their direction cannot be assumed constant. For the reverse solution of the small deflection model for force identification, the variation of the forces through time can be included by tailoring the amount of time throughout insertion in which the forces are identified via the model, and as such the model itself is not altered. It must be noted that the type of model being used for the reverse solution must be selected based on the large/small deflection assumptions and include the necessary assumptions, as have been discussed and will be further explained.

For the prediction of the deflection of the needle as a consequence of the forces acting on it through insertion, which as mentioned in chapter one, is called the progressive solution, the difference in the small and large deflection modelling arises in the initial state from which each deflection is calculated at each step. For the small deflection solution, at each state of insertion, the forces can be assumed to be acting on an initially straight, undeformed shape of the needle, causing it to deflect to its current state. For the large deflection solution, the

direction of the forces at each step is a function of the deflected shape of the needle, and as such the initial state for each step of insertion should be assumed as the deflected shape from the previous insertion step in time. In addition, for small deflections, due to the small amount of tip deflection, the axial component of the cutting forces has little effect. This is due to the impact of the axial component of the cutting force on the deflection of the needle being through its moment, which is in turn dependent on the amount of deflection of the tip. The moment of the vertical component of the cutting force is a function of the length of needle currently inserted within the substrate, and, as such, the difference in large or small deflection does not affect it as much as it affects the deflection due to the axial component of the cutting force. Consequently, the axial component of the cutting force, which may be of less impact in the small deflection equilibrium equations due to the small amount of deflection causing minor moments, must be included in the assumptions of the large deflection model. This assumption introduces heavy calculation complexities, as the effect of the axial cutting force on the deflection of each step is a function of the deflection at the same step, which will be shown later in equation 5-1 to 5-7.

As far as the moments are concerned, the main difference between small and large deflection assumptions stem from the rotation of the tip and contact loads in the large deflection scenario. In addition to these differences, which concern moments, the basic relationship between the moments and the curvature of the beam, as equation (4-2), must be altered for large and small deflections, producing a “nonlinear” model for large deflections, as opposed to a “linear” model for small deflections.

It must be emphasised here that the nonlinear identification process cannot be started unless the linear identification process is undertaken first. This is due to the fact that, for nonlinear identification, there is a need to have an initial guess of the loads acting on the beam. This initial guess is best provided by the linear identification process. Based on these observations, in order to develop the model from the basic equilibrium equations (4-10 to 4-14) explained in chapter 4 into a nonlinear large deflection model, the following assumptions must be added to the model:

1. The addition of the rotating axial and vertical components of the cutting force at the tip of the needle during insertion.
2. The addition of the rotation of the forces of springs acting between the substrate boundary and the needle along its length, to account for the variation of the contact

forces along the length because of the variation of the deflection along the length of the needle.

3. Addition of an insertion model to link the deflection of the needle at any step throughout insertion to its deflection at the previous step, and include the effect of the increased length due to insertion in the deflection of the needle.
4. Addition of the nonlinear Euler Bernoulli beam assumption, where the denominator $(1 + y'^2)^{\frac{3}{2}}$ cannot be assumed to be approximately equal to 1, as is the case in small deflection.

In this chapter, a linear model that potentially can demonstrate the effects of the first two nonlinear properties in its load identification results will be introduced, allowing force identification for the contact forces and the cutting force acting on the needle. This model is called the "*quasi-nonlinear*" model in this work. Subsequently, in following chapters, an insertion model will be developed, which, in conjunction with the developed nonlinear model, allows development of the progressive model, which then allows prediction of the deflection of the needle during insertion into the substrate.

5.2. QUASI-NONLINEAR MODEL DEVELOPMENT

As previously explained, in order to develop the model of the needle such as to be applicable in large deflection modelling during insertion, the first step is the introduction of the variation of contact forces along the length, and the rotation of the axial and vertical cutting forces at the tip. The free body diagram of a section of the beam model of the needle, including these assumptions, is presented in figure (5-1). The free body diagram does not include the offset geometry, as it is defined for an element along the beam and, as will be explained, the offset geometry is included in the moment of inertia calculations.

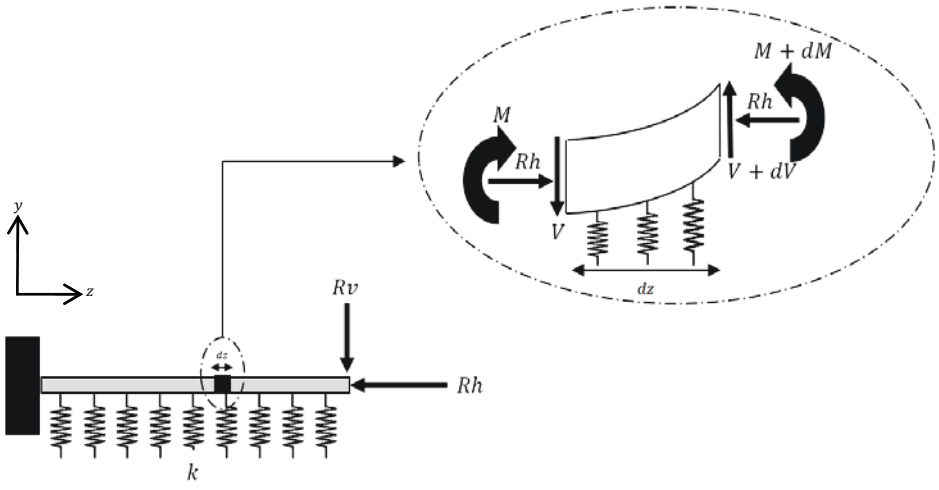

Figure 5-1 Free body diagram of a section of the beam model of the needle, including the assumption of varying contact forces along the length, as well as rotation of the cutting force acting on the tip of the needle

Here, z is the direction of insertion of the needle, for any element of length dz of the beam, M and $(M + dM)$ are the moments acting on the two ends of the element, V and $(V + dV)$ are the shear forces acting on the two ends of the element, and Rh is the internal compressive force acting on the element. At the tip, the vertical and horizontal components of the cutting force are shown as Rv and Rh. The contact forces acting along the length of the beam are shown as springs of stiffness k, for which the following assumptions are made:

1. The springs representing the contact forces from the substrate are assumed to be of equal stiffness along the length of the beam. This is due to the assumption of a homogenous nature of the surrounding substrate. As the needle deflects along its length, the force acting from the spring onto the needle will be relative to the amount of its deflection via the springs, and as such represents a varying force in relation to the amount of deflection. For nonlinear identification of these forces, the spring stiffness and the forces must be recalculated at every step, to allow for the change of the overall stiffness of the substrate due to its deformation as the needle progresses inside it. For quasi-linear identification, however, the variation of k will be assumed to be negligible.
2. The springs are assumed to be acting on one side of the beam model of the needle, representing the total contact force acting on the needle at each cross section. This has been previously explained in section 4.1.3 as being due to the nature of the deflection of the needle and the subsequent compression force from the substrate it is inserted within.

In order to account for the changes in the contact forces along the length of the beam, the free body diagram is drawn for one differential element of length dz, as can be seen from figure (5-1). As defined previously, the purpose of the definition of the force assumptions and subsequently the equilibrium equations is to form the boundary value problem of the needle's beam deflection model. For the element shown in figure (5-1), the equilibrium equation (5-1) can be defined as a boundary value problem as follows:

$$\frac{d^2}{dz^2}\left(EI\frac{d^2y}{dz^2}\right) + \frac{d}{dz}\left(Rh\frac{dy}{dz}\right) + ky = 0 \qquad (5\text{-}1)$$

This equation is derived from writing the equilibrium equations of the differential element in the lateral and bending directions, as defined in equation (5-2) for the lateral direction:

$$-V - ky\Delta z + (V + \Delta V) = 0 \tag{5-2}$$

and equation (5-3) for the moment equilibrium:

$$-M - ky\frac{(\Delta z)^2}{2} + (V + \Delta V).\Delta z + (M + \Delta M) + Rh\Delta y = 0 \tag{5-3}$$

Where, in equations (5-1), (5-2) and (5-3), z is the direction of insertion of the needle into the substrate, and y is the direction of bending. ky is the amount of contact force acting on the differential element at z, deflected an amount y. As dz is a differential element, if $\Delta z \to 0$ in equation (5-2), it can be said that:

$$\frac{dV}{dz} = ky \tag{5-4}$$

The same can be said for equation (5-3), where, as $\Delta z \to 0$, it can be said that:

$$\frac{dM}{dz} + V + Rh\frac{dy}{dz} = 0 \tag{5-5}$$

Differentiating equation (5-5) with respect to z once yields equation (5-6):

$$\frac{d^2M}{d^2z} + \frac{dV}{dz} + Rh\frac{d^2y}{d^2z} = 0 \tag{5-6}$$

Inserting the linear Euler Bernoulli as defined in chapter (3) as $M = EI\frac{d^2y}{dz^2}$, and substituting equation (5-4) into equation (5-6) yields:

$$\frac{d^2}{dz^2}\left(EI\frac{d^2y}{dz^2}\right) + \frac{d}{dz}\left(Rh\frac{dy}{dz}\right) + ky = 0 \tag{5-7}$$

Having defined the boundary value problem from the equilibrium equations, a relationship between the deflection of the beam and the forces acting on it is obtained. In order to solve this equation, a solution approximating computational method is needed. Based on the smooth deformed shape of the needle and subsequently its beam model, and the strength of the computational method, the Galerkin method is chosen for a solution approximation.

The natural and essential boundary conditions of the problem must now be defined. The trial functions of the Galerkin approximation are usually defined so as to satisfy these essential

boundary conditions. If the trial functions do not satisfy the natural boundary conditions, the error must be included in the Galerkin equations. If the trial functions are defined such that they do not satisfy the essential boundary conditions, the system's stiffness matrix is rendered asymmetric, leading to calculation complexities. The selection of the trial functions of the Galerkin solution are discussed at length in chapter 6.

Initially, the essential and natural boundary conditions of the beam model are defined in equations (5-8) and (5-9) for the tip and the end of the beam:

Essential Boundary condition at the end of the beam: $z = 0\,, y = 0, y' = 0$ (5-8)

Natural Boundary Condition at the tip of the beam: $z = L\ , y^{"} = 0\,, -EIy''' - Rhy' = Rv$ (5-9)

At the end of the beam, as it is fully constrained, it is obvious that $y = 0$ and $y' = 0$. For the tip of the beam, substituting $\frac{dM}{dz} = \frac{d^3y}{d^3z}$ into equation (5-5), and at $z = L$, from figure (1) $V = Rv$, equation (5-10) is derived for the natural boundary condition at the tip:

$$\left(\frac{d^3y}{d^3z}\right)_{z=L} + \left(Rh\frac{dy}{dz}\right)_{z=L} + Rv = 0 \tag{5-10}$$

Having defined the natural and essential boundary conditions, the weak form Galerkin solution can now be defined as equation (5-11):

$$\int_0^L N_i \frac{d^2}{dz^2}\left(EI\frac{d^2y}{dz^2}\right)dz + \int_0^L N_i\left(Rh\frac{d^2y}{dz^2}\right)dz + \int_0^L N_i\,(ky)dz + (N_i y'')_{z=L} + \left(EI.N_i\left(\left(\frac{d^3y}{d^3z}\right)_{z=L} + \left(Rh\frac{dy}{dz}\right)_{z=L} + Rv\right)\right)_{z=L} = 0 \tag{5-11}$$

Where N_i are the test functions of the Galerkin method, which will be defined in chapter 6. Using the approximate solution:

$$y = \sum_{i=1}^{n} a_j N_j \tag{5-12}$$

and applying the integration by parts on the first two integrals of (5-11), the Galerkin error minimisation defined in chapter (3) and presented here as a reminder in equation (5-13) can be obtained:

$$\int_0^L N_i[R_\Omega] = 0 \tag{5-13}$$

The addition of the last three terms on the left hand side of equation (5-11) caters for the residual of the substitution of the natural boundary conditions of equation (5-7) into equation (5-11). Some of these terms will be eliminated after the integration by parts mentioned above. A general term of the stiffness matrix is derived in equation (5-14):

$$k_{ij} = EI_1 \int_0^{L_1} N"_i N"_j dz + EI_2 \int_{L_1}^{L} N"_i N"_j dz - Rh \int_0^L N'_i N'_j dz + k \int_0^L N_i N_j dz \tag{5-14}$$

Where N_i are the test functions associated with residual minimisation in equation (5-13), and N_j are the trial functions associated with the substitution of the Galerkin approximation of y. For the Babnov Galerkin method, as mentioned in chapter (3), the test and trial functions are chosen to be the same, and the number of trial functions is shown with n in equation (5-12). It can be seen that the first term of equation (5-11) ($\int_0^L N_i \frac{d^2}{dz^2}\left(EI\frac{d^2y}{dz^2}\right)dz$), results in the two terms $\int_0^{L_1} N"_i N"_j dz$ and $\int_{L_1}^{L} N"_i N"_j dz$ in equation (5-14). This is due to the change in geometry at the offset from the rest of the needle, which results in a change in the moment of inertia of the cross section subject to deflection. The integrals are written between 0 to L, effectively minimising the error of the approximated solution along the length of the beam. All the terms in equation (5-11) except the resulting term $RvN_i(L)$ and those present in equation (5-14) are eliminated by integration by parts of the integrals in equation (5-11). The integration process is demonstrated as an example for the first term $\int_0^L N_i \frac{d^2}{dz^2}\left(EI\frac{d^2y}{dz^2}\right)dz$ as follows.

The general integration by parts is defined as:

$$\int udv = uv - \int vdu \tag{5-15}$$

To apply integration by parts to the first term on the left hand side of equation (5-14), which is $\int_0^L N_i \frac{d^2}{dz^2}\left(EI\frac{d^2y}{dz^2}\right)dz$, the two terms U and V are defined in equations (5-16) and (5-17) :

$$u = N_i \rightarrow du = \frac{dN_i}{dz}.dz \tag{5-16}$$

$$dv = \frac{d^2}{dz^2}\left(EI\frac{d^2y}{dz^2}\right) \rightarrow v = EI\frac{d^3y}{dz^3} \tag{5-17}$$

Substituting (5-16) and (5-17) into equation (5-15) yields:

$$\int_0^L N_j \frac{d^2}{dz^2}\left(EI\frac{d^2y}{dz^2}\right)dz = EI.N_j.\frac{d^3y}{dz^3}\Big|_0^L - \int_0^L EI\frac{d^3y}{dz^3}.\frac{dN_j}{dz}.dz \tag{5-18}$$

It has been mentioned that the trial functions chosen should satisfy the essential boundary conditions, so that, at $z = 0$, $N_i = 0$. Hence, from the first term $N_j.\frac{d^3y}{dz^3}\Big|_0^L$, only $(N_j.\frac{d^3y}{dz^3})_{z=L}$ remains. The second term, $\int EI\frac{d^3y}{dz^3}.\frac{dN_j}{dz}.dz$, must be again be integrated using the integration by parts rule, as shown in equation (5-15). The terms u and v are redefined as follows:

$$u = \frac{dN_j}{dz} \rightarrow du = \frac{d^2N_j}{dz^2}.dz \tag{5-19}$$

$$dv = EI\frac{d^3y}{dz^3}.dz \rightarrow v = EI\frac{d^2y}{dz^2} \tag{5-20}$$

Substituting equations (5-19) and (5-20) into equation (5-15) yields equation (5-21):

$$-\int_0^L EI\frac{d^3y}{dz^3}.\frac{dN_j}{dz}.dz = \frac{dN_j}{dz}.EI\frac{d^2y}{dz^2}\Big|_0^L - \int_0^L EI\frac{d^2y}{dz^2}.\frac{d^2N_j}{dz^2}.dz \tag{5-21}$$

Due to the trial functions chosen such as to satisfy the essential boundary conditions at $z = 0$, where $\frac{dy}{dz}$ is zero due to the constraint, in equation (5-21), $\frac{dN_j}{dz}$ at $z = 0$ must also be 0. As no moments are acting on the tip of the needle, at $z = L$, $\frac{d^2y}{dz^2}$ must be equal to 0. Hence, the first

term on the right hand side ($\frac{dN_j}{dz}.EI\frac{d^2y}{dz^2}\Big|_0^L$) is equal to zero, and only the second term remains. Substituting equation (5-21) into equation (5-18) yields equation (5-22):

$$\int_0^L N_j \frac{d^2}{dz^2}\left(EI\frac{d^2y}{dz^2}\right)dz = EI.(N_j.\frac{d^3y}{dz^3})_{z=L} + \int_0^L EI\frac{d^2y}{dz^2}.\frac{d^2N_j}{dz^2}.dz \tag{5-22}$$

Substituting $y = \sum_{i=1}^{n} a_i N_i$ from equation (5-13) into equation (5-22), and accounting for the change in the moment of the area of the cross section as a result of the change in geometry at the offset, equation (5-22) results in the general term, as shown in equation (5-23):

$$\int_0^L EI\frac{d^2y}{dz^2}.\frac{d^2N_j}{dz^2}.dz = a_i(EI_1\int_0^{L_1} N"_iN"_jdz + EI_2\int_{L_1}^{L} N"_iN"_jdz) \tag{5-23}$$

From equation (5-22) and (5-23), it can be said that:

$$\begin{aligned}\int_0^L N_j \frac{d^2}{dz^2}\left(EI\frac{d^2y}{dz^2}\right)dz \\ = a_i(EI_1\int_0^{L_1} N"_iN"_jdz + EI_2\int_{L_1}^{L} N"_iN"_jdz) - (N_j.\frac{d^3y}{dz^3})_{z=L}\end{aligned} \tag{5-24}$$

Substituting equation (5-24) into the weak form equation, as defined in equation (5-11), the final term of equation (5-24) ($-(N_j.\frac{d^3y}{dz^3})_{z=L}$) is cancelled out with the same term in equation (5-11), arising from the inclusion of the residual term of the natural boundary condition. Thus, the first term of the right hand side of equation (5-11) ($\int_0^L N_i\frac{d^2}{dz^2}\left(EI\frac{d^2y}{dz^2}\right)dz$) results in the final general term defined in equation (5-24), ($a_i(EI_1\int_0^{L_1} N"_iN"_jdz + EI_2\int_{L_1}^{L} N"_iN"_jdz)$). The same method is applied to the second integral term in equation (5-11), where, after factoring out a_i, the final form of the previously presented equation (5-14) is created. The only resulting term of equation (5-11) not including a_i is $RvN_i(L)$, which is a result of the inclusion of the residual of the trial functions at the natural boundary condition ($z = L$), where the vertical forces equal Rv.

Using equation (5-14) and taking the term $RvN_i(L)$ to the right hand side of equation (5-13), the matrix form of the equations can be written as:

$$\left[[K] + k\left[\overline{\overline{K}}\right] - [\overline{K}(Rh)]\right]_{nxn} \{a\}_{n\times 1} = \{f\}_{n\times 1} \tag{5-25}$$

Where K is the term $(EI_1 \int_0^{L_1} N"_i N"_j dz + EI_2 \int_{L_1}^{L} N"_i N"_j dz)$, $\left[\overline{\overline{K}}\right]$ is equal to $\int_0^L N_i N_j dz$, $[\overline{K}(Rh)]$ is equal to $Rh \int_0^L N'_i N'_j dz$, and $f_i = RvN_i(L)$. It can be said that the term $[K]$ introduces the contribution of the needle material to the relationship between the forces acting on the needle and the deflection of the needle. The term $k\left[\overline{\overline{K}}\right]$, which includes the stiffness of the springs representing the contact forces acting on the needle, introduces the contribution of the substrate material, in the relationship between the forces acting on the needle and the deflection of the needle. The term $[\overline{K}(Rh)]$, being negative, includes the effect of the axial force on the deflection, effectively counteracting the stiffness of the needle during its deflection. The index n denotes the number of trial functions, and as the residual has to be minimised for all the trial functions, it is made orthogonal for all of them. For each length of the beam, equation (5-14) is written and the integration along the length of the beam results in one value for each k_{ij}. This results in $n \times n$ number of k_{ij} elements, which together minimise the residual of the Galerkin solution for the length of the needle, and form the matrix on the left hand side of equation (5-25).

Should the forces acting on the needle at each time step be known, substituting for k, Rh and Rv, the participation factor of trial functions ($\{a\}$) can be found. Substituting the calculated $\{a\}$ into the Galerkin approximation of equation (5-12) allows derivation of the deflections of each point along the length of the needle model as a function of the forces acting on the needle. As previously explained, the forces acting on the needle are unknown, necessitating their identification. The methodology for identification of the loads throughout insertion from equation (5-23) is presented in the next section.

5.3. Methodology of Reverse Solution For Identification of Forces

The forces acting on the needle for each step of insertion are to be identified from the tip deflections of the needle. Having developed equation (5-25), a relationship between the forces acting on the needle, and the trial function and participation factors of the Galerkin

approximation of the deflection of the points along the needle length, has been established. In this section, the method of identification of the forces acting on the needle during different steps of insertion is defined.

Assuming that the loads acting on the needle for a small enough number m of insertion steps (lengths) are constant and, assuming that for these m steps equation (5-25) is valid, i.e. the quasi linear behaviour assumption is valid, one can write equation (5-25) for each length of the needle, minimising the residual of the Galerkin along the length, as previously defined. Applying equation (5-25) to the different insertion steps, one can write the matrix equation as defined in equation (5-26).

$$\begin{bmatrix} \left[[K]+k\left[\overline{\overline{K}}\right]-[\overline{K}(Rh)]\right]_{nxn}^{1} & \dots & 0 \\ \vdots & \ddots & \vdots \\ 0 & \dots & \left[[K]+k\left[\overline{\overline{K}}\right]-[\overline{K}(Rh)]\right]_{nxn}^{m} \end{bmatrix}_{(nxm)x(nxm)} * \begin{Bmatrix} \{a\}_{nx1}^{1} \\ \vdots \\ \{a\}_{nx1}^{m} \end{Bmatrix}_{(mxn)x1} = \begin{Bmatrix} \{f\}_{nx1}^{1} \\ \vdots \\ \{f\}_{nx1}^{m} \end{Bmatrix}_{(mxn)x1} \tag{5-26}$$

Equation (5-26) provides a relationship between the forces acting on the needle throughout m insertion steps, and the n trial functions of the Galerkin approximation of each length. The Galerkin approximation itself, as written in equation (5-12), can be written for the tip deflections Y_t of m lengths throughout insertion by equation (5-27):

$$\begin{bmatrix} [N_1(L^1)\ N_2(L^1)\ \dots\ N_n(L^1)] & \dots & 0 \\ \vdots & \ddots & \vdots \\ 0 & \dots & [N_1(L^m)\ N_2(L^m)\ \dots\ N_n(L^m)] \end{bmatrix}_{mx(mxn)} * \begin{Bmatrix} \{a\}_{nx1}^{1} \\ \vdots \\ \{a\}_{nx1}^{m} \end{Bmatrix}_{(mxn)x1} = \{Y_t\}_{mx1} \tag{5-27}$$

This equation provides a relationship between the n trial functions for each needle length of the m insertions of the needle, and the deflection of the tip Y_t. Both equations (5-26) and (5-27) have the common matrix $\{a\}_{m\times n\times 1}$, which can be substituted from equation (5-26) into equation (5-27). In order to do so, the matrix on the left hand side of equation (5-26) is split into the sum of sub-matrixes based on $[K]$, $\left[\overline{\overline{K}}\right]$ and $[\overline{K}]$ elements into $\left[\hat{G}\right]$, $\left[\check{G}\right]$ and $\left[\tilde{G}\right]$ matrixes, as shown in equation (5-28).

$$[G]_{(nxm)x(nxm)} = \left[\hat{G}\right]_{(nxm)x(nxm)} + k\left[\check{G}\right] - Rh\left[\tilde{G}\right]_{(nxm)x(nxm)} \tag{5-28}$$

Where $[G]$ is the matrix being multiplied by the matrix of participation factors $\{a\}$ on the left hand side of equation (5-26). Deriving the $\{a\}$ matrix from equation (5-26) yields:

$$\begin{Bmatrix} \{a\}_{nx1}^{1} \\ \vdots \\ \{a\}_{nx1}^{m} \end{Bmatrix}_{(mxn)x1} = \begin{bmatrix} \left[[K] + k[\bar{\bar{K}}] - [\bar{K}(Rh)]\right]_{nxn}^{1} & \dots & 0 \\ \vdots & \ddots & \vdots \\ 0 & \dots & \left[[K] + k[\bar{\bar{K}}] - [\bar{K}(Rh)]\right]_{nxn}^{m} \end{bmatrix}_{(nxm)x(nxm)}^{-1} \begin{Bmatrix} \{f\}_{nx1}^{1} \\ \vdots \\ \{f\}_{nx1}^{m} \end{Bmatrix}_{(mxn)x1} \tag{5-29}$$

Substituting $\{a\}$ from equation (5-29) into equation (5-27) and substituting the left side of equation (5-27), as defined in equation (5-28), yields equation (5-30):

$$[\bar{N}]_{mx(mxn)} \left[\left[\hat{G}\right]_{(nxm)x(nxm)} - Rh\left[\tilde{G}\right]_{(nxm)x(nxm)} + k\left[\check{G}\right] \right]_{(nxm)x(nxm)}^{-1} \begin{Bmatrix} \{f\}_{nx1}^{1} \\ \{f\}_{nx1}^{2} \\ \{f\}_{nx1}^{m} \end{Bmatrix}_{(mxn)x1} = \{Y_t\}_{mx1} \tag{5-30}$$

Where $[\bar{N}]$ is the matrix of trial functions, as defined on the left hand side of equation (5-27). Equation (5-30) establishes a direct relationship between the n trial functions of the length of the needle, the forces acting on the needle, and the deflections of the tip of needle $\{Y_t\}$ throughout a small enough m number of insertion lengths, where the forces acting on the needle can be considered as constant. In order to identify these forces from tip deflections, an inverse solution to equation (5-30) is needed. To this end, in equation (5-31), the matrix $\{f\}$ is defined as a function of the vertical component of the cutting force throughout the m insertion lengths, based on $f_i = RvN_i(L)$, as previously explained:

$$\begin{Bmatrix} \{f\}_{nx1}^{1} \\ \{f\}_{nx1}^{2} \\ \{f\}_{nx1}^{m} \end{Bmatrix}_{(mxn)x1} = [A]_{(mxn)x1} Rv \tag{5-31}$$

Where matrix $[A]$ is the matrix of n number of trial functions for each length, $(N_i(L))$ in m insertion steps.

Substituting from equation (5-31) for $\{f\}$ in equation (5-30) yields equation (5-32):

$$[\bar{N}]_{mx(mxn)}\left[\left[\hat{G}\right]_{(nxm)x(nxm)}-Rh\left[\tilde{G}\right]_{(nxm)x(nxm)}+k\left[\check{G}\right]\right]^{-1}_{(nxm)x(nxm)}[A]_{(mxn)x1}Rv=\{Y_t\}_{mx1} \tag{5-32}$$

To develop an inverse solution, matrix B is defined in equation (5-33):

$$[B]_{mx1}=[\bar{N}]_{mx(mxn)}\left[\left[\hat{G}\right]_{(nxm)x(nxm)}-Rh\left[\tilde{G}\right]_{(nxm)x(nxm)}+k\left[\check{G}\right]\right]^{-1}_{(nxm)x(nxm)}[A]_{(mxn)x1} \tag{5-33}$$

From equation (5-33) and equation (5-32), the inverse solution is defined as equation (5-34):

$$[B]_{mx1}Rv=\{Y_t\}_{mx1}\Rightarrow Rv=[B]^{+}_{1xm}\{Y_t\}_{mx1} \tag{5-34}$$

Where, $[B]^{+}_{1xm}$ indicates the pseudo inverse of $[B]$. The forces Rh and k can be extracted from $[B]^{+}_{1xm}$, as will be explained shortly. The reason for the pseudo inverse is that equation (5-34) includes one unknown Rv for m insertion lengths, rendering the inverse solution in equation (5-34) over determined. As previously explained in chapter (3), in order to solve an over determined inverse problem, the pseudo inverse can be employed. In order to define the unknown values of Rh and k in $[B]^{+}_{1xm}$, a solution space to equation (5-32) is defined such that:

1- The instability (buckling) limit of the needle-elastic-substrate system must be observed, i.e. matrix G of equation (5-32) must be positive definite. This will be tested through the smallest SVD of the G matrix.
2- The minimum least squares error solution of equation (5-32) must be sought, i.e. the set of (Rh, Rv, k) must be found that renders the least square error a minimum.
3- The physical fact that Rh cannot become negative (i.e. the substrate cannot pull the needle tip) must be observed.

A solution space can be defined for equation (5-32) by choosing a reasonable range for Rh and k values, and by keeping one constant and iterating another, identifying the corresponding Rv value and considering the RMSE of the solution to equation (5-32).

Simultaneously, the SVD of the $[G]$ matrix for each combination of (Rh, Rv, k) must be studied, as singularity of $[G]$ must be avoided. Should $[G]$ become singular, the buckling point of the needle has been reached, i.e. the point where the relationship between the axial cutting force Rh and the compressive forces ky results in instability and the system loses stiffness. To validate this method, experimental needle insertions must be run, where the system's trial functions, geometrical and mechanical parameters, and tip deflections as the needle is progressed inside a substrate for m insertion lengths, is defined. The matrix system of equation (5-32) can then be defined, and the (Rh, Rv, k) combination resulting in minimum error identified. These identified loads can then be inputted into a Finite Element Model (FEM) of the same setup in order to compare the tip deflections and the deflections along the length of the needle from experiments, with those resulting from the FEM simulation subject to the identified forces. This process will be further explained in chapters 8 and 10.

5.4. CONCLUSION

In this chapter, a quasi-nonlinear model of needle deflection has been developed, by introducing axial force in the needle model, i.e. to the linear Euler Bernoulli beam equations. The contact forces and the tip forces have been assumed to vary during insertion, and can only be considered as constant for a small enough window of time, comprising of m insertion lengths. The model has been developed for each step in time, thus allowing identification of the forces acting on the needle by imposing mathematical constraints on the solution to the force identification problem, and then checking the stability of the needle during each step of insertion. It has been seen that the trial functions N_i play a significant role in the calculations throughout the math, and thus the process of selection of the trial functions will be discussed in the following chapter. Having defined the trial functions and resulting governing equations, an insertion model of the needle, including its increase in length and subsequent change in loading, will be developed and applied to the Euler Bernoulli model, thus allowing progressive modelling of the needle's deflection through time. This model will then be developed to include nonlinear Euler Bernoulli assumptions, resulting in a large deflection nonlinear model, which can be verified through experimental data and compared against FEM simulations. The next step is the selection of the trial functions and the inclusion of the insertion model, as will be explained in the following chapter.

6. TRIAL FUNCTIONS AND INSERTION MODELLING

6.1. INTRODUCTION

Previously, in chapters 4 and 5, the equilibrium equations of the beam model of the needle were developed, and the deflection of the tip in the linear domain defined as a function of the forces acting on it. A boundary value problem of the needle's deflection has thus been developed, and the Galerkin method suggested as a method for solution approximation. The next step, in order to utilise these equations such as to develop a model of the needle during insertion, is to define the trial functions of the Galerkin method, and apply the insertion model to the equations, thus linking the calculated deflections at each step throughout insertion. In this chapter, the definition of the trial functions and the modelling of the insertion process are presented.

6.2. SELECTION OF TRIAL FUNCTIONS

Generally speaking, for boundary value problems of systems, the common nature of the approximate solution can be predicted from the behaviour of the system. For most problems of practical interest, the general nature of the solution is known. An advantage of the weighted residual solution approximation is that the trial functions can be chosen such as to replicate the behaviour of the solution. Efficiency of computational calculations must also be considered in the selection of trial functions. For weighted residual methods, such as the traditional Galerkin, the trial functions should be selected such as to satisfy the essential boundary conditions of the problem, be linearly independent, and preferably imitate the behavioural characteristics of the solution. For boundary value problems of structural behaviour, where the traditional Galerkin method is applied, the mode shapes of the structure are popular choices for trial functions, as they already satisfy essential B.Cs and are linearly independent. A brief explanation of structural mode shapes is presented below.

6.2.1. MODE SHAPES OF STRUCTURES

The mode shapes of a structure are defined as the shape of the normal modes of the structure, which are the system's natural response under free vibration (without external loading). In this state, all the particles of the structure are vibrating sinusoidally at equal frequency, with fixed phase relation. The mode shapes of structures are defined based on the structure and the boundary conditions of the structure. For the needle being defined as a beam, the mode shapes are derived for the needle geometry as follows.

For any structure, an unlimited number of mode shapes exist. For a beam, using the Euler-Bernoulli beam model, one can write the general solution for the nth mode shape φ_n as:

$$\varphi_n = C_1[cos(k_n z) + cosh(k_n z)] + C_2[cos(k_n z) - cosh(k_n z)] + C_3[sin(k_n z) + sinh(k_n z)] + C_4[sin(k_n z) - sinh(k_n z)] \quad (6\text{-}1)$$

Where constants C_1 to C_4 must be found through boundary condition imposition, as will be explained bellow. Also, k_n^4 is defined in equation (6-2) as follows:

$$k_n^4 = \frac{\omega_n^2 \rho A}{EI} \quad (6\text{-}2)$$

Where ω_n^2 is the square of the nth natural frequency of the beam, ρ is the material density, A is the cross sectional area and EI is the beam section rigidity.

For a beam with two cross sectional properties, (A_1, I_1) for length $L_1$and (A_2, I_2) for the offset length $l = L - L_1$, where L is the total length of the beam at any step of the insertion of the needle, equation (6-1) can be written for each section separately. The constants C_1 to C_4 can then be found by imposing the boundary conditions at the beginning and the end of the original beam, as well as imposing the compatibility constraints at the junction of the two sections, as follows.

For the section of the beam before the offset of length L_1, named section one, it can be said that $k_{n_1}^4 = \frac{\omega_n^2 \rho A_1}{EI_1}$ and the essential boundary conditions can be imposed at the base of the needle as follows:

$$\text{At } z = 0 \text{ , } \varphi_n = 0 \text{ and } \varphi_n' = 0 \quad (6\text{-}3)$$

For the second section of the beam, after the offset, it can be said that $k_{n_2}^4 = \frac{\omega_n^2 \rho A_2}{EI_2}$, and the natural boundary condition imposition at the tip is as follows:

$$\text{At } z = l = L - L_1 \text{ , } \varphi_n'' = 0 \text{ and } \varphi_n''' = 0 \quad (6\text{-}4)$$

For the offset geometry, where the change in geometry of the beam occurs (junction of the beam), it can be said that at both $z = L_1$ for the first segment, where the mode shape can be defined as $(\varphi_n)_1$, and $z = 0$ for the second segment, where the mode shape can be defined as $(\varphi_n)_2$, the compatibility conditions are as follows:

$$(\varphi_n)_1|_{L_1} = (\varphi_n)_2|_0 \ , \qquad (\varphi_n')_1|_{L_1} = (\varphi_n')_2|_0 \ , \qquad I_1(\varphi_n'')_1|_{L_1} = I_2(\varphi_n'')_2|_0 ,$$
$$I_1(\varphi_n''')_1|_{L_1} = I_2(\varphi_n''')_2|_0 \tag{6-5}$$

Also, since for the two sections $\omega_n^2\rho$ is equal, it can be said that:

$$k_{n_2}^4 = \frac{I_1 \times A_2}{I_2 \times A_1} k_{n_1}^4 \tag{6-6}$$

Imposing the constraint equations specified in (6-3) to (6-5) in equation (6-1), for each n, will yield the system of equations in matrix form, as per equation (6-7). The constraints are imposed by writing equations (6-3), (6-4) and (6-5) at the base for $z = 0$, tip for $z = L$ and the offset geometry for $z = l$, creating six equations. Solving the equations of the mode shapes at the boundary conditions for the tip, base and offset geometry provides a means to define the constants of the mode shapes such as to incorporate the effects of the geometry and physical constraints of the beam, i.e. having an offset geometry and being constrained at the base. In order to define these constants, these six equations are put into matrix form, and the constants are derived from solving equation (6-7).

$$\begin{bmatrix} cos(k_{n_1}L_1) - Cosh(k_{n_1}L_1) & sin(k_{n_1}L_1) - Sinh(k_{n_1}L_1) & -2 & 0 & 0 & 0 \\ k_{n1}[-sin(k_{n_1}L_1) - Sinh(k_{n_1}L_1)] & k_{n_1}[cos(k_{n_1}L_1) - Cosh(k_{n_1}L_1)] & 0 & 0 & -2k_{n_2} & 0 \\ k_{n_1}^2[-cos(k_{n_1}L_1) - Cosh(k_{n_1}L_1)] & k_{n_1}^2[-sin(k_{n_1}L_1) - Sinh(k_{n_1}L_1)] & 0 & 2\frac{I_2}{I_1}k_{n_2}^2 & 0 & 0 \\ k_{n_1}^3[sin(k_{n_1}L_1) - Sinh(k_{n_1}L_1)] & k_{n_1}^3[-cos(k_{n_1}L_1) - Cosh(k_{n_1}L_1)] & 0 & 0 & 0 & 2\frac{I_2}{I_1}k_{n_2}^3 \\ 0 & 0 & -cos(k_{n_2}l) + Cosh(k_{n_2}l) & -cos(k_{n_2}l) - Cosh(k_{n_2}l) & -sin(k_{n_2}l) + Sinh(k_{n_2}l) & -sin(k_{n_2}l) - Sinh(k_{n_2}l) \\ 0 & 0 & sin(k_{n_2}l) + Sinh(k_{n_2}l) & sin(k_{n_2}l) - Sinh(k_{n_2}l) & -cos(k_{n_2}l) + Cosh(k_{n_2}l) & -cos(k_{n_2}l) - Cosh(k_{n_2}l) \end{bmatrix}$$

$$\begin{Bmatrix} C_2^1 \\ C_4^1 \\ C_1^2 \\ C_2^2 \\ C_3^2 \\ C_4^2 \end{Bmatrix} = \begin{Bmatrix} 0 \\ 0 \\ 0 \\ 0 \\ 0 \\ 0 \end{Bmatrix}$$

(6-7)

Where C_m^1 are constants of the equations derived at the boundary conditions for the first segment, C_m^2 are constants of the equations derived at the boundary conditions for the second segment, and m is the index of the constant C. Satisfying conditions in equation (6-3) yields $C_1^1 = C_3^1 = 0$. As is evident from (6-7), the system has a non-trivial solution only if the determinant of $[C]$ is zero. So, we should search for values of k_{n_1}, and in turn ω_n^2, which will render the determinant of $[C]$ to be zero. Also, with each value of ω_n^2, there is a non-unique

{C} vector which can be calculated from (6-7) and hence the relevant mode shape can be calculated from (6-1).

The above method, although yielding valid trial functions for the beam with varying geometry at the offset, is computationally difficult. This is due to the fact that, as can be seen, the right hand side of equation (6-7) is zero. Hence, determining the correct trial functions necessitates the calculation of the determinant of the matrix on the left hand side of equation (6-7). Thus, determination of the values of k_{n_1}, and in turn ω_n^2, that will render the determinant zero can be time consuming, and must be obtained via an iterative method. As such, in addition to the mode shapes of the beams, the exact linear equations obtained in section 4.3 are also used as the trial functions. This is allowed, as they all satisfy the essential boundary conditions, and are linearly independent. The mode shapes satisfy the essential boundary conditions, but not necessarily the natural boundary conditions. This is due to the fact the mode shapes are derived for an unloaded beam, while the natural boundary conditions are affected by loading. Mode shapes also incorporate the change in the geometry due to the offset between segments, making them good candidates for use in estimating the behaviour of the beam. In general, trial functions should definitely satisfy the essential boundary conditions, but not necessarily the natural boundary conditions. If the natural boundary conditions are not satisfied, the errors have to be included into the residuals of the approximation, as was discussed in 3.4.2.

At this stage, the trial functions of the Galerkin method, which are needed to obtain the solutions of the equilibrium equation to calculate the deflection of the needle at every step in time, has been explained. In order to apply this deflection calculation throughout insertion, a mathematical model of the relationship between the deflections at each step of insertion has to also be established. This is explained in the following section.

6.3. INSERTION MODELLING

In this section, a methodology to model the extension of the needle length during its insertion into the substrate is presented. It is worth noting that the methodology of insertion modelling is of high importance and is different for quasi-nonlinear and nonlinear needle insertion. This is because, in contrast to quasi nonlinear insertion, the needle's deflection during a nonlinear process cannot be modelled as beginning from an un-deflected state prior to application of external forces, and the deflection at each step is a function of the deflection at the previous step in time, i.e. it is deflection-history dependent. This means that, once the deflection enters

the large deflection range and the nonlinear equations dictate the deflection of the beam, the final deflected shape calculated in the linear range must be used as the initial unloaded shape, for the first nonlinear step of deflection.

As explained in section 5.2 (equation (5-25)) for the quasi-nonlinear process which is associated with small deflection of the needle, it is assumed that each insertion starts from a straight needle configuration and hence, for each insertion, only the total length is modified in trial functions.

For the nonlinear process, in order to incorporate insertion, it is assumed that the insertion process occurs during i small steps, where the total length of the needle is changing an amount Δl_i from insertion step $i-1$ to insertion step i. The length extension process can be shown by the following equations:

$$L_i = L1_i + L_o \tag{6-8}$$

$$L1_i = L1_{i-1} + \Delta l_i \tag{6-9}$$

Where, in equations (6-8) and (6-9), the index *"i"* stands for the i-th insertion step, $L1$ is the length of the needle from its base to offset beginning, L_i is the total length of the needle, L_o is the offset length and Δl_i is the length increment for each insertion step, i, as shown in figure (6-1). It should be noted that the above definitions and equations only apply to a straight needle and modifications are required for a deflected needle, as will be discussed.

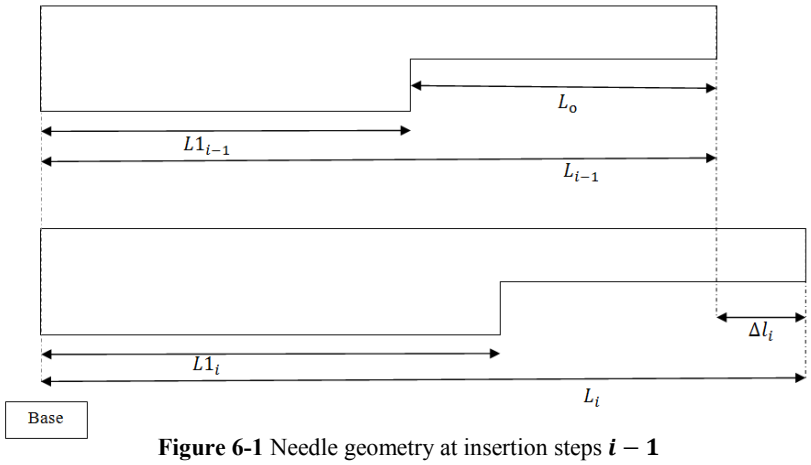

Figure 6-1 Needle geometry at insertion steps $\boldsymbol{i-1}$ and $\boldsymbol{i}$

For ease of explanation, it is assumed that the beam will enter large deflection range after step $i = 5$ of insertion. At this point, in order to solve equation (5-34), the length of the beam

is comprised of "d" discretised points, resulting in a vector of $\{Y_i\}_{(d+1)x1}$and $\{Z_i\}_{(d+1)x1}$ coordinates along the length of the beam. These vectors will include $d+1$ points, with one repeated point at the offset, which is due to the discontinuity at the offset base. As the geometry changes at the offset length z_{o_i}, the deflection y_{o_i} and slope y'_{o_i} of the offset geometry does not vary immediately before and after the offset, but y''_{o_i} would vary due to the change in the section properties. As a result, the final vector of coordinates includes two points at the offset geometry, allowing accurate inclusion of the curvature at the point immediately before and after the offset. These are called y_{o1_i} and y_{o2_i}, y'_{o1_i} and y'_{o2_i} and y''_{o1_i} and y''_{o2_i}.

After completion of the final linear step $i=5$, the beam is inserted a length $\Delta l_i \ll \mathrm{L_{i-1}}$ and enters the nonlinear range at step $i=6$. This means that the unbent length L_{i-1}, should be extended an amount Δl_i to account for the new length of the beam. At this point, d points along the length of the beam exist where, after the added insertion length Δl_i, the added length will be discretised such that the distance between new added points remains as close to $\Delta l_{s,5}$ as possible. Thus, with new points added, a new number of points *d* will result. When the needle is horizontal, the distance between the discretised points or "dz"s will be equal to $\Delta l_{s,5}$ for points positioned in $L1_5$ segment of $L1_6$ and would be slightly different for those positioned on the Δl_6 segment of $L1_6$.

For the 1st nonlinear solution, $i=6$, a 1st nonlinear extension Δl_6 is added to $L1_5$ and the new beam length in its horizontal state, i.e. L_1, is divided into "d" spans and $\{Z^0_{s,6}\}_{(d+1)x1}$ is calculated. The notation "i" of the terms have been dropped so as to avoid confusion, since all of the following occurs in one step of insertion $i=6$. At this stage, the final deflected shape at the end of the linear step $i=5$ has not yet been taken into account during extension, as the length Δl_6 has been added to the undeflected length of the beam. It is incorrect to manually add the insertion length Δl_6 along the deflected shape of the beam at the tip, as this would necessitate assuming the extra length to have the same curvature as the point on the tip, leading to zero moment for more than one point (the tip) along the length of an Euler Bernoulli beam. Thus, a method of determining the final shape of the deflected beam, with added insertion length, is required.

From the final step of the linear deflection $i = 5$, the variables N_{j_5} and a_{j_5} are known for the Galerkin approximation, as shown in equation (6-10). As a reminder:

$$y_5 = \sum_{j=1}^{n} a_{j_5} N_{j_5} \tag{6-10}$$

Where the number of trial functions is described with the j subscript such as to avoid confusion with the insertion step counter i. In order to calculate the 1st estimation of the deflection vector $y_6 = \{Y_{s,6,mapped}\}_{(d+1)x1}$ at $i = 6$ after insertion, the following equation is used:

$$y_6 = \sum_{j=1}^{n} a_{j_5} N_{j_6} \tag{6-11}$$

In equation (6-11), the trial functions N_{j_6} being functions of the length variables of the beam, are recalculated for the new values of $\{Z^0_{s,6}\}_{(d+1)x1}$ for length $L_6 = L_5 + \Delta l$. The values of a_j are assumed to be the same as in the previous step $i = 5$. As mentioned above, equation (6-11) gives the first estimation of the deflection of the needle with the extended length. Application of equation (6-11) can be justified as follows. For N_{j_6}, one can write:

$$N_{j_6} = N_{j_5} + \frac{\partial N_{j_5}}{\partial l}\Delta l + \ ignored\ O(\Delta l^2) \tag{6-12}$$

And the same can be written for a_{j_6}:

$$a_{j_6} = a_{j_5} + \frac{\partial a_{j_5}}{\partial l}\Delta l + \ ignored\ O(\Delta l^2) \tag{6-13}$$

Where, a_{j_6} is the participation factor for the minimum error solution with extended length L_6.

Equation (6-12) is valid only if N_{j_5} and a_{j_6} are smooth functions of l and Δl is small. Both of these prerequisites are valid for insertion applications. Now, insertion of (6-12) into (6-11) yields:

$$y_6 = \sum_{j=1}^{n} a_{j_5} N_{j_6} = \sum_{j=1}^{n} a_{j_5} N_{j_5} + \left(\sum_{j=1}^{n} a_{j_5} \frac{\partial N_{j_5}}{\partial l} \right) \Delta l \tag{6-14}$$

Also, defining y_6^{me} as:

$$y_6^{me} = \sum_{j=1}^{n} a_{j_6} N_{j_6} \tag{6-15}$$

As the minimum error, final, solution for the needle deflection, with length L_6, and inserting equations (6-12) and (6-13) into (6-15) yields:

$$\begin{aligned} y_6^{me} &= \sum_{j=1}^{n} a_{j_6} N_{j_6} \\ &= \sum_{j=1}^{n} a_{j_5} N_{j_5} + \left(\sum_{j=1}^{n} a_{j_5} \frac{\partial N_{j_5}}{\partial l} \right) \Delta l + \left(\sum_{j=1}^{n} N_{j_5} \frac{\partial a_{j_5}}{\partial l} \right) \Delta l \\ &+ ignored\ O(\Delta l^2) \end{aligned} \tag{6-16}$$

From (6-16) and (6-14) it can be said that:

$$y_6^{me} = \sum_{j=1}^{n} a_{j_6} N_{j_6} = y_6 + \left(\sum_{j=1}^{n} N_{j_5} \frac{\partial a_{j_5}}{\partial l} \right) \Delta l \tag{6-17}$$

As can be seen from equation (6-17), y_6 calculated from (6-11) not only preserves the essential and natural properties of y_5, but is also slightly different from the minimum error solution $y_6^{me} = \sum_{j=1}^{n} a_{j_6} N_{j_6}$. So, as (6-17) indicates, y_6 is not the minimum error solution, but just a first estimation. Obviously, the minimum error y_6^{me} will be calculated by taking into account the variation in a_{j_5}in equation (6-17) in the following steps and, eventually, using equation (7-18) , which is explained in the following chapter.

As stated above, y_6 values, shown as $\{Y_{s,1,mapped}\}_{(d+1)x1}$, which with the $\{Z_{s,1}^0\}_{(d+1)x1}$ provide the coordinates of the discretised points along the extended length of the deflected beam, do not satisfy the equilibrium equations and a further step of solving equation (7-18) is required, in order to gain equilibrium and hence $y_6^{me} = \{Y_{s,6}\}_{(d+1)x1}$. However, before attempting to solve equation (7-18), $\{Y_{s,1,mapped}\}_{(d+1)x1}$ must be modified such that the total,

extended, length of the beam must be preserved, i.e. the bent shape of the beam must not result in an increase in the total length of L_6. This is not naturally preserved during application of equation (6-11) and derivation of $\{Y_{s,1,mapped}\}_{(d+1)x1}$, and must be imposed as a constraint. In order to correct the length of the beam, it is imposed that the length between each two discretised points 's' and '$s+1$' must not change for $\{Y_{s,1,mapped}\}_{(d+1)x1}$ and $\{Y_{s,linear}\}_{(d+1)x1}$. This is called an "end shortening" constraint and is shown in figure (6-2) for $d = 4$.

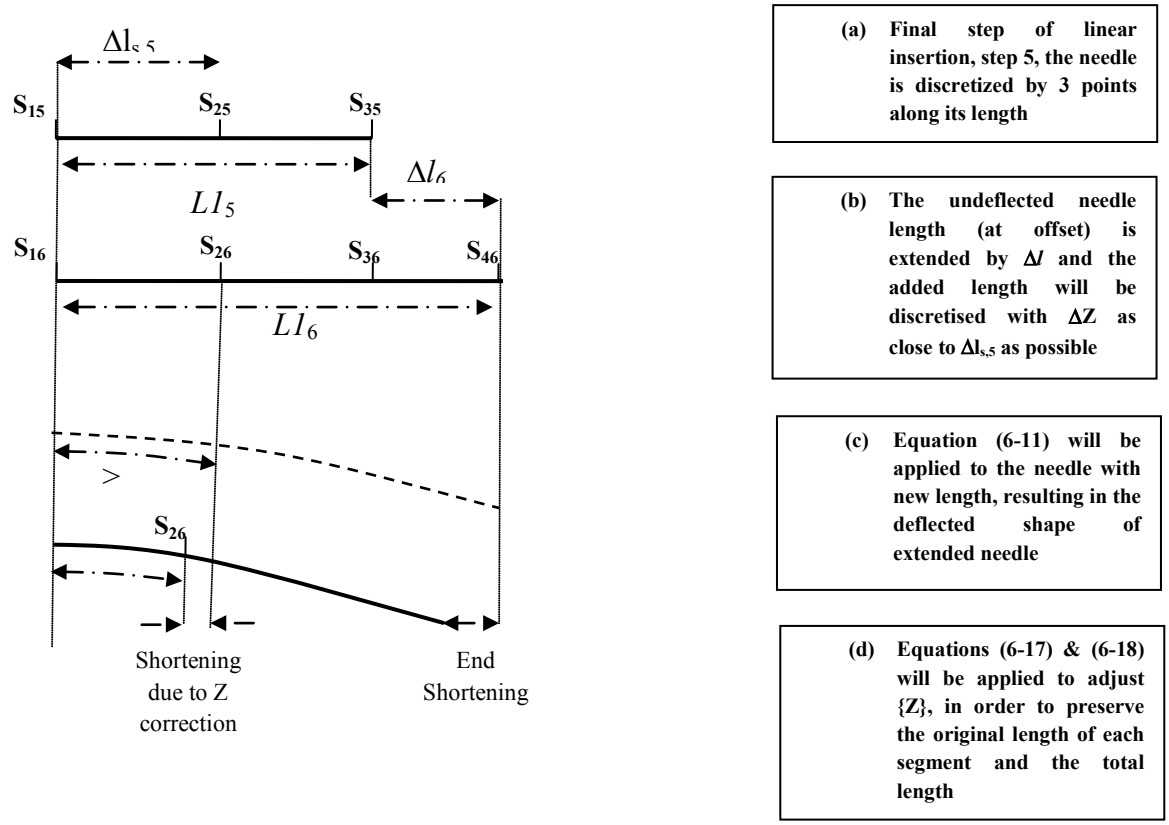

Figure 6-2. Schematic of length shortening method for extension of beam length during insertion modelling.

As can be seen in figure (6-2), initially, in step (a), the length L_5 at step $i = 5$ of the insertion is shown, which is discretised by d=3 points s_{1_5}, s_{2_5} and s_{3_5} into segments of length $\Delta l_{s,5}$. After the beam length is extended by Δl to $L1_6$, the beam is again re-discretised at step (b), by into new points s_{1_6}, s_{2_6} $s_{3_6}$and s_{4_6}, with segments of length $\Delta l_{s,6}$, yielding $\{Z^0_{s,6}\}_{(4)x1}$. Note that the beam is still undeflected. Next, N_{j_6} functions will be evaluated at $\{Z^0_{s,6}\}_{(4)x1}$ and equation (6-11) will be applied and the corresponding y values for the deflected shape of $y_6 = \{Y_{s,1,mapped}\}_{(d+1)x1}$ calculated (6-2c). Here, in order to keep the total length of the

needle, $L1_6$, constant, the end shortening constraint must be applied. This will be achieved by modifying $\{Z^0_{s,6}\}_{(4)x1}$ to $\{Z^c_{s,6}\}_{(4)x1}$, as shown in (6-2d). The same process is repeated for each point along the length of the beam, resulting in a total shortening of SL. The end shortening constraint is imposed through the satisfying of equation (6-17):

$$\Delta Z_{s,6} = \sqrt{(\Delta l_{s,6})^2 - (\Delta Y_{s,6})^2} \tag{6-18}$$

$$Z^c_{s+1,6} = Z^c_{s,6} + \Delta Z_{s,6} \tag{6-19}$$

Where, in equation (6-18), $\Delta Z_{s,6}$ is the necessary adjustement to the element of $\{Z^0_{s,6}\}_{(d+1)x1}$ and $\Delta Y_{s,6}$ is the difference in the calculated deflections or elements of $\{Y_{s,1,mapped}\}_{(d+1)x1}$ for the two discretisation points 's' and '$s+1$' on the two sides of the segment, as shown in figure (6-3). $Z^c_{s+1,6}$ denotes the corrected element of $\{Z^c_{s,6}\}_{(d+1)x1}$ at the next discretised point $s+1$, as a function of the correction of the previous point s along the beam, $Z^c_{s,6}$, since, for each point, the correct $\Delta Z_{s,6}$ must be calculated and summed with the point before $Z^c_{s,6}$ to determine the correct $Z^c_{s+1,6}$. Note that, for the first point, i.e. $s = 1$, which is on the clamp support, $Z^c_{1,6} = 0$ and hence equation (6-19) must be started from support of the beam (which for the needle is the point of insertion into the gelatine).

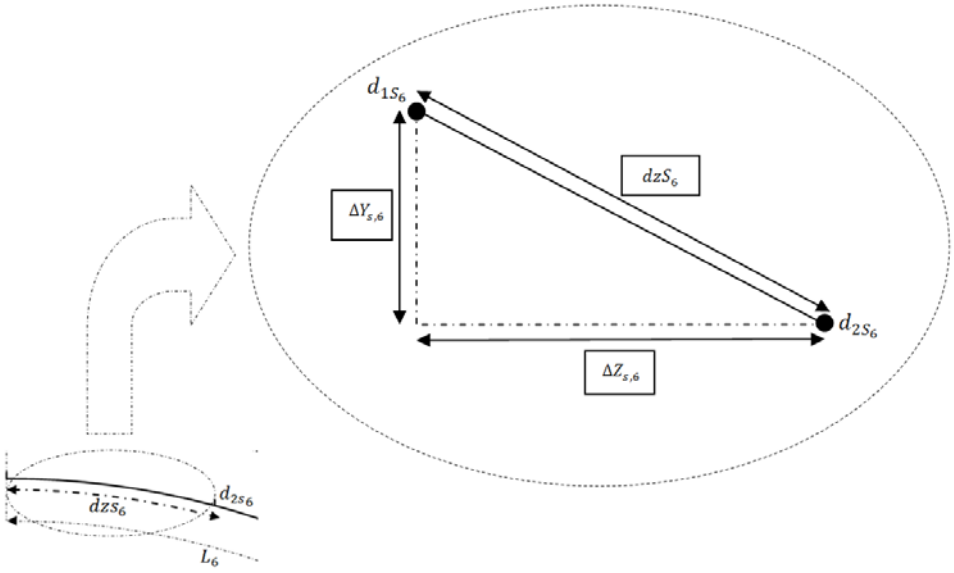

Figure 6-3. Schematic of length shortening method, as captured in equations (6-17) and (6-18). A discretised segment of the beam is magnified, showing that the $\Delta Z_{s,6}$ must be modified such that the $\Delta Y_{s,6}$ between the two discretisation points allow preservation of the length of the segment after deflection.

It must be noted that the deflected shape at this stage of step $i = 6$ has not yet been subjected to loading, and the deflected shape is a result of extension while being deflected from a previous step.

Now, the loads calculated from the last step can be loaded onto equation (5-25) and solved with the Newton Raphson method, such as to predict deflections as a function of loading. After the beam's final deflected shape has been derived, the preservation of length must again be applied to its geometry as explained above.

The insertion modelling process can be summarised as follows:

1- After the linear solution is completed, $\{Y_{s,linear}\}_{(d+1)x1}$ calculated at $\{Z_{s,linear}\}_{(d+1)x1}$ coordinates. For a linear solution, it is assumed that the deflection is small and hence the beam length remains unchanged and thus no correction to $\{Z_{s,linear}\}_{(d+1)x1}$ is required.

2- For the 1st nonlinear solution, $i = 1$, 1st extension Δl_1 is added to $L1_{linear}$ and the new beam length in its horizontal state, i.e. L_1, is discretised such that the Δl_s for the points from the previous step is unchanged and the points on the added length will be such that the segments length will be as close to Δl_s as possible. So the number of points "d" is increased, and $\{Z^0_{s,1}\}_{(d+1)x1}$ is calculated.

3- Using the known values of a_j from the previous step and calculating the trial functions N_j for the new insertion length, the $\{Y_{s,linear}\}_{(d+1)x1}$ is mapped to the beam, with the extended length. This is termed $\{Y_{s,1,mapped}\}_{(d+1)x1}$.

4- Using equations (6-18) and (6-19), the constraint of constant beam length is imposed, using $\{Y_{s,1,mapped}\}_{(d+1)x1}$ and $\{Z^0_{s,1}\}_{(d+1)x1}$. This will result in the first correction to $\{Z^0_{s,1}\}_{(d+1)x1}$ and is termed $\{Z^{c1}_{s,1}\}_{(d+1)x1}$.

5- Now, using $\{Z^{c1}_{s,1}\}_{(d+1)x1}$, $\{Y_{s,1,mapped}\}_{(d+1)x1}$ and the load vector from the 1st nonlinear stage, equation (5-34) is setup and solved iteratively by the Newton-Raphson method. This will result in $\{Y_{s,1}\}_{(d+1)x1}$.

6- Here, again, the "constant beam length" constraint is applied, using equations (6-18) and (6-19), plus $\{Y_{s,1}\}_{(d+1)x1}$ and $\{Z^{c1}_{s,1}\}_{(d+1)x1}$. This will yield the second correction on the Z vector, which will transform it to its final value $\{Z_i\}_{(d+1)x1}$.

7- Using the new $\{Z_i\}_{(d+1)x1}$, step 5 is repeated to find a modified $\{Y_{s,1}\}_{(d+1)x1}$. This then will result in a new $\{Z_i\}_{(d+1)x1}$ in step 6. The iteration in steps 5 and 6 is repeated until convergence is achieved.
8- For subsequent insertion steps, $i > 1$, steps 1 to 7 are repeated with the previous step {Y} and {Z} vectors being used for each subsequent step.

6.4. CONCLUSION

In this chapter, the methodology of the selection of the trial functions of the Galerkin solution to the deflection of the beam has been explained, allowing quasi-nonlinear force identification. Subsequently, the insertion of the needle has been captured, using an insertion model to be used in conjunction with the equations developed in chapter 5, providing the link between the deflection at each step of insertion in both the nonlinear and quasi-nonlinear insertion stages. In order to identify forces acting on the needle during nonlinear insertion and model the deflection of the needle in the nonlinear range, the nonlinear Euler Bernoulli equation must be defined for the beam model of the needle, the insertion model must be applied to the equation, and the sensitivity matrix generated (as has been done for linear and quasi-nonlinear models). This is further explained in the following chapters.

7. NONLINEAR MODELLING OF NEEDLE INSERTION

7.1. INTRODUCTION

In previous chapters, in order to model the deflection of the highly flexible needle during insertion and identification of the forces acting on the needle, initially a linear beam model of the needle deflection was developed, and the governing equations derived. The effect of varying the axial force on the tip of the needle was then incorporated into the model, developing a quasi-nonlinear model of needle deflection. Subsequently, a boundary value problem was defined and solved via the Galerkin method. Inserting the position of the tip of the needle at a point in time, coupled with the trial functions of the Galerkin, an inverse solution was developed, allowing identification of the forces acting on the needle at that time. In order to apply the beam model to the needle during insertion, an insertion model was then defined, and the trial functions for the Galerkin solution derived, incorporating the geometry of the needle, and the linear deflection equations. In this chapter, in order to extend the model to be applicable to large deflection, the nonlinear Euler Bernoulli model is developed for the beam model of the needle. The insertion model and trial functions, as defined in the previous chapter, are incorporated into the model, and the methodology of the progressive modelling of the needle in the nonlinear range is developed.

7.2. NONLINEAR EULER BERNOULLI: ASSUMPTIONS AND EQUATIONS

As was mentioned in section 4.2.3, nonlinear beam modelling differs from linear beam modelling in assumptions regarding the force behaviour, and the relationship between the moments of those forces and the deflection of the beam, i.e. the nonlinear Euler Bernoulli equation governs the behaviour of the beam. Nonlinear Euler Bernoulli is applicable to large deflection situations, wherein the deflection of the beam cannot be assumed to change linearly throughout different steps of insertion. This effectively means that, in order to model the nonlinear deflection of a beam at any step of deflection, its last deflected shape must be taken into consideration, and it cannot be solved accurately by applying loading to a straight un-deflected beam.

In the case of the needle in this study, as mentioned in chapter 4, the length of the needle also increases as it is inserted into the material, and as such the needle's deflection during insertion cannot be modelled as one Nonlinear Euler Bernoulli beam undergoing deflection. As the deflection of the beam varies considerably throughout nonlinear deflection, the forces acting on the beam have to be adjusted in small steps such-as to correspond to the current configuration of the beam, and an insertion model must be applied, as explained in chapter 6. The forces at each step of insertion must be fed to the nonlinear Euler Bernoulli equation, calculating deflection at each time increment. By iteratively calculating the nonlinear deflection at each step as a function of the previous deflected shape of the beam, predicting the final shape of the beam becomes possible. The nonlinear Euler Bernoulli equation of the beam model must then be developed.

The general form of nonlinear Euler Bernoulli is presented in equation (7-1):

$$EIy^{"}.\left(1+y'^{2}\right)^{-\frac{3}{2}}=M(z) \tag{7-1}$$

Where E is the Young's modulus of the beam, I is the moment of inertia of the cross section of the beam, $y^{"}$ is the curvature of the beam at any point z along the length of the beam deflected an amount y (and slope of y'), and $M(z)$ is the net moment acting on the centre of gravity of the cross section z. The linear Euler Bernoulli equation is applicable when the term y'^{2} becomes negligible, thus reducing the left hand side of equation (7-1) to $EIy^{"}$. This physically means that deflections cease where y' (i.e. the slope) is small enough i.e. that the beam being modelled has not deflected much. In order to calculate the total moment acting on z on the right hand side of equation (7-1) ($M(z)$), the forces acting on the model, and the assumptions regarding their application, must be defined. This is discussed in the following section.

7.3. Model Description and Mathematical Derivation: Nonlinear Progressive Model

As was the case with the linear and quasi-linear model, the first step in developing the nonlinear model is to define the assumptions of the loading on the needle, i.e. the assumptions regarding the points of application, behaviour and variation of the forces along the needle, and during insertion. The geometry of the needle model is the same as previously defined for the linear and quasi-nonlinear model in figure 4.3. The assumptions regarding the

contact and tip forces are explained in the following section. As explained in 4.1.3, frictional forces are neglected.

7.3.1. CONTACT FORCES

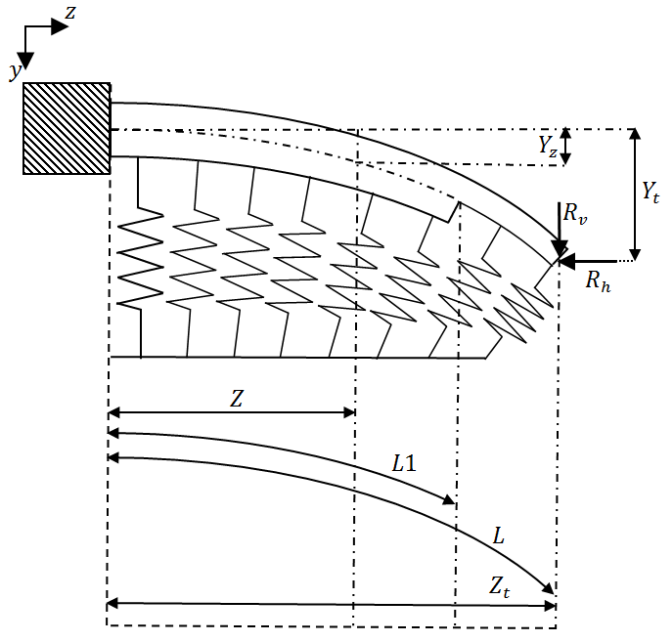

Figure 7-1 Schematic of Nonlinear Beam model of the needle during insertion

The normal contact forces acting on the needle from the substrate are modelled as forces ky, resulting from the displacement off the neutral axis of the beam (y) of a series of springs, with equal stiffness k, at every point z on one side along the length of the beam, as was the case with the quasi-nonlinear model. As a result, the total moment acting due to the springs at the cross section Z, is the net total of the moment of these forces, i.e. the integral of the moment of ky along the length of the beam(shown mathematically in chapter 8). In the quasi-nonlinear model, these forces are always vertical due to the assumption of small deflection, whereas in the nonlinear model these forces must be normal to the beam at every point along its length. This results in two forces acting on every point in the z (axis of insertion) and y (axis of deflection) directions. The force is assumed to vary during the insertion of the needle, and varies because of the deflection (y) along the length of the needle as well. The schematic of the beam model of the needle, including these forces, is shown in figure (7-1), the parameters of which are defined in table 7-1.

Parameter	Definition	Unit
Z	The section with respect to which the moments are being calculated for the Euler Bernoulli	[m]

Y_z	The deflection of the beam at section Z	[m]
Z_t	The z coordinate of the tip of the beam	[m]
Y_t	The deflection of the tip of the beam	[m]
R_v	The vertical component of the cutting force at the tip.	[N]
R_h	The axial component of the cutting force at the tip	[N]
$L1$	The deflected length from base of the needle to the offset	[m]
L	The deflected length from the base of the needle to the tip	[m]

Table 7-1 Definition of notations in figure 1

7.3.2. AXIAL FORCES

As was the case with the quasi-nonlinear model, the axial forces acting on the tip of the needle are composed of two elements, R_v in the direction of y, and R_h in the direction of z. The forces are assumed to act on the point where the neutral axis of the beam dissects the tip end geometry. The net cutting force acts on the tip, with the cutting angle γ, as was the case in chapter 5. This cutting angle may vary with insertion, and must be re-identified throughout the insertion, and re-applied throughout forward modelling. Taking these assumptions into account, the Nonlinear Euler Bernoulli equation (7-1) can be written for the beam illustrated in figure (7-1), the notations of which are explained in table (7-1):

$$\begin{aligned} EI.Y_Z^{''}.\left(1+{Y_Z}'^2\right)^{-\frac{3}{2}} \\ = R_h(Y_t - Y_Z) + R_v(Z_t - Z) \\ - \int_Z^{Z_t} (kyds)cos(\alpha)(z-Z) - \int_Z^{Z_t} (ky\,ds)\sin(\alpha)\,(y-Y_Z) \end{aligned} \tag{7-2}$$

Where E is the Young's modulus of the beam, I is the moment of inertia of the beam cross section at z, α is the angle of curvature of the beam at point z, and z represents the position of the infinitesimal strip of elastic load representing the soft tissue, while Z represents the section with respect to which the moment is being calculated .The same applies to y and Y_z. R_h and R_v are the horizontal and vertical components of the cutting force respectively, as shown in figure (7-1). The first and second terms on the right hand side of equation (7-2) are the moments of these forces, while the third and fourth terms are the moments of the horizontal and vertical components of the forces ky acting along infinitesimal lengths of ds in width, along the needle. Considering the arc length relation:

$$dz = ds \times \cos\alpha \tag{7-3}$$

Equation (7-2) can be rewritten as;

$$EI.Y_Z{}^{"}.\left(1+Y_Z{}'^{2}\right)^{-\frac{3}{2}} = R_h(Y_t - Y_Z) + R_v(Z_t - Z) - \int_Z^{Z_t}(ky)(z-Z)dz - \int_Z^{Z_t}(ky\,y')(y - Y_Z)dz \tag{7-4}$$

The integro-differential equation (7-4) is the governing equation for the nonlinear behaviour of the needle. In order to put equation (7-4) in a format suitable for a progressive insertion solution, it will be assumed that:

$$Y_{Z_{i+1}} = Y_{Z_i} + \bar{Y_Z} \;\;, y_{i+1} = y_i + \bar{y} \tag{7-5}$$

Where $Y_{Z_{i+1}}$is the solution for load step/insertion step $+1$, Y_{Z_i} represents the same for load step/insertion step i and $\bar{Y_Z}$ shows the difference between the two solutions. The same goes for y, which, as previously mentioned, is defined as the deflection of every point along the length of the beam at which a spring is present, resulting in contact forces, the total moment of which contributes to the amount $\bar{Y_Z}$. It should be noted that $\bar{Y_Z}$ has the following characteristics:

a- It represents the increase in deflection from one load step to the next or, from one insertion step to the next. In the latter case, the length of the needle will change from step i to step $i+1$.

b- $\bar{Y_Z} \ll Y_{Z_i}$, which is justified by the very small load increase between load steps, or, by very small sampling intervals for "Y_Z" measurements, which in turn guarantee small increases in "Y_Z" from one sample to next. This assumption would be invalidated if the insertion process became associated with rapid changes and jumps, which is uncharacteristic of the insertion process of a needle.

Substituting the term $Y_Z{}^{"}.\left(1+Y_Z{}'^{2}\right)^{-\frac{3}{2}}$ from equation (7-5) into equation (7-4) yields:

$$Y_Z{}^{"}.\left(1+Y_Z{}'^{2}\right)^{-\frac{3}{2}} = \frac{\bar{Y_Z}{}^{"} + Y_{Z_i}{}^{"}}{[1+\bar{Y_Z}{}'^{2} + Y_{Z_i}{}'^{2} + 2.\bar{Y_Z}{}'.Y_{Z_i}{}']^{\frac{3}{2}}} \tag{7-6}$$

Now, using Taylor's binomial expansion for the denominator of the left hand side of (7-6):

$$\left[1 + {Y_{Z_i}}'^2 + {\bar{Y}_Z}'^2 + 2.\bar{Y}_Z'.Y_{Z_i}'\right]^{-\frac{3}{2}} = \left(1 + {Y_{Z_i}}'^2\right)^{-\frac{3}{2}} - \frac{3}{2}.\left(1 + {Y_{Z_i}}'^2\right)^{-\frac{5}{2}}.\left(2Y_{Z_i}'.\bar{Y}_Z' + {\bar{Y}_Z}'^2\right) \tag{7-7}$$

Inserting the expanded denominator from equation (7-7) into the right hand side (rhs) of equation (7-6):

$$Y_Z{}''.\left(1 + {Y_Z}'^2\right)^{-\frac{3}{2}} \cong \left(\bar{Y}_Z{}'' + Y_{Z_i}{}''\right).\left[\left(1 + {Y_{Z_i}}'^2\right)^{-\frac{3}{2}} - \frac{3}{2}.\left(1 + {Y_{Z_i}}'^2\right)^{-\frac{5}{2}}.2Y_{Z_i}'.\bar{Y}_Z' - \frac{3}{2}.\left(1 + {Y_{Z_i}}'^2\right)^{-\frac{5}{2}}{\bar{Y}_Z}'^2\right] \tag{7-8}$$

Expanding the rhs of equation (7-8) leads to equation (7-9):

$$Y_Z{}''.\left(1 + {Y_Z}'^2\right)^{-\frac{3}{2}} = F(Z) \cong Y_{Z_i}{}''.\left(1 + {Y_{Z_i}}'^2\right)^{-\frac{3}{2}} + \bar{Y}_Z{}''.\left(1 + {Y_{Z_i}}'^2\right)^{-\frac{3}{2}} - 3.\left(1 + {Y_{Z_i}}'^2\right)^{-\frac{5}{2}}.Y_{Z_i}'.\bar{Y}_Z{}''.\bar{Y}_Z' - 3.\left(1 + {Y_{Z_i}}'^2\right)^{-\frac{5}{2}}.Y_{Z_i}'.Y_{Z_i}{}''.\bar{Y}_Z' - \frac{3}{2}.\left(1 + {Y_{Z_i}}'^2\right)^{-\frac{5}{2}}.{\bar{Y}_Z}'^2.\bar{Y}_Z{}'' - \frac{3}{2}.\left(1 + {Y_{Z_i}}'^2\right)^{-\frac{5}{2}}.Y_{Z_i}{}''.{\bar{Y}_Z}^{''2} \tag{7-9}$$

Inserting equation (7-5) into the rhs of equation (7-4) yields equation (7-10):

$$r.h.s\ (4) = R_h(Y_{ti} + \bar{Y}_t - Y_{Zi} - \bar{Y}_Z) + R_v(Z_t - Z) - \int_Z^{Z_t}\left(k(y_i + \bar{y})\right)(z - Z)dz - \int_Z^{Z_t}(k(y_i + \bar{y})(y_i' + \bar{y}'))((y_i + \bar{y}) - (Y_{Zi} + \bar{Y}_Z))dz \tag{7-10}$$

Substituting equations (7-9) and (7-10) into equation (7-4) yields the final form of the nonlinear Euler Bernoulli equation of the beam model of the needle, determining the change in deflection ($\bar{Y}_Z$) of the beam from step i to step $i + 1$ of insertion, for any point Z along its length, previously being Y_{Zi} at step i. This $\bar{Y}_Z$ is a function of the force acting on the needle,

and the deflection of the needle at step i, as depicted in equation (7-5) in the folllwing page. Where, in the integro-differential equation (7-11), all of the terms that depend on $\bar{y}$ or $\bar{Y}_Z$ are on the left hand side (lhs) and all the terms depending on the previous state deformation parameters are on the rhs.

$$
\begin{aligned}
\rightarrow EI\Bigg[& \bar{Y}_Z{}''.\left(1+{Y_{Z_i}}'^2\right)^{-\frac{3}{2}} - 3.\left(1+{Y_{Z_i}}'^2\right)^{-\frac{5}{2}}.{Y_{Z_i}}'.\bar{Y}_Z{}''.\bar{Y}_Z{}' \\
& - 3.\left(1+{Y_{Z_i}}'^2\right)^{-\frac{5}{2}}.{Y_{Z_i}}'.{Y_{Z_i}}''.\bar{Y}_Z{}' - \frac{3}{2}.\left(1+{Y_{Z_i}}'^2\right)^{-\frac{5}{2}}.\bar{Y}_Z{}'^2.\bar{Y}_Z{}'' \\
& - \frac{3}{2}.\left(1+{Y_{Z_i}}'^2\right)^{-\frac{5}{2}}.{Y_{Z_i}}''.\bar{Y}_Z{}'^2\Bigg] - R_h\,(\bar{Y}_t - \bar{Y}_Z) \\
& + \int_Z^{Z_t}\big(k(\bar{y})\big)(z-Z)dz + \int_Z^{Z_t}(k(y_i\bar{y}' + \bar{y}\,y_i' + \bar{y}\,\bar{y}'))\big((y_i+\bar{y}) \\
& - (Y_{Zi} + \bar{Y}_Z)\big)dz \\
& \cong R_h(Y_{ti} - Y_{Zi}) + R_v(Z_t - Z) \\
& - \int_Z^{Z_t}\big(k(y_i)\big)(z-Z)dz - \int_Z^{Z_t}(k(y_i y_i'))\left((y_i) - \left(Y_{Z_i}\right)\right)dz \\
& - EI\left(Y_{Z_i}{}''.\left(1+{Y_{Z_i}}'^2\right)^{-\frac{3}{2}}\right)
\end{aligned}
\tag{7-11}
$$

It must be noted that, in the quasi-nonlinear model as defined in chapter 5, the Euler Bernoulli equation was written in the weak form (fourth degree differential form) for an element dz, and the residuals as a result of the inclusion of the natural boundary conditions were included in the equation, resulting in the existence of the term R_v. In this case, the residuals resulting from the inclusion of the natural boundary conditions automatically arise on the rhs, and not manually included. This is expected, as equation (7-1) is the fourth integration of the weak form Euler Bernoulli equation, as presented in the quasi-nonlinear model.

In order to be able to solve equation (7-11) such as to predict the nonlinear deflection of the needle under loading or identify the loads acting in the nonlinear range from the deflection, a computational method is needed, as terms such ${Y_{Z_i}}'.\bar{Y}_Z{}''.\bar{Y}_Z{}'$ introduce a high level of nonlinearity in the maths. This will be explained in the following section.

7.4. COMPUTATIONAL METHOD

To be able to solve the incremental non-linear integro-differential equation of the nonlinear deflection of the needle at step i, as defined in equation (7-11), a powerful and accurate computational method is needed. Amongst various computational techniques applicable to nonlinear boundary value problems, as has been explained in 3.4.2., the Babnov-Galerkin method is one of the most efficient methods and is chosen here to be applied to equation (7-11).

Applying the Babnov-Galerkin method to equation (7-11) generates an approximate solution to $\bar{Y}_Z(Z)$ in equation (7-12):

$$\bar{Y}_Z(Z) \cong \sum_{j=1}^{n} a_j N_j(Z) + \varphi(Z) \tag{7-12}$$

Where $N_j(Z)$ designates the jth trial function, with j between 1 to n, a_j is the jth trial function's participation factor or weight and $\varphi(Z)$ is an arbitrary function satisfying essential boundary conditions, when trial functions are zero on the essential boundaries. It should be noted that, as was mentioned in chapter 6, the trial functions must be selected such that they are linearly independent, must constitute a complete space, and, if trial functions are selected such that they satisfy the essential boundary conditions, then $\varphi(Z) = 0$. As was the case for the quasi-nonlinear model, the trial functions are selected as the solution to the exact linear Euler Bernoulli beam equations, as derived in section 4.3, and the mode shapes of the beam, as derived in chapter 6. Selecting $N_j(Z)$ such that $\varphi(Z) = 0$, the approximate $\bar{Y}(Z)$ equation (7-12) must be inserted into equation (7-11). As equation (7-11) also includes the terms $\bar{Y}_Z{}'$ and $\bar{Y}_Z{}''$, they have been defined in equation (7-13).

$$\bar{Y}'(Z) \cong \sum_{j=1}^{n} a_j N_j{}'(Z)\,, \bar{Y}_Z{}'' \cong \sum_{j=1}^{n} a_j N_j{}''(Z) \tag{7-13}$$

It can be seen that, as the term a_j is not a function of Z, it is not factored into the derivation, and $\varphi(Z) = 0$, as needed. Approximations for $\bar{Y}(Z)$, $\bar{Y}'(Z)$ and $\bar{Y}_Z{}''$ are also included into the nonlinear integro-differential equation (7-11). The fundamental relation of Babnov-Galerkin for error minimisation, as shown in equation (7-13), must then be applied to the approximated solution:

$$\int_0^{Z_t} N_l(Z) R_\Omega dZ \tag{7-14}$$

Where, $N_l(Z)$ is the j^{th} test function, which is the same as the l^{th} trial function and R_Ω is the residual error resulting from the insertion of equation (7-12) into equation (7-13). This means that, if the $\overline{Y_Z}$ and $\bar{y}$ approximated by the Galerkin were equal to the exact solutions, the rhs and lhs of equation (7-11) would be equal. As they are approximated values, the residual R_Ω is equal to the difference between the two sides of the equation. This residual is then multiplied by $N_l(Z)$, and integrated between 0 and Z_t, resulting in l equations which are equal to zero. This means that, by having defined l test functions and creating l equations including j unknown participation factors a_j, a system of equations is defined, providing a solution to the unknown a_j values. It is obvious that there must at least be j test functions to provide a solution and avoid an ill-posed system.

The test and trial functions in the Bubnov Galerkin method are the same, and thus $l = j$. The trial functions for the approximation of $\bar{y}$ and $\overline{Y_Z}$ are also the same, as they are points on the same beam and have the same patterns of deflection. To avoid confusion, it must be mentioned that the approximation $\sum_{j=1}^{n} a_j N_j(Z)$ is defined for $\overline{Y_Z}$, while for $\bar{y}$, the variable Z (which is the point for which the Euler Bernoulli is being defined), is substituted for z (which are the points along the length under contact force), resulting in $\sum_{j=1}^{n} a_j N_j(z)$. For the residual minimisation in equation (7-13), all terms are multiplied by each $N_l(Z)$ (or in this formulation $N_j(Z)$, as the test and trial functions are the same), as the residual of the Euler Bernoulli is being minimised for each point along the length of the beam, Z, and the points z are for the purpose of force definition, as was shown in equation (7-2).

The integration in equation (7-13) between 0 and Z_t is split into an integration between 0 and Z_o (the offset), and Z_o and Z_t. This is due to the fact that the geometry before and after the offset results in two different moments of inertia of the cross section, namely I_1 and I_2 respectively. Implementing the aforementioned integrations along the length and substituting for R_Ω from the insertion of equation (7-12) and (7-13) into equation (7-11) results in the final form of the nonlinear equation, as presented in equations (7-15) (lhs) and (7-16) (rhs).

$$l.h.s \to EI_1 \int_0^{Z_o} N_l(Z).(\sum_{j=1}^{n} a_j N^{"}{}_j(Z)).\left(1+Y_{z_i}{}'^2\right)^{-\frac{3}{2}} dZ$$

$$- EI_1 \int_0^{Z_o} N_l(Z).3.\left(1+Y_{z_i}{}'^2\right)^{-\frac{5}{2}}.Y_{z_i}'.(\sum_{j=1}^{n} a_j N^{"}{}_j(Z)).(\sum_{j=1}^{n} a_j N'{}_j(Z))\,dZ$$

$$- EI_1 \int_0^{Z_o} N_l(Z).3.\left(1+Y_{z_i}{}'^2\right)^{-\frac{5}{2}}.Y_{z_i}'.Y_{z_i}^{"}.(\sum_{j=1}^{n} a_j N'{}_j(Z))\,dZ$$

$$- EI_1 \int_0^{Z_o} N_l(Z).\frac{3}{2}.\left(1+Y_{z_i}{}'^2\right)^{-\frac{5}{2}}(\sum_{j=1}^{n} a_j N'{}_j(Z))^2.(\sum_{j=1}^{n} a_j N^{"}{}_j(Z))\,dZ$$

$$- EI_1 \int_0^{Z_o} N_l(Z).\frac{3}{2}.\left(1+Y_{z_i}{}'^2\right)^{-\frac{5}{2}}.Y_{z_i}^{"}(\sum_{j=1}^{n} a_j N'{}_j(Z))^2\,dZ$$

$$+ EI_2 \int_{Z_o}^{Z_t} N_l(Z).(\sum_{j=1}^{n} a_j N^{"}{}_j(Z)).\left(1+Y_{z_i}{}'^2\right)^{-\frac{3}{2}} dZ$$

$$- EI_2 \int_{Z_o}^{Z_t} N_l(Z).3.\left(1+Y_{z_i}{}'^2\right)^{-\frac{5}{2}}.Y_{z_i}'.(\sum_{j=1}^{n} a_j N^{"}{}_j(Z)).(\sum_{j=1}^{n} a_j N'{}_j(Z))\,dZ$$

$$- EI_2 \int_{Z_o}^{Z_t} N_l(Z).3.\left(1+Y_{z_i}{}'^2\right)^{-\frac{5}{2}}.Y_{z_i}'.Y_{z_i}^{"}.(\sum_{j=1}^{n} a_j N'{}_j(Z))\,dZ$$

$$- EI_2 \int_{Z_o}^{Z_t} N_l(Z).\frac{3}{2}.\left(1+Y_{z_i}{}'^2\right)^{-\frac{5}{2}}(\sum_{j=1}^{n} a_j N'{}_j(Z))^2.(\sum_{j=1}^{n} a_j N^{"}{}_j(Z))\,dZ$$

$$- EI_2 \int_{Z_o}^{Z_t} N_l(Z).\frac{3}{2}.\left(1+Y_{z_i}{}'^2\right)^{-\frac{5}{2}}.Y_{z_i}^{"}(\sum_{j=1}^{n} a_j\, N'{}_j(Z))^2\,dZ$$

$$- R_h \int_0^{Z_t} N_l(Z)\left(\sum_{j=1}^{n} N_j(Z_t)a_j) - \sum_{j=1}^{n} N_j(Z)a_j)\right)dZ$$

$$+ \int_0^{Z_t} N_l \left\{ \int_Z^{Z_t} (ky_i)(z-Z)dz + \int_Z^{Z_t} k\,(\sum_{j=1}^{n} N_j(z)a_j)\,(z-Z)dz \right.$$

$$+ 2\int_Z^{Z_t} (ky_i y_i')(\sum_{j=1}^{n} N_j(z)a_j)\,dz + 2\int_Z^{Z_t} (ky_i)\left(\sum_{j=1}^{n} N'{}_j(z)a_j\right)(\sum_{j=1}^{n} N_j(z)a_j)\,dz$$

$$+ \int_Z^{Z_t} (ky_i')(\sum_{j=1}^{n} N_j(z)a_j)\left(\sum_{j=1}^{n} N_j(z)a_j\right)dz$$

$$+\int_{Z}^{Z_t}(ky_i)(y_i)y_i'dz+\int_{Z}^{Z_t}(ky_i^2)\left(\sum_{j=1}^{n}N'_j(z)a_j\right)dz$$

$$-Y_{Z_i}\int_{Z}^{Z_t}(ky_i)y_i'dz-(\sum_{j=1}^{n}N_j(z)a_j)\int_{Z}^{Z_t}(ky_i)y_i'dz$$

$$+\int_{Z}^{Z_t}k\left(\sum_{j=1}^{n}N'_j(z)a_j\right)\left(\sum_{j=1}^{n}N_j(z)(z)a_j\right)(\sum_{j=1}^{n}N_j(z)a_j))dz$$

$$-Y_{Z_i}\int_{Z}^{Z_t}k\left(\sum_{j=1}^{n}N'_j(z)a_j\right)((\sum_{j=1}^{n}N_j(z)a_j)\,dz)$$

$$-(\sum_{j=1}^{n}N_j(Z)a_j)\int_{Z}^{Z_t}k\left(\sum_{j=1}^{n}N'_j(z)a_j\right)(\sum_{j=1}^{n}N_j(z)a_j)\,dz$$

$$-Y_{Z_i}\int_{Z}^{Z_t}(ky_i)\left(\sum N_j'(z)a_j\right)dz-(\sum N_j(Z)a_j)\int_{Z}^{Z_t}(ky_i)\left(\sum N_j'(z)a_j\right)dz$$

$$-Y_{Z_i}\int_{Z}^{Z_t}ky_i'(\sum N_j(z)a_jdz-(\sum N_j(Z)a_j)\int_{Z}^{Z_t}ky_i'(\sum N_j(z)a_j)\,dz\Bigg\}\,dZ$$

(7-15)

$$r.h.s\rightarrow\int_{0}^{Z_t}N_l(Z).R_h\left(y_{t_i}-Y_{Z_i}\right)dZ+\int_{0}^{Z_t}N_l(Z).R_v(z_t-Z)dZ$$

$$-\int_{0}^{Z_t}N_l(Z)\left(\int_{Z}^{Z_t}\left(k(y_i)(z-Z)dz\right)\right)dZ$$

$$-\int_{0}^{Z_t}N_l(Z)\left(\int_{Z}^{Z_t}\left(k(y_iy_i')(y_i-Y_{Zi})dz\right)\right)dZ$$

$$-\int_{0}^{Z_0}EI_1N_l(Z)\left(Y_{z_i}^{"}.\left(1+Y_{z_i}^{'2}\right)^{-\frac{3}{2}}\right)dZ-\int_{Z_0}^{Z_t}EI_2N_l(Z)\left(Y_{z_i}^{"}.\left(1+Y_{z_i}^{'2}\right)^{-\frac{3}{2}}\right)dZ$$

(7-16)

As is evident from equations (7-14) and (7-15), the final form of the equation governing $\bar{Y}(Z)$, i.e. the displacement increment behaviour of the needle from load step i to load step $i+1$/ insertion step i to insertion step $i+1$, can be written as follows:

$$P_l\left(a_j, R_h, k, Y_i, Y_i', Y_i^{"}, E, I_1, I_2, Z_t, Z_o\right) = f_l\left(R_v, R_h, k, Y_i, Y_i', Y_i^{"}, E, I_1, I_2, Z_t, Z_o\right) \qquad (7\text{-}17)$$

Where a_j , $j = 1,2, \ldots . n$, are the unknown participation factors in equation (7-15) and Z_t, Z_o are horizontal coordinates of the needle tip and offset start point, respectively. Also, l designates the index of the test function N_l used in equation (7-15) or equation (7-16). The remaining terms are as have been defined previously.

The rhs of equation (7-17) is a function of known parameters (assuming that the forces R_v, R_h and the variable k are known in the progressive solution). In the case where they are not known, a sensitivity matrix is defined, as will be explained in the following chapter.

As has been mentioned, with the definition of $l = 1, \ldots n$ test functions, n equations in the form of equation (7-15) and (7-16) are defined. This results in n algebraic nonlinear equations, with n unknowns a_j. Equations (7-15) and (7-16) (which are the lhs and rhs of the same equation) are nonlinear in a_j and can be efficiently solved by a Newton-Raphson iterative method, as all the terms on the rhs in equation (7-16) are known. To this end, and using the Taylor series expansion of function *P* in equation (4-5), one can write:

$$for\ the\ lth\ equation\ \&\ r+1\ iteration\text{:} \quad P_l\left(a_j\right)_r + \sum_{j=1}^{n}\left(\frac{\partial P_l}{\partial a_j}\right)_r \Delta a_j = f_l \qquad (7\text{-}18)$$

Where r is the Newton Raphson iteration step. The details of the numerical methodology are provided in chapter 8.

As has been discussed, in forward progressive modelling, the Δl_i or increase in length and applied load variations for each insertion step, is known and the deflection pattern is desired. So, for the forward solution, applying the steps as have been defined is straight forward. In the case of the inverse load identification, neither Δl_i nor force measurements are available. In fact, what is available are $\{Y_t\}_{Tx1}$ and $\{Z_t\}_{Tx1}$, which are the measured tip deflections and their corresponding Z coordinates. Also, "T" designates the total number of insertion steps. In turn, the forces acting on the system, as depicted in figure (7-1), are desired. The methodology for their determination is presented in the following chapter.

7.5. CONCLUSION

In this chapter, the nonlinear Euler Bernoulli equation has been applied to the beam model of the needle during its progression. The model has been defined such as to incorporate the length extension model previously defined in chapter (equation (7-6)), providing the relationship between the nonlinear deflections at every insertion step. The final form of the equation governing the beam's nonlinear deflection has been defined as a function of the forces acting on the beam model from the surrounding substrate (contact and axial forces), the increase in length of the needle, and previous state parameters (including the deflection and its derivatives). Substituting these parameters, the forward modelling of the beams nonlinear deflection is defined by a Galerkin solution to the nonlinear Euler Bernoulli, which is iteratively solved using the Newton Raphson formulation. As has been previously stated, the forces acting from the substrate onto the needle are not easily defined if at all, and as such, an inverse solution to the governing nonlinear Euler Bernoulli is also desired, allowing identification of these forces. The methodology for inverse load identification is presented in the following chapter.

8. NONLINEAR MODELLING OF NEEDLE

8.1. INTRODUCTION

The final equation governing the nonlinear behaviour of the beam model of the needle is presented in equation (8-1):

$$f_l\left(a_j, R_h, R_v, k, Y_i, Y_i', Y_i'', Z_{t_i}, Z_{o_i}, E, I_1, I_2\right) = g_l(R_h, R_v, k, Y_i, Y_i', Y_i'', Z_{t_i}, Z_{o_i}, E, I_1, I_2) \tag{8-1}$$

Where E, I_1, I_2 values are known mechanical and geometrical parameters of the needle, $Y_i, Y_i', Y_i'', Z_{t_i}, Z_{o_i}$are position and curvature matrixes of the points along the length of the needle at the previous insertion step solution (after adding Δl length shortening), R_h, R_v, k are forces acting on the needle, and a_j are the participation factors of the Galerkin solution dictating the deflection of the needle as a result of the forces acting, shown in equation(8-2):

$$Y_{Z_{i+1}} = Y_{Z_i} + \bar{Y}_{Z_i}, \qquad \bar{Y}_{Z_i}(Z) \cong \sum_{j=1}^{n} a_j N_j(Z) + \varphi(Z) \tag{8-2}$$

As mentioned in chapter 7, this equation governs the deflection of the beam at any step. This means that, if a beam of known parameters $Y_i, Y_i', Y_i'', Z_{t_i}, Z_{o_i}, E, I_1, I_2$, is subject to the known forces R_v, R_h and k, a_j can be identified by solving the *rhs* and *lhs* of (8-1). The deflection $\bar{Y}_Z(Z)$ can then be calculated as a function of that a_j in equation (8-2) (with the trial functions $N_j(Z)$ previously defined, as mentioned in chapter (7)). To be able to identify a_j from equation (8-1), the Newton Raphson method in employed, which is explained shortly. First, an overview of the entire methodology of the model developed, is needed, encompassing the extension technique, as explained in chapter 6, and the forward progressive and reverse force identification model. Each stage of the model is then explained, resulting in the final deflection shape, and the forces acting on the needle at a given time step.

8.2. MODEL OVERVIEW

Assuming that the needle tip is at Y_t at an initial deflection step i, the schematic chart in figure 8-1 illustrates the multiple stages of the modelling process to calculate the deflection at step $i + 1$, after the beam length is increased an amount Δl.

Figure 8-1. Chart of The Model Process, Parts A, B, C and D are illustrated in figure (2) depicting the needle deflection at each stage of the process.

A. Length Extension Δl

The Length Δl is added to the final deflected length at the previous step i, resulting in the tip moving from Y_{t_i} to $Y_{t_{i(ext)}}$ and Z_{t_i} to $Z_{t_{i(ext)}}$.

B. Y Calculation and Correction of C_1

The new $Z_{t_{i(ext)}}$ are substituted into $Y_{i(C_1)} = \sum_{j=1}^{n} a_j N_j \left(\mathrm{Z}_{i(ext)}\right)$, where $N_j(Z)$ is defined for the new length of the beam, and the a_j identified at the previous step i are used, resulting in the corrected deflections along the length of the beam $Y_{i(C_1)}$ and the tip deflection $Y_{t_{i(C_1)}}$.

The corrected $Y_{i(C_1)}$ and $\mathrm{Z}_{i(ext)}$ are corrected again via end shortening, such as to preserve the length of the beam (as explained in 6.3) resulting in corrected deflections along the length of the beam $Y_{i(C_2)}$ and tip deflection $Y_{t_{i(C_2)}}$ at $Z_{t_{i(C_2)}}$.

C. Force application and Correction C_2, C_3, C_4

$Y_{i(C_2)}$ at $Z_{i(C_2)}$ from the previous stage are substituted into the nonlinear equation (7-17), with forces acting on the needle from the previous stage. The a_j values for the new step $i+1$ are calculated via the Newton-Raphson method, and substituted into $Y_{i(C_3)} = \sum_{j=1}^{n} a_j N_j \left(Z_{i(C_2)}\right)$, resulting in the tip deflection parameters $Y_{t_{i(C_3)}}$ and $Z_{t_{i(C_2)}}$.

$Y_{(C_3)}$ and $Z_{i(C_2)}$ from the previous stage are corrected via end shortening (same as step (B)), resulting in the corrected tip deflection $Y_{t_{i(C_4)}}$ and $Z_{t_{i(C_4)}}$ for step $i+1$.

D. Force Identification by Comparison of the Modelled Deflection $Y_{t_{i(C_4)}} = Y_{t_{i+1(Model)}}$ and Experimental Tip Deflections $Y_{t_{i+1(Experiment)}}$

The difference ΔY between the modelled tip deflection $Y_{t_{i(C_4)}} = Y_{t_{i+1(M)}}$ for step i+1 and the experimental tip deflection $Y_{t_{i+1(Experiment)}}$ is calculated and formulated as a function of $\frac{\delta a}{\delta R_h}$, $\frac{\delta a}{\delta R_v}$ and $\frac{\delta a}{\delta R_k}$ from equation (8-14), allowing calculation of the necessary changes ΔR_h, ΔR_v and Δk to the forces from step i, such as to minimise the difference ΔY. The derivatives $\frac{\delta a}{\delta R_h}$, $\frac{\delta a}{\delta R_v}$ and $\frac{\delta a}{\delta R_k}$ are separately formulated by solving equation (4-5) at $a_j = 0$ for $Y_{t_{i+1(m)}}$ and R_h, R_v and k from step i.

The calculated corrections ΔR_h, ΔR_v and Δk, are added to forces R_h, R_v and k respectively, resulting in new identified values for R_h, R_v and k at step $i+1$. If $\Delta Y \to 0$ the identified forces are verified. If $\Delta Y \gg 0$, these forces are then re-inserted into step C and the correction process repeated iteratively until $\Delta Y \to 0$.

If $\Delta Y \gg 0$

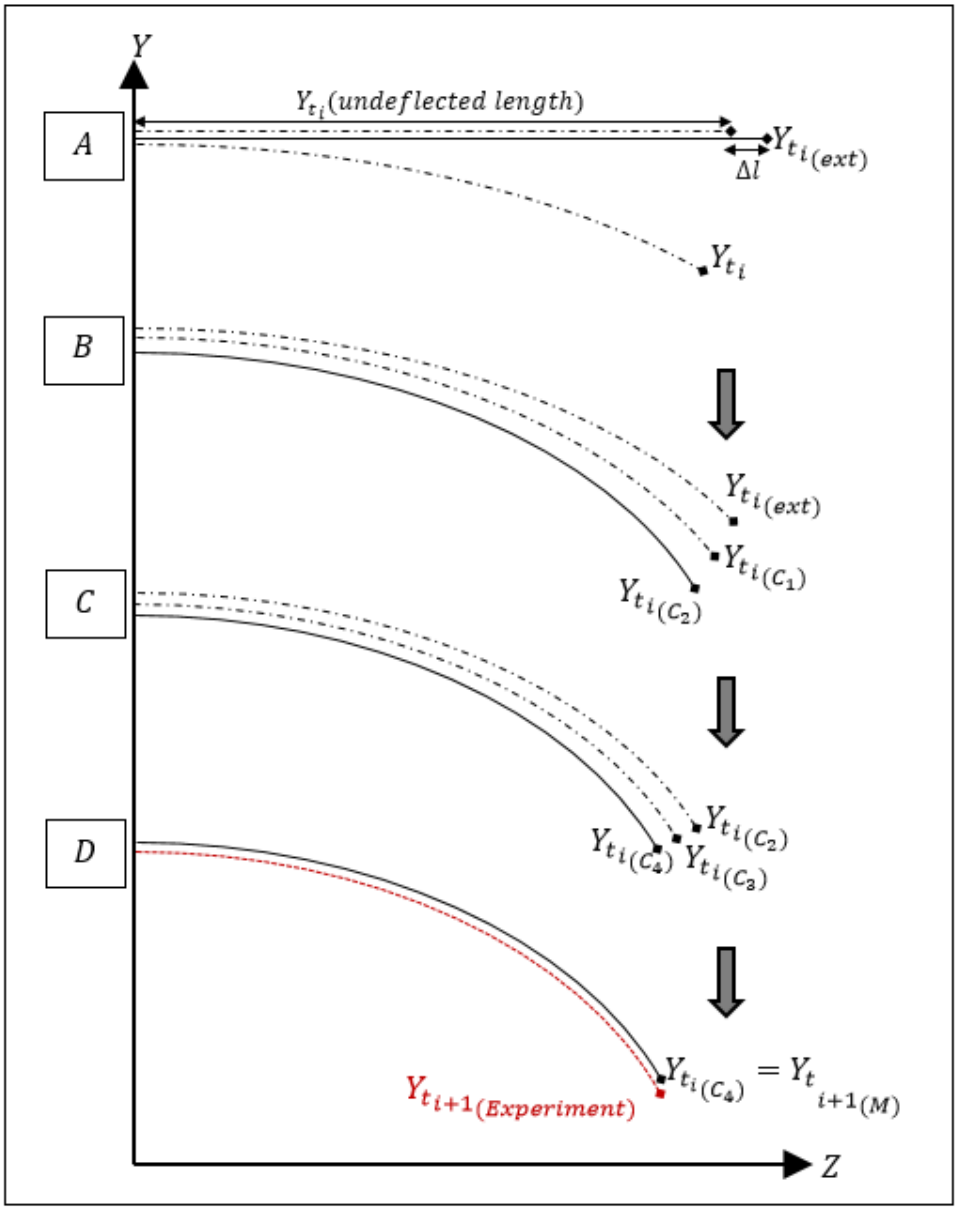

Figure 8-2. Schematic of the modelling process at one step **i**, stages A to D.

As can be seen from figure (8-1), the two initial stages, namely "A. Length Extension Δl " and "B. Y Calculation and Correction C_1" have been explained in 6.3. In these two stages, no force is applied to the needle, and the needle's change in shape due to insertion is determined via assuming that the a_j participation factors from the previous step i of insertion are applicable to N_j for the new extended length at step $i+1$. This is a valid assumption considering the speed and subsequent small Δl of the insertion process.

It must be noted that the needle is not assumed to physically extend in length due to insertion, but that for each step of insertion i, the needle is mathematically modelled as a beam of a new extended length, subject to loading. Hence, after having increased the length of the needle by

Δl (where the tip moves from Y_{t_i} to $Y_{t_{i_{(ext)}}}$ and Z_{t_i} to $Z_{t_{i_{(ext)}}}$) in stage A, and application of N_j to $Z_{i_{(ext)}}$of the extended length of the needle to determine $Y_{i_{(C_1)}}$, the needle's $Z_{i_{(ext)}}$ is corrected such as to preserve the length. This results in the correct extended shape of the needle, and the tip is corrected to $Y_{t_{i_{(C_2)}}}$at $Z_{t_{i_{(C_2)}}}$ at the end of stage B.

In stage "C. Force application and Correction C_2, C_3, C_4 ", having determined the extended shape of the needle at the end of stage B of step $i+1$, the loads from the previous step R_{h_i}, R_{v_i}, k_i are applied to the extended shape, and the subsequent shape of the loaded needle in equilibrium is needed. The previous step (i) loads R_{h_i}, R_{v_i}, k_i, extended shape parameters, and subsequent values of N_j are then inserted into equation (8-1), and the a_j values identified via the Newton Raphson method. These a_j values govern $\bar{Y}_Z(Z)$, or the change in shape of the needle such as to be in equilibrium under the loading from the previous step i. The $\bar{Y}_Z(Z)$ values as a function of the identified a_j are calculated from equation (8-2), and the shape of the needle under equilibrium, with the loading from the previous step, is determined, moving the needle's tip to $Y_{t_{i_{(C_3)}}}$and $Z_{t_{i_{(C_2)}}}$.

As was the case with the length extension at stage A, the new shape of the needle must be corrected such as to conserve the length of the needle. The length shortening process applied in stage A is then applied to the shape of the needle under equilibrium, with the forces from the previous step R_{h_i}, R_{v_i}, k_i, and the tip of the needle moves to $Y_{t_{i_{(C_4)}}}$and $Z_{t_{i_{(C_4)}}}$.

Till now, in the modelling process, the shape of the needle after insertion and change in length Δl subject to know forces, have been determined. But, as was previously explained, the model must be developed such as to allow identification of the loads acting on the needle during its insertion, as a function of its known tip deflection. This is addressed in stage "D. Force Identification by Comparison of the Modelled Deflection $Y_{t_{i_{(C_4)}}} = Y_{t_{i+1_{(M)}}}$and Experimental Tip Deflections $Y_{t_{i+1_{(Experiment)}}}$".

In this stage, it is assumed that a needle tip has physically deflected to a point $Y_{t_{i+1_{(Experiment)}}}$, and that the forward progressive model has been solved till step i , where the forces acting on the needle at step i have been identified by continuous running of the inverse model throughout the insertion progression. This means that, at any step $i+1$, the forces R_{h_i}, R_{v_i}, k_i, and the shape of the needle at step i, have been pre-determined by the

model. In stage C, it has been assumed that the needle is still subject to the forces from the previous step i (R_{h_i}, R_{v_i}, k_i), and the shape of the extended needle at equilibrium under those forces calculated. By defining the error ΔY as the difference between the modelled deflection at step $i+1$ ($Y_{t_{i_{(C_4)}}} = Y_{t_{i+1_{(M)}}}$) and the actual deflection of the tip $Y_{t_{i+1_{(Experiment)}}}$ at step $i+1$, the error can be minimised by adjusting the difference ΔR_h, ΔR_v and Δk between the assumed forces R_{h_i}, R_{v_i}, k_i, and the actual forces acting on the needle $R_{h_{i+1}}, R_{v_{i+1}}, k_{i+1}$. Equation (8-1) is then written in derivative form and the necessary adjustment to the forces ΔR_h, ΔR_v and Δk are identified. Having adjusted the forces and identified $R_{h_{i+1}}, R_{v_{i+1}}, k_{i+1}$, these are fed into the model, and the difference ΔY is recalculated. As $\Delta Y \to 0$, these forces are then verified as the forces acting on the needle at step $i+1$. If $\Delta Y \gg 0$, they are fed back into the model at stage C, and the process is iteratively repeated until $\Delta Y \to 0$.

Having defined the outline and progression of the model through stages A to D at step i, and having provided the explanation to stages A and B of the model in the previous chapter, the mathematics of stages C and D will now be explained.

8.2.1. Stage D: Force Application and Correction C_2, C_3, C_4

As was mentioned in the previous section, in order to derive the final deflected shape Y_{i+1} of the needle at step $i+1$, equation (8-1) is solved by converging the right and left hand sides of the equation and deriving a_j, and subsequently calculating $\overline{Y_{Z_i}}$ from equation (8-2) .Having inserted the known parameters E, I_1, I_2 and the $Y_i, Y_i', Y_i'', Z_{t_i}, Z_{o_i}$ matrices from the previous step of insertion i, the integrated form of the equation (8-1) is as follows:

$$f_{l_{i+1}}\big((a_1, \dots, a_n)_{i+1}, R_{h_i}, k_i\big) = g_{l_{i+1}}(R_{h_i}, R_{v_i}, k_i) \tag{8-3}$$

Where $f_{l_{i+1}}$ is comprised of the terms that are dependent on $a_1, \dots, a_n$ and R_{h_i}, R_{v_i}, k_i and are moved to the lhs of the equation (as can be seen in equation (7-15) and (7-16)), and the independent terms are moved to the rhs of $g_{l_{i+1}}$. A simplified example of a possible final form of this equation is presented in equation (8-4) for ease of understanding of the subsequent calculations in this chapter:

$$\begin{aligned} B_1 a_1 + B_2 a_1^2 + B_3 a_1 a_2 + B_4 a_1 a_2 a_3 + C_1 a_1 R_{h_i} + \dots + D a_1 a_2 k_i \\ = E_1 + .. + H R_{h_i} + L R_{v_i} + M k_i \end{aligned} \tag{8-4}$$

Where $B_1, B_2, B_3, B_4, C_1, C_2, D, E_1, H, L, M$ are possible constants arising from the integral, which encompass the effect of E, I_1, I_2 and the Y_i, Y_i', Z_t, Z_o . In order to calculate the deflection $\bar{Y}_{Z_i}$, the forces R_{h_i}, R_{v_i}, k_i are substituted into equation (8-4) and the $a_1, \dots, a_n$ satisfying the equation are calculated. In order to do so, the Newton Raphson method is applied to equation (8-3), as is illustrated in figure (8-3).

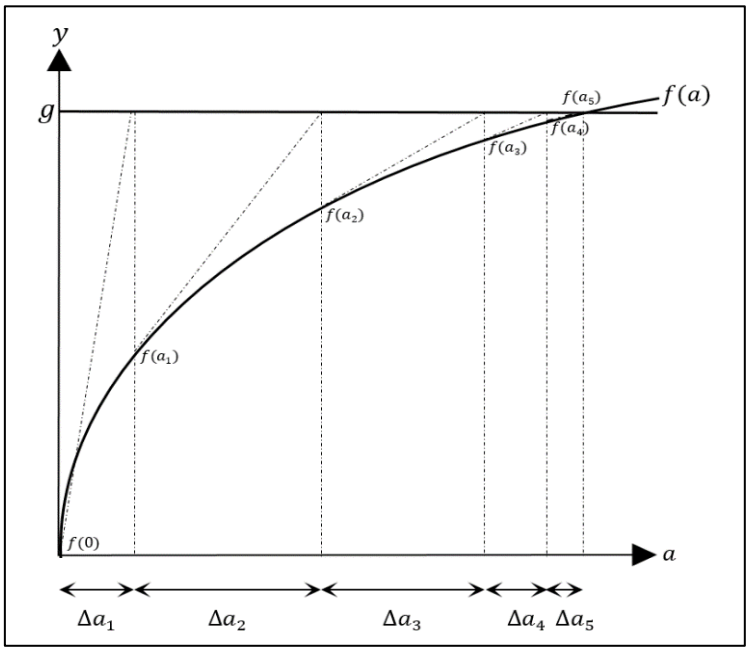

Figure 8-3 Illustration of the Newton-Raphson Method applied to equation (8-3) for a participation factor a.

Where Δa_i in figure (8-3) is defined via equation (8-5) and minimised iteratively till a solution is reached:

$$\left.\frac{\partial f}{\partial a}\right|_{a_j^k} \Delta a_j^{k+1} = g - f\left(a_j^k\right), a_j^{k+1} = a_j^k + \Delta a_j^{k+1} \tag{8-5}$$

This is the general form of the Newton Raphson method as applied to one of the parameters a_j of the iteration process to reach a solution a_j^{k+1}, where, for the example in figure (8-3), $k = 4$. It must be mentioned that, as previously mentioned, for each insertion step i, j is the coefficient factor for equation (8-1), where $j = 1 \dots n$, and k is the number of iterations needed for a solution to equation (8-5).

The Newton Raphson method is applied to each a_j, where $j = 1 \dots n$. For one a_j, the convergence process after a series of iterations is shown below:

$$
\begin{gathered}
f(0) + \left.\frac{\partial f}{\partial a}\right|_0 \Delta a_j^1 = g \rightarrow \Delta a_j^1 \rightarrow a_j^1 = 0 + \Delta a_j^1 \\
f\left(a_j^1\right) + \left.\frac{\partial f}{\partial a}\right|_{a_j^1} \Delta a_j^2 = g \rightarrow \Delta a_j^2 \rightarrow a_j^2 = a_j^2 + \Delta a_j^2 \\
\vdots \\
where\ g - f\left(a_j^m\right) \rightarrow 0\ and\ \Delta a_j^{m+1} \rightarrow 0 \\
\vdots \\
f\left(a_j^m\right) + \left.\frac{\partial f}{\partial a}\right|_{a_j^m} \Delta a_j^{m+1} = g \rightarrow \Delta a_j^{m+1} \rightarrow a_j^{m+1} = a_j^m + \Delta a_j^{m+1}
\end{gathered}
\tag{8-6}
$$

Where $a_j = 0$ at the initial step, and the solution a_j^{m+1} is reached after m iterations. Applying the first step $k = 1$ of the Newton Raphson process in equation (8-6) to all the $a_1, \dots, a_n$ parameters in equation (8-3) yields the following solution:

$$
\begin{gathered}
f_1(a_1^1, a_2^1, \dots, a_n^1 = 0) + \left.\frac{\partial f_1}{\partial a_1}\right|_{a_1^1=0} \Delta a_1^1 + \left.\frac{\partial f_1}{\partial a_2}\right|_{a_2^1=0} \Delta a_2^1 \dots + \left.\frac{\partial f_1}{\partial a_n}\right|_{a_n^1=0} \Delta a_n^1 = g \\
f_2(a_1^1, a_2^1, \dots, a_n^1 = 0) + \left.\frac{\partial f_2}{\partial a_1}\right|_{a_1^1=0} \Delta a_1^1 + \left.\frac{\partial f_2}{\partial a_2}\right|_{a_2^1=0} \Delta a_2^1 \dots + \left.\frac{\partial f_2}{\partial a_n}\right|_{a_n^1=0} \Delta a_n^1 = g \\
\vdots \\
\vdots \\
f_l(a_1^1, a_2^1, \dots, a_n^1 = 0) + \left.\frac{\partial f_l}{\partial a_1}\right|_{a_1^1=0} \Delta a_1^1 + \left.\frac{\partial f_l}{\partial a_2}\right|_{a_2^1=0} \Delta a_2^1 \dots + \left.\frac{\partial f_l}{\partial a_n}\right|_{a_n^1=0} \Delta a_n^1 = g
\end{gathered}
\tag{8-7}
$$

Where l is the number of trial functions, resulting in l number of equations in the form of equation (8-4). Writing equation (8-7) in matrix form results in equation (8-8):

$$
\begin{bmatrix}
\left.\frac{\partial f_1}{\partial a_1}\right|_{a_1^1=0} & \left.\frac{\partial f_1}{\partial a_2}\right|_{a_2^1=0} & \dots & \left.\frac{\partial f_1}{\partial a_n}\right|_{a_n^1=0} \\
\left.\frac{\partial f_2}{\partial a_1}\right|_{a_1^1=0} & \left.\frac{\partial f_2}{\partial a_2}\right|_{a_2^1=0} & \dots & \left.\frac{\partial f_2}{\partial a_n}\right|_{a_n^1=0} \\
\vdots & \vdots & & \vdots \\
\left.\frac{\partial f_l}{\partial a_1}\right|_{a_1^1=0} & \left.\frac{\partial f_l}{\partial a_2}\right|_{a_2^1=0} & \dots & \left.\frac{\partial f_l}{\partial a_n}\right|_{a_n^1=0}
\end{bmatrix}
\begin{bmatrix}
\Delta a_1^1 \\ \Delta a_2^1 \\ \vdots \\ \Delta a_n^1
\end{bmatrix}
= [g] -
\begin{bmatrix}
f_1(a_1^1, a_2^1, \dots, a_n^1 = 0) \\
f_2(a_1^1, a_2^1, \dots, a_n^1 = 0) \\
\vdots \\
f_l(a_1^1, a_2^1, \dots, a_n^1 = 0)
\end{bmatrix}
\tag{8-8}
$$

Writing the equations in the matrix form shown in equation (8-8) allows determination of the $\Delta a_1 \dots \Delta a_n$ values that minimise the residual of the Galerkin solution, as formulated in equation (8-2) for all l trial functions and n participation factors a_n (where, as previously mentioned, $l = n$) for an initial step $a_j = 0$. Having iteratively defined the solutions

$a_1, \dots, a_n$ at step i, they are inserted into equation (8-2), and $\bar{Y}_Z(Z)$ is calculated. This determines the extended shape of the needle, subject to forces R_{h_i}, R_{v_i}, k_i.

As was mentioned in the previous section, after calculation of $Y_{i_{(C_3)}}$and $Z_{i_{(C_2)}}$, the new needle coordinates are corrected such as to preserve length of the needle and the tip moves to $Y_{t_{i_{(C_4)}}}$and $Z_{t_{i_{(C_4)}}}$, which has been previously explained and is not repeated here. In the next section, Stage D of the model, involving the identification of the forces acting on the needle, is explained.

8.2.2. D: Force Identification by Comparison of the Modelled Deflection $Y_{t_{i_{(C_4)}}} = Y_{t_{i+1_{(M)}}}$ and Experimental Tip Deflections $Y_{t_{i+1_{(Experiment)}}}$

As has been previously explained, the forces acting on the needle at any step of insertion must be identified as a function of its tip position. In order to do so, in stage A, for the needle shape at step $i+1$, initially the undeflected needle length is extended an amount Δl, subject to the shape functions from step i. Then, in stage B, it has been initially assumed that the forces acting on the needle at step $i+1$ are the forces from the previous step i, namely; R_{h_i}, R_{v_i}, k_i. The deflection of the needle with added length at $i+1$ subject to these forces has been calculated and the needle tip modelled to be at $Y_{t_{i_{(C_4)}}}$and $Z_{t_{i_{(C_4)}}}$ at the end of stage B.

In order to calculate the actual forces acting on the needle at $i+1$, namely $R_{h_{i+1}}, R_{v_{i+1}}, k_{i+1}$, the errors $\Delta R_{h_{i+1}}, \Delta R_{v_{i+1}}, \Delta k_{i+1}$ are defined as a function of the error between the actual tip position $Y_{t_{i+1_{(Experiment)}}}$ and the tip position subject to forces R_{h_i}, R_{v_i}, k_i, namely $Y_{t_{i+1_{(M)}}}$(which in its initial stage of calculation, is the final calculated tip position at stage B, $Y_{t_{i_{(C_4)}}}$). This allows minimisation of the error between the modelled needle tip position and the actual needle tip position, by correction of the forces assumed to be acting on the needle. Hence, ΔY_t is defined in equation (8-9):

$$\Delta Y_{t_{i+1}} = Y_{t_{i+1_{(Experiment)}}} - Y_{t_{i+1_{(M)}}} \tag{8-9}$$

From equation (8-2) one can write:

$$\Delta Y_t = \sum_{j=1}^{n} N_j^{t_{i+1}}(Z)\frac{\partial a_j}{\partial R_v}.\Delta R_{v_{i+1}} + \sum_{j=1}^{n} N_j^{t_{i+1}}(Z)\frac{\partial a_j}{\partial R_h}.\Delta R_{h_{i+1}} + \sum_{j=1}^{n} N_j^{t_{i+1}}(Z)\frac{\partial a_j}{\partial k}.\Delta k_{i+1} \tag{8-10}$$

Writing equation (8-10) for three consecutive tip deflections $i+1$, $i+2$ and $i+3$ in matrix form yields equation (8-11):

$$\begin{bmatrix} \sum_{j=1}^{n} N_j^{t_{i+1}}(Z)\frac{\partial a_j}{\partial R_h} & \sum_{j=1}^{n} N_j^{t_{i+1}}(Z)\frac{\partial a_j}{\partial R_v} & \sum_{j=1}^{n} N_j^{t_{i+1}}(Z)\frac{\partial a_j}{\partial k} \\ \sum_{j=1}^{n} N_j^{t_{i+2}}(Z)\frac{\partial a_j}{\partial R_h} & \sum_{j=1}^{n} N_j^{t_{i+2}}(Z)\frac{\partial a_j}{\partial R_v} & \sum_{j=1}^{n} N_j^{t_{i+2}}(Z)\frac{\partial a_j}{\partial k} \\ \sum_{j=1}^{n} N_j^{t_{i+3}}(Z)\frac{\partial a_j}{\partial R_h} & \sum_{j=1}^{n} N_j^{t_{i+3}}(Z)\frac{\partial a_j}{\partial R_v} & \sum_{j=1}^{n} N_j^{t_{i+3}}(Z)\frac{\partial a_j}{\partial k} \end{bmatrix} \begin{Bmatrix} \Delta R_{h_{i+1}} \\ \Delta R_{v_{i+1}} \\ \Delta k_{i+1} \end{Bmatrix} = \begin{Bmatrix} \Delta Y_{t_{i+1}} \\ \Delta Y_{t_{i+2}} \\ \Delta Y_{t_{i+3}} \end{Bmatrix} \tag{8-11}$$

Where $\Delta Y_{t_{i+1}}$, $\Delta Y_{t_{i+2}}, \Delta Y_{t_{i+3}}$ and $N_j^{t_{i+1}}$, $N_j^{t_{i+2}}, N_j^{t_{i+3}}$ are calculated for three different insertion lengths $i+1, i+2$ and $i+3$. It must be noted that, as will be shown in the results, every three steps $i+1, i+2$ and $i+3$ will be solved simultaneously for three Δl values, allowing force identification from equation (8-11).

In order to be able to identify $\Delta R_{h_{i+1}}, \Delta R_{v_{i+1}}, \Delta k_{i+1}$ from equation (8-11), the terms $\frac{\partial a_j}{\partial R_h}, \frac{\partial a_j}{\partial R_v}, \frac{\partial a_j}{\partial k}$ are needed. These derivatives define the sensitivity of the deflection of the needle to the change in the forces acting on the tip *in its current shape*. In order to calculate the derivatives, the differential of equation (8-1) is written as a function of a_j in equation (8-12):

$$l.h.s \rightarrow df_l = \frac{\partial f_l}{\partial a_1}.da_1 + \frac{\partial f_l}{\partial a_2}.da_2 + \cdots + \frac{\partial f_l}{\partial a_n}.da_n + \frac{\partial f_l}{\partial R_h}.dR_h + \frac{\partial f_l}{\partial R_v}.dR_v + \frac{\partial f_l}{\partial k}.dk \tag{8-12}$$

$$R.h.s \rightarrow dg_l = \frac{\partial g_l}{\partial R_h}.dR_h + \frac{\partial g_l}{\partial R_v}.dR_v + \frac{\partial g_l}{\partial k}.dk$$

Dividing df_l and dg_l in equation (8-12) by the differential dR_h yields equation (8-13):

$$\begin{gathered} l.h.s \rightarrow \frac{df_l}{dR_h} = \frac{\partial f_l}{\partial a_1}.\frac{da_1}{dR_h} + \frac{\partial f_l}{\partial a_2}.\frac{da_2}{dR_h} + \cdots + \frac{\partial f_l}{\partial a_n}.\frac{da_n}{dR_h} + \frac{\partial f_l}{\partial R_h} \\ R.h.s \rightarrow \frac{dg_l}{dR_h} = \frac{\partial g_l}{\partial R_h} \end{gathered} \tag{8-13}$$

Where the derivatives of terms R_v and k with respect to R_h are 0, and $\frac{dR_h}{dR_h} = 1$. Equation (8-13) is written for each $l = 1 \ldots n$, for R_v and k, resulting in the matrix of equations (8-14):

$$\begin{gathered} \begin{bmatrix} \frac{\partial f_1}{\partial a_1} & \frac{\partial f_1}{\partial a_2} & \cdots & \frac{\partial f_1}{\partial a_n} \\ \frac{\partial f_2}{\partial a_1} & \frac{\partial f_2}{\partial a_2} & \cdots & \frac{\partial f_2}{\partial a_n} \\ \vdots & \vdots & \ddots & \vdots \\ \frac{\partial f_l}{\partial a_1} & \frac{\partial f_l}{\partial a_2} & \cdots & \frac{\partial f_l}{\partial a_n} \end{bmatrix} \begin{Bmatrix} \frac{da_1}{dR_h} \\ \frac{da_2}{dR_h} \\ \vdots \\ \frac{da_n}{dR_h} \end{Bmatrix} = \begin{Bmatrix} \frac{\partial g_1}{\partial R_h} - \frac{\partial f_1}{\partial R_h} \\ \frac{\partial g_2}{\partial R_h} - \frac{\partial f_2}{\partial R_h} \\ \vdots \\ \frac{\partial g_l}{\partial R_h} - \frac{\partial f_l}{\partial R_h} \end{Bmatrix} \\ \begin{bmatrix} \frac{\partial f_1}{\partial a_1} & \frac{\partial f_1}{\partial a_2} & \cdots & \frac{\partial f_1}{\partial a_n} \\ \frac{\partial f_2}{\partial a_1} & \frac{\partial f_2}{\partial a_2} & \cdots & \frac{\partial f_2}{\partial a_n} \\ \vdots & \vdots & \ddots & \vdots \\ \frac{\partial f_l}{\partial a_1} & \frac{\partial f_l}{\partial a_2} & \cdots & \frac{\partial f_l}{\partial a_n} \end{bmatrix} \begin{Bmatrix} \frac{da_1}{dR_v} \\ \frac{da_2}{dR_v} \\ \vdots \\ \frac{da_n}{dR_v} \end{Bmatrix} = \begin{Bmatrix} \frac{\partial g_1}{\partial R_v} - \frac{\partial f_1}{\partial R_v} \\ \frac{\partial g_2}{\partial R_v} - \frac{\partial f_2}{\partial R_v} \\ \vdots \\ \frac{\partial g_l}{\partial R_v} - \frac{\partial f_l}{\partial R_v} \end{Bmatrix} \\ \begin{bmatrix} \frac{\partial f_1}{\partial a_1} & \frac{\partial f_1}{\partial a_2} & \cdots & \frac{\partial f_1}{\partial a_n} \\ \frac{\partial f_2}{\partial a_1} & \frac{\partial f_2}{\partial a_2} & \cdots & \frac{\partial f_2}{\partial a_n} \\ \vdots & \vdots & \ddots & \vdots \\ \frac{\partial f_l}{\partial a_1} & \frac{\partial f_l}{\partial a_2} & \cdots & \frac{\partial f_l}{\partial a_n} \end{bmatrix} \begin{Bmatrix} \frac{da_1}{dk} \\ \frac{da_2}{dk} \\ \vdots \\ \frac{da_n}{dk} \end{Bmatrix} = \begin{Bmatrix} \frac{\partial g_1}{\partial k} - \frac{\partial f_1}{\partial k} \\ \frac{\partial g_2}{\partial k} - \frac{\partial f_2}{\partial k} \\ \vdots \\ \frac{\partial g_l}{\partial k} - \frac{\partial f_l}{\partial k} \end{Bmatrix} \end{gathered} \tag{8-14}$$

Where each matrix for R_h, R_v and k is solved separately and the variables are defined as follows:

a. $Y_i, Y_i', Y_i'', Z_{t_i}, Z_{o_i}$ are replaced with the shape variables at step $i+1$, namely $Y_{i+1}, Y_{i+1}', Y_{i+1}'', Z_{t_{i+1}}, Z_{o_{i+1}}$, before integration, in equation (8-3).

b. R_h, R_v and k are substituted with their values at the previous step i, namely R_{h_i}, R_{v_i}, k_i.

c. The variables $\frac{\partial f_l}{\partial a_j}$ for $l = 1..n$ and $j = 1 \dots n$ are defined at $a_j = 0$ in matrix (8-14). This is due to the fact that, as has been mentioned in (a), the deflection variables substituted are the resultant of the a_j value that has been calculated as a function of R_{h_i}, R_{v_i}, k_i. Inserting R_{h_i}, R_{v_i}, k_i into the equations with the already deflected $Y_{i+1}, Y'_{i+1}, Y''_{i+1}, Z_{t_{i+1}}, Z_{o_{i+1}}$ renders the a_j values equal to zero.

As a result of solving matrixes (8-14) and (8-15), the variables $\Delta R_{h_{i+1}}, \Delta R_{v_{i+1}}, \Delta k_{i+1}$ from equation (8-10) can be extracted, and added to the forces R_{h_i}, R_{v_i}, k_i, and the forces $R_{h_{i+1}}, R_{v_{i+1}}, k_{i+1}$ defined. These forces should then, if applied to the needle, result in a tip deflection with small error compared to the actual tip deflections from experiments. To test this, the forces are then fed into stage C of the model and the new ΔY_t errors measured. If the error is very small (ϵ), then the forces at step $i+1$ are identified, if not the procedure is repeated with the new correction to the forces $\Delta {R_{h_{i+1}}}^k, \Delta {R_{v_{i+1}}}^k, \Delta {k_{i+1}}^k$, until $\Delta {Y_t}^k \rightarrow \epsilon$.

8.3. CONCLUSION

By completing stage D of the model, the methodology of the nonlinear mathematical modelling of the needle's deflection and identification of the forces acting on the needle in the nonlinear range have been completed. The initial step of the nonlinear model is the final step of the quasi-nonlinear model, as has been defined in chapter (6). As can be seen by looking at figure (8-1) and from the explanation of the methodology of the model, forward progressive modelling of the needle deflection under known forces can be completed in stages A and B of the model. From there on, the forces acting on the needle are identified in stages C and D. This means that, in order to be able to identify the forces acting on the needle at any step, the forward model must also be solved from its non-deflected state to complete the prerequisite stages A and B. The modelling progression ,and validation and verification of the model are presented in the next chapter.

9. EXPERIMENTAL PROCEDURE AND DATA ANALYSIS

9.1. INTRODUCTION

In the previous chapter, the modelling procedure needed for prediction of the needle deflection during its forward progression inside a soft material, and identification of the forces acting on the needle, was presented. In order to obtain the set of reference data and trajectories required to validate the needle insertion model presented in this work, experiments were conducted, where a two-part flexible needle was inserted into a soft material, having imposed a fixed offset between the parts. By embedding electromagnetic tracking sensors at the tip of the needle, the path of the tip of the needle during insertion was recorded, thus obtaining a set of data for each experiment, where the tip of the path is a function of the geometric and mechanical parameters of the needle. By inserting the tip path and the experimental variables into the reverse identification model for $Y_{t_{i_{(C_4)}}}$ as defined in 8.2.2, the forces acting on the needle can be extracted. These forces can then be fed into FEM software, such as ANSYS (ANSYS inc., Pennsylvania, USA), to replicate the deflection of the needle, and validate the identification model. The identified forces (or arbitrary forces) can also be fed into the forward model and FEM, allowing comparisons of the results of the two modelling methods.

The details of the experimental procedure are initially presented in this section. Having recorded the tip path during insertion from experiments, the data from these needs to be examined before input into the model, as will also be explained in this chapter.

9.2. EXPERIMENTAL SETUP

The experimental setup and needle design is provided by Alexander Todtheide as a part of his work on his masters thesis in the MIM lab (Tödtheide 2013). The general setup was previously designed by Seong Young ko and Luca Frasson (Frasson 2010) as previously shown in figure (9-1). A flexible needle prototype of 4 mm outer diameter, with a 20˚ bevel angle, is inserted through a guiding trocar into a gelatine sample, placed within a Plexiglas box with size $245\text{mm}x260\text{mm}x90\text{mm}$. The needle is pushed forward inside the tissue via actuators connected to its base, through holes on the sides of the box. As the needle is being inserted, the path generated by the tip is recorded through time by means of position sensors embedded into the needle tips. Details of the flexible needle, gelatine sample, sensors and the trocar is presented in the following sections.

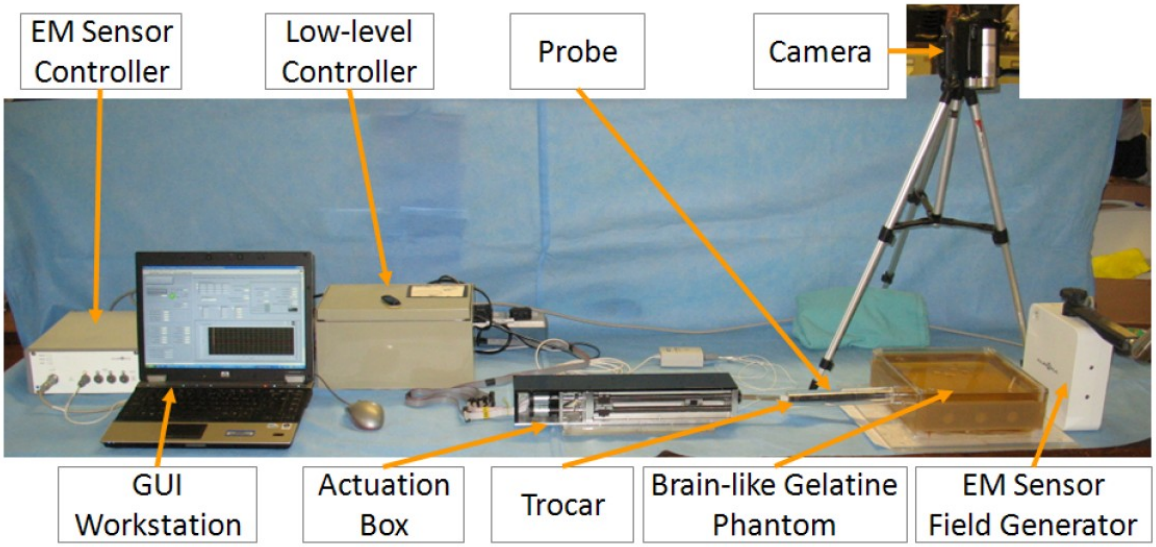

Figure 9-1 Overview of the experimental setup (as in (Frasson 2010))

9.2.1. Flexible Needle and Trocar Specifications

The flexible needle used in the experiments is of length 220 mm and 4 mm diameter. As shown in figure (9-2), the needle is comprised of a *male* and a *female* part, joined together by a specifically designed interlock geometry. The interlock geometry is designed such that, during the insertion, the male and female segments are allowed to slide with respect to each other, while preventing the forces acting on the needle base to cause them to detach. The geometry of the interlock is designed such as to reduce friction during sliding, which is aided by the use of wetting the segments with a water-based lubricant prior to assembly of the needle parts.

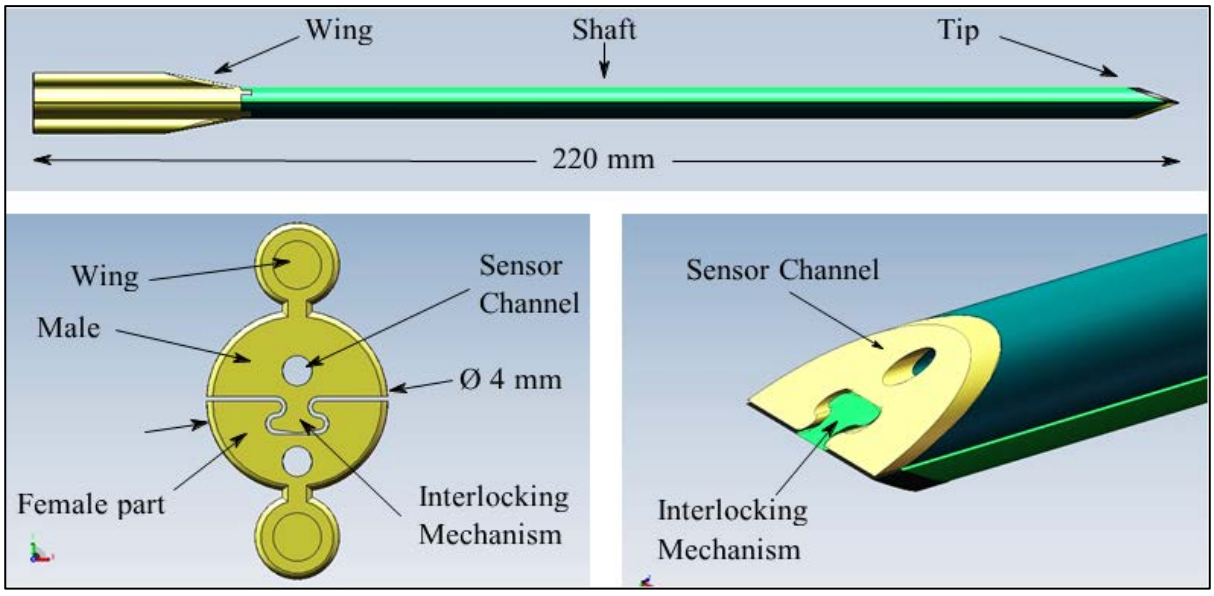

Figure 9-2 Geometry of the 4 mm flexible needle (as in (Tödtheide 2013))

The design of the base of the needle includes wings at the sides of the segments, which are connected via metal beams to electric actuators. These wings allow the transfer of the forward pushing forces from the actuator to the shaft of the flexible needle. As can be seen in figure (9-2), the end or tip of the needle is shaped into a bevel, allowing the "steering" of the needle as was described in chapter 1. To incorporate the sensors, a channel is designed inside the diameter of the needle, throughout its length between the base and the tip, with a diameter of 0.5mm. A LabVIEW-based graphical user interface is integrated into the setup to program trajectories, control performance and log control parameters. Two electromagnetic tracking sensors (Aurora, Northern Digital, Inc., 5DOF long-life sensors, with 1.1 mm diameter and root mean square accuracy of 0.9 mm/0.3◦) measure the needle's tip and offset position. For the female part, the sensor wire is glued to the channel. For the male, the sensor is glued to the tip of the segment, and the wire is loosely connected to the outer surface (Tödtheide 2013).

The needle materials are chosen as previously by Ko et al (Baena 2012). The base, tip, and the shaft of the needle are made of different materials; the tip and base material is Vero White (tensile strength of 50Mpa; hardness of 83 Shore Scale D; elongation at break 20%), which has relatively high hardness and stiffness, such as to allow the cutting and forward progression inside the gelatine sample. The shaft of the needle consists of the material Tango Black DM_9895 (tensile strength of 20MPa; hardness of 95 Shore Scale A; elongation at break of 30 %), which is a soft and flexible material, allowing needle bending and curving along defined trajectories. Due to its soft nature, in order to ensure the needle is straight prior to insertion into the gelatine, the needle is passed through a trocar before crossing the threshold of the Plexiglas box and entering the sample. This is also in order to avoid buckling of the needle segments with respect to each other, while they are pushed from the back, during insertion of the needle. The trocar is shown in Figure (9-3). It includes three channels, one for the flexible needle shaft, and two for the wings at the base, the design of which allows prevention of the twisting of the needle around its axis. The trocar is positioned between the actuator box and the Plexiglas gelatine box, and the outer diameter of the trocar rests against the wall of the Plexiglas box itself. The tip of the trocar touches the boundary wall of the gelatine through the holes in the side of the Plexiglas box, effectively connecting the actuators to the gelatine, the specifications of which are explained next.

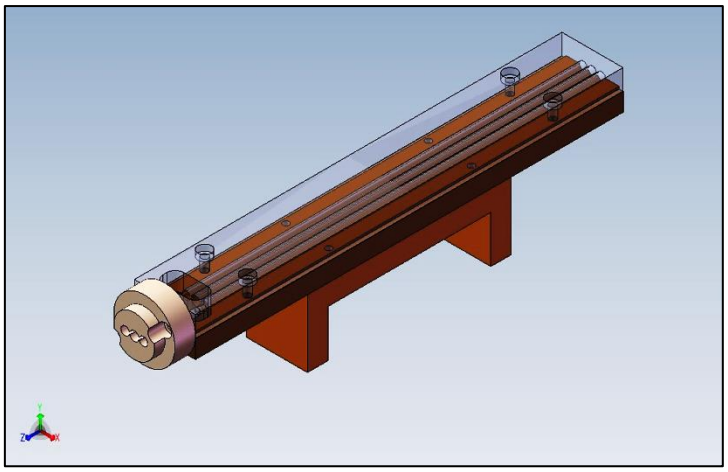

Figure 9-3. Trocar Geometry (Tödtheide 2013)

9.2.2. ACTUATORS AND GELATINE

A set of linear actuators are controlled via a compactRIO embedded controller, programmed in LabVIEW (National Instruments, Inc.). The actuators, the metal rods connecting them to the needle base, and other elements involved in creating the motion, are placed inside an "actuator box", as shown in figure (9-4). The box contains four motors connected to one lead screw each, with a ratio of 4.4:1. The motors specifications are: 6 Watt, direct current, stroke motion motors (A-max22; Maxon Inc., USA) controlled by Pulse Width Modulation (PWM) (Tödtheide 2013). The existence of four motors is due to the possible design of a needle comprised of four parts, while only the two upper motors were employed in the forward motion of the two-part needle studied in this work.. The linear movement from the lead screws is transferred to the wings of the needle by means of the metal rods (Tödtheide 2013). The rods exit the box through holes, shown as "A" in figure (9-4). The end of the actuator box is in contact with the base of the trocar, pushing the needle through the trocar during insertion into the gelatine.

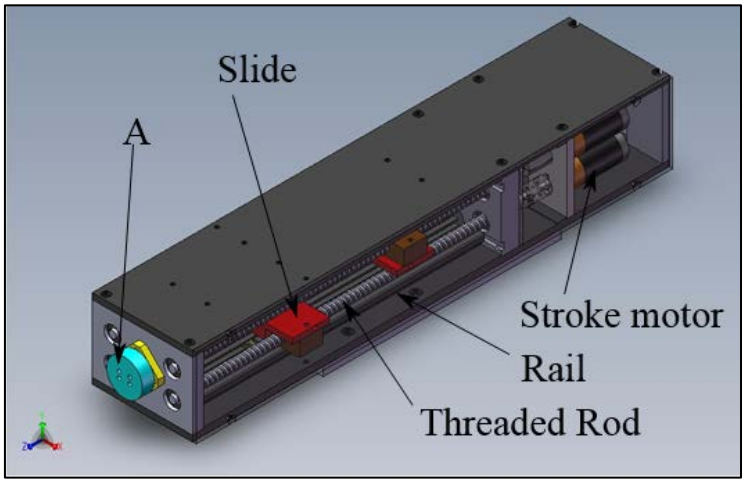

Figure 9-4 Actuator Box (as in (Tödtheide 2013))

Previously, (Frasson 2010), (Frasson, Ferroni et al. 2012) (Seong Young, Davies et al. 2010, Seong Young, Frasson et al. 2011) showed that gelatine at 21 degrees has similar mechanical properties to that of brain tissue, and as such, gelatine with similar percentage weight concentration is used here as the soft substrate for needle insertion experiments. The gelatine sample is comprised of 65g gelatine powder per one litre of boiled water. The solution is made by mixing 5 litres of water with gelatine powder (Dr. Oetker Gelatin), covering it with plastic film, and living it to set in a 24.5 cm × 26 cm × 90 cm Plexiglas box in a controlled room temperature for 18 hours. This results in homogenous a temperature distribution for the gelatine, as the needle steering performance has shown to be sensitive to temperature (Tödtheide 2013). The two opposite walls of the box contain three holes each, allowing multiple experiments on one gelatine sample to be carried out. In the next section, the experimental process is defined.

9.3. Insertion Procedure

As mentioned in chapter 2, the insertion process is completed in 4 stages, allowing control and observation of each part of motion. This also allows separation of the part of the motion being modelled, minimising complications and inaccuracies associated with assumptions regarding the motion of the needle. As the needle is pushed forward while the sensors at the tip are used to record its path in separate files for analysis. The four stages of motion are: pre-insertion and puncture, Part A: forward insertion without offset, Part B: offset creation, and Part C: forward insertion with offset. Each part is explained as follows.

9.3.1. Pre-insertion and Puncture

Prior to insertion, the male and female segments of the needle are lubricated and assembled. The needle is checked to be straight and un-deflected from previous experiments. The needle is then connected to the actuator box and passed through the trocar, with its tip resting at the edge of the gelatine wall through one of the three holes on the wall of the Plexiglas box. It is then manually pushed forward such that its tip punctures the wall, and rests just within the sample. This segment of insertion is not recorded via the sensors and the actuators are not employed in the motion yet. It is assumed during the modelling process that, at the end of this stage, the two parts of the needle should remain straight and un-deflected.

9.3.2. Part A: Forward Insertion Without Offset

At the beginning of this stage, the needle tip is un-deflected and resting inside the gelatine sample. At this point, both the actuators are simultaneously employed and both segments of

needle are pushed forward 15 mm inside the gelatine. The actuator is then stopped and the tip path data of this stage of motion is stored separately. Based on the assumption that the offset causes the deflection of the needle, at the end of this stage, the needle is symmetric and the deflection should be negligible, though the recorded path of the tip of the needle incorporates any deflections of the tip, such that it can be accounted for during post processing of the data.

9.3.3. PART B: OFFSET CREATION

At this stage of motion, the female segment of the needle is kept stationary while the male is pushed forward in the amount of a predetermined amount of offset. Here, we assume that the forward moving segment will deflect as a function of its bevel tip and offset, as will be demonstrated in the results later on.

9.3.4. PART C: FORWARD INSERTION WITH OFFSET

At this stage, both segments of the needle are pushed forward 60 mm inside the gelatine, via both actuators. The insertion speed is 1 $^{mm}/_{s}$ for all three stages of movement, allowing the implications of rate-dependent material parameters for both the needle and the sample to be disregarded. Insertion tests with arbitrarily defined constant steering offsets of $22\ \text{mm}, 33\ \text{mm}$ and 44mm were performed. To avoid any overlapping of subsequent needle paths inside the gelatine, six experiments were conducted (through three holes on two sides of the box), as shown in figure (9-5). Each experiment was performed ten times, the final results of which are not presented here. In order to be able to substitute the tip path data from these experiments in the model, the data must be statistically analysed, and parts A, B and C "sewn" together. This is presented in the following section.

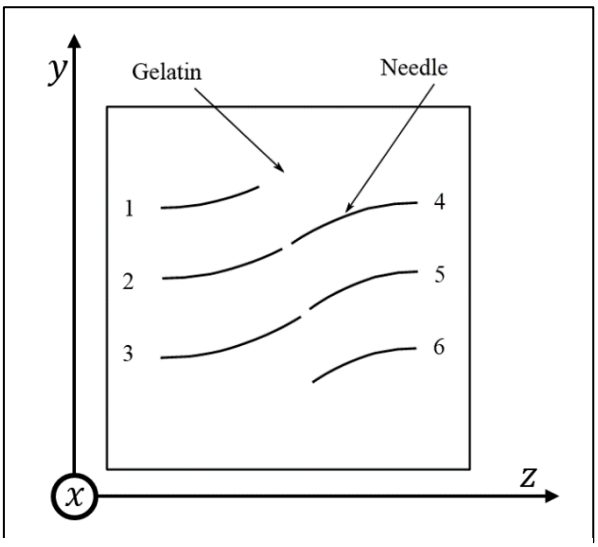

Figure 9-5 Gelatin and needle insertion setup, top view. For each gelatine box, 6 experiments are performed. The electromagnetic sensor is calibrated such that its local x,y,z coordinates are defined as shown in the image.

9.4. DATA ANALYSIS OF PARTS A, B AND C OF THE MODEL

As shown in figure (9-5), the sensors at the tip of the needle are calibrated such that the needle's insertion axis is recorded as z, the deflection as y, and the off-plane deflection as x. As the needle assembly and trocar design are such that the twist of the needle is minimised, and the needle geometry has no off-plane asymmetry, it is expected that the needle will not deflect off-plane significantly. The off-plane deflection and best-plane of fit of the needle's tip path is recorded nonetheless, during analysis, and will be shortly explained. The first part of the data analysis is performed for stage A, and is explained below, with the steps of the process explained with images from one experiment with a 22mm offset.

Initially, the data from the tip are sorted such as to be in ascending order for the z coordinate, as insertion depbth should be increasing during the insertion process. This is shown in figure (9-6) for one experiment with offset equal to 22mm, where the z coordinates are plotted against their ascending number of order (row) in the data matrix.

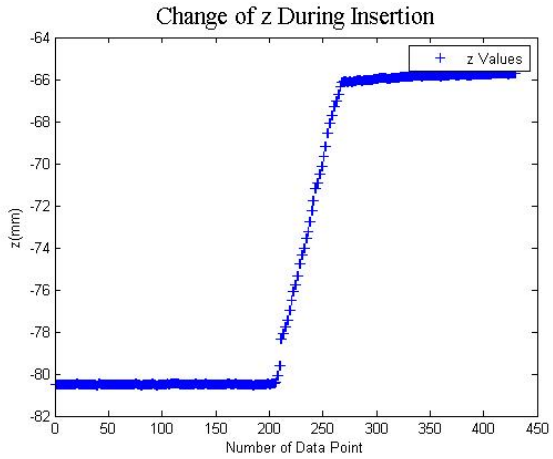

Figure 9-6. Plot of z against number of data point in ascending order for Stage A

It can be seen from the graph, that the initial points, between 0-200, and the final recorded points, between 260-450 of insertion, all have z values very close to each other, compared to the data points between 200-260. Also, the average Δz during the motion of needle for the points between 200-250 is needed. Δz versus z is plotted and the boundary for Δz shown in figure (9-7).

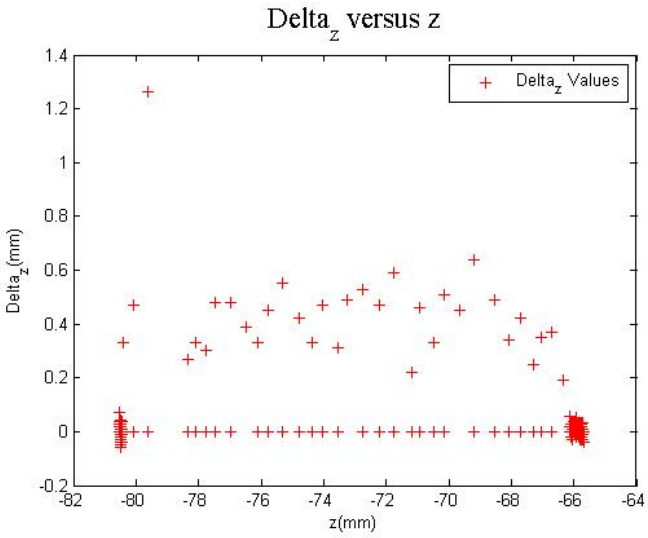

Figure 9-7. Plot of delta_z versus z for Stage A of motion

It can be seen in figure (9-7) that the low threshold for Δz for this experiment is about 0.2. Hence, the data must be filtered such that consecutive data points for which $\Delta z < 0.1$ (for extra caution) are eliminated, and replaced with one point with the average value of the repeated points. This is shown in figure (9-8), where y is plotted against z, and the unfiltered data are shown in blue.

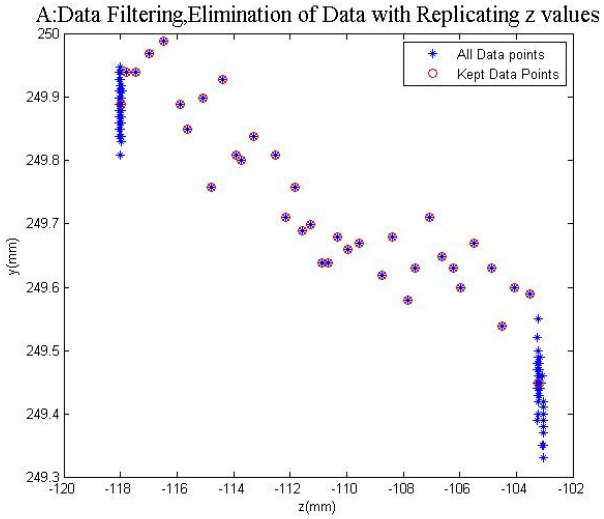

Figure 9-8. Plot of Filtered and Unfiltered Data Points

The same data processing is conducted for stages B and C of the insertion. Having cleaned the data for both sensors (leading and lagging segments) for stages A, B and C, the three data sets are compiled in one data set for the whole insertion process. It must be mentioned that the row number of the data point at which stage C of motion begins is noted, as the model developed in this work is valid for stage C of motion, and must be adjusted if modelling motions for stages

A and B. The data for the complete insertion process is then projected to the plane of best fit for each segment, and both leading and lagging segments transferred to the same initial point of motion. This is shown for the 22mm experiment in figure (9-9).

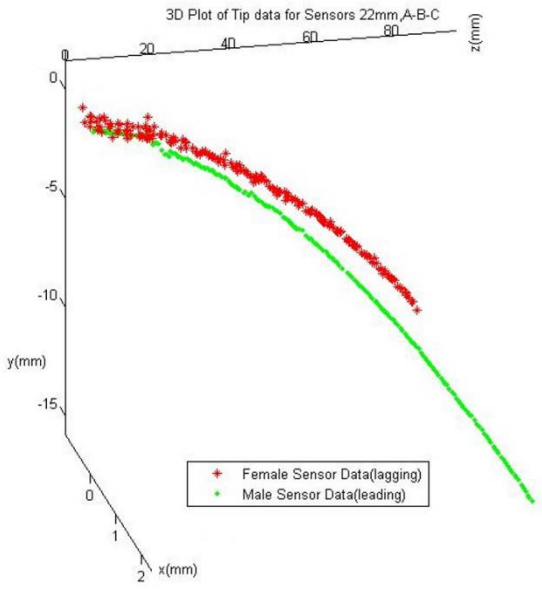

Figure 9-9. 3D plot of x-y-z data for 22mm insertion, male and female segments, stages A-B-C

Figure (9-9) shows that, for the lagging segment, the data in stage A of motion is less smooth and includes more repeated points (which is not investigated further, as the lagging segment's tip path is not an input to the developed model). It must be noted that the data for stages A, B and C are filtered separately and the standard deviation, variance and confidence interval for each data set calculated separately.

Having the projected data from the whole motion, the data points corresponding to stage C of the insertion are used for $Y_{ti_{(C_4)}}$, as defined in section 8.2.2. As defined in chapter 8, other inputs needed from the insertion to be inputted into the reverse model are the geometrical and mechanical variables of the needle, including the flexural modulus of the needle material. In order to obtain the modulus, three point bending test experiments on the needle were conducted, the summary and results of which are presented below.

9.5. Experimental Determination of Young's Modulus: Three Point Bending Test

The three point bending tests were conducted on two, 4 mm diameter, 120 mm long cylindrical specimens of the needle material (TangoBlackPlus, 95 Shore A, DM9895, Objet inc.) in order for its flexural modulus to be computed accurately. The schematic in figure 9-10a represents the flexural test setup which utilised a 100 N Instron load cell, with a crosshead velocity of 9-10 mm/min. The flexural results are given in figure (9-10.b):

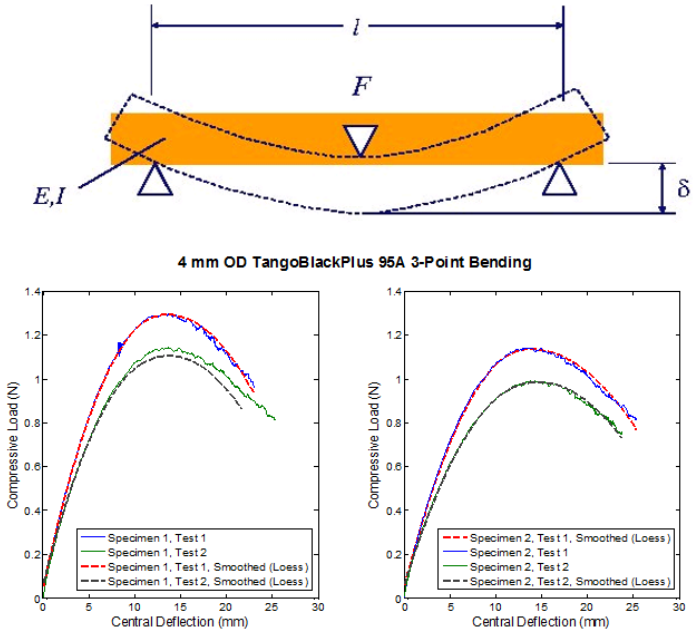

Figure 9-10 a. Experimental setup for three point bending, and **b**. results of flexural three point tests on specimen of the needle material.

In order to calculate the stress strain curve, the load versus deflection profile for each specimen was measured off the graphs in fig. (9-10.b) and inputted into equation (9-1)(Grote 2007):

$$E_f = \frac{p.l^3}{48.\delta I} \tag{9-1}$$

Where E_f is the flexural modulus, p is the force acting on the middle of the specimen, l is the length of the specimen, δ is the deflection of the middle point and I is the moment of area of the cross section. Solving for deflection on both specimens and calculating their average, an estimate of E_f for each sample was computed. The flexural strain can be calculated as:

$$\epsilon_f = \frac{6d\delta}{l^2} \tag{9-2}$$

Solving for deflection on both specimens and calculating their average, an estimate of E_f for each sample was computed. The flexural strain can be calculated as:

$$E_f = \frac{\sigma_f}{\varepsilon_f} \tag{9-3}$$

The resulting stress strain curve can be seen in figure 9-12. Table (9-1) lists the flexural modulus for the needle at different strain rates, and the average flexural modulus employed for different strain ranges are presented in Table (9-2). The flexural modulus chosen for the validation of the model is 56Mpa, though, for higher accuracy, the strain should be measured for the needle deflection and the corresponding strain substituted accordingly.

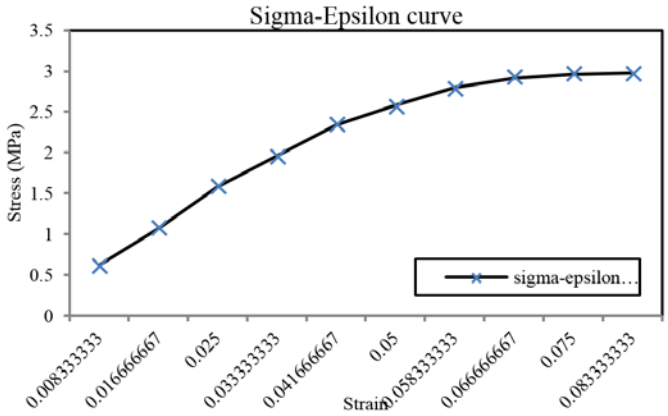

Figure 9-11. Stress Strain curve generated by flexural tests on the needle material

Table 9-1 Flexural modulus vs Strain Range

ϵ_f	*Average* $E_f(Mpa)$
0.008333	74.52229
0.016667	62.34076
0.025	58.99682
0.033333	55.17516
0.041667	51.87898
0.05	48.24841
0.058333	44.42675
0.066667	41.11266
0.075	37.42038
0.083333	34.10828

Table 9-2 Flexural Modulus vs Strain Range

Epsilon Range	$E_f(Mpa)$
0-2.5%	65.2
2.5-5%	40.13
5-7.5%	23.61

9.6. CONCLUSION

In the previous chapter, the methodology of solving the nonlinear model of the needle's deflection during insertion into a soft substrate was developed. In this chapter, in order to test the accuracy of the model, an experimental setup was described, where the needle with three offsets of 22mm, 33mm and 44mm were inserted into a gelatine substrate, and its tip path during insertion recorded. As the model is developed for forward insertion with a fixed offset, in order to extract the input variable into the model $Y_{t_{i_{(C_4)}}}$, the data was filtered and processed. In addition, the flexural modulus of the needle E must be extracted, and as such three point bending experiments were conducted on the needle material. Having the flexural modulus (E_f), the tip path data($Y_{t_{i_{(C_4)}}}$) and the geometrical parameters of the needle, these can be inputted into the model, identifying the forces acting on the needle during insertion. These forces can then be verified by inserting them into the forward model and FEM, and comparing the resulting deflection with that obtained during experiments. This is further explained in the following chapter.

10. RESULTS AND DISCUSSIONS

10.1. INTRODUCTION

Previously in chapter 8, the forward and reverse nonlinear model of the needle's deflection during insertion was developed, and the input variables for the forward and reverse force identification were defined. In chapter 9, in order to verify and validate the model, experiments were described in which the input variable $Y_{t_{i_{(C_4)}}}$ (tip path) was collected from experiments. By inserting the experimental tip path into the reverse force identification model, the forces acting on the needle during insertion will be determined. These forces can then be inserted into the forward progressive model, as well as FEM, for comparison and subsequent validation of the resulting tip path deflection. Arbitrary forces can also be inserted into the forward progressive model and a FEM simulation of the needle, and the results compared for accuracy of the nonlinear modelling of the needle.

In this chapter, initially, the proposed method and developed code is verified against ANSYS. It should be noted that only forward solutions with constant needle length will be used for verification purposes, as none of the available commercial software can solve any progressive, length changing, needle insertion. Consequently, the results of investigations regarding the identification of the loads acting on the needle during insertion, using experimental results of chapter 9, will be presented here. It will be endeavoured to discuss the trends as well as other details, which can be deduced from the identification process.

10.2. QUASI NON-LINEAR AND NONLINEAR VERIFICATION: ANSYS

In this section, initially the results of the forward solution of the proposed methods for both quasi-nonlinear and nonlinear needle behaviour, using equations (5-25) and (7-17) respectively, are benchmarked against results of ANSYS under the same conditions. A cantilever beam is modelled in ANSYS and the model codenamed “nlbeam”. The developed mathematical model, as explained in chapter 8, is solved iteratively, and as such, initially the quasi-nonlinear model (5-25) is employed. When the needle enters into the nonlinear domain (large deflection), the model automatically switches to the nonlinear solver (equation 7-17).

For the FE model, the ANSYS BEAM188 element was used for modelling. The input variables into both models are as follows:

a) Rh = Horizontal tip force, always in global Z direction, Positive in compressive sense [N]

b) Rv = Vertical tip force, always in global Y direction, Positive in $+Y$ direction [N]

c) k = Soft medium stiffness per unit length, [N/m2]

d) L = Total length of the needle [m]

e) $L1$ = length of the needle at offset point [m]

It should be mentioned that there are assumptions made in like-to-like modelling and comparison of the results between ANSYS and nlbeam, which are as follows:

a- As ANSYS V.13 lacks the capability of defining a distributed spring for BEAM188 (and beam elements in general), the equivalent springs were defined on the nodes of the beam elements. For this purpose, k was multiplied by each individual beam element length, and the obtained value was divided by 2, and each half was applied to one of the nodes of the element.

b- The slope at the tip being less than 25^o was arbitrarily taken as the linearity criterion.

c- The ranges for the forces and distributed stiffness considered in the benchmarking was taken to be the average values identified through using the nlbeam identification capabilities, as is explained in section 10.3.

10.2.1. QUASI NON-LINEAR BENCHMARKING VS ANSYS

In this section, the performance of the code 'nlbeam' developed based on the quasi non-linear forward solution in equation (5-25) is examined and benchmarked against the ANSYS nonlinear solution. It is worth mentioning that, for cases where axial load Rh is involved along with Rv, ANSYS will use a full nonlinear solution and no linear solution option is available for this case. As mentioned before, this is due to the fact that, when Rv and Rh are both present, behaviour of the needle will not follow the superposition principle and hence, at best, it can be said its behaviour is quasi-nonlinear. The setup of the ANSYS model is shown in figure (10-1).

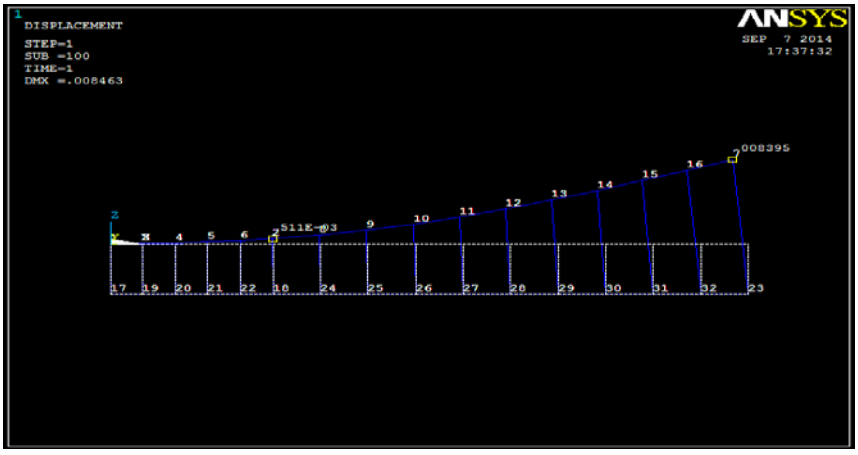

Figure 10-1 Figure of beam modelled in ANSYS for comparison of the accuracy of the needle deflection for developed nonlinear model

As was mentioned, the needle is modelled using beam elements and the bevel tip is neglected, as is in the mathematical model. The offsets of 22 and 33 mm were inputted into the quasi-nonlinear model, while the offset of 44mm was omitted so as to avoid entering the large deflection domain at this stage. The boundary of the quasi-nonlinear domain is defined as deflection up to 25 degrees at the tip of the needle max. Also, to allow comparison, for quasi-nonlinear nlbeam solving, the forces are not rotated during the needle deflection, allowing a like-to-like comparison with ANSYS, which does not rotate concentrated forces throughout the deflection.

The results for 7 case studies are presented in the tables below. The first 3 are simulations, where only Rh and Rv, only Rv, and Rv and k are acting on the needle, and the last four include all three forces acting simultaneously. The ranges are chosen within the results of the identified forces from experiments, which will be explained shortly.

The deflections of the tip of the needle and the offset in the two models are compared in each case. For each case the first column of the table indicates which model is being used. The second column: total length of the needle $L\,(m)$, third column: offset of the needle, fourth column: deflection for the tip $Yt(m)$, fifth column: deflection of the point of offset $YL1(m)$, sixth and seventh columns: error of the two deflections $Yt(m)$ and $YL1(m)$ for the ANSYS and nlbeam models, respectively.

Case 1						
Rh	***Rv***		***k***			
0.3	-0.085605		0			
sol type	***L (m)***	***Offset (m)***	***Yt(m)***	***YL1(m)***	***error Yt%***	***error YL1%***
nlbeam	0.033212	0.022	-0.002597	-0.000294	3.14	-0.51
ANSYS	0.033212	0.022	-0.002518	-0.000295		
nlbeam	0.037553	0.022	-0.003731	-0.000662	3.09	0.21
ANSYS	0.037553	0.022	-0.003619	-0.000660		

Table 10-1. Quasi Nonlinear ANSYS vs Nlbeam, Case 1

Case 2		
Rh	***Rv***	***k***
0	-0.085605	0

sol type	***L (m)***	***Offset (m)***	***Yt(m)***	***YL1(m)***	***error Yt%***	***error YL1%***
nlbeam	0.033212	0.022	-0.000917	-0.000225	-6.60	-0.56
ANSYS	0.033212	0.022	-0.000982	-0.000227		

Table 10-2. Quasi Nonlinear ANSYS vs Nlbeam, Case 2

Case 3		
Rh	***Rv***	***k***
0	-0.085605	3000

sol type	***L (m)***	***Offset (m)***	***Yt(m)***	***YL1(m)***	***error Yt%***	***errorYL1%***
nlbeam	0.033212	0.022	-0.000325	-0.000142	-7.14	-5.36
ANSYS	0.033212	0.022	-0.000350	-0.000150		

Table 10-3. Quasi Nonlinear ANSYS vs Nlbeam, Case 3

Case 4		
Rh	***Rv***	***k***
0.3	-0.085605	3000

sol type	***L (m)***	***Offset (m)***	***Yt(m)***	***YL1(m)***	***error Yt%***	***errorYL1%***
nlbeam	0.033212	0.022	-0.001457	-0.000166	10.3	9.69
ANSYS	0.033212	0.022	-0.001321	-0.000151		

Table 10-4. Quasi Nonlinear ANSYS vs Nlbeam, Case 4

Case 5		
Rh	***Rv***	***K***
0.3	0.1	2500

sol type	***L (m)***	***Offset (m)***	***Yt(m)***	***YL1(m)***	***error Yt%***	***errorYL1%***
nlbeam	0.044302	0.033	0.003265	0.000142	6.80	-12.26
ANSYS	0.044302	0.033	0.003057	0.000162		

Table 10-5. Quasi Nonlinear ANSYS vs Nlbeam, Case 5

Case 6						
Rh	***Rv***		***K***			
0.1	0.1		500			
sol type	***L (m)***	***Offset (m)***	***Yt(m)***	***YL1(m)***	***error Yt%***	***errorYL1%***
nlbeam	0.044302	0.033	0.005276	0.000308	2.53	-1.85
ANSYS	0.044302	0.033	0.005146	0.000314		

Table 10-6. Quasi Nonlinear ANSYS vs Nlbeam, Case 6

Case 7						
Rh	***Rv***		***K***			
0.1	0.2		500			
sol type	***L (m)***	***Offset (m)***	***Yt(m)***	***YL1(m)***	***error Yt%***	***errorYL1%***
nlbeam	0.044302	0.033	0.010550	0.000616	-3.08	-8.95
ANSYS	0.044302	0.033	0.010885	0.000677		

Table 10-7. Quasi Nonlinear ANSYS vs Nlbeam, Case 7

It should be noted that, for equal lengths of the needle and equal offset, the error values are higher when k is present in the model, compared to similar cases where k was eliminated, as is seen by comparing errors in case 1 to case 4, and case 2 to case 3. This is due to the fact that ANSYS does not allow application of a distributed spring on the beam elements and hence, the equivalent springs were applied on the nodes, creating discrepancies between the two models.

10.2.2. NON-LINEAR BENCHMARKING VS ANSYS

In this section, the performance of the nonlinear forward solution in equation (7-17) is examined and benchmarked against the ANSYS nonlinear solution. Here, both solution techniques are nonlinear. 5 case studies are presented for comparison, the first is similar to the first case in quasi-nonlinear benchmarking described in section 10.2.1. This was intended to show the competency of nonlinear code to solve the linear range problems with higher accuracy.

It is also worth mentioning that, for the nonlinear case, besides comparison of Yt and $YL1$ with the ANSYS solution, it is also very important to compare the length of the needle at the

end of each step Zt (sixth column of the tables) to check the accuracy and performance of the end-shortening effect formulation proposed in equation (6-10 to 6-12).

Nonlinear Case 1						
Rh	***Rv***		***K***			
0	0.1		0			
sol type	***L (m)***	***Offset (m)***	***Yt(m)***	***YL1(m)***	***error Yt%***	***errorYL1%***
nlbeam	0.044302	0.033	0.000582	0.000037	-0.22	-0.54
ANSYS	0.044302	0.033	0.000583	0.000037		

Table 10-8 Nonlinear ANSYS vs Nlbeam, Case 1

Nonlinear Case 2								
Rh	***Rv***		***K***					
0.2	0.1		0					
sol type	***L (m)***	***Offset (m)***	***Yt(m)***	***YL1(m)***	***error Yt%***	***errorYL1%***	***Zt***	***Zt error%***
nlbeam	0.044302	0.033	0.007844	0.000465	-6.56	-9.00	0.043033	-0.45
ANSYS	0.044302	0.033	0.008395	0.000511			0.043229	

Table 10-9 Nonlinear ANSYS vs Nlbeam, Case 2

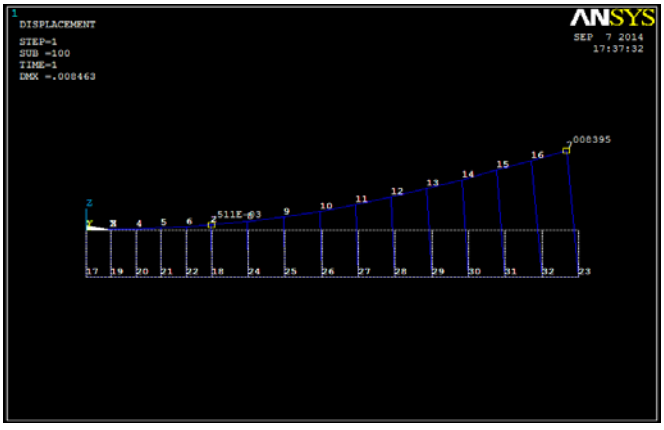

Figure 10-3 Nonlinear ANSYS model:Case 2

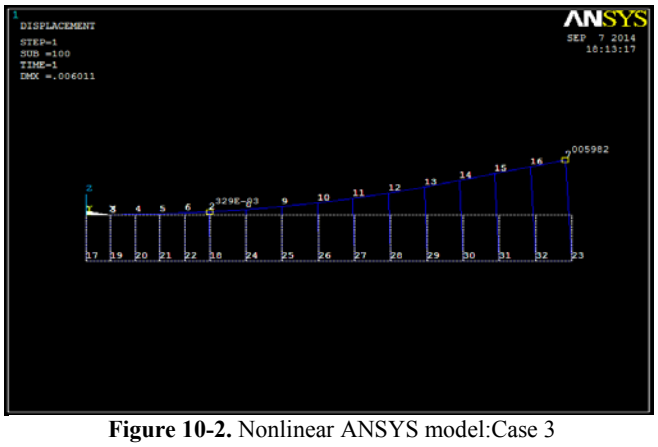

Figure 10-2. Nonlinear ANSYS model:Case 3

Nonlinear Case 3								
Rh	***Rv***		***K***					
0.4	0.05		500					
sol type	***L (m)***	***Offset (m)***	***Yt(m)***	***YL1(m)***	***error Yt%***	***errorYL1%***	***Zt***	***Zt error%***
nlbeam	0.044302	0.033	0.005226	0.000294	-12.64	-10.60	0.043896	0.41
ANSYS	0.044302	0.033	0.005982	0.000329			0.043716	

Table 10-10 Nonlinear ANSYS vs Nlbeam, Case 3

Nonlinear Case 4								
Rh	***Rv***		***K***					
0.1	0.1		500					
sol type	***L (m)***	***Offset (m)***	***Yt(m)***	***YL1(m)***	***error Yt%***	***errorYL1%***	***Zt***	***Zt error%***
nlbeam	0.044302	0.033	0.005382	0.000361	-6.51	3.42	0.043849	0.11
ANSYS	0.044302	0.033	0.005756	0.000349			0.043801	

Table 10-11 Nonlinear ANSYS vs Nlbeam, Case 4

Nonlinear Case 5								
Rh	***Rv***		***K***					
0.2	0.1		500					
sol type	***L (m)***	***Offset (m)***	***Yt(m)***	***YL1(m)***	***error Yt%***	***errorYL1%***	***Zt***	***Zt error%***
nlbeam	0.044302	0.033	0.006298	0.000404	-8.52	-0.56	0.043647	0.17
ANSYS	0.044302	0.033	0.006884	0.000407			0.043572	

Table 10-12 Nonlinear ANSYS vs Nlbeam, Case 5

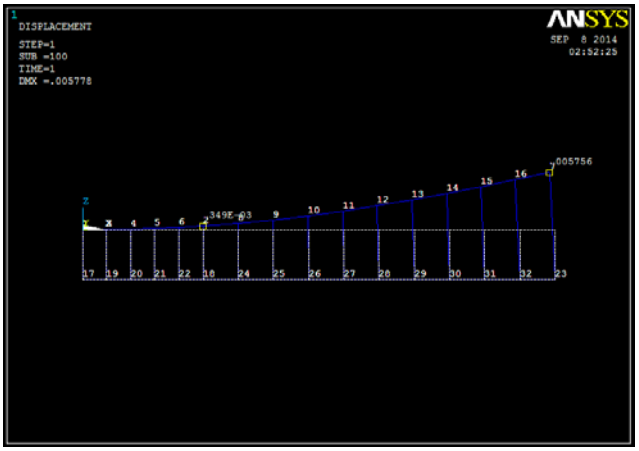

Figure 10-5 Nonlnear ANSYS model: Case 4

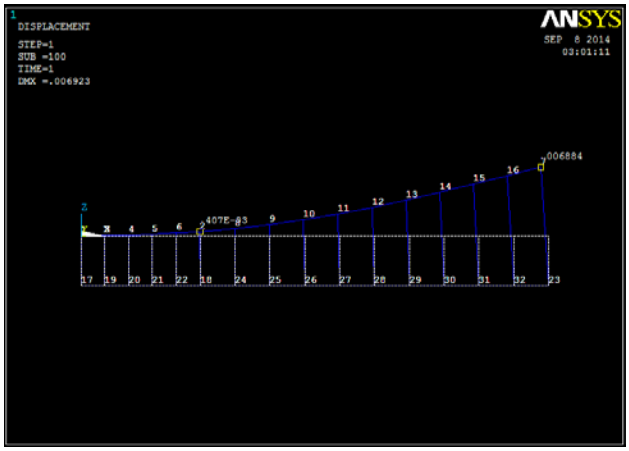

Figure 10-4. Nonlinear ANSYS model: Case 5

As is evident from benchmarking, approximately 10% error exists between ANSYS and the results from equation (7-17). As mentioned before, part of this error is due to the problem associated with modelling of the distributed spring in ANSYS. The nonlinear case 1, where the forces acting on the needle are similar to the quasi-nonlinear case 2, has 0.22% error compared to 6.6% error of the quasi nonlinear model. This can be due to the fact that both ANSYS and nlbeam are incorporating nonlinear deflections in this case. The maximum error for Zt is 0.45% for the nonlinear case 2, showing good accuracy for the end-shortening model incorporated into nlbeam. Comparison of nonlinear cases 1 and 2 shows that, for equal length and equal offset, the inclusion of Rh makes a difference in the errors, increasing them from -0.22% for Yt and -0.54% for $YL1$ for $Rh = 0$ to -6.56% and -9% for $Rh = 0.2$, and equal Rv and k. This can be due to the fact that the rotation of the tip force Rh is expected to make a significant difference to the results, and, as has been mentioned previously, ANSYS does not include the rotation of the forces, while the nonlinear nlbeam rotates the forces acting on the tip. In the next section, the quasi-nonlinear identification model is compared against experiments and the results shown.

10.3. Force Identification Results

For one set of experimental data measured for a needle with 22, 33 and 44 mm offset, the results of identification for quasi non-linear and nonlinear processes are first presented for each offset length, and then the common trends are discussed. Before presenting the results, it is necessary to clarify and define some common characteristics of the presentation, as follows:

a- The main criteria used for the identification of the loads in the quasi non-linear process, based on equation (5-32), is to find the set of loads, k, Rh and Rv for which the error between $\{Y_{tc}\}$ calculated from equation (5-30) and the corresponding, measured, $\{Y_{tx}\}$from the experiments is minimum. Obviously, this minimum value will depend on the number of insertion points, m, used in equation (5-32).

b- As explained in section 5.3, matrix $[B]_{mx1}$in equation (5-32) is a function of Rh and k and since these parameters are unknown, it is needed to consider a range of values for Rh and k and create a solution space for equation (5-32). Obviously, the Rv found for each pair of (Rh, k) is the least squares solution. Now, amongst all of the least squares solutions, the one with the minimum (least squares error) will be selected as the one most likely to be correct. This is found by searching the least squares error space

drawn against (Rh, k), as shown in figures 10-6 to 10-10 for one experiment with a 22mm offset.

c- The range of values for Rh and k mentioned in 'b' above are determined by choosing (0,0) as a lower bound. The upper bound will be selected such that the buckling instability boundary is crossed.

d- The error percentage used as the convergence criteria for a nonlinear identification process is calculated in equation 1, where Y_{tx} is the experimental tip deflection, and Y_{tc} the calculated (modelled) tip deflection:

$$\varepsilon\% = RMS\left(\frac{|\{Y_{tx}\} - \{Y_{tc}\}|_2}{|Y_{tx}|_2}\right).100 \qquad (10\text{-}1)$$

e- For the nonlinear process, as indicated in equation (8-11), $m \geq 3$ insertion data are used for each identification step. For each of the identification steps, the error index defined in equation (10-1) will be used to assess the quality of $\{Y_{tc}\}$ defined in step 'c' of section 8.2.2. If ε < 1%, then the identified loads resulting in $\{Y_{tc}\}$ will be considered to have converged to a minimum.

It should be noted that many sets of results are generated for each offset length. In addition to the results presented here, the starting point for nonlinear solving, number of points chosen for each nonlinear and quasi-nonlinear step, and the least norm solution was also calculated as part of a sensitivity study. The discussions and conclusions presented here are drawn from all of the case studies undertaken. However, for the sake of briefness, only one set of results will be presented for each offset length.

10.3.1. NEEDLE WITH 22MM OFFSET, CASE STUDY C22-2

For this case, the following parameters are used:

a) m = No. of insertion steps used in each step of quasi non-linear identification (equation (5-32)) = 15. As was shown in chapter 9, the dz between subsequent tip deflections is between 0.2 to 0.6 mm. As such, if an approximate average of 0.4mm is assumed for dz, 15 insertion points will result in a 6mm insertion, for which the forces acting on the needle are considered to be constant for identification. This would not violate the quasi non-linear solution assumption significantly, as in the case of the 22mm offset, the needle is short enough to have its 15 insertion steps within a linear range. The choice of 15 points is due to the fact that the first 10 points of measured

insertion data were fluctuating and hence 15 points are used to eliminate the effects of noise and oscillations in input data.

b) m = No. of insertion steps used in each step of nonlinear identification (equation (8-11)) = 5, starting insertion step for nonlinear solution = 3. As explained above, this amounts to approximately a 2mm insertion, for which the forces acting on the needle are considered to be constant for identification. This is a small range of insertion and can be decreased if higher measuring accuracy is present, though for the model developed, a minimum of 3 points is needed. The 5 points can include overlapping points for higher continuity, as is shown in the results further on.

c) k, Rh and Rv from quasi non-linear identification = 3700 N/m2, 0.8 N, -0.1093 N

d) Quasi non-linear identification Error% (least square) = 0.66 %

In this case study, similar values to those of another case study 22mm are used for k and Rh. However, instead of entering the nonlinear identification process from insertion point 16, here the nonlinear process will be started from insertion step 3. The reason for this is to try to eliminate any errors originating from the assumption of linear behaviour for insertion steps beyond 2. In the same respect, the number of insertion steps used in the nonlinear identification process, equation (8-11), is reduced to 5.

It should be noted that, using $k = 3700\ N/m^2$ and $Rh = 0.8\ N$, which represent the MIN (Errors% of the least squares solutions) from images 6 to 10 for quasi non-linear solution with 15 insertion steps before entering nonlinear solver, will not necessarily be the MIN (Errors% of least squares solutions) for the case where the nonlinear solver is employed after 2 insertion steps, as is presented in this section. This is evident from the identified Rv values from the sensitivity study results and C22-2, where the nonlinear solver was started from the second step, as the two values are slightly different. This is shown in the following sections, where initially the quasi-nonlinear, and then the nonlinear results are presented.

10.3.1.1. QUASI NONLINEAR FORCE IDENTIFICATION (C22-2)

As was explained in section 5.3, in equation (5-32), $[B]^{+}_{1xm}$ indicates the pseudo inverse of [B]. Now, $[B]^{+}_{1xm}$ cannot be calculated, as it contains the unknown values Rh and k. Hence, in order to define Rh and k from $[B]^{+}_{1xm}$, a solution space was defined such that:

4- The minimum least squares error solution of equation (5-32) must be sought, i.e. the set of (Rh, Rv, k) must be found that renders the least squares error a minimum.

5- The instability (buckling) limit of the needle-elastic-substrate system must be observed, i.e. matrix G of equation (5-32) must be positive definite. This will be tested by inspecting the smallest SVD of the G matrix.
6- The physical fact that Rh cannot become negative (i.e. the substrate cannot pull on the needle tip) must be observed.

The first condition is met by first defining a solution space for equation (5-32) for a reasonable range of Rh and k values, then keeping one constant and iterating another, thus identifying the corresponding Rv value and considering the RMSE of the solution to equation (5-32). This is shown in figure 10-6 for case study C22-2, for Rh between 0--1.6N and k between 0--6000 N/m^2.

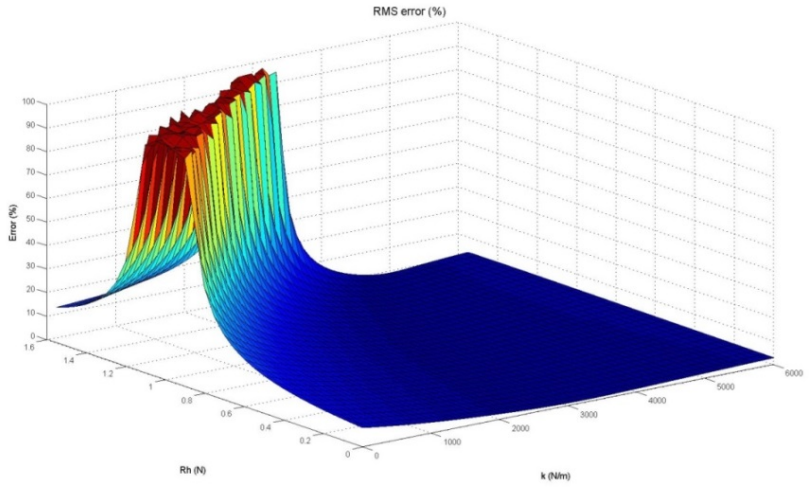

Figure 10-6 3D plot of the Error% space of least square solution of (5-32) versus Rh and k, C22-2

Within the blue area in figure (10-6), the RMS is close to 1, and the coordinates of the possible solution points where the RMS is close to 1 are shown in the top view of the solution space shown in figure (10-7) for C22-2. The lowest RMS is 0.9785, at point $X, Y, Z =$ 3700,0.8,0.9785.

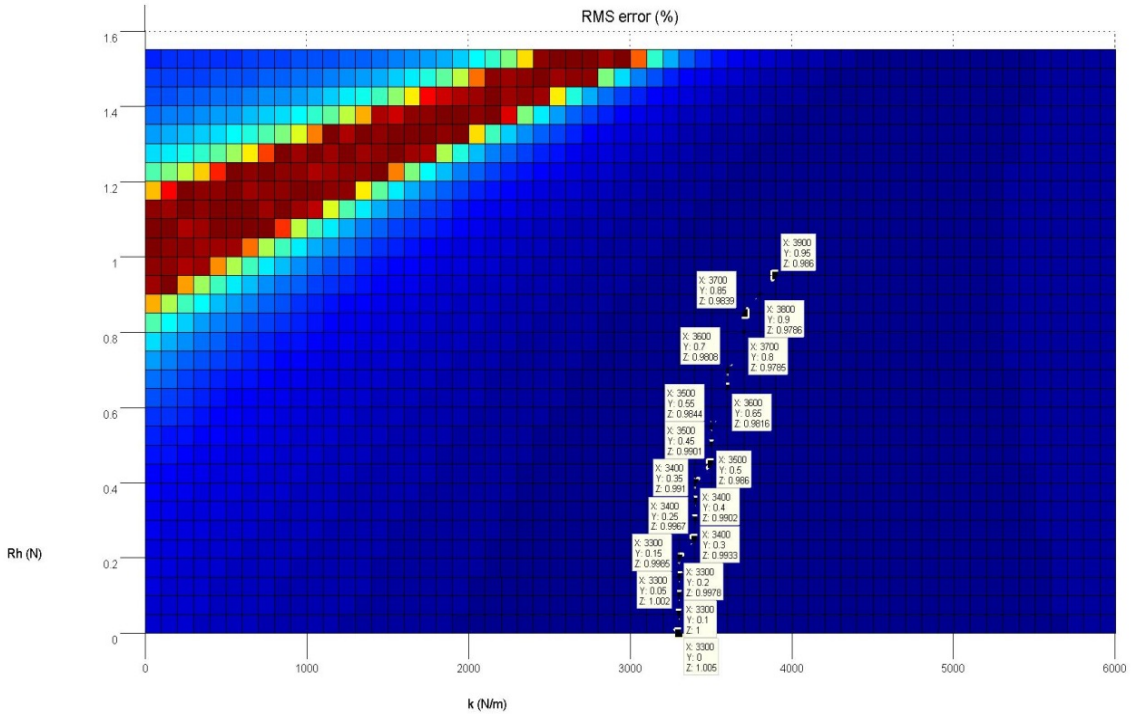

Figure 10-7 2D plot of the Error% space of the least squares solution of (5-32) versus Rh and k, for C22-2

To meet the second condition, simultaneously, the SVD of the $[G]$ matrix for each combination of (Rh, k) must be studied, as a singularity of $[G]$ must be avoided. Should $[G]$ become singular, the buckling point of the needle has been reached, i.e. the point where the relationship between the axial cutting force Rh and the compressive forces ky generates instability and the system loses stiffness. The minimum SVD vs Rh and k is shown in figure 6 for case study C22-2, for Rh between 0--1.6N and k between 0--6000 N/m^2.

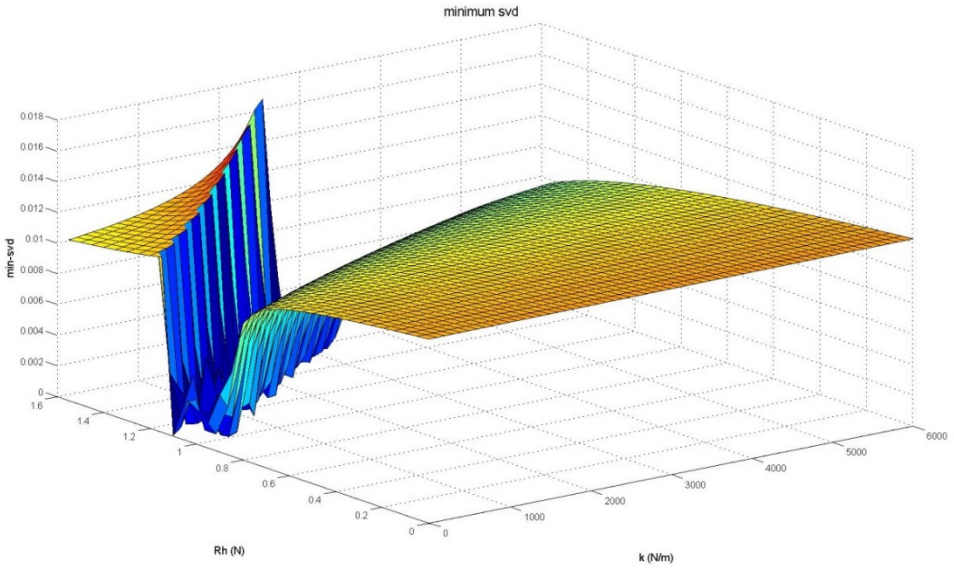

Figure 10-8 3D plot of the MIN(SVD) space of [G] of equation (5-28) versus Rh and k, C22-2

The top view of the space in figure (10-7) is shown in figure (10-8), where the point in the blue range has entered a buckling zone, and the point in the yellow range is acceptable. The lowest RMS=0.9785 point is shown.

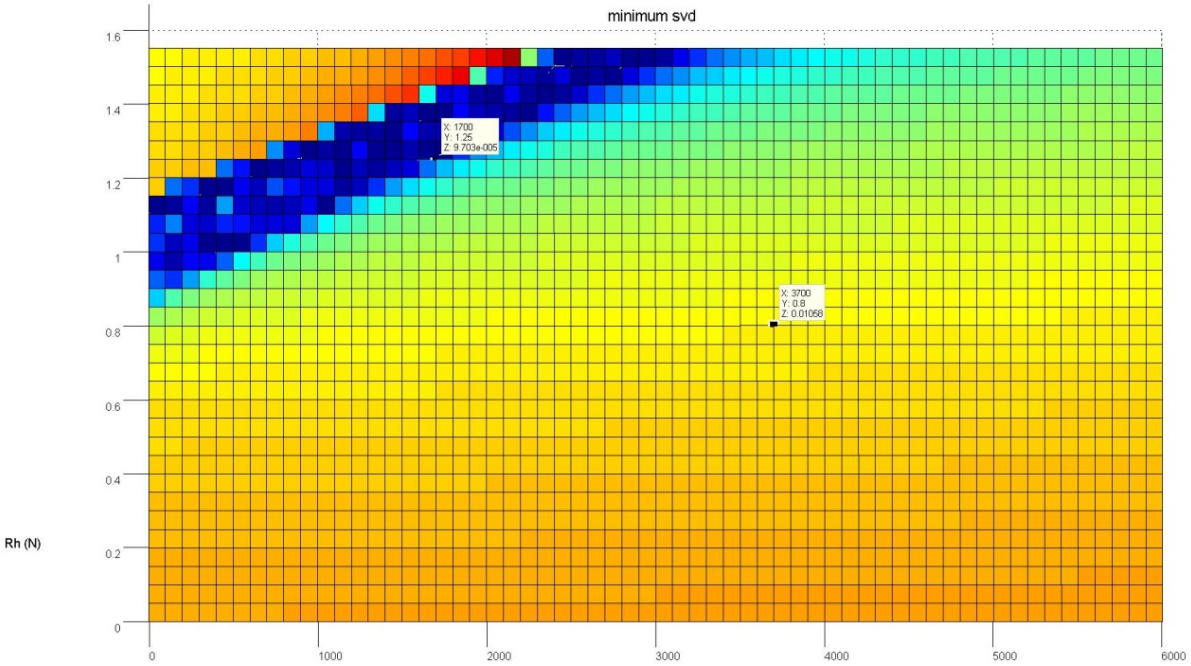

Figure 10-9 2D plot of the MIN(SVD) space of [G] of equation (5-28) versus Rh and k, for C22-2

Having identified a valid Rv value of 0.8, the space for Rh, Rv, k solutions for Rv, in the range close to the solution (between -0.3 to 0.1) is illustrated in figures (10-10) and (10-11).

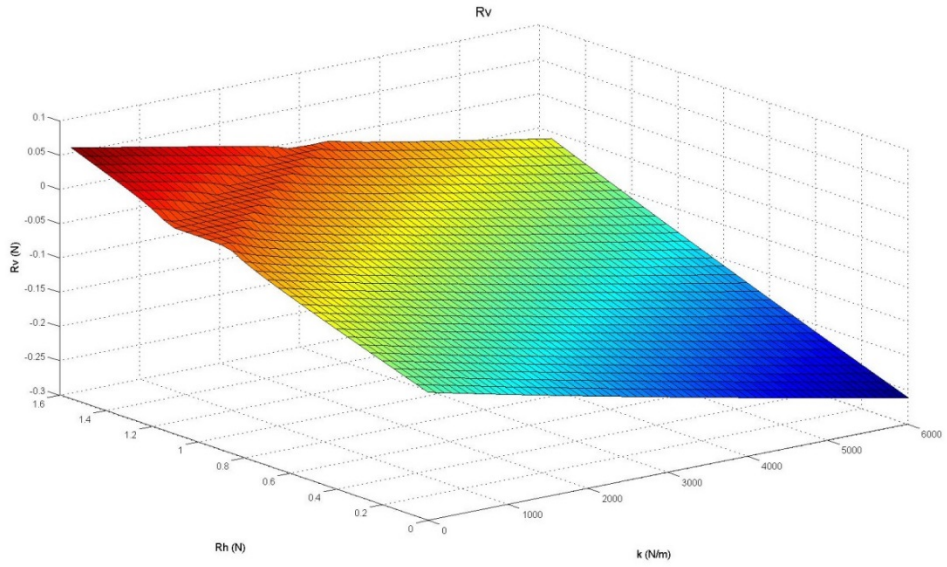

Figure 10-10 3D plot of the Rv space of solution of equation (5-32) versus Rh and k, for C22-2

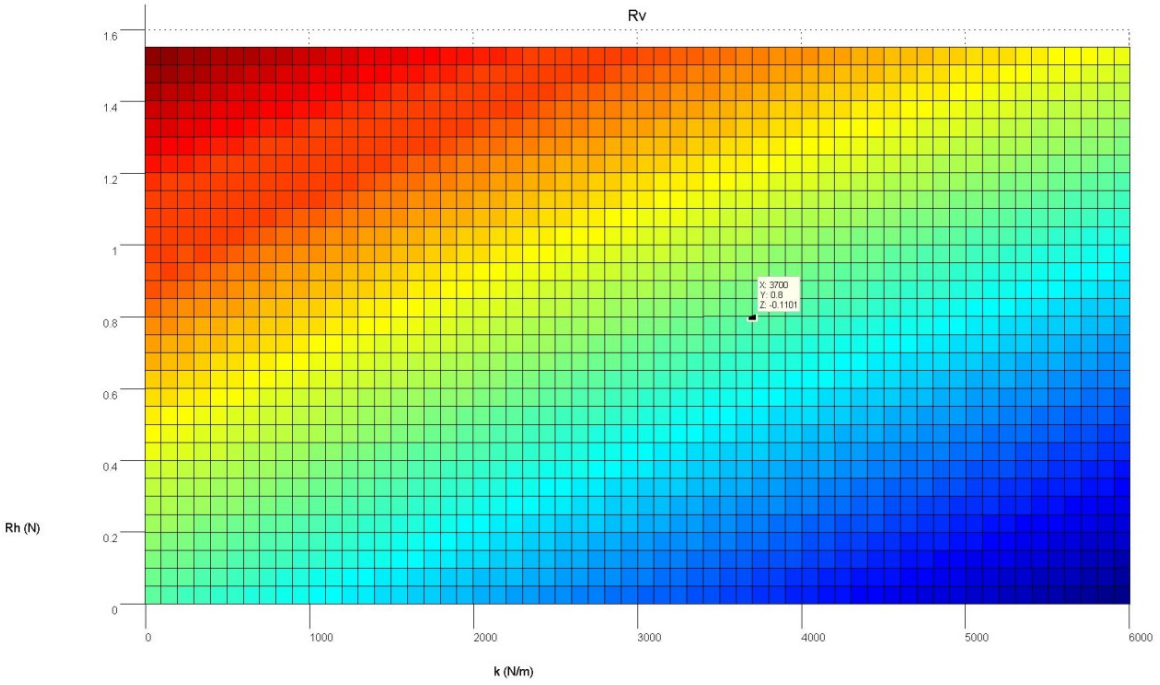

Figure 10-11 2D plot of the Rv space of solution of equation (5-32) versus Rh and k

The force acting on the needle for the deflection range for 15 steps is thus identified. These forces must now be verified by checking the corresponding theoretical modelled deflections with experiments. This is presented in the following section.

10.3.1.2. QUASI NONLINEAR FORCE IDENTIFICATION: VERIFICATION AND VALIDATION (C22-2)

Having identified the forces acting on the needle from the quasi-nonlinear model presented in equation (5-32) and looking at the solution spaces illustrated in images 10-6 to10-10, the forces are then inputted into equation (5-30), and the tip deflections compared. As has been mentioned, k, Rh and Rv from the quasi non-linear identification are $3700N/m^2$, $0.8N$, $-0.1093N$ respectively. Inserting these forces into equations (5-15) and (5-25) provides the deflection along the length of the needle for each step of insertion. Initially, as was previously mentioned, the forces identified from the 15 steps are applied to the first two tip deflections for comparison, as shown vs the experimental data in figure (10-12). The modelled shape of the needle for the first two steps of insertion (steps before entering the nonlinear range) is shown in figure (10-13).

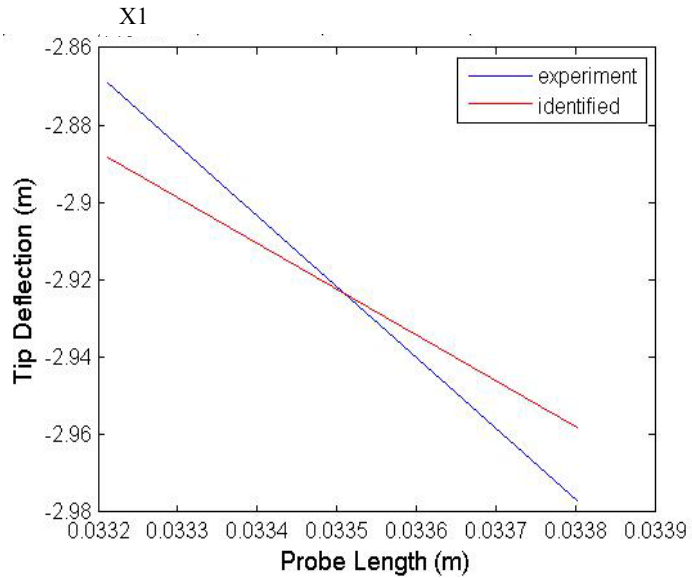

Figure 10-12 Plot of the measured and calculated tip paths for quasi-nonlinear range, using identified loads with 15 insertion steps, in equation (5-30).

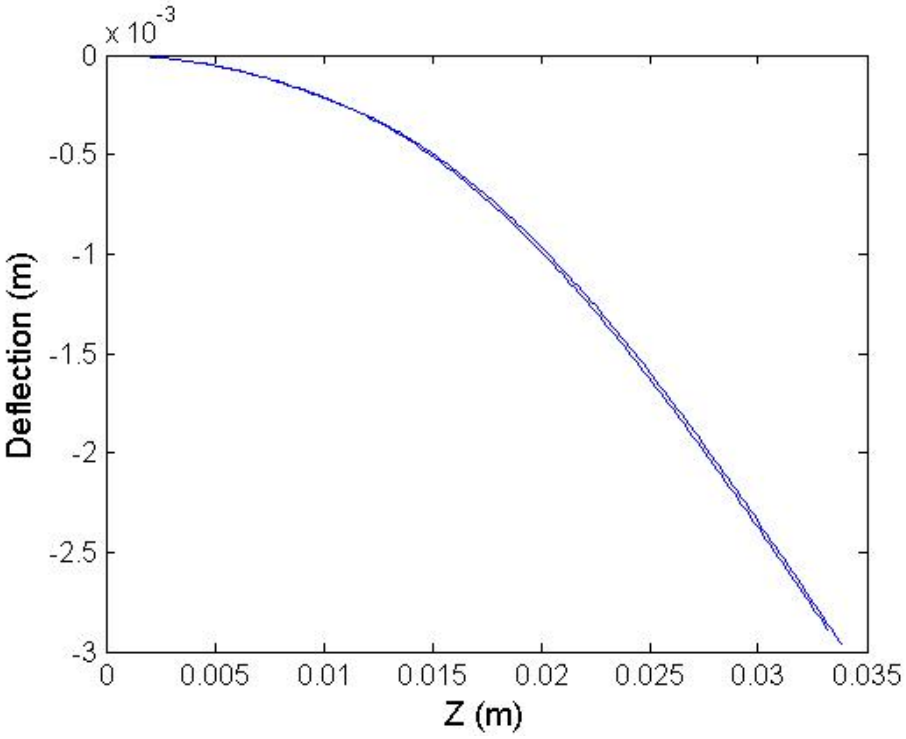

Figure 10-13 plot of calculated needle deflections for quasi-nonlinear range, using identified loads with 15 insertion steps, in equations (5-13) and (5-25). Both points are the two consecutive steps modelled in the quasi-nonlinear solver.

10.3.1.3. NONLINEAR FORCE IDENTIFICATION: (C22-2)

Having identified forces for two quasi-nonlinear insertion steps with the first 15 steps, for the rest of the insertion process, the nonlinear force identification is employed. As was mentioned, the forces are identified for every $m = 5$ steps of insertion, and the results are

presented below. These forces are then inputted into the forward progressive nonlinear model and compared against experimental results for verification, in the next section.

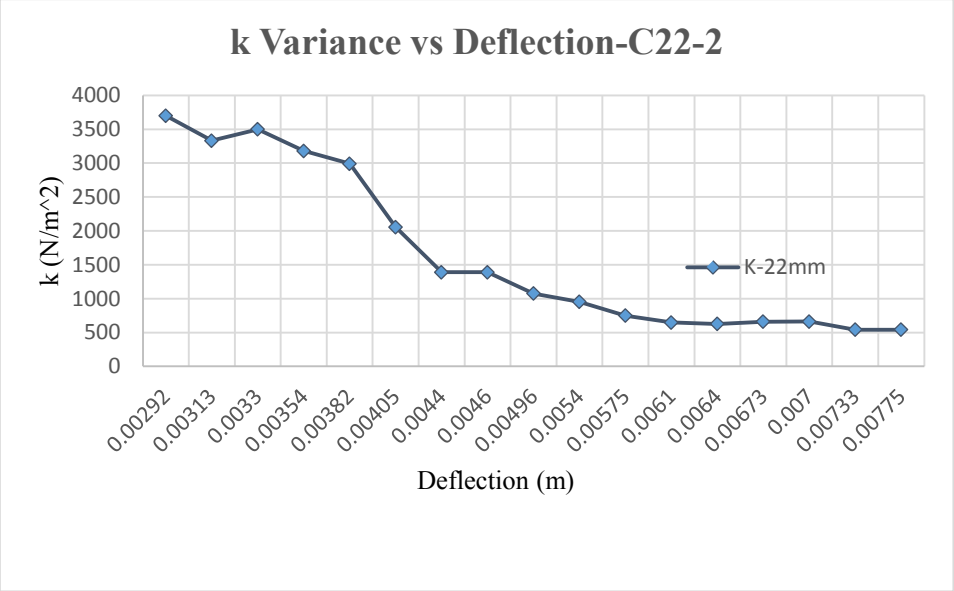

Figure 10-14 Plot of identified k values in nonlinear range vs deflection, for C22-2

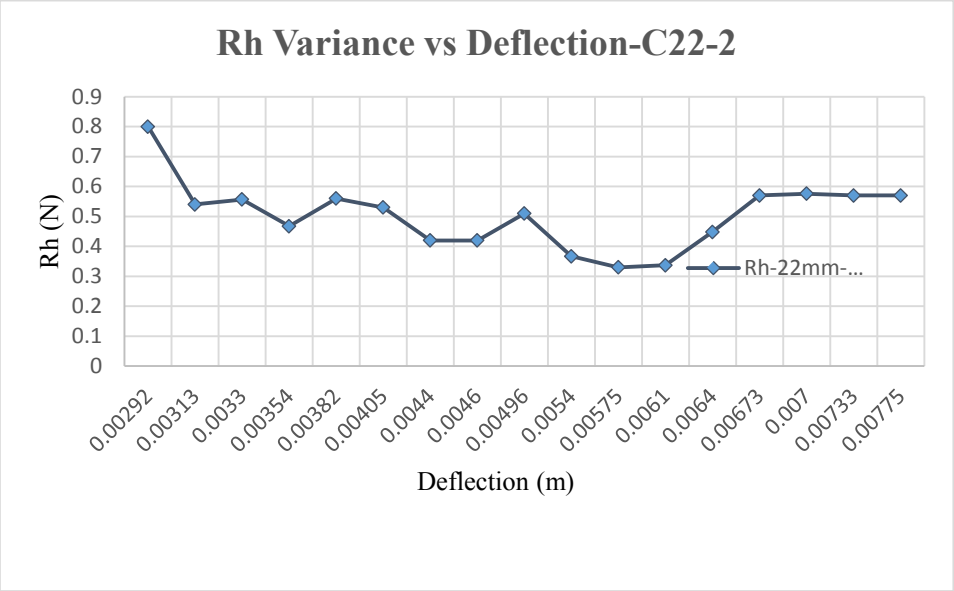

Figure 10-15 Plot of identified Rh values in nonlinear range vs deflection, for C22-2

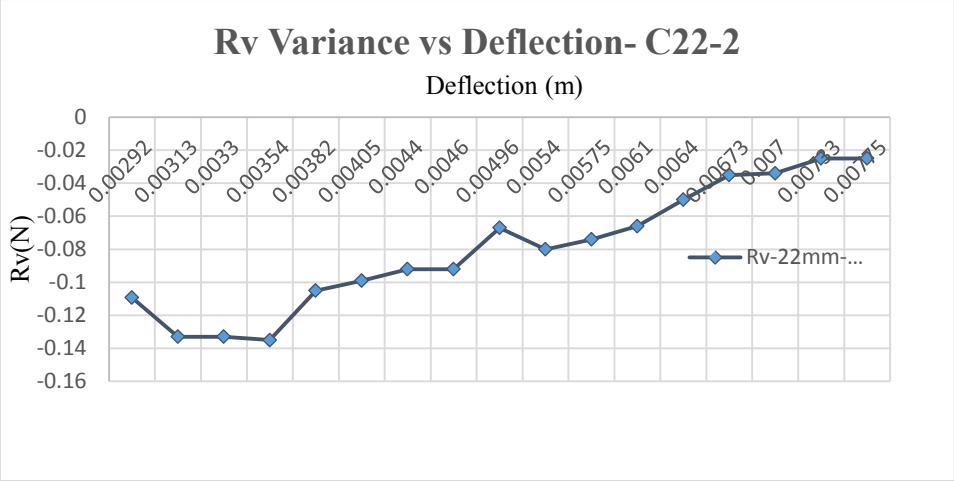

Figure 10-16 Plot of identified Rv values in nonlinear range vs deflection, for C22-2

10.3.1.4. NONLINEAR FORCE IDENTIFICATION: VERIFICATION AND VALIDATION (C22-2)

Using these identified forces, the tip deflection is then modelled via the nonlinear progressive model and results and errors are shown in figures (10-17) and (10-18). Two different progressive cases were compared; in one case, the forces identified for the previous step were applied to the subsequent step, and the errors between the corresponding tip deflections checked against experiments. If the error is less than 1%, the forces are considered to be the same for the two steps, if not, the forces are identified for the new step. In the second case, the tip deflection errors are not checked at every step and the forces identified for one step are applied to the subsequent step regardless. This comparison is designed to measure the impact of re-identification of the forces at every step of the model.

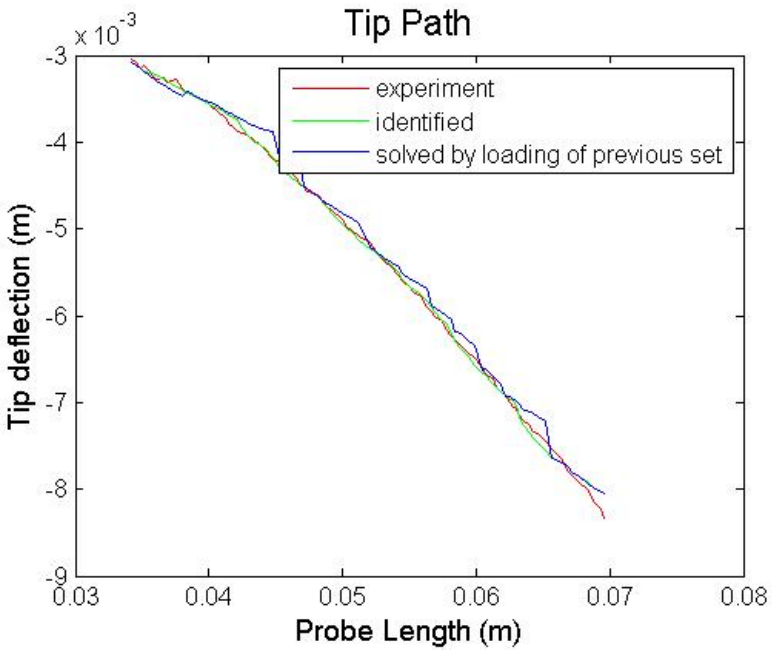

Figure 10-17 Plot of the measured and calculated tip paths for nonlinear (including linear) range, using progressive nonlinear identification. In the case labelled "identified", forces from the previous step of identification are used, in the second case, "solved by loading of previous set", the forces are re-identified for each step of the progressive solution.

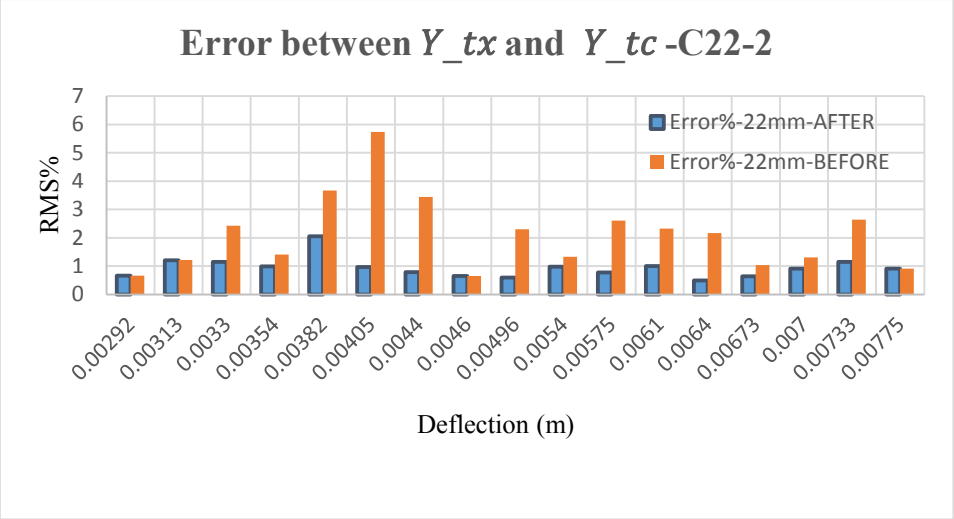

Figure 10-18 plot of Error% in equation (1) versus tip deflection value, Ytc , 'before' and 'after' updating each step's loads with the identified loads, as described in D, section 8.2.1

Having identified the forces acting on the needle, the shape of the needle body throughout the deflection is generated and shown in figure (10-19). The green line is the modelled tip path of the needle, and the blue is the needle's body for each tip point generated by the model.

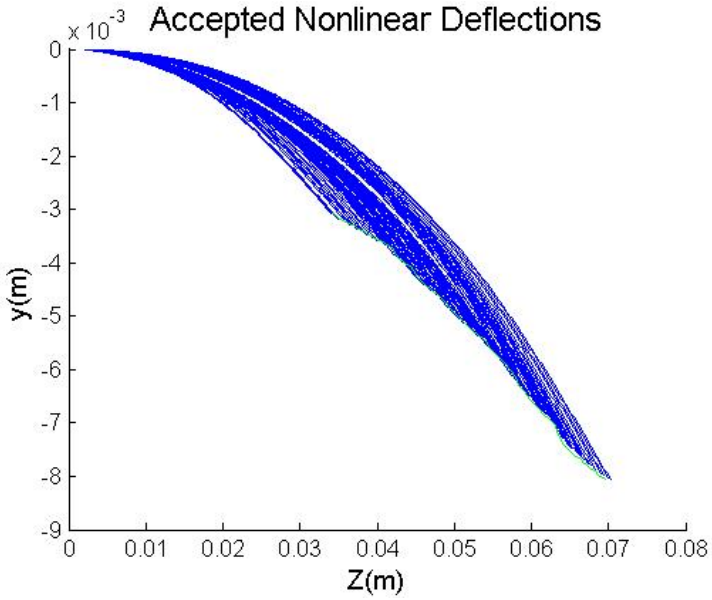

Figure 10-19 Plot of needle deflection for the nonlinear (including linear) range, using identified loads generated with the progressive nonlinear identification procedure of chapter 8. The green line is the tip deflection and the blue lines are the various shapes of the needle's body during insertion.

As is evident from figure 10-18, the error% values are low, and are less for this case compared to those of the aforementioned similar case. This proves that starting from lower insertion steps for the nonlinear identification process is advantageous, as the process will correct approximations involved in quasi non-linear identification for those steps. For example, in one case in the sensitivity study named C22-1, 15 insertion data were used in the quasi non-linear identification stage. This was justified by the short offset and total length. As such, for this case, the nonlinear process started from insertion step 16 and carried on to subsequent steps. However, in C22-2, although 15 points were used in the quasi nonlinear process, the nonlinear process started from insertion step 3 (as if 2 insertion data were used in the quasi non-linear process), using loads identified in the quasi non-linear process with 15 insertion data. So, practically, the nonlinear calculations for insertion step 3, described in section 8.2, are based on the Y, Y' and Y'' of step 2 and insertion step 2 is much closer to that of the linear beam, than insertion step 15. So, in C22-1, the insertion data from 3 to 15 are adapted to the quasi non-linear behaviour, while in C22-2 insertion step 3 and onward are calculated by the nonlinear process. Also, in this case study, 5 insertion (averaging) data are used in each identification step and hence more identification steps are involved, which leads to more accurate results. Figure 10-14 shows a stable, decreasing, characteristic for k and general behaviour. Also, figures 10-15 and 10-16 show a closer to monotonic trend. These trends will be further discussed and summarised later in the chapter. In the next sections, the same procedure will be performed on 2 other experiments, for 33 and 44 mm offset insertions. As the procedure has been explained for this experiment and is the same for all insertion lengths, only the specifications and results are shown, and the conclusions drawn in the final section of the chapter.

10.3.2. NEEDLE WITH 33MM OFFSET, CASE STUDY C33-4

For this case, the following parameters are used:

a) m = No. of insertion steps used in each step of Quasi non-linear identification of Rh and $k = 10$ (equation (5-32)), insertion steps 1 to 10
b) m = No. of insertion steps used in the nonlinear identification (equation (8-11)) $= 5$
c) Starting insertion step for nonlinear solution $= 3$
d) No. of insertion steps used in quasi nonlinear identification of $Rv\_1 = 2$, insertion steps 1 to 2. This case study is intended to demonstrate the sensitivity of the nonlinear identification process to slight variations in the starting load values, identified in the

quasi nonlinear process, and the Y, Y' and Y'' associated with them. Here, similar to case C22-2, k, Rh and Rv_1 are found using 10 insertion points in the quasi non-linear solution, such that MIN(error% of least squares solutions) is identified. Now using the k and Rh found as said, it is attempted to enter the nonlinear solution from the 3rd insertion point, as if 2 insertion data were used in the quasi non-linear process. Here, there are two choices; namely: (1) to use k and Rh in equation (32) and find the Rv_1 which gives least squares solution, using 2 insertion data points, or, (2) to use the Rv_2 which gave MIN(error% of least squares solutions) with 10 points involved in quasi non-linear process which, obviously, will present neither the MIN(error% of least squares solutions) nor the least squarse solution of (32) with 2 insertion point involved.

e) No. of insertion steps used in quasi nonlinear identification of $Rv\_2 = 10$, insertion steps 1 to 10
f) k, Rh (using insertion steps 1 to 10) and Rv_1 (using insertion steps 1-2) from the quasi non-linear identification = 1100 N/m2, 0.65 N, -0.04375 N
g) k, Rh and Rv_2 from quasi non-linear identification (using insertion steps 1 to 10) = 1100 N/m2, 0.65 N, -0.04386 N
h) MIN(error% of least squares solutions), $k, Rh\ and\ Rv$ using 2 insertion points in the quasi non-linear process = 8.e-5, 500N/m2, 0., -.1279
i) Quasi non-linear identification Error% (least squares) with k, Rh, Rv_1= 0.1739
j) Quasi non-linear identification Error % with $k, Rh\ and\ Rv\_2$= 0.3129%

Two cases with $Rv\_1\ and\ Rv\_2$ will be considered. As is evident from the data given above, two values of Rv are only 0.25% apart, however, it will be shown that this small difference leads to 45% difference in Y_{tc} error% for the quasi non-linear range which, in turn, implies large differences in starting Y, Y' and Y'' of the nonlinear process.

10.3.2.1. QUASI NONLINEAR FORCE IDENTIFICATION (C33-4)

As was the case with C22-2, the first step is defining a solution space for equation (5-32) for a reasonable range for the Rh and k values, then keeping one constant and iterating the other, thus identifying the corresponding Rv value and considering the RMSE of the solution to equation (5-32). This is shown in figure 6 for case study C33-4, for Rh between 0--1.5N and k between 0--6000 N/m^2.

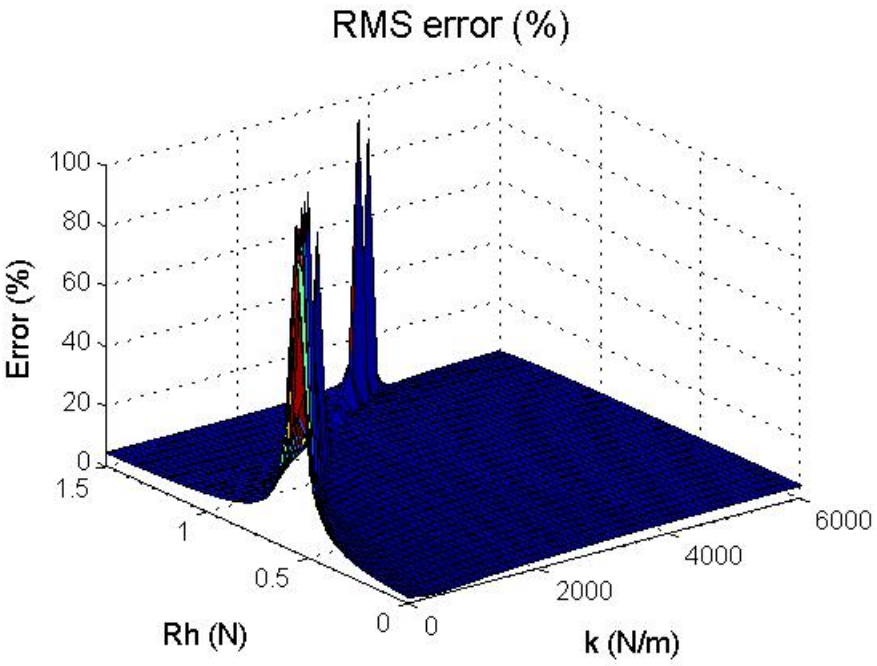

Figure 10-20 3D plot of the Error% space of least square solution of (5-32) versus Rh and k, for C33-4

In figure (10-21), the possible solution points where the RMS is close to 1 are shown in the top view of the solution space shown in figure (10-7) for C33-4. The lowest RMS is 0.554, at $X, Y, Z = 1100, 0.65, 0.554$.

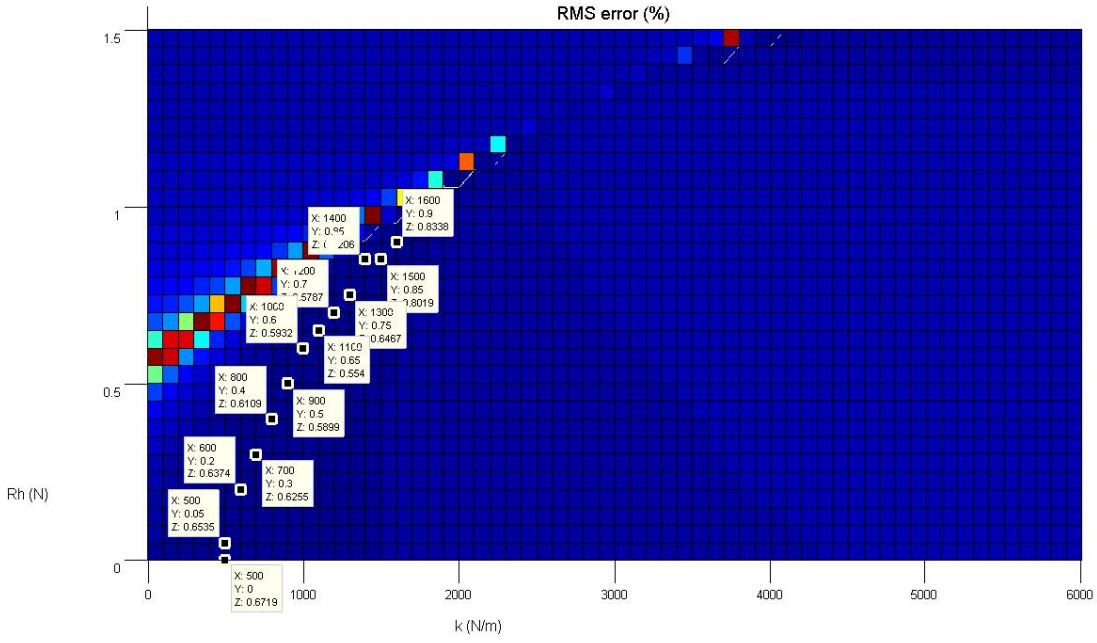

Figure 10-21 2D plot of the Error% space of least square solution of (5-32) versus Rh and k, for C33-4

Next, simultaneously, the SVD of the $[G]$ matrix for each combination of (Rh, k) is studied as singularity of $[G]$ must be avoided to avoid buckling. For the minimum SVD vs Rh,k is shown in figure 6 for case study C33-4,for Rh between 0--1.5N and k between 0--6000 N/m^2.

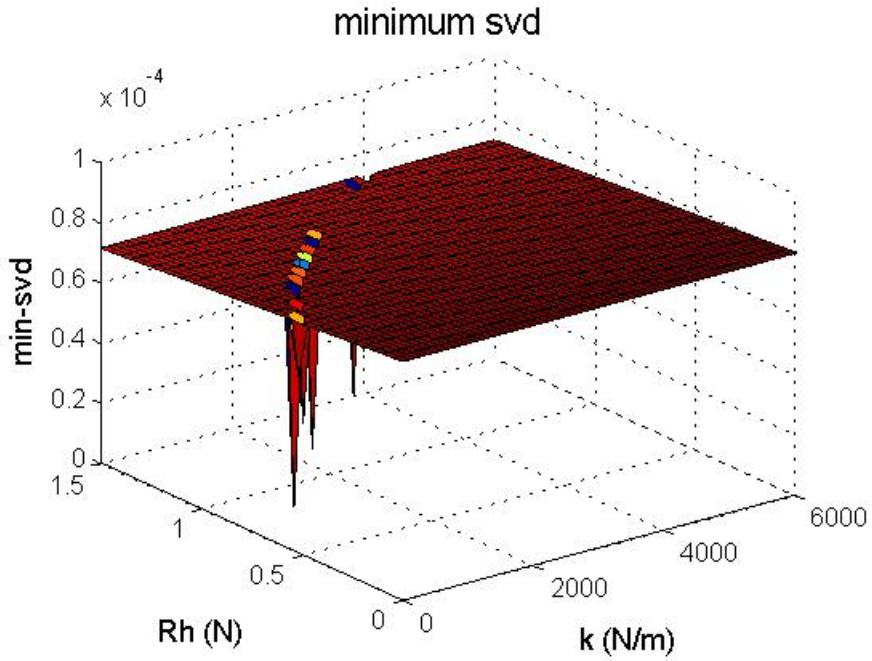

Figure 10-22 3D plot of the MIN(SVD) space of [G] of equation (5-28) versus Rh and k, for C33-4

The top view of the space in figure (10-22) is shown in figure (10-23), where the point in the blue range has the lowest RMS=0.554.

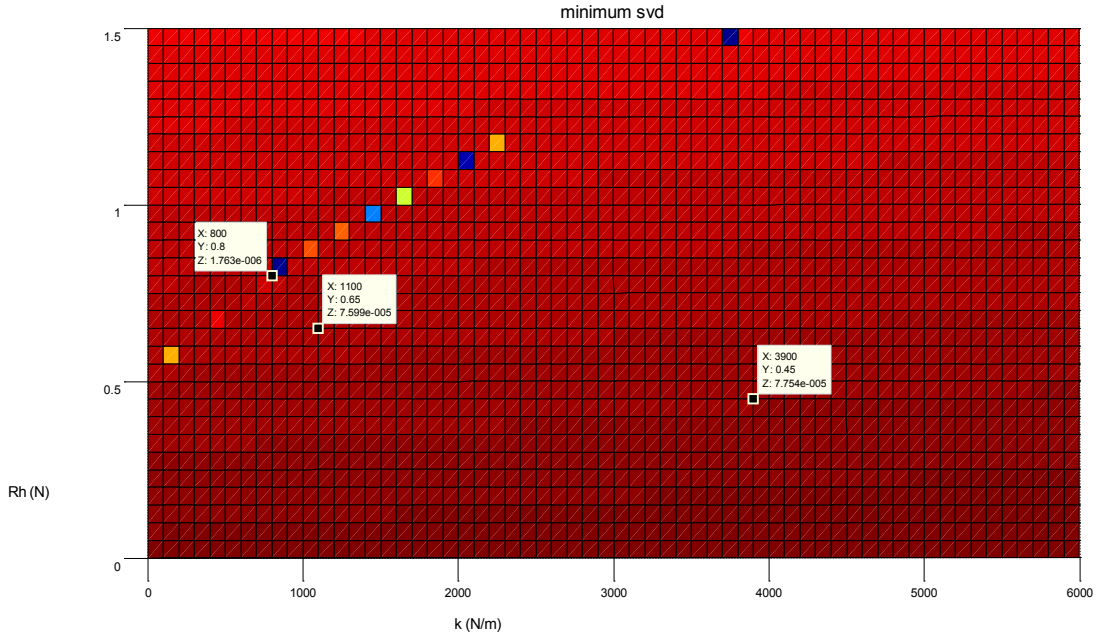

Figure 10-23 2D plot of the MIN(SVD) space of [G] of equation (5-28) versus Rh and k, forC33-4

The solution space for Rh, Rv and k is shown in figures (10-24) and (10-25).

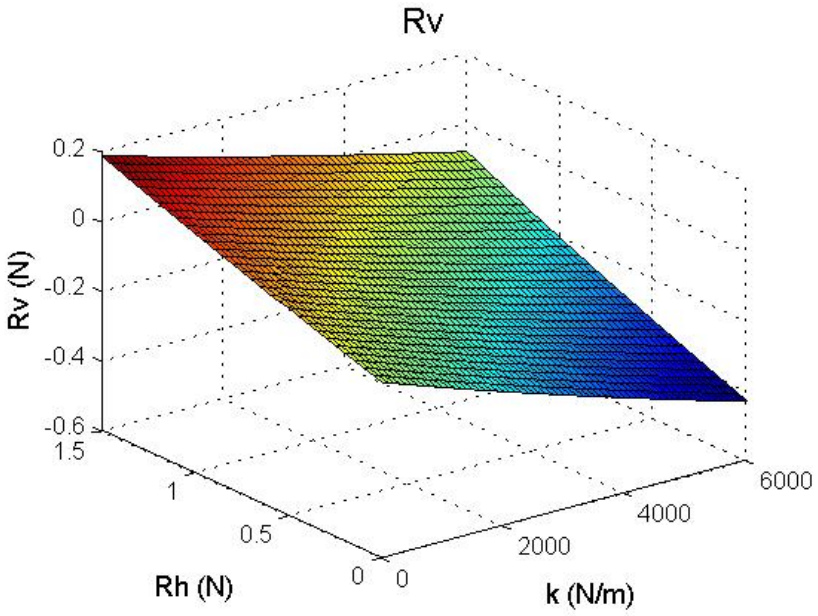

Figure 10-24 3D plot of the Rv space of solution of equation (5-32) versus Rh and k, for C33-4

The solution point is shown in figure (10-25), where $X, Y, Z = 1100{,}0{,}65, -0.04386$.

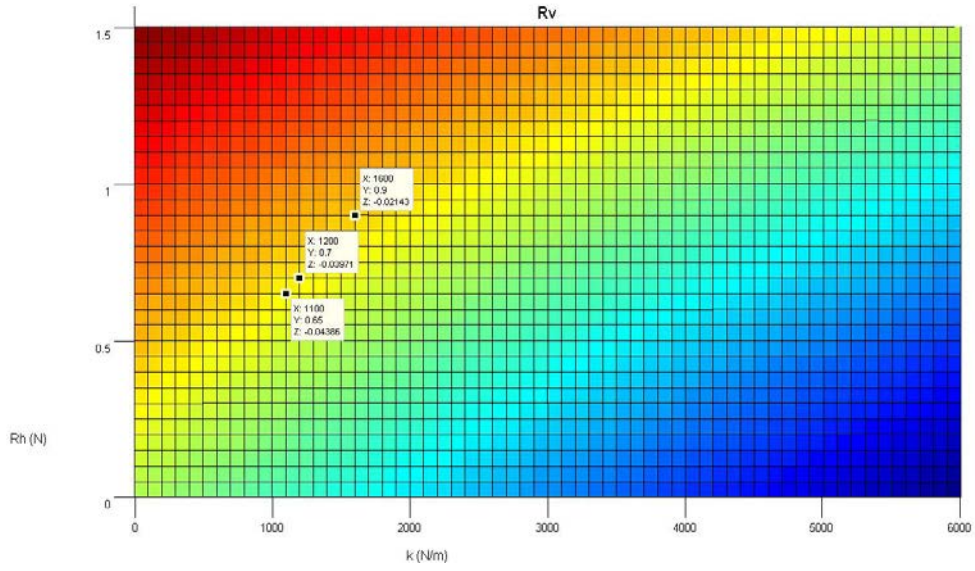

Figure 10-25 3D plot of the Rv space of solution of equation (5-32) versus Rh and k, for C33-4

10.3.2.2. QUASI NONLINEAR AND NONLINEAR FORCE IDENTIFICATION AND VERIFICATION (C33-4)

As was explained, there are two approaches to the identification of Rv. Having identified $Rh, k, Rv\_1 = 1100\ N/m2,\ 0.65\ N,\ -0.04375\ N$ and $Rh, k, Rv\_2 = 1100\ N/m2,\ 0.65\ N,\ -0.04386\ N$, the resultant tip deflections and needle shapes are presented bellow for comparison in figure (26) and (27). Having progressed onto the nonlinear solver for tip path and needle shape in figures 10-28 and 10-29, it is shown that Rv_1 yields better results for both quasi-nonlinear and nonlinear results.

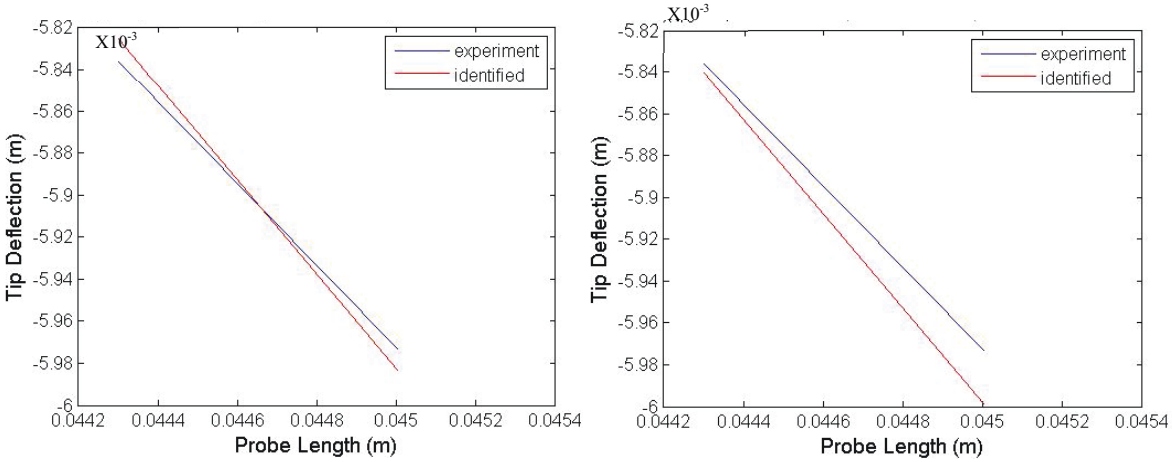

Figure 10-26 plot of the measured and calculated tip paths for linear range, using Rv_1 (left) and Rv_2 (right) identified by solving equation (32,ch5) with k=1100 N/m2 & Rh=0.65N and then applying the identified values in equation (30,ch5), for C33-4

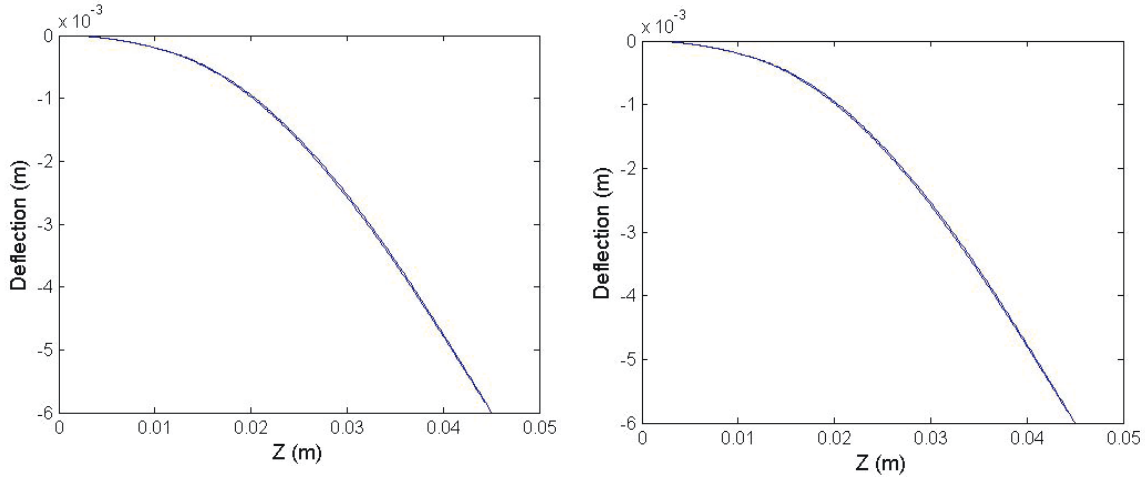

Figure 10-27 plot of calculated deflected needle shapes for linear range, using u Rv_1 (left) and Rv_2 (right)with k=1100 N/m2 & Rh=0.65N in equations (5-25) and then using (5-13), for C33-4

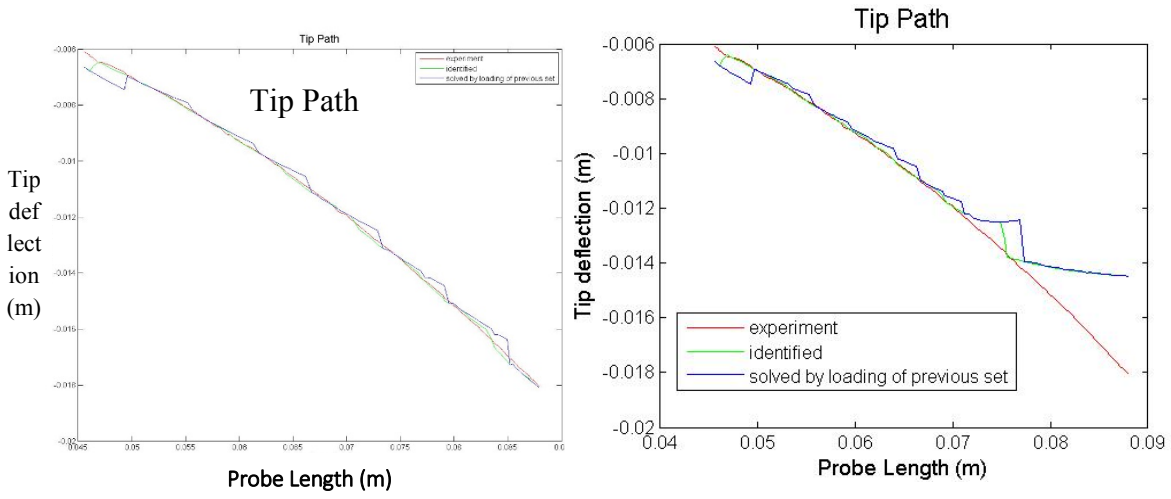

Figure 10-28 plot of calculated needle deflections for linear range, using Rv_1(left) and Rv_2(right) (identified by solving equation (5-32), with k=1100 N/m2 & Rh=0.65N) in equations (5-25) and then using (5-13).

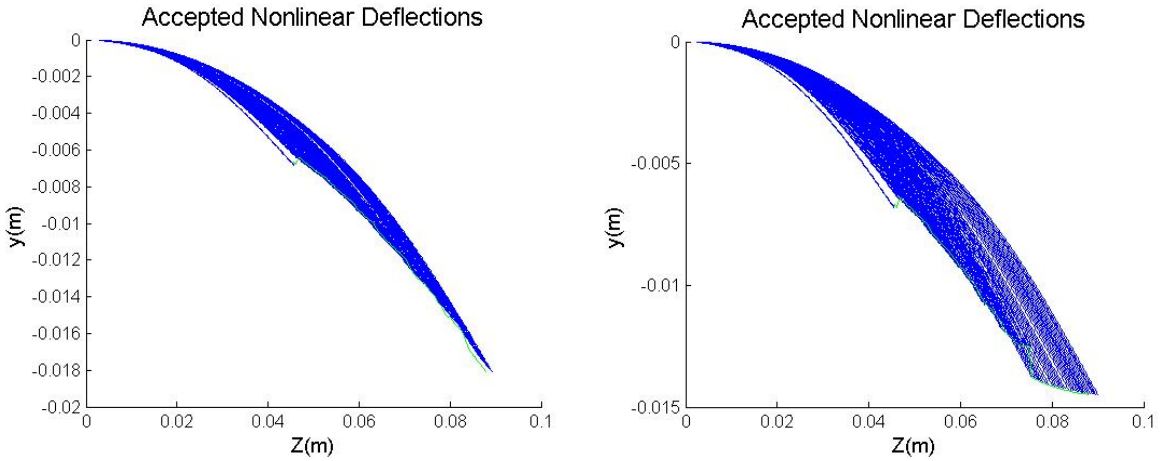

Figure 10-29 plot of the measured and calculated tip paths for nonlinear (including linear) range, using Rv_1 (left) and Rv_2 (right), using the progressive nonlinear identification procedure of chapter 8

As is evident from figures (10-26),(10-28) and (10-29), the slight difference in starting Rv_1 is associated with significant changes in starting Y, Y' and Y'', which leads to two different behaviours of the needle. It is obvious from figure (10-28) that, with Rv_2, the measured and modelled tip paths do not converge. As such, the forces identified in the nonlinear domain with Rv_1 from the quasi nonlinear domain are chosen as the results with higher accuracy. The identified forces for the nonlinear domain are shown in figures (10-30),(10-31) and (10-32) for k, Rh and Rv_1.

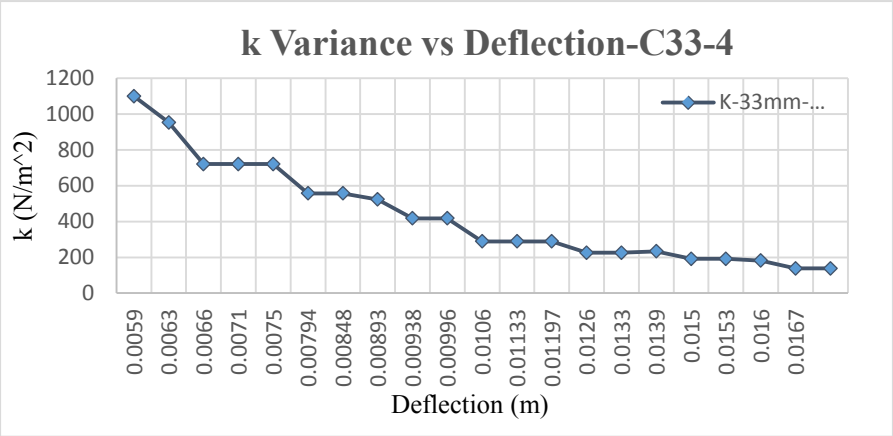

Figure 10-32 plot of identified k versus tip deflection value, Ytc, Rv_1 used, C33-4

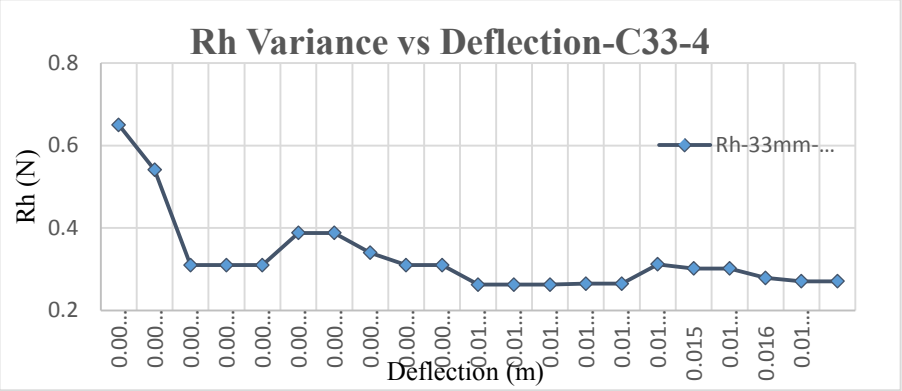

Figure 10-31 plot of identified Rh versus tip deflection value, Ytc, Rv_1 used, C33-4

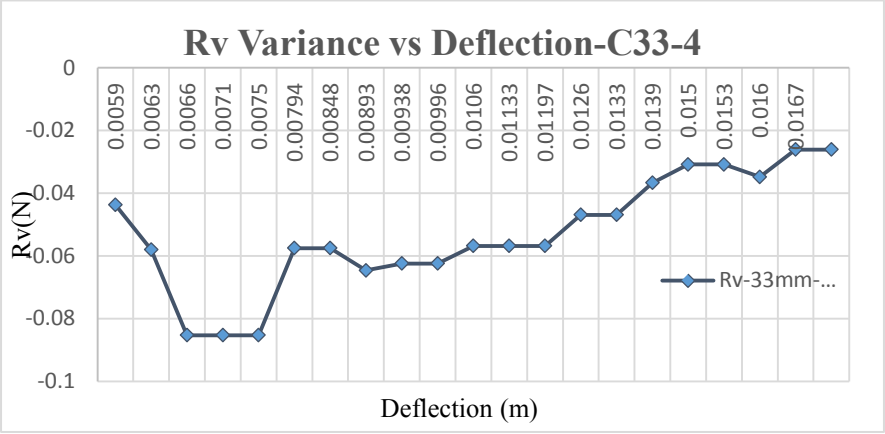

Figure 10-30 plot of identified Rv versus tip deflection value, Ytc, Rv_1 used, for C33-4

The errors between the experimental tip deflections and modelled tip deflections as shown in figure10- 28 (left) are shown in figure 10-33 for the two loading scenarios, as has been explained for C22-2.

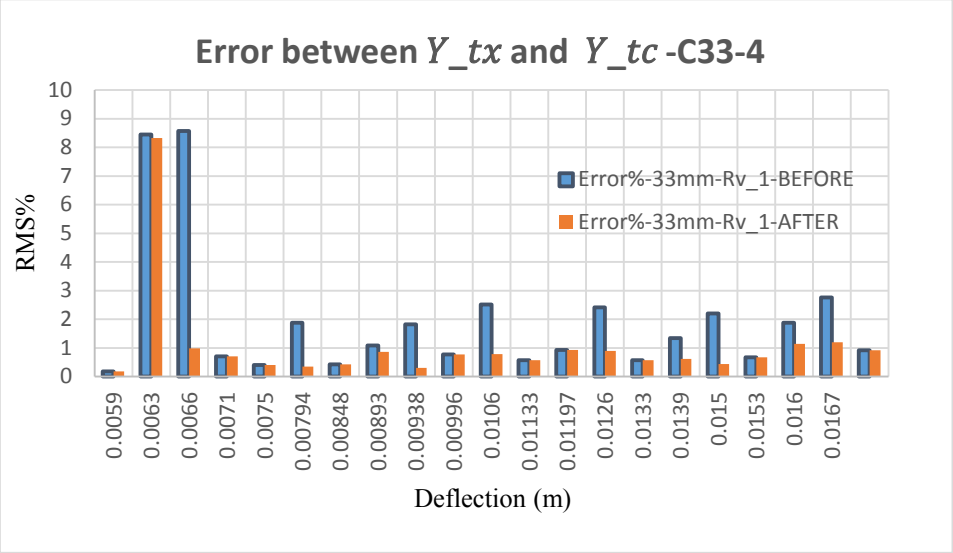

Figure 10-33 Plot of Error% between modelled versus experimental tip deflection value, Ytc , before and after updating each step's loads with the identified loads, as described in D of section 8.2.1 (Rv_1 used)

From the error% plot in figure 10-33, it is interesting to note that for the first nonlinear identification step (second column on the graph) the starting values of k, Rh and Rv_1 produce Y_{tc} error% as large as 9% and this value was not reduced much by the nonlinear identification process, as the blue and red curves coincide for this point. Then the calculation enters a 2nd nonlinear identification step, with a large error again (point 3, blue column). This large error is due to the fact that the results at the end of the 1st nonlinear identification step were not satisfactory. However, for the second nonlinear identification step, error% is reduced significantly to below 1% (3rd point red column). This means that the starting parameters were so much off the mark that the 1st nonlinear identification step was not able to reduce the error to an acceptable level, even though the error was reduced slightly. From the 2nd point in figures 29 to 31, one can see that this slight reduction in error has been associated with about 25% change in k, Rv, Rh. The significant change in loads is in the right direction and enables the 2nd nonlinear identification step to converge to a correct solution. The discrepancy associated with the 1st nonlinear identification step is also observable in figures 10-28 and 10-29.

10.3.3. NEEDLE WITH 44MM OFFSET, CASE STUDY C44-3

For this case, the following parameters are used

a) m = No. of insertion steps used in the Quasi non-linear identification of Rh and k = 10 (equation (5-32)), insertion steps 1 to 10
b) m = No. of insertion steps used in the nonlinear identification (equation (8-11)) = 5
c) Starting insertion step for nonlinear solution = 3,
d) No. of insertion steps used in quasi nonlinear identification of Rv = 2, insertion steps 1 to 2
e) k, Rh (using insertion steps 1 to 10) and Rv (using insertion steps 1-2) from Quasi non-linear identification = $200\ N/m2,\ \ 0.25\ N,\ \ -0.03\ N$
f) Quasi non-linear identification Error% (least square) with k, Rh, Rv, using insertion steps 1&2 = .026

10.3.3.1. QUASI NONLINEAR FORCE IDENTIFICATION (C44-3)

As the procedure for the quasi-nonlinear method has been explained previously, here are the resultant graphs for the least squares solution, minimum SVD check, and solution space for C44-3, as shown in figures 10-34 to 10-36.

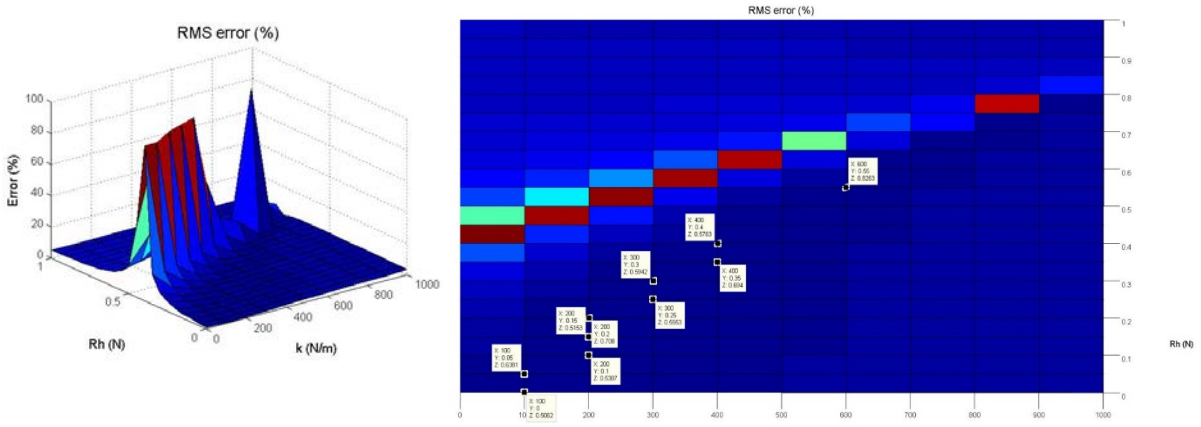

Figure 10-35 3D plot (left) and 2D plot (Right) of the Error% space of least square solution of (5-32) versus Rh and k, for C44-3

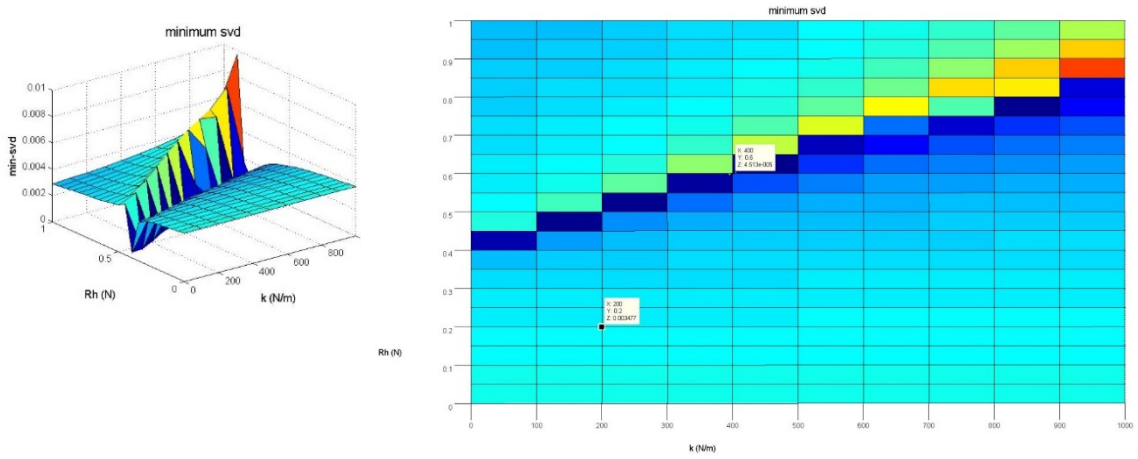

Figure 10-34 3D (left) and 2D (Right) plot of MIN(SVD) space of [G] of equation (5-28) versus Rh and k, for C44-3

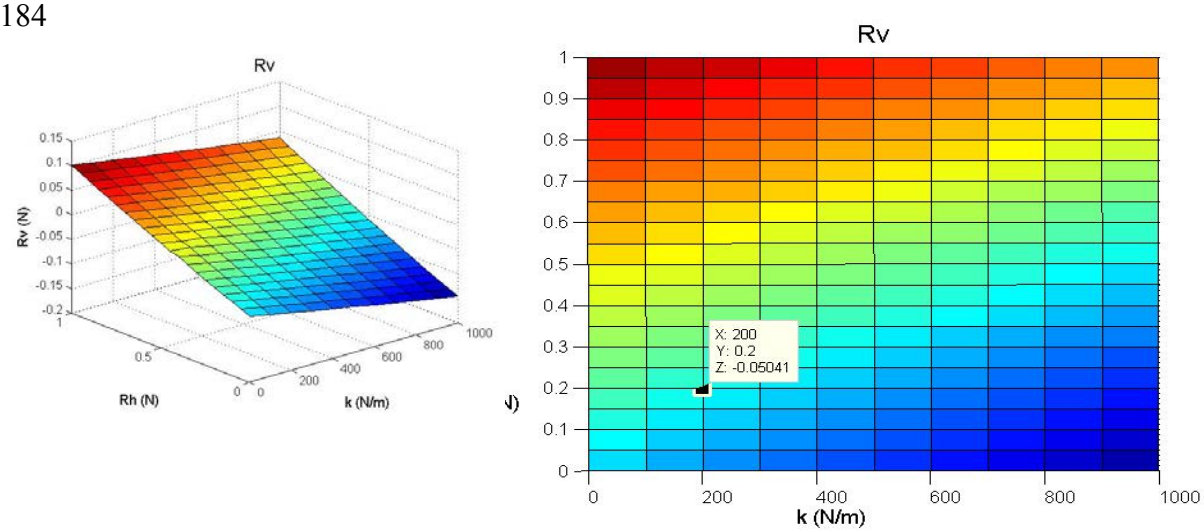

Figure 10-36 3D plot (left) and 2D plot (right) of the Rv space of solution of equation (5-32) versus Rh and k, for C44-3

10.3.3.2. NONLINEAR FORCE IDENTIFICATION (C44-3)

The forces identified from the nonlinear solver are shown in figures 10-37 to 10-39 and the resultant tip deflection and errors between experimental and modelled tip deflections are shown in figures 10-40 and 10-41.

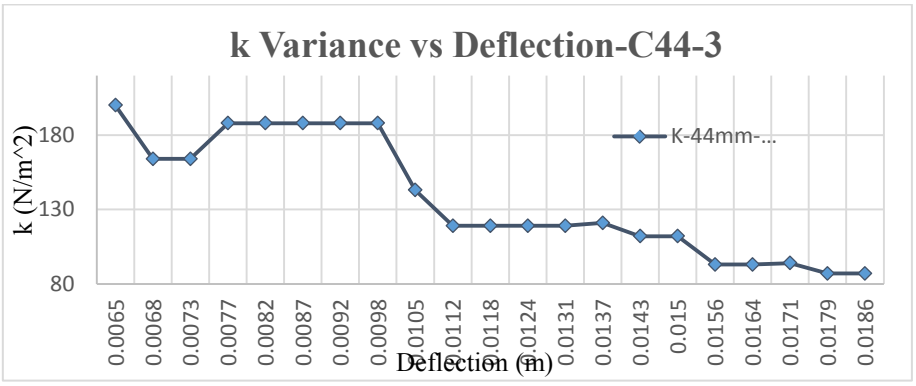

Figure 10-37 plot of identified k versus tip deflection value, Ytc C44-3

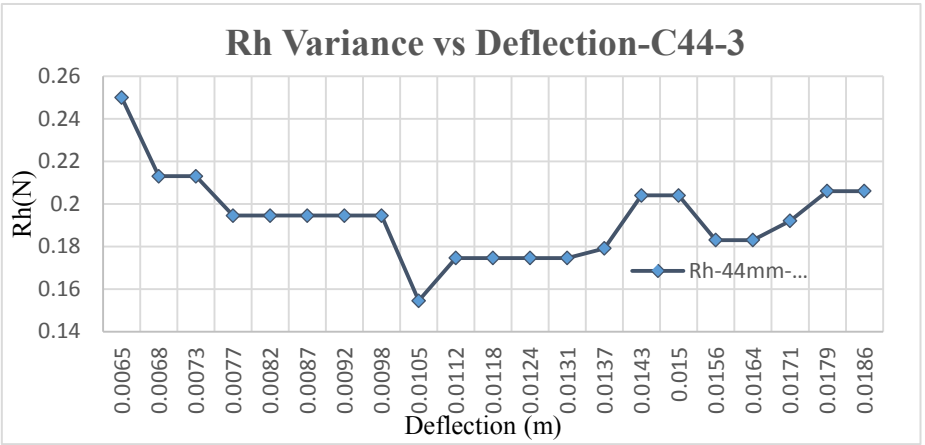

Figure 10-38 plot of identified Rh versus tip deflection value, Ytc C44-3

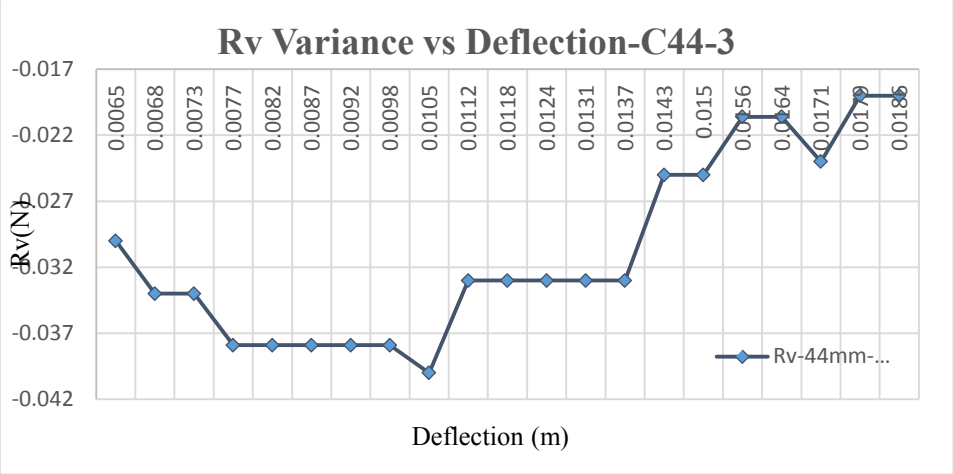

Figure 10-39 plot of identified Rv versus tip deflection value, Ytc C44-3

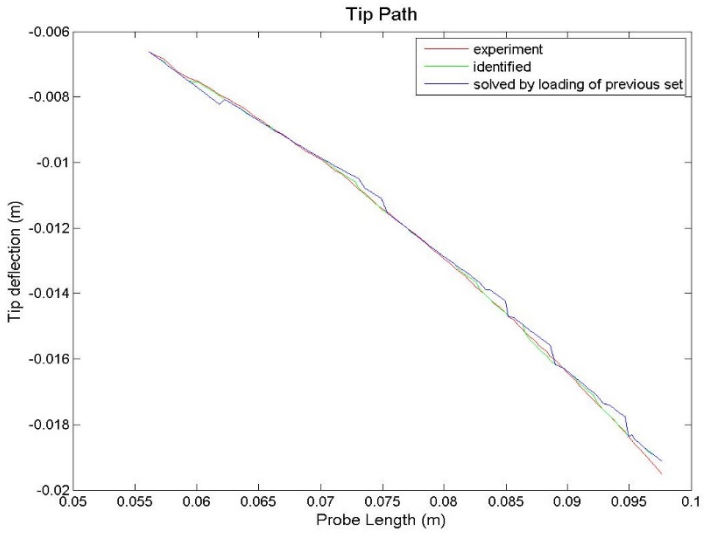

Figure 10-41 plot of the measured and calculated tip paths for the nonlinear (including linear) range, using identified loads using the progressive nonlinear identification procedure of chapter 8, for C44-3

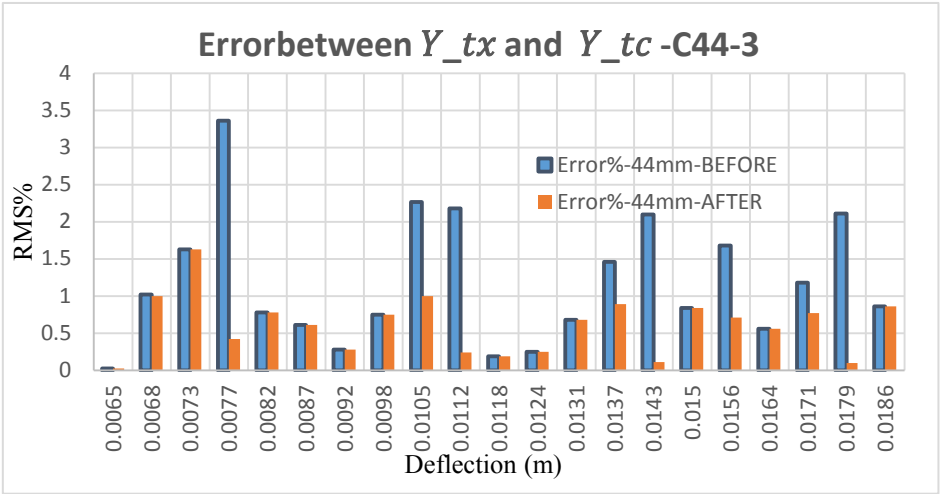

Figure 10-40 plot of Error% experimental vs modelled tip deflection value, Ytc , before and after updating each step's loads with the identified loads, as described in D of section 8.2.1, for C44-3

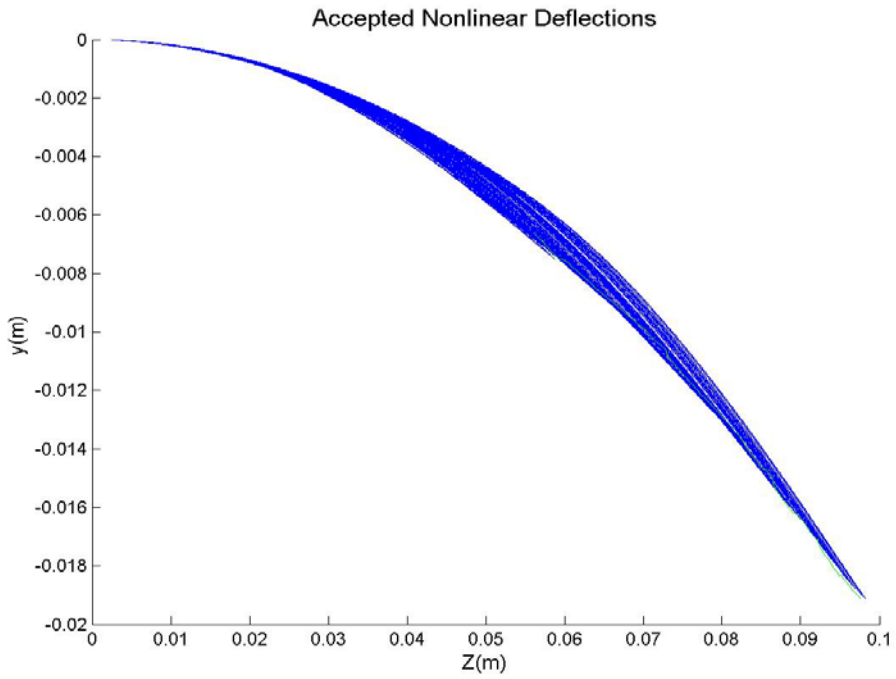

Figure 10-42 plot of deflection curves of the needle for the nonlinear (including linear) range, using identified loads using the progressive nonlinear identification procedure of chapter 8, for C44-3

Based on the results generated for the experiments C22-2, C33-4 and C44-3, the collective trend of the forces are shown in figures 10-43 to 10-45, and the final conclusions are drawn. In order to be able to verify the validity of the assumptions regarding force application in both the reverse and progressive models, as a final test, the forces for another set of 22, 33 and 44 mm offsets are inputted into the quasi-nonlinear forward progressive model and ANSYS, and the resulting tip deflection is compared against that obtained in experiments. These are shown in tables 10-13.

Table 10-13 Identified forces from experiments and results from both ANSYS and the forward model.

Offset (m)	Z Experimental (m)	Y Experimental (m)	Y Identified (m)	ANSYS Y (m)	Error: ANSYS vs experimental results	Error: modelled results vs experimental results
0.022	0.044178	-0.00508	-0.00508	-0.0053	0.0433	0.0013
0.033	0.03752	-0.00291	-0.00289	-0.0031	0.0652	-0.00687
0.044	0.07846	-0.012752	-0.012934	-0.01382	0.0837	0.01427

It can be seen from table 13 that the errors between the experimental results and the model are less than those off ANSYS. This can be due to two major factors: first that ANSYS does not incorporate insertion into the model and second, it does not incorporate the rotation of

concentrated forces, as has been explained. It must be noted that ideally a similar comparison would be of value for the nonlinear model, but that finite element packages such as ANSYS do not incorporate the dependency of the deflection at each step as a function of the previous step, which arises in Nonlinear deflection.

10.4. General Conclusions Related to the Case Studies

Based on the results achieved in this chapter and results of the sensitivity study not included here, general conclusions related to various offset lengths can be drawn.

10.4.1. General Conclusions and Trends for the 22mm Offset Needle

1) Except for the Least Norm Solution, as shown in this chapter, for all other cases k has a decreasing trend versus deflection increase, which suggests either stress softening behaviour for the soft medium or decreasing effect of the soft medium elasticity in the insertion process.
2) The values of k start from around 2000 N/m2 and consistently decrease to 500 N/m2 for a maximum deflection of 10 mm.
3) Except for the Least Norm Solution, in other cases the absolute value of Rv increases first and then decreases with deflection. The range of variation of Rv is between -0.1 and -.02 N.
4) Except for the Least Norm Solution, in other cases Rh decreases with deflection. The range of variation of Rh is between .55 and 0.3 N.
5) Decreasing values for Rh and Rv seem to be compatible with stress softening behaviour of the soft medium, or it can be attributed to lesser involvement of the tip in the rupturing of soft medium, as insertion progresses.
6) The Least Norm Solution presents a very accurate tip path solution and very smooth variations for Rh and Rv. For this case, the absolute value of Rv increases with deflection and varies between -0.1 and -0.2N. Also, Rh increases with deflection and varies between 0.45 and 0.5N.
7) The increasing trend in Rh and Rv for the case of the Least Norm Solution is compatible with the constant k observed for this solution.

10.4.2. General Conclusions and Trends for the 33mm Offset Needle

1) Except for the Least Norm Solution, for all other cases, k has a decreasing trend versus deflection increase, which suggests either stress softening behaviour for the soft medium or a decreasing effect of the soft medium elasticity in the insertion process.
2) The values of k starts from around 800 N/m2 and consistently decreases to 150 N/m2 for a maximum deflection of 20 mm.
3) Except for the Least Norm Solution, in other cases the absolute value of Rv increases first and then decreases with deflection. The range of variation of Rv is between -0.09 and -.02N.
4) Except for the Least Norm Solution, in other cases Rh decreases with deflection. The range of variation of Rh is between .45 and 0.3N.
5) Decreasing values of Rh and Rv seem to be compatible with stress softening behaviour of the soft medium, or it can be attributed to lesser involvement of the tip in the rupturing of soft medium, as the insertion progresses.
6) The Least Norm Solution presents a very accurate tip path solution and very smooth variations for Rh and Rv. For this case, the absolute value of Rv increases with deflection and varies between -0.05 and -0.15N. Also, Rh increases with deflection and varies between 0.65 and 0.69N.
7) The increasing trend in Rh and Rv for the case of the Least Norm Solution is compatible with the constant k observed for this solution.
8) The nonlinear identification process is very sensitive to the starting parameters, achieved in the quasi linear identification process.

10.4.3. General Conclusions and Trends for the 44mm Offset Needle

1) Except for the Least Norm Solution, for all other cases, k has a decreasing trend versus deflection increase, which suggests either stress softening behaviour for the soft medium or a decreasing effect of the soft medium elasticity in the insertion process.
2) The values of k start from around 250 N/m2 and consistently decrease to 100 N/m2 for a maximum of insertion deflection of 20 mm.

3) Except for the Least Norm Solution, in other cases the absolute value of Rv first increases and then decreases with deflection. The range of variation of Rv is between -0.04 and -.015N.
4) Rh fluctuates with deflection. The range of variation of Rh is between 0.2 and 0.3N.
5) Decreasing values of Rh and Rv seem to be compatible with stress softening behaviour of the soft medium, or it can be attributed to lesser involvement of the tip in the rupturing of soft medium, as the insertion progresses.
6) The Least Norm Solution presents a very accurate tip path solution and very smooth variations for Rh and Rv. For this case the absolute value of Rv increases with deflection and varies between -0.04 and -0.06N. Also, Rh increases with deflection and varies between 0.2 and 0.21N.
7) The increasing trend in Rh and Rv for the case of the Least Norm Solution is compatible with the constant k observed for this solution.
8) The nonlinear identification process is very sensitive to starting parameters, achieved in the quasi linear identification process.

10.5. General Conclusions and Discussion of Needle Behaviour

From all the case studies undertaken so far, the following deductions can be drawn:

1) Except for the Least Norm Solution, for all offset values, k has a decreasing trend versus deflection increase, which suggests either stress softening behaviour for the soft medium or decreasing effect of the soft medium elasticity in the insertion process. This is shown in figure 10-43.

Figure 10-43 K variance trend for all experiments 22,33, and 44 mm offset.

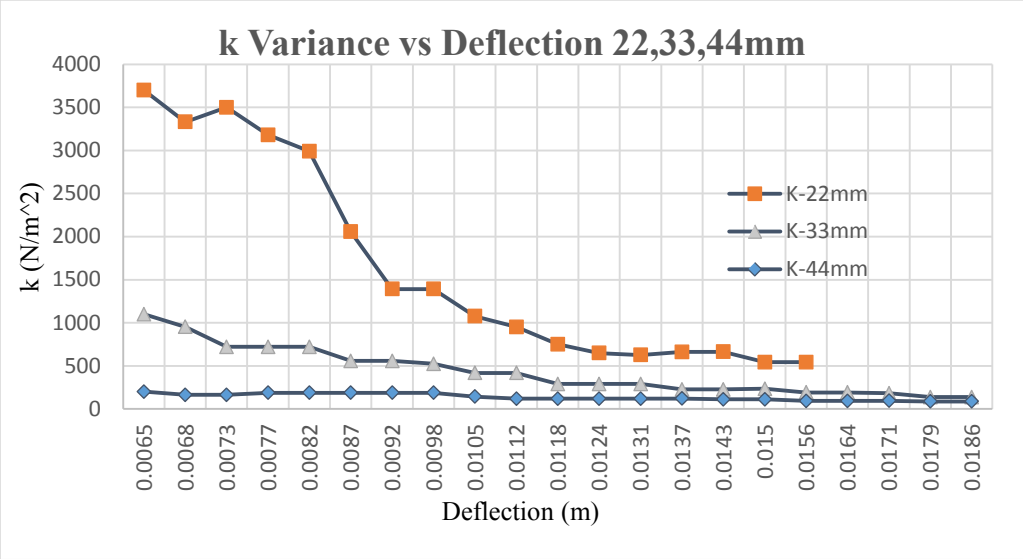

2) Although some degree of stress softening is reported for the gelatine that was used to produce the soft medium, the significant decrease in k values is more indicative of the latter reason, i.e. as the insertion progresses and the needle becomes weaker (due to the increasing length), the significant part of the effect of the elasticity of the soft medium is due to the material of the soft medium being pushed sideways to let the needle through and the elastic reaction to needle deflection diminishes.
3) The values of k starts from around 3500 N/m2 and consistently decreases to 500 N/m2 for 22mm, around 1000 N/m2 and consistently decreases to 150 N/m2 for 33mm, and around 250 N/m2 and consistently decreases to 100 N/m2 for 44mm, offset needles, respectively. This is compatible with the observations made in point 1 above.
4) Except for the Least Norm Solution, in other cases, the absolute value of Rv increases first and then decreases with deflection, as shown in figure 10-44. The range of variation of Rv is between, -0.1 and -.02 for 22mm, -0.09 and -.02 for 33mm, -0.045 and -.015 for 44mm, offset needles, respectively. As a mean value, one can take $Rv = -0.13\ [N]$ as the average constant value for most of the analyses.

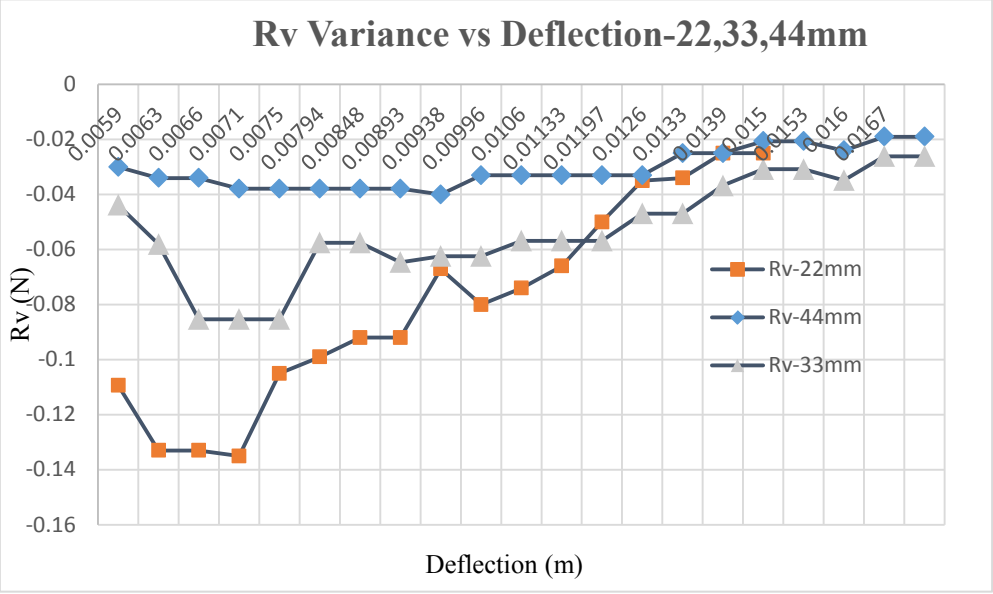

Figure 10-44. Rv Variance across experiments with 22,33 and 44mm offset

5) Except for the Least Norm Solution, in other cases Rh decreases with deflection, as shown in figure 10-45. The range of variation of Rh is between, 0.8 and 0.3 for 22mm, 0.65 and 0.3 for 33mm and 0.2 and 0.3 for 44mm, offset needles, respectively.

As a mean value, one can take $Rh = 0.35$ [N] as the average constant value for most of the analyses. Okamura et al. (Okamura, Simone et al. 2004) performed insertion tests with a bevel tipped needle of 1.27mm OD at 3mm/s in bovine liver, and observed a relatively steady trend in cutting of 0.8N and total axial force of 1N after initial puncture, which agrees with the trend seen in figure 10-45 and the approximate values identified here (see figure 8 in (Okamura, Simone et al. 2004)). It must be noted that the method for the measurement and calculation of the forces in the work differs (but does not disagree) with the model developed in this work. Hing et al. (Hing, Brooks et al. 2006) also performed needle insertion tests inside bovine liver, and observed a total insertion force between 0.5N to 1.5 N, and a calculated an almost constant cutting force of 5N (from defining a relationship between friction, total insertion force and cutting force, see figure 8 in (Hing, Brooks et al. 2006)). Due to the difference in geometry, material, and surrounding substrate between these studies, a conclusive quantification of insertion forces during insertion cannot be determined, though the literature and this work are in agreement regarding the general trend of the cutting force during insertion. Further experimentation can provide additional verification of the forces, as can be addressed in future work and has not been expanded upon here due to time limitations.

6) Decreasing values of Rh and Rv seem to be compatible with stress softening behaviour of the soft medium, or it can be attributed to a lesser involvement of the tip in the rupturing of soft medium, as the insertion progresses. It seems that, as the needle progresses, the compressive loads are applied to the soft medium in a sidewise direction (indicated in point 1 above), which responsible for rupture of the soft medium. The cutting force identified is comparable to the survey done by van Gerwen et al. (van Gerwen, Dankelman et al. 2012), showing the cutting force in literature to range between 0.05N (Wittek, Dutta-Roy et al. 2008) to 1.3N (Okamura, Simone et al. 2004).

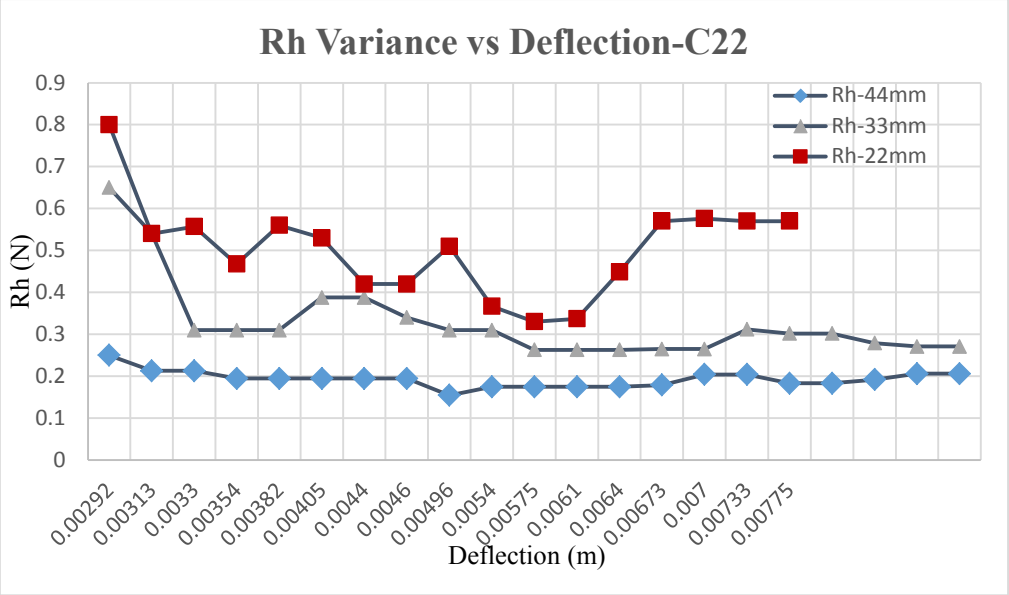

Figure 10-45 Rv Variance across experiments with 22,33 and 44mm offset

7) For all values of the needle offset, the Least Norm Solution presents a very accurate tip path solution and very smooth variations for Rh and Rv. For this case, the absolute value of Rv increases with deflection and varies between, -0.1 and -0.2 for 22mm, -0.05 and -0.15 for 33mm and -0.04 and -0.06 for 44mm, offset needles, respectively. Also, Rh increases with deflection and varies between, 0.45 and 0.5 for 22mm, 0.65 and 0.69 for 33mm and 0.2 and 0.21, offset needles, respectively.
8) The increasing trend in Rh and Rv for the case of the Least Norm Solution is compatible with the constant k observed for this solution.
9) The nonlinear identification process is very sensitive to the starting parameters, achieved in the quasi linear identification process.
10) In general, a unique solution does not exist and different solutions can be achieved for both quasi nonlinear and nonlinear identification cases, by changing the solution parameters. However, this does not mean that all of the solutions are meaningful. For example, for the quasi nonlinear case, if a proper number of insertion averaging, m, is not selected, then values for Rh, k and Rv associated with MIN(least squares error) of equation (5-34) will not make physical sense, e.g. $k = 0$ or $Rh = 0$ or $Rv > 0$ values will result, or the solution would be in the minimum SVD zone of the solution space. The same notion applies to nonlinear identification, i.e. if the nonlinear process is started with unreasonable initial estimates, the solution will not converge, as indicated in point 8 above.

10.6. CONCLUSION

In this chapter, the performance of the quasi-nonlinear and nonlinear forward and reverse models were studied by comparison of simulated results with experimental results, conducted as explained in chapter 9. Initially, the quasi-nonlinear reverse identification model was used to predict the forces acting on the needle for three insertion experiments of 22, 33 and 44mm offset. These forces were then inputted into the nonlinear progressive insertion model to compare predicted tip deflections against those measured in the experiments. The forces were identified for a subset of the tip path data, and the insertion over the corresponding regions modelled with their respective force sets. The results showed a tip deflection error of less than 1% for the final insertion stage of the 44 mm offset needle, when the needle is in a large deflection domain of over 20% tip slope, which is high in accuracy. The reverse identification and progressive insertion models were also compared with FE models of the same setup, with a maximum error between FEM and modelled results of 0.08%, which was experienced for the final insertion stage of the 44 mm offset needle. It must be noted that the average flexural modulus of the needle in the small strain region is 56 MPa, which is significantly lower than the stiffness of virtually all other needles described in the literature. Despite this, the errors of the progressive insertion model are comparable to previous models, with errors between 2.1% and 35% for 45 GPa insertion modelled via a small deflection linear insertion model, wherein the cutting angle and forces are assumed constant during the insertion process.

11. CONCLUSION

11.1. SUMMARY

As has been discussed in chapter 1, a mathematical model which accurately predicts the deflection of the needle as a function of its mechanical variables is required, to aid in the optimisation of the design and to improve the closed-loop control of the needle tip path. Due to the fragile/unpredictable nature of biological soft tissue and the uniqueness of any given setup, experiments that can be conducted on actual specimen are limited. Given the tight radii of curvature achievable with the STING (down to 70 mm), the model developed must also be applicable to large deflection insertion, and models relying on soft material parameters during

large deflection are complex and very time consuming, as they require constant parameter recalculation over their geometry.

In this work, a method is developed and proposed for the nonlinear forward and reverse modelling of a highly flexible, multi part, needle insertion process. The forward procedure will enable the tip path determination of the needle during insertion, under a known set of tip loads and substrate stiffness. On the other hand, the reverse process will enable the determination of tip loads and substrate stiffness during insertion, using the tip path data only.

The need for such a model and procedure development originates from the following:

- None of the commercial packages can forward-model a progressive insertion process;
- None of the works reported so far consider geometrical, large deflection nonlinearity;
- None of the works reported so far can consider material nonlinearity;
- Most of the works reported so far assume known tip loads and/or a constant cutting angle;
- None of the works reported so far can handle a reverse solution.

The developed methodology will have the following applications, which can significantly impact the needle and needle path design and optimisation, as well as the design of the needle controlling system:

- Identification of the typical loads acting on the needle during real world surgeries and hence obtain a realistic view of the needle interaction with the tissue involved. This can subsequently be assembled into a database. It should be noted that the direct measurement of the loads acting on the needle in a real surgical procedure is very difficult, if not impossible.
- Using the identified loads mentioned above, to analyse the sensitivity of the needle loads to various parameters, such as age, physical conditions of the patient, etc.
- The identified loads and database can be used, along with the forward-model, to predict the needle's behaviour prior to surgery, and to optimise its parameters.

Based on the currently available models and the advantages and disadvantages of each in application to the highly flexible needle, as discussed in chapter 1 and 2, it is proposed that a

large deflection nonlinear, progressive, beam model be employed for the modelling of the highly flexible multipart needle during insertion into soft tissue, and inverse solving the model for the identification of the loads acting on the system.

It was then endeavoured to develop, throughout the thesis, a model which, without need of the material properties of surrounding substrate, can identify the forces acting on the needle during insertion, including rotating axial and vertical forces at the tip. Additionally, it should not make any presumption that the needle tip trajectory during insertion coincides with the final shape of the needle, as it relies solely on the tip path as input. It also eliminates the assumption of a constant cutting angle at the tip of the needle, allowing instead its recalculation during insertion.

In order to achieve this, initially, in chapter 3, the theoretical background of inverse force identification and the related mathematical issues were studied, and the mathematical methodology to obtaining inverse load identification from the beam model established. On this basis, it was proposed that a boundary value problem in the form of the equilibrium equation of an Euler Bernoulli beam be formulated for estimation of the needle deflection, the inverse solution of which would allow identification of the forces acting on the needle. It was seen that the inverse solution methodology involves the solving of PDEs through a weighted residual method (WRM) which, in turn, necessitates numerical conditioning of the resulting model matrixes. To this end, the Tikhonov Regularization method and the Galerkin WRM were proposed for further study, and a simplified physical model of the needle as a beam was explained, for which an equilibrium equation was written and the boundary value problem subsequently developed.

The Euler Bernoulli beam theory and the basic assumptions regarding the small deflection of the needles beam model was described in chapter 4. It was explained that the governing assumptions of the model are reliant on whether the needle's deflection is small or large, and whether the large deflection assumptions present complexities in the beam equilibrium equations, which can be neglected in small deflection. Subsequently, the linear equations governing small deflection of the needle, as a function of each of the forces acting on it, was developed, and the individual contribution of different forces to the needle's deflection defined through equations, providing a means to make preliminary observations about the role of each of these acting forces on needle deflection. In chapter 5, the first two steps towards developing a nonlinear model from the basic linear beam model were made, namely:

(1) including the rotating axial component of the cutting force at the tip of the needle during insertion; and (2), the addition of springs acting between the substrate boundary and the needle, accounting for the variation of the contact forces along the length throughout insertion. This model was named the “quasi-nonlinear” model, the solution of which required selection of the trial functions of the Galerkin weighted residual method. A model of the needle insertion was also developed, providing the link between the deflections at each step of insertion with the deflection of the previous insertion step.

In order to extend the model to be applicable to large deflection modelling, the nonlinear Euler Bernoulli model of the needle was developed in chapter 6, incorporating the length extension model previously defined in chapter 7. The final form of the equation governing the beam was defined as a function of forces acting on beam model from the surrounding substrate, the increase in length of the needle, and previous state parameters. By substituting these parameters, the forward modelling of the beam’s nonlinear deflection is the Galerkin solution to the nonlinear Euler Bernoulli equation. The methodology to obtaining the inverse solution to the governing nonlinear Euler Bernoulli, allowing identification of the forces acting on the needle in nonlinear range, was explained in chapter 8. It was shown that, in order to be able to identify the forces acting on the needle at any step, the forward model must also be solved from its last deflected state to complete the prerequisite stages.

Experiments designed for validation and verification of the model were presented in chapter 9, where a needle prototype was inserted into a soft substrate and the tip path recorded for insertions with varying offset geometries of 22, 33 and 44mm. Three point flexural tests on specimen of the needle material were carried out and a stress strain curve was derived for use in the nonlinear progressive insertion model and reverse force identification model. In chapter 10, the nonlinear reverse identification model was subsequently used to predict the forces acting on the needle during the three insertion experiments, which were then inputted into the nonlinear progressive insertion model to compare predicted tip deflections against those measured in the experiments. The forces were identified for the tip path data for each experiment, and the deflection throughout the insertion modelled with their respective identified force set. The results showed a tip deflection error of less than 1% for the final insertion stage of the 44mm offset needle, when the needle is in nonlinear deflection regime. The reverse identification and progressive insertion models were also compared with FE models of the same setup, with a maximum approximate error between FEM and modelled results of 10%, which was experienced for the final insertion stage of the 33 mm offset

needle. It must be noted that the average flexural modulus of the needle in the small strain region is 56 MPa, which is significantly lower than the stiffness of virtually all other needles described in the literature. Despite this, the errors of the progressive insertion model are comparable to previous models (Misra, Reed et al. 2010), with errors between 2.1% and 35% for a needle of stiffness 45 GPa. For all these references, the deflection during insertion was computed via a small deflection linear insertion model, wherein the cutting angle and forces are assumed constant during the insertion process.

11.2. LIMITATIONS

The main sources of error in this work can be defined in the following:

- The physical model of the needle as a beam with no interlock and no bevel tip introduces errors due to the inaccuracies resulting from the geometrical simplifications.
- The mechanical parameters of the needle such as the flexural modulus have been defined for a small strain window of deflection and assumed to be valid during comparison of experimental and modelled results.
- The discretization although providing satisfying results between the experimental and modelled results, can include smaller elements thus leading to higher accuracy in results. This is turn will necessitate higher calculation time and a compromise between the two must be reached.
- The boundary condition simplifications of the model specifically at point of entry of the needle into the substrate neglects the effect of the trocar and the effects of the forces acting on the needle prior to its point of entry into the substrate.
- The initial point of entry into the substrate includes puncture of the substrate via needle tip. As such, residual stresses are existent within the needle-substrate system, which have been neglected for simplification.

Current limitations of the model include the fact that it has been modelled in 2D. The model's expansion to 3D would allow modelling and studying the effect of possible rotation of the needle, as well as expanding it to model the 4 part needle geometry, as has been mentioned in chapter 1. The model can be further improved by including the bevel tip of the needle in the physical Euler Bernoulli model, although the effect has been assumed to be included through the angle of the tip forces. Although, due to the very small diameter, the exact determination of the neutral axis along the length of the needle has been removed from the equilibrium equations, for larger offsets or thicker needles, it may be of importance, and thus including it would increase the accuracy. For larger deflections also, including the accurate flexural material model for the respective strain will enhance the accuracy of the modelled deflections and identified forces. However, the high accuracy of the results shown

when assuming one flexural modulus for all deflections, suggests a low impact for the case of this specific material.

As far as the substrate is concerned, the proposed method assumes constant contact stiffness for substrate material. This assumption may not hold true for substrate materials which have strong material nonlinearity such as strain softening or hardening. For materials with including layers of substrate which would include non-homogenous properties, the force identification system would have to be discretized into smaller steps along the length as well as during identification steps, such as to allow correct calculation of the forces throughout insertion.

Another limitation of the proposed method would be the rapid insertion process. In such cases, the dynamic effects of probe vibrations, as well as the visco-elastic behaviour of the substrate may become important.

12. FUTURE WORK

Based on the observations made throughout the research, it is felt that there are certain areas which can be improved to enhance the performance of the proposed method. The suggested improvements will have different impacts on the performance of the proposed identification method, thus the improvement suggestions will be discussed next in an increasing order of significance.

12.1. Using Two Points of Calibration in the Identification Process

In the way the proposed identification method currently works, the only input parameter which is used for both quasi non-linear and non-linear identification procedures is the measured tip deflection, $\{Y_{tx}\}$. As a result, all identified forces and stiffness values are calibrated to $\{Y_{tx}\}$. On the other hand, as indicated in point 9 of section 11.3, the identified solutions are not unique. In order to increase the degree of uniqueness, it is proposed to use more measured deflection values in the identification process. Obviously, the more measured points are used in the identification process, the more accurate and unique the solution which can be achieved. However, having more points measured will, in turn, mean more sensors being mounted on the needle, which is not practical and alters the very parameters which are under identification. It is suggested to use the data from additional sensors at the offset to improve the performance of the method.

12.2. Removing The Assumption of Fixed Offset Length

As experimental observations indicate, the two parts of the probe slide on each other, during insertion. This will result in slight variations in offset length through insertion process. I a sensor is placed at offset point, as suggested in 11.2.1., then one can calculate the true offset length at each insertion step and use the true length in the identification process.

12.3. Length Conservation Method and $\{Z\}$ Correction

As indicated in section 6.3, equations (6-12) and (6-13) should be used in order to keep the length of the needle constant by modifying {Z}, through the forward solution which is necessary during the identification process (see 8.2). Due to the very slow nature of the insertion, as well as the high sampling frequency, a sequential, iterative, method was used in the current work for {Z} correction. In other words, in the nonlinear identification phase, first equation (7-17) is solved for the $\{Y_i\}$ associated with L_i (total length of the needle at insertion step i) and then, equations (7-12) and (7-13) of chapter 6 are used to modify $\{Z_i\}$. The modified $\{Z_i\}$ is then back substituted in equation (7-17) and a new $\{Y_i\}$ is found. This process is iterated until the changes in $\{Z_i\}$ and $\{Y_i\}$ from subsequent iterations are small enough. It is suggested to use equation (6-12) in conjunction with equation (7-17) to find the a_j values that yield the minimum error $\{Y_i\}$ solution and at the same time modify the $\{Z_i\}$ vector.

12.4. Assuming Nonlinear Contact Stiffness For Substrate Material

The assumption that the forces along the length of the needle act as springs has also removed the necessity of assuming a specific force pattern acting from the substrate onto the tissue. The pattern of forces acting along the length of the needle can thus be found from inspection of the results for each experiment. A possible improvement on this would be to assume nonlinear springs instead of the linear ones included in this model. This would provide a means to study the deformation of the surrounding material and allow possible identification of a material model for the surrounding substrate.

12.5. Conclusion

In the work presented in this thesis, the author has strived to present a quasi-nonlinear and nonlinear model of the deflection of a biologically inspired flexible needle during insertion into a soft substrate. The model has shown the ability to, through a reverse identification process, identify the forces acting on the needle at any point of insertion, without the need to have the material properties of the substrate surrounding the needle.

Additionally, the model has demonstrated the ability to identify the forces acting on the needle, by inputting only the tip deflection of the needle throughout the insertion, eliminating the need to assume a relationship between the tip path and the body shape of the needle. In the progressive model, the needle's deflection at any point of its geometry has been predicted by inputting the forces acting on the needle at any point in time, onto the model. Comparison of the FEM results, the model's, and the experimental deflections has shown the added ability to include the effect of the insertion into the model, as well as the effects of rotation of the concentrated forces acting on the tip during nonlinear insertion, which FEM does not automatically do. Comparison of the FEM results with those of the model, in which the forces were identified from experiments, has also demonstrated the validity of the forces assumed acting on the needle throughout insertion. The effect of the inclusion of the horizontal component of the tip force was, as had been anticipated, pronounced, showing the benefit of the development of the quasi-nonlinear model for small deflection ranges.

The model is capable of producing reasonably accurate results, with as little as three data points from experiments, allowing the removal of any assumption regarding the relationship between the offsets and the curvature of the needle, as well as the general shape of the needle. The iterative nature of the model allows the inclusion of a varying offset geometry

throughout insertion, by inputting different offset values at any step during which it increases. This theoretical capability must, however, be tested in future experimental work.

The work presented here is by no means complete nor does it claim to be the only possible approach to the needle insertion problem. However, it provides a systematic approach to the tackling of a highly complex and nonlinear process, providing the necessary structure that allows considering complicated processes such as identification, insertion, contact and large deflection all together. In this sense, the work is unique.

13. REFERENCES

A. N. Tikhonov "Solution of incorrectly formulated problems and the regulariza-

tion method." Dokl. Akad. Nauk. SSSR(151): 501{504.

A. N. Tikhonov & V. Y. Arsenin (1977). Solutions of Ill-Posed Problems,. Washington, D.C., Winston &

Sons.

Abayazid, M., et al. (2013). "Integrating Deflection Models and Image Feedback for Real-Time Flexible Needle Steering." Robotics, IEEE Transactions on **29**(2): 542-553.

Abolhassani, N., et al. (2007). Needle control along desired tracks in robotic prostate brachytherapy. Systems, Man and Cybernetics, 2007. ISIC. IEEE International Conference on.

Abolhassani, N., et al. (2007). "Needle insertion into soft tissue: A survey." Med Eng Phys **29**(4): 413-431.

Abolhassani, N. and R. V. Patel (2006). Deflection of a Flexible Needle during Insertion into Soft Tissue. Engineering in Medicine and Biology Society, 2006. EMBS '06. 28th Annual International Conference of the IEEE.

Alterovitz, R., et al. (2005). Planning for Steerable Bevel-tip Needle Insertion Through 2D Soft Tissue with Obstacles. Robotics and Automation, 2005. ICRA 2005. Proceedings of the 2005 IEEE International Conference on.

Alterovitz, R., et al. (2003). Needle insertion and radioactive seed implantation in human tissues: simulation and sensitivity analysis. Robotics and Automation, 2003. Proceedings. ICRA '03. IEEE International Conference on.

Alterovitz, R., et al. (2005). Steering flexible needles under Markov motion uncertainty. Intelligent Robots and Systems, 2005. (IROS 2005). 2005 IEEE/RSJ International Conference on.

Anger, G. (1988). "Cannon, J. R.; Hornung, U. (eds.), Inverse Problems. Proceedings of the Conference held at the Mathematical Research Institute at Oberwolfach, Black Forest, May 18–24, 1986. Basel etc., Birkhäuser Verlag 1986. 192 pp., sfr. 60.–. ISBN 3-7643-1842-2 (ISNM 77)." ZAMM - Journal of Applied Mathematics and Mechanics / Zeitschrift für Angewandte Mathematik und Mechanik **68**(6): 230-230.

Anger, G. (1990). Inverse Problems in Differential Equations. Berlin, Springer.

Asadian, A., et al. (2012). "A Novel Force Modeling Scheme for Needle Insertion Using Multiple Kalman Filters." Instrumentation and Measurement, IEEE Transactions on **61**(2): 429-438.

Baena, S. Y. K. a. F. R. y. (2012). "Towards a miniturized needle steering system with path planning for obstacle avoidance." IEEE Trans Biomed Eng.

Barbé, L., et al. (2007). "Needle insertions modeling: Identifiability and limitations." Biomedical Signal Processing and Control **2**(3): 191-198.

Boroomand, A., et al. (2014). "Dynamical modeling and controllability analysis of a flexible needle in soft tissue." International Journal of Modeling, Simulation, and Scientific Computing **05**(02): 1350031.

Bro-Nielsen, M. (1998). "Finite element modeling in surgery simulation." Proceedings of the IEEE **86**(3): 490-503.

Burrows, C., et al. (2013). Experimental Characterisation of a Biologically Inspired 3D Steering Needle, IEEE**:** 1252-1257.

Busby, H. R. and D. M. Trujillo (1987). "Solution of an inverse dynamics problem using an eigenvalue reduction technique." Computers & Structures **25**(1): 109-117.

Choi, K. S., et al. (2004). "An efficient and scalable deformable model for virtual reality-based medical applications." Artif Intell Med **32**(1): 51-69.

Comas, O., et al. (2008). Efficient Nonlinear FEM for Soft Tissue Modelling and Its GPU Implementation within the Open Source Framework SOFA. Proceedings of the 4th international symposium on Biomedical Simulation. London, UK, Springer-Verlag**:** 28-39.

Cotin, S., et al. (2000). "A hybrid elastic model for real-time cutting, deformations, and force feedback for surgery training and simulation." The Visual Computer **16**(8): 437-452.

Cover, S., et al. (1993). "Interactively Deformable Models for Surgery Simulation." IEEE Comput. Graph. Appl. **13**(6): 68-75.

Crouch, J. R., et al. (2005). A velocity-dependent model for needle insertion in soft tissue. Proceedings of the 8th international conference on Medical image computing and computer-assisted intervention - Volume Part II. Palm Springs, CA, Springer-Verlag**:** 624-632.

Davies, B. (2006). "Essay: Medical robotics?a bright future." The Lancet **368**: S53-S54.

Deussen, O., et al. (1995). Using Simulated Annealing to Obtain Good Nodal Approximations of Deformable Bodies. In Sixth Eurographics Workshop on Simulation and Animation, Springer.

DiMaio, S. P. and S. E. Salcudean (2002). Needle insertion modelling and simulation. Robotics and Automation, 2002. Proceedings. ICRA '02. IEEE International Conference on.

Dobson, B. J. and E. Rider (1990). "A Review of the Indirect Calculation of Excitation Forces from Measured Structural Response Data." Proceedings of the Institution of Mechanical Engineers, Part C: Journal of Mechanical Engineering Science **204**(2): 69-75.

Famaey, N. and J. Vander Sloten (2008). "Soft tissue modelling for applications in virtual surgery and surgical robotics." Comput Methods Biomech Biomed Engin **11**(4): 351-366.

Frasson, L. (2010). A Novel Flexible and Steerable Probe for

Minimally Invasive Soft Tissue Intervention. Mechanical Engineering. London, Imperial College. **PhD:** 170.

Frasson, L., et al. (2012). "Experimental evaluation of a novel steerable probe with a programmable bevel tip inspired by nature." Journal of Robotic Surgery **6**(3): 189-197.

Frasson, L., et al. (2010). "STING: a soft-tissue intervention and neurosurgical guide to access deep brain lesions through curved trajectories." Proc Inst Mech Eng H **224**(6): 775-788.

Fung, Y. C. (1993). Biomechanics: Mechanical Properties of Living Tissues, Springer.

Garlapati, R. R., et al. (2014). "More accurate neuronavigation data provided by biomechanical modeling instead of rigid registration." J Neurosurg **120**(6): 1477-1483.

Giergiel, J. and T. Uhl (1989). "Identification of the input excitation forces in mechanical structures.Arch.Transp." **1**(1): 8-24.

Goksel, O., et al. (2009). "Modeling and simulation of flexible needles." Medical Engineering & Physics **31**(9): 1069-1078.

Góral, G., et al. (2002). "Intelligent Transducers of In-Operational Loads in Construction Fatigue Monitoring." Machine Dynamics Problems **Vol. 26, No. 2/3**: 73-88.

Grote, K.-H. a. F., J. (2007). Dubbel-Taschenbuch für den Maschinenbau, Berlin/Heidelberg/New York: Springer.

Hadamard, J. (1923). Lectures on Coughy's Problem in Linear Partial Differential Equations. New Haven, Yale University Press.

Hansel, E. (1991). Inverse Theory and Applications for Engineers. Englewood Cliffs.

Hansen, P. (1989). "Regularization,GSVD and truncatedGSVD." BIT Numerical Mathematics **29**(3): 491-504.

Hansen, P. C. (2008). Regularization Tools

A Matlab Package for Analysis and Solution of Discrete Ill-Posed Problems

Version 4.1 for Matlab 7.3. I. a. M. Modelling, T. U. o. D. Building 321 and D. DK-2800 Lyngby.

Hing, J. T., et al. (2006). Reality-based needle insertion simulation for haptic feedback in prostate brachytherapy. Robotics and Automation, 2006. ICRA 2006. Proceedings 2006 IEEE International Conference on.

Horton, A., et al. (2010). "A Meshless Total Lagrangian explicit dynamics algorithm fpr surgical simulation." international journal for numerical for numerical methods in biomedical engineering(26): 997-998.

Jin, X., et al. (2014). "Meshless algorithm for soft tissue cutting in surgical simulation." Comput Methods Biomech Biomed Engin **17**(7): 800-811.

Joldes, G. R., et al. (2009). "Computation of intra-operative brain shift using dynamic relaxation." Computer methods in applied mechanics and engineering **198**(41): 3313-3320.

Kataoka, H., et al. (2002). Measurement of the Tip and Friction Force Acting on a Needle during Penetration. Proceedings of the 5th International Conference on Medical Image Computing and Computer-Assisted Intervention-Part I, Springer-Verlag**:** 216-223.

Kerl, J., et al. (2012). "Tissue deformation analysis using a laser based digital image correlation technique." Journal of the Mechanical Behavior of Biomedical Materials **6**(0): 159-165.

Ko, S. Y., et al. (2010). Two-Dimensional Needle Steering with a "Programmable Bevel"

Inspired by Nature: Modeling Preliminaries. 2010 IEEE/RSJ International Conference on Intelligent Robotics and Systems. Taipei,Taiwan.

Ko, S. Y. and F. Rodriguez y Baena (2013). "Toward a miniaturized needle steering system with path planning for obstacle avoidance." IEEE Trans Biomed Eng **60**(4): 910-917.

Kobayashi, T., et al. (2009). "Phase I/II clinical study of percutaneous vertebroplasty (PVP) as palliation for painful malignant vertebral compression fractures (PMVCF): JIVROSG-0202." Ann Oncol **20**(12): 1943-1947.

Kühnapfel, U., et al. (2000). "Endoscopic surgery training using virtual reality and deformable tissue simulation." Computers & Graphics **24**(5): 671-682.

Kyle B.Reed, V. K., Ron Alterovitz, Ken Goldberg, Allison M.Okamura, Noah J.Cowan (2008). Integrated Planning and Image Guided Control For Planar Needle Steering International Conference Biomed Robot Biomechatron**:** 819-824.

Lehmann, T., et al. (2013). "Force-Sensor-Based Estimation of Needle Tip Deflection in Brachytherapy." Journal of Sensors **2013**: 10.

Leibinger, A., et al. (2014). Multi-objective Design Optimization for a Steerable Needle for Soft Tissue Surgery. The 15th International Conference on Biomedical Engineering. J. Goh, Springer International Publishing. **43:** 420-423.

Li, M., et al. (2015). "Patient-specific biomechanical model as whole-body CT image registration tool." Medical Image Analysis **22**(1): 22-34.

Mendis, K. K., et al. (1995). "A constitutive relationship for large deformation finite element modeling of brain tissue." J Biomech Eng **117**(3): 279-285.

Miller, K. (1999). "Constitutive model of brain tissue suitable for finite element analysis of surgical procedures." Journal of Biomechanics **32**(5): 531-537.

Miller, K. and K. Chinzei (1997). "Constitutive modelling of brain tissue: Experiment and theory." Journal of Biomechanics **30**(11): 1115-1121.

Miller, K. and K. Chinzei (2002). "Mechanical properties of brain tissue in tension." Journal of Biomechanics **35**(4): 483-490.

Miller, K., et al. (2007). "Total Lagrangian explicit dynamics finite element algorithm for computing soft tissue deformation." Communications in Numerical Methods in Engineering **23**(2): 121-134.

Miller, K., et al. (2011). Biomechanical Modeling of the Brain for Computer-Assisted Neurosurgery. Biomechanics of the Brain. K. Miller, Springer New York**:** 111-136.

Miller, K., et al. (2010). "Modelling brain deformations for computer-integrated neurosurgery." International Journal for Numerical Methods in Biomedical Engineering **26**(1): 117-138.

Misra, S., et al. (2008). Needle-tissue interaction forces for bevel-tip steerable needles. Biomedical Robotics and Biomechatronics, 2008. BioRob 2008. 2nd IEEE RAS & EMBS International Conference on.

Misra, S., et al. (2010). "Mechanics of Flexible Needles Robotically Steered through Soft Tissue." The International Journal of Robotics Research.

Mostayed, A., et al. (2013). "Biomechanical Model as a Registration Tool for Image-Guided Neurosurgery: Evaluation Against BSpline Registration." Annals of Biomedical Engineering **41**(11): 2409-2425.

Okamura, A. M., et al. (2004). "Force modeling for needle insertion into soft tissue." Biomedical Engineering, IEEE Transactions on **51**(10): 1707-1716.

Oldfield, M. J., et al. (2014). "Highly resolved strain imaging during needle insertion: Results with a novel biologically inspired device." Journal of the Mechanical Behavior of Biomedical Materials **30**(0): 50-60.

Paz, M., Leigh,William (2003). Structural Dynamics,Theory and Computation. Springer**:** 840.

Phillips, D. L. (1962). "A Technique for the Numerical Solution of Certain Integral Equations of the First Kind." J. ACM **9**(1): 84-97.

Pieper, S. D. (1989). More Than Skin Deep, Physical Modeling of facial Tissue. Media Arts and Sciences Section, Massachusetts University of Technology. **Master of Science:** 121.

Quinn, K. P. and B. A. Winkelstein (2010). "Full field strain measurements of collagenous tissue by tracking fiber alignment through vector correlation." J Biomech **43**(13): 2637-2640.

Radetzky, A. and A. Nürnberger (2002). "Visualization and simulation techniques for surgical simulators using actual patient's data." Artificial intelligence in medicine **26**(3): 255-279.

Raffel, M., et al. (20017). Particle Image Velocimetry. Springer-Verlag Berlin Heidelberg, Springer-Verlag Berlin Heidelberg.

Reed, K. B., et al. (2009). "Modeling and Control of Needles with Torsional Friction." IEEE Trans Biomed Eng **56**(12): 2905-2916.

Robert, A. L. G., et al. (2013). "A generic three-dimensional static force distribution basis for a medical needle inserted into soft tissue." Journal of the Mechanical Behavior of Biomedical Materials **28**(0): 156-170.

Roesthuis, R. J., et al. (2014). "Three-Dimensional Needle Shape Reconstruction Using an Array of Fiber Bragg Grating Sensors." Mechatronics, IEEE/ASME Transactions on **19**(4): 1115-1126.

Rucker, D. C., et al. (2013). "Sliding Mode Control of Steerable Needles." Robotics, IEEE Transactions on **29**(5): 1289-1299.

Seong Young, K., et al. (2010). Two-dimensional needle steering with a “programmable bevel” inspired by nature: Modeling preliminaries. Intelligent Robots and Systems (IROS), 2010 IEEE/RSJ International Conference on.

Seong Young, K., et al. (2011). "Closed-Loop Planar Motion Control of a Steerable Probe With a “Programmable Bevel” Inspired by Nature." Robotics, IEEE Transactions on **27**(5): 970-983.

Swaney, P. J., et al. (2013). "A Flexure-Based Steerable Needle: High Curvature With Reduced Tissue Damage." Biomedical Engineering, IEEE Transactions on **60**(4): 906-909.

Szegedi, M., et al. (2012). "Tissue characterization using a phantom to validate four-dimensional tissue deformation." Medical Physics **39**(10): 6065-6070.

Terzopolous and Waters (1991). "Techniques for realistic facial modeling and animation." Springer: 59-73.

Terzopoulos, D., et al. (1987). Elastically deformable models. Proceedings of the 14th annual conference on Computer graphics and interactive techniques, ACM**:** 205-214.

Tödtheide, A. (2013). Steering Behaviour Analysis of a Robotic Catheter Used for Soft Tissue Surgery. Mechanical Engineering, Imperial College. **Msc:** 96.

Tödtheide, A. (2013). Steering Behaviour Analysis of a Robotic Catheter Used for Soft Tissue Surgery

Mechanical Engineering, Imperial College London. **Masters:** 96.

Trujillo, D. M., Busby, H.R. Practical Inverse Engineering. London, CRC Press, London.

Uhl, T. (1998). Computer Assisted Identification of Mechanical Structures (In Polish). Warszawa, WNT.

Uhl, T. (2002). "Identyfication pf loads in mechanical structures-helicopter case study." Computer Assisted Mechanics and Engineering Sciences **Vol. 9, No. 1**: 151-160.

Uhl, T. (2007). "The inverse identification problem and its technical application

" Archive of Applied Mechanics **77**(5): 325-337.

Uhl, T. (2007). "The inverse identification problem and its technical application." Archive of Applied Mechanics **77**(5): 325-337.

Uhl, T. and K. Mendrok (2005). IInverse Identification Problems: Theory and Practical Applications. (in Polish). Krakow, ITE Press.

Uhl, T., Pieczara, J (2003). "Identification of operational loading forces for mechanical structures,Arch,Transp." **16**(2): 109-126.

van Gerwen, D. J., et al. (2012). "Needle-tissue interaction forces--a survey of experimental data." Med Eng Phys **34**(6): 665-680.

van Veen, Y. R., et al. (2012). "Macroscopic and microscopic observations of needle insertion into gels." Proc Inst Mech Eng H **226**(6): 441-449.

Vincent, J. F. V. (1995). "The mechanism of drilling by wood wasp ovipositors." Biomimetics **v. 3(4)** p. 187-201.

Webster, R. J., et al. (2006). "Nonholonomic Modeling of Needle Steering." The International Journal of Robotics Research **25**(5-6): 509-525.

Webster, R. J., et al. (2005). Design Considerations for Robotic Needle Steering. Robotics and Automation, 2005. ICRA 2005. Proceedings of the 2005 IEEE International Conference on.

Wittek, A., et al. (2008). "Subject-specific non-linear biomechanical model of needle insertion into brain

" Comput Methods Biomech Biomed Engin **11**(2): 135-146.

Wittek, A., et al. (2010). "Patient-specific non-linear finite element modelling for predicting soft organ deformation in real-time: application to non-rigid neuroimage registration." Prog Biophys Mol Biol **103**(2-3): 292-303.

Yan, K. G., et al. (2009). "Flexible needle-tissue interaction modeling with depth-varying mean parameter: preliminary study." IEEE Trans Biomed Eng **56**(2): 255-262.

Zha, H. and P. C. Hansen (1990). "Regularization and the General Gauss-Markov Linear Model." Mathematics of Computation **55**(192).